Para conocimiento de la Comisión Académica: En el ínterim de tiempo transcurrido desde que la EDONA envía a la Comisión Académica los informes de los revisores informes (14/08/2023) y el día 29/08/2023 (la CA todavía no se ha pronunciado al respecto), la doctoranda presenta una nueva versión de la tesis, por iniciativa propia, atendiendo las recomendaciones de los revisores externos.

3D-printable composites for magnetic refrigeration based on Ni-Mn-In-Co shape memory alloys

Memory presented by:

Deepali Khanna

Supervisors:

José Ignacio Pérez de Landazábal Berganzo

Vicente Sánchez-Alarcos Gómez

https://doi.org/10.48035/Tesis/2454/46629

ACKNOWLEDGMENTS

This thesis has been carried out with the support of institution Public University of Navarra (UPNa) with a financial support during four years with a PhD contract "Contratos Pre-doctorales adscritos a Grupos e Institutos de Investigación de la Universidad Pública de Navarra", and also I would like to acknowledge my gratitude towards the following people.

First, I would like to sincerely thank my thesis supervisors, Iñaki Pérez-Landazábal and Vicente Sánchez-Alarcos, for providing the opportunity to work with them in this project. Above all, I also would like to emphasize how approachable, dedicated, committed and trusting they have been throughout the project, demonstrating their excellent human qualities and making work with them a pleasure. Likewise, I would like to express my gratitude to Vicente Recarte, who, as a member of the research team, has demonstrated tremendous availability by offering a critical assessment of the project, the experiments and the publications.

I also would like to thank Cristina Gómez-Polo, who supported me during all this time.

In addition, I would also like to thank my fellow mates that I met during my stay at the UPNa. Firstly to Paulo La Roca, who supported and guided me excellently during my thesis. His unconditional support and availability I cannot forget. Secondly, to Jesus, Laura, Itziar, Alberto, Eneko, Maitane, Lucia, Maialen, Izazkun and Zuberoa, who made the office very friendly place to work.

I would also like to thank my friends Harry, Shilpa, Sonu, Abhinay and Dhanya, who never failed to show their support even from India. To my friends from Indian community in Spain, Jabir, Reshmi, Preeti, Mayank, Mahima, and Dinesh, with whom the problems of the week vanished and unforgettable weekends were spent.

I would like to thank my husband, Javier López García, who I met luckily during my thesis. You did not just support me as a partner but also as a researcher. Big and heartfelt thanks to you for supporting and guiding me on my tough times and helping me refine the XRD data. Without you, this milestone would have been difficult to cross.

I will now change the language to thank the rest of the people in my life.

जिन लोगों के बिना,भारत से यहां तक का सफ़र अस्तित्व में ही नहीं होता, वो है मेरा परिवार और मेरे निकट संबंधी. मेरे पिता श्री लाजपत राय, मेरी मां श्रीमती आशु, मेरे बड़े पापा आदरणीय अरुण, मेरे बड़ी

माँ श्रीमती मीनाक्षी को नमन करती हूँ. मेरे दिल के बहुत निकट मेरे दादी माँ (माताजी) और दादा जी (दादू) को, जिन्होंने प्यार के साथ-साथ अपने संस्कारों से बड़ा किया. मित्रता के आचरण में हम बड़े हूए बहन-भाई दिव्या, श्वेता, प्रियंका, तीक्षण, खुशदीप को, जिन्होंने हमेशा मेरा समर्थन किया, के लिए बहुत-बहुत धन्यवाद. मैं आप सभी का आभार शब्दों में कभी व्यक्त नहीं कर सकती.संदीप चाचू का मार्ग-दर्शन, मीनू चाची, अंकु, दिविजा और माधवन को, जिनका साथ मैं कभी नहीं भूल सकती। उन्होंने मुझे हमेशा स्वतंत्र और मजबूत बनने के लिए प्रोत्साहित किया. इसके अलावा, मैं अपनी मासी, पूनम को भी धन्यवाद देना चाहती हूं, जो मुझ पर विश्वास करना बंदन हीं करती हैं और हमेशा मेरे तनाव और रहस्यों को साझा करती हैं. साथ ही मेरे सभी नाना और दादा पक्ष के सभी बड़े और मेरे सभी भाई-बहन, जो हमेशा समर्थन के लिए मौजूद थे, ये सब मेरे लिये इतना सहज हो सका. मेरे भतीजे और भतीजियों हर्षिव, एहसास और आद्या को भी प्यारा धन्यवाद, ज़िनके वीडियो कॉल काम के कठिन दिनों में हमेशा एक तनाव मुक्त होने का बेहतरीन साधन. परिवार से हटकर भी परिवार जैसे आत्मीयजन जिन्होंने मुझे समय-समय पर पथ-प्रदर्शन किया, उनका भी मेरे हृदय से आभार.

Especial agradecimiento se llevan los amigos del pueblo: Adrián, Grillo, Raquel, Irene, Aser, Elena, Inés, Chisco y Carmen, que me acogieron en el grupo con los brazos abiertos haciendo que me siente una más del grupo. Como olvidarme de ellos si hasta se molestaron en ir a mi boda. Unas palabras de agradecimiento también para Rodrigo y Blanca, también presentes en mi boda, que siempre se han interesado por mi y por mi tesis durante estos años. También una mención a Eli, quien siempre estuvo ahí cuando lo necesité durante estos años.

Por último, pero no por ellos menos importante, mil gracias a mis suegros Gabriel y Margarita, que me han soportado un montón y me han tratado como una más de la familia. A mí cuñado Samuel que siempre es capaz de hacernos reír con alguna bobada ingeniosa. También a mi cuñada Irene, que siempre está para ayudarme en cualquier duda de la vida. A mi preciosa sobrina Aitana, que siempre nos trae una sonrisa y para la que siempre seré su Chachi Deepali. A los tíos Juanjo y Tomás, que siempre me tratan como su sobrina y nunca me dejan irme del pueblo sin pasar por el supermercado de tío Tomás. Agradezco también a la abuela Anastasia, que siempre me da sus bendiciones y mucho cariño.

Summary

Ni-Mn-Z (Z = In, Sn and Sb) Meta-Magnetic Shape Memory Alloys (MMSMA) have attracted considerable interest in past few decades due to their unique properties associated with a structural transformation called the Martensitic Transformation (MT) between a ferromagnetic austenite phase and weakly magnetic martensitic phase. As a result, a significant drop in magnetization takes place during the martensitic transformation. This feature allows the induction of the transformation by applying a magnetic field, leading to multi-functional properties such as giant magneto-resistance, magnetic shape memory effect, and large inverse magnetocaloric effect. These properties have practical applications in sensing and magnetic refrigeration. The transformation temperatures, magnetization of different phases, entropy change associated with the transformation, and other magneto-structural characteristics determining the functional properties depend on the composition, structure and microstructure of the alloys. While structure and composition (including atomic order) has been extensively analyzed, the role of microstructure has received less attention, despite its potential for controlling the magneto-structural properties. Therefore, this Ph.D. thesis is partially focused on examining the influence of microstructure in meta-magnetic shape memory alloys (specifically in Co-doped Ni-Mn-In) on the magneto-structural properties of micro-particles produced by milling. On the other side, the high MCE found in Ni-Mn-In-Co alloys, make them an attractive material for use in energy-efficient technologies. However, these alloys are very brittle and their use in commercial devices (heat exchanger for example) is limited to simple geometries. To overcome this issue, the present work demonstrates that the use of composites synthesized employing magnetic shape memory micro-particles (functionality) and polymers (geometrical integrity) could be an alternative in the future. The main goal is to be able to obtain micro-particles with enhanced functional properties (sizes compatible with a standard 3D-printer nozzle) that can be embedded in a polymer matrix which results in a homogeneous 3D-printable magnetic composite.

In this framework, thermo-mechanical treatments were employed (including hand-crushing, ball-milling and thermal annealing) to produce $Ni_{45}Co_5Mn_{36.7}In_{13.3}$ micro-particles. The influence of mechanical milling on the structural and magnetic properties (MT characteristics, crystallographic structures, saturation magnetization and magnetic susceptibility) and on the microstructural parameters such as the internal strains and crystallite sizes of micro-particles has been analyzed. The analysis was carried out in samples milled in both austenite and martensite and subjected to different milling times. A deeper understanding of the role played by the

microstructure in the magneto-structural properties of these meta-magnetic shape memory alloys was achieved. For each milling time, the particles have been sieved into different size intervals and a comparative analysis of the magneto-structural and microstructural parameters of the particles within the same size range have been performed. The correlation between the degree of deformation and particle size opened new possibilities to enhance the functional properties of the alloys, where by mere selecting the particle size (irrespective of the duration, time and environment of milling), specific magneto-structural properties and transformation characteristics can be selected. The MCE and relative cooling power have been estimated in those particles suitable for been embedded into printable polymeric filaments.

Finally, the fabrication of magnetic Polymer–MMSMA composites was carried out. The effect of the addition of the micro-particles onto the phase transformations and the thermal stability of the polymers has also been analyzed. Filaments were extruded from the composites with the higher particle concentration and mechanical consistency. The printability of these filaments was also demonstrated. As a proof of concept, a 3D printed heat exchanger for magnetic refrigeration was successfully produced using the developed filament.

Resumen

Las Aleaciones con Memoria de Forma Metamagnética (MMSMA) Ni-Mn-Z (Z = In, Sn y Sb) han atraído un gran interés en las últimas décadas debido a sus propiedades asociadas con una transformación estructural llamada Transformación Martensítica (MT) entre un fase austenítica ferromagnética y una fase martensítica débilmente magnética. Como resultado, se produce una variación significativa de la magnetización durante la transformación martensítica. Esta característica permite la inducción de la transformación mediante la aplicación de un campo magnético, lo que da lugar a propiedades multifuncionales tales como la magneto-resistencia gigante, el efecto de memoria de forma magnético y un gran efecto magnetocalórico inverso. Estas propiedades tienen aplicaciones prácticas en detección y refrigeración magnética. Las temperaturas de transformación, la magnetización de las distintas fases, el cambio de entropía asociado a la transformación y otras características magneto-estructurales que determinan las propiedades funcionales dependen de la composición, estructura y microestructura de las aleaciones. Si bien la estructura y la composición (incluido el orden atómico) se han analizado ampliamente, el papel de la microestructura ha recibido menos atención, a pesar de su potencial para controlar las propiedades magneto-estructurales. Por lo tanto, esta tesis doctoral se centra por un lado en examinar la influencia de la microestructura (específicamente en Ni-Mn-In co-dopado) en las propiedades magneto-estructurales de las micro-partículas producidas por molienda. Por otro lado, el alto MCE que demuestran las aleaciones de Ni-Mn-In-Co las convierte en un material atractivo para su uso en tecnologías de eficiencia energética. Sin embargo, estas aleaciones son muy quebradizas y su uso en dispositivos comerciales (por ejemplo, intercambiadores de calor) se limita a geometrías simples. Para superar este problema, el presente trabajo de tesis demuestra que el uso de compuestos sintetizados empleando micro-partículas con memoria de forma magnética (funcionalidad) y polímeros (integridad geométrica) podría ser una alternativa en el futuro. El objetivo principal es poder obtener micro-partículas con propiedades funcionales mejoradas (tamaños compatibles con una boquilla de impresora 3D estándar) que se puedan incrustar en una matriz polimérica que dé como resultado un compuesto magnético imprimible en 3D homogéneo.

En este marco, se emplearon tratamientos termo-mecánicos (que incluyen trituración manual, molienda de bolas y recocido térmico) para producir micro-partículas de $Ni_{45}Co_5Mn_{36.7}In_{13.3}$. Se ha analizado la influencia d la molienda mecánica en las propiedades estructurales y magnéticas (características de la MT, estructuras cristalográficas, magnetización de saturación y susceptibilidad magnética) y en los parámetros microestructurales como las tensiones internas y los tamaños de cristalitos de las micropartículas. El análisis se realizó en muestras molidas tanto

en austenita como en martensita y sometidas a diferentes tiempos de molienda. Se logró una comprensión más profunda del papel que desempeña la microestructura en las propiedades magneto-estructurales de estas aleaciones meta-magnéticas con memoria de forma. Para cada tiempo de molienda, las partículas se tamizaron en diferentes intervalos de tamaño y se realizó un análisis comparativo de los parámetros magnetoestructurales y microestructurales de las partículas dentro del mismo rango de tamaño. La correlación entre el grado de deformación y el tamaño de partícula abrió nuevas posibilidades para mejorar las propiedades funcionales de las aleaciones, donde con la mera selección del tamaño de partícula (independientemente de la duración, el tiempo y el entorno de la molienda), se puede seleccionar unas propiedades magneto-estructurales específicas con características de transformación definidas. Se ha estimado el MCE y el poder refrigerante de aquellas partículas aptas para ser embebidas en filamentos poliméricos imprimibles.

Finalmente, se llevó a cabo la fabricación de compuestos magnéticos en base a mezclas polímero-MMSMA. Se ha analizado el efecto de la adición de las micropartículas sobre las transformaciones de fase y la estabilidad térmica de los polímeros. Los filamentos se extruyeron a partir de los materiales compuestos con una alta concentración de partículas y se obtuvo una adecuada consistencia mecánica. También se demostró la capacidad de impresión de estos filamentos. Como prueba de concepto, se imprimió un intercambiador de calor en 3D para refrigeración magnética utilizando el filamento desarrollado.

Index

Chapter 1

Introduction

Magnetic Shape Memory alloys (MSMAs) have gained significant attention due to different potential applications based on the first order Martensitic Transformation (MT) they undergo and on the different magnetic properties of the austenite and martensitic phases. In fact, the magnetic field induced martensitic transformation (MFIMT) makes them suitable for magnetic actuation or magnetic refrigeration applications based on the magnetocaloric effect (MCE). The MCE refers to the change in temperature of the material when subjected to a magnetic field. When exposed to a magnetic field, these alloys undergo the martensitic (magnetic) transition, which leads to a significant change in the magnetic entropy of the material. This change in entropy results in temperature change in the materials, which can be exploited for refrigeration applications. However, the practical application of MSMAs is limited by their cost, mechanical properties, processing difficulty, efficiency and low transformation reversibility. To overcome these drawbacks, researchers have been investigating the modifications of the magneto-structural properties of MSMAs mainly via composition, atomic order, and microstructure.

The high MCE found in Ni-Mn-In-Co alloys, make them an attractive material for use in energy-efficient technologies. However, these alloys are not without their drawbacks. One major issue is their inherent brittleness, which limits their use in certain applications and reduces their reliability and durability. To overcome this issue, the use of magnetic shape memory polymer composites could be explored. These composites would combine the desirable properties of the magnetic shape memory alloys with the flexibility and toughness of polymers. The resulting materials should exhibit improved mechanical properties, including increased ductility and fracture toughness, without compromising the martensitic transformation inherent to the metallic particles. In particular, Poly-lactic acid (PLA) and poly-caprolactone (PCL) are two commonly used polymers in magnetic alloy polymer composites due to their biodegradability, biocompatibility and ease of processing. The polymer matrix also provides a way to tailor the properties of the composite to meet specific requirements for different applications. For example, the addition of PCL to Ni-Mn-In-Co alloy can improve their ductility and toughness, making them suitable for use in applications such as soft robotics and biomedical devices.

In this context, 3D printing is a promising technique for the fabrication of magnetic shape memory alloys polymer composites due to its ability to produce complex geometries with high precision and accuracy. Additionally, it offers the ability to tailor the magnetic properties of the composite by controlling the orientation, size, and concentration of the magnetic particles. This allows the customization of MSMA polymer composites for specific applications. Moreover, 3D printing of MSMA polymer composites enables the fabrication of multi-material structures, allowing the integration of different functionalities into a single component. As this technology continues to advance, it is expected that it will find wider applications in various industries.

1.1 Shape memory alloys (SMAs)

"Shape Memory Alloys" (SMAs) or "Magnetic Shape Memory Alloys" (MSMAs) are materials capable to remember and recover their original shape after being subjected to deformation. The shape recovery is usually driven by temperature changes, magnetic fields or external stresses applications. This Shape Memory Effect (SME) occurs because these alloys undergo a thermoelastic Martensitic Transformation (MT) between two different phases (austenite and martensite) and have attracted a huge interest in terms of fundamental investigation; the alloy deformed in martensitic state regains its original shape when heated up to the austenite state. In particular, the high temperature austenite transforms bellow MT to a heavily twinned martensite structure. A stress or magnetic field applied to this twinned martensite induces a shape change that occurs by accommodations of the different variants (see figure 1.1).

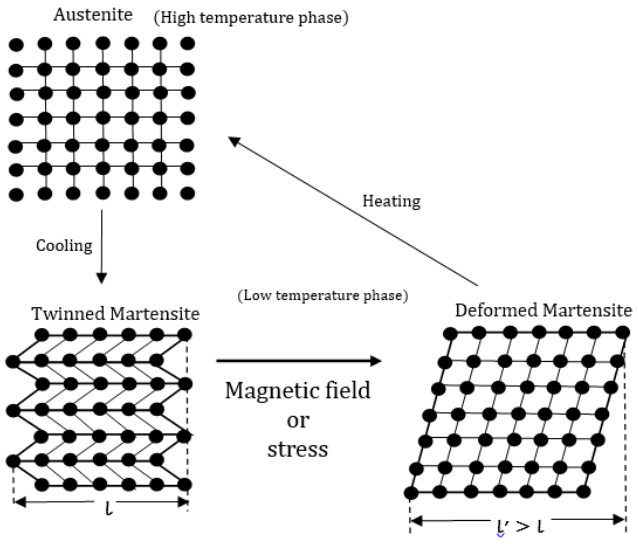

Fig. 1.1. Schematic representation of shape-memory mechanism.

Consequently, de-twining occurs and a single variant is formed [1]. These changes, in turn, lead to the change of shape of the material. Upon demagnetization or removal of the applied stress, the de-twinned structure remains. However, upon sufficient heating, the sample returns to the austenite phase recovering the original shape.

1.1.1 Martensitic transformation

Adolf Martens performed the very first studies on Martensitic Transformations (MT) on steel at the end of the 19th century. The microstructure found in the quenched steel was described as the word "martensite" and the phase existing above the critical eutectoid temperature was called as 'austenite" phase after Sir William Chandler Roberts-Austen. The MT can be distinguished into two types taking into account the kinetics of the transformation: a) thermoelastic b) non-thermoelastic (burst types). The latter ones undergo a large volume change. During the transformation, the thermal hysteresis is fairly wide with the implication of presence of the plastic deformation. On the other hand, during the thermoelastic transformation, the associated volume change is very small. The absence of plastic deformation due to a minute mismatch between the cell parameters of the parent and the product phase, leads to low thermal hysteresis.

Therefore, the thermoelastic MT is a first order solid-state structural transformation that takes place between a highly ordered cubic phase (called "austenite") and a low symmetrical phase (called "martensite"). These transformations are diffusion-less, and displacive. The atoms move within their inter-atomic distance, instead of long-range order movement, maintaining their local neighborhood during the transformation via dominant shear mechanism [2]. The interface between both phases is known as the "habit plane". As a characteristic of first-order transitions, MT undergoes an associated enthalpy change (ΔH), volume change (ΔV), the existence of an interface and the possibility of coexistence of both phases in thermodynamic equilibrium. In some cases, the volume change accompanied by the phase transformation leads to significant lattice distortions and stresses. It is possible to think of the MT as the superposition of two processes: a homogeneous crystal lattice deformation and an invariant shear of the new lattice. The homogeneous deformation leads to the changes in the crystal structure by shearing certain austenitic atomic planes. This deformation entails the emergence of elastic and surface energies in the area surrounding the altered zone, which obstruct and may even prevent the transformation to occur. Therefore, to reduce the emerging energies and accommodate a new martensite structure, the new lattice undergoes a distortion by the means of invariant shearing mechanism. As a result, a new degenerate martensite structure is formed with different orientation of the variants. Figure 1.2 shows the accommodation process during the transformation that can occur either by twinning or by gliding. The low symmetry of martensite

phase than the austenite phase means that the martensite phase is structurally inhomogeneous, since there are several compatible orientations of martensite with austenite. With the growth of martensitic variants, the elastic energy associated with the transformational deformation increases. In order to avoid the transformational volume change at the macroscopic scale due to the deformation, the martensitic variants accommodate each other's strain. This process is known as "self-accommodation". Each variant is subsequently created with an orientation that negates the accumulated energy during the creation of previous variant.

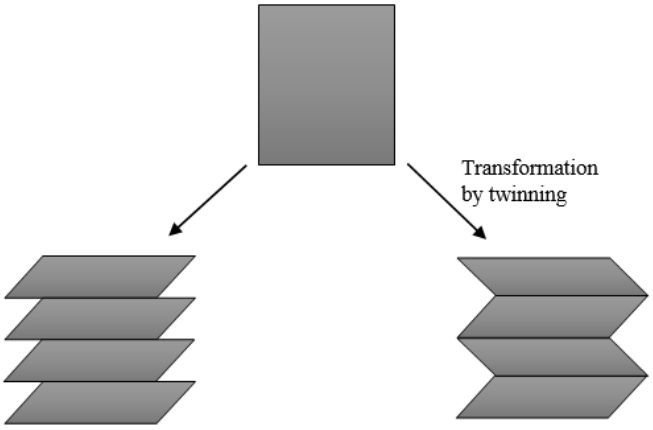

Fig. 1.2. Schematic representation of the accommodation processes by gliding and twining during the transformation.

The majority of theoretical justifications related to the fundamental mechanism of MT are the phenomenological studies based on the free energy. Therefore, the elementary mechanism of the MT based on the concept of free energy needs to be understood in details. During the transformation, the Gibbs free energy difference is generally given by,

$$\Delta G^{A\rightarrow M} = \Delta G_C^{A\rightarrow M} + \Delta G_{NC}^{A\rightarrow M} \quad 1.1$$

where, $\Delta G_C^{A\rightarrow M}$ gives the difference in the chemical free energy, $\Delta G_{NC}^{A\rightarrow M}$ gives the difference in the non-chemical energies like elastic strain and surface energies. A→M represents the transition from austenite to martensite phase. The temperature dependence of ΔG is shown in figure 1.3. The Gibbs free energy of the austenite and the martensite phase are the linearly decreasing temperature functions. The austenite and start and finish temperatures A_s and A_f and martensite start and finish temperatures M_s and M_f are also shown in the figure. A thermodynamic equilibrium is reached at the intersecting point between two curves at the equilibrium temperature (T_o), where $\Delta G^{A\rightarrow M}$ becomes zero. At $T < T_o$, the martensite phase is more thermodynamically stable than the austenite phase due to lower Gibb's free energy,

whereas, at $T > T_o$, the austenite phase is more stable. $\Delta G^{A\rightarrow M} > 0$ in the reverse transformation region and $\Delta G^{A\rightarrow M} < 0$ in the forward transformation region. As the transformation from austenite to martensite progress, with the formation of martensite variants, more and more non-chemical strain energy is stored elastically. In this case, $\Delta G_{NC}^{A\rightarrow M}$ increases and gives a positive contribution to the total $\Delta G^{A\rightarrow M}$. Hence, inhibiting the transformation. Thus, the transformation from one phase to another occurs depending upon the temperature and the existing driving forces ($\Delta G_{A_s}^{M\rightarrow A}$ and $\Delta G_{M_s}^{A\rightarrow M}$). However, the dissipative processes associated with the motion of martensite variants and the austenite-martensite interfaces lead to loss of energy that result in the transformation hysteresis [3].

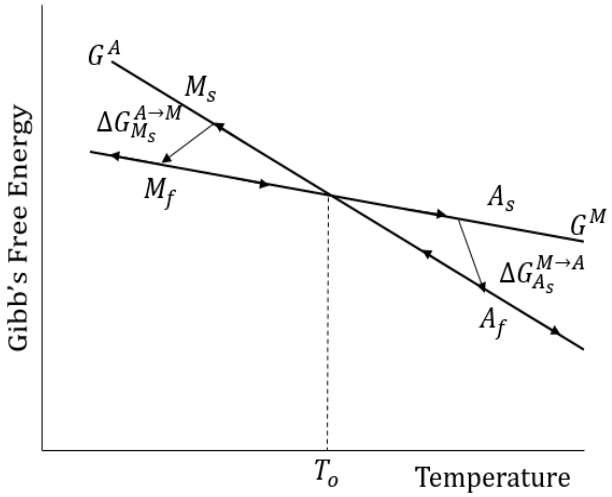

Fig. 1.3. Schematic diagram of Gibb's free energy of martensite and austenite in MT region.

The hysteresis during the transformation is a defining characteristic of martensitic transformation. Figure 1.4 provides a schematic representation of the temperature dependence of parameters like magnetization, strain, etc. The arrows represent the direction of heating and cooling. During the transformation from austenite to martensite upon cooling, at M_s the formation of martensite phase starts. Until M_f austenite and martensite phases coexist and below this temperature, pure martensite phase exists. However, upon heating the martensite phase starts transforming into the austenite phase at temperature marked by A_s and at and beyond A_f, the whole austenite phase exists. The transformation upon cooling from austenite to martensite is called as the "forward martensitic transformation" (FMT) and upon heating from martensite to austenite is called as the "reverse martensitic transformation" (RMT). The hysteresis linked to the transformation is therefore realized by the difference between the A_s and M_f. The values of these temperatures can be determined by experimental techniques like differential scanning

calorimetry (DSC) and magnetic measurements. The other characteristic temperatures can also be known by these techniques like Curie temperature or the martensitic transformation temperature.

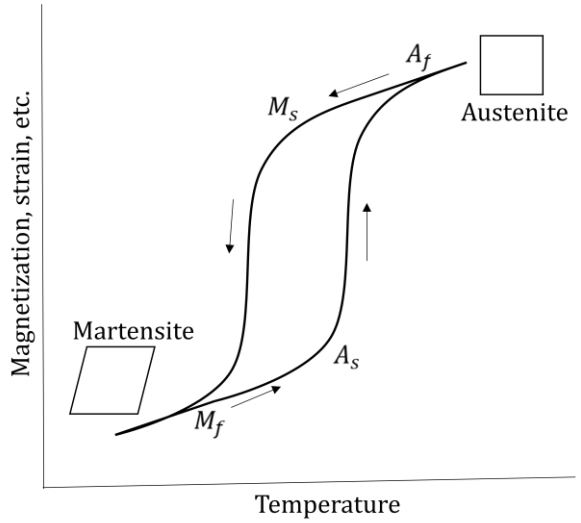

Fig. 1.4. Temperature dependence of physical properties for during cooling and heating ramps.

1.2 Ni-Mn based Heusler alloys

Heusler alloys discovered in 1903 [4], are intermetallic ternary compounds with stoichiometry X_2YZ (full-Heusler) with $L2_1$ cubic structure and XYZ (half-heusler) with $C1_b$ structure. Many off-stoichiometric compositions also refer to as Heusler compounds. Substituting Y with Mn, the resulting Heusler alloy is magnetic, X sub lattices are taken by transition elements and Z is usually occupied by elements from the group IIIA-VA of the periodic table. The $L2_1$ cubic structure (space group $Fm\bar{3}m$ and cell parameter a = 5.949Å) for full-Heusler alloy consists of four interpenetrating face centered cubic sub-lattices with atomic positions (1/4,1/4,1/4) and (3/4,3/4,3/4) occupied by X atoms, and (0,0,0) occupied by Y atoms and (1/2,1/2,1/2) occupied by Z atoms [5]. In terms of Wyckoff positions, Z and Y atoms occupy the 4b and 4a positions respectively, whereas X atoms occupy the 8c positions (see figure 1.5).

Some Heusler alloys undergo a martensitic transformation (MT) between two magnetically ordered phases. The transformation occurs from a high temperature austenite phase with $L2_1$ structure to a low temperature martensite phase with lower crystallographic symmetry. Some of these Heusler alloys also are capable of exhibiting the magnetic shape memory effect with magnetic super elasticity and Magnetocaloric effect which makes these alloys promising smart

materials for commercial use [6–9]. Ni-Mn-X (X= Ga, In, Sn, Sb) are the most studied system so far due to the coupling between the magnetic and the structural properties of the alloys. The difference in the magnetic properties of the austenite and martensite phases leaves a vast area to investigate, as the structural transformation involves a change in the overall magnetic properties of the alloys. In fact, the martensitic transformation in stoichiometric Heusler alloys only appears in Ni_2MnGa [10–12]. Nevertheless, off-stoichiometric composition also show the martensitic transformation in Ni_2MnIn, Ni_2MnSn and Ni_2MnSb [13, 14]. T. Krenke investigated the initial studies on $Ni_2Mn_{1-x}Z_x$ (Z = In, Sn) off-stoichiometric Heusler compounds in detail during his Ph.D. study [15]. In addition to their application feature, the complex interplay between their crystal structure and the magnetic properties linked to these alloys, make them very interesting for the fundamental investigation point of view.

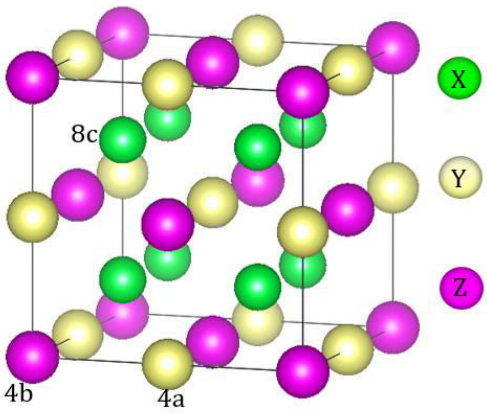

Fig. 1.5. The $L2_1$ crystal structure of X_2YZ Heusler alloys.

Depending upon the composition, a transformation occurs from $L2_1$ to B2 (space groups $Pm\bar{3}m$ with only two different sub-lattices, one occupied by Ni and the other by Mn and X atoms) through a second order transition at different temperatures. Neutron diffraction measurements in Ni-Mn-In [16], Co doped Ni-Mn-In [17] and Ni-Mn-Ga [18, 19] alloys confirm such transition. However, in Ni-Mn-Sn and Ni-Mn-Sb alloys, $L2_1$ structure has been reported to be stable up to melting point temperatures, and no B2-$L2_1$ transition has been detected [20].

The MT in Ni_2MnGa was found to occur due to shear stress on the (110) planes in the $[1\bar{1}0]$ direction of cubic $L2_1$ austenite. Due to this tetragonal deformation of the cubic lattice, the material was found to be macroscopically contracted along [110] axis of austenite. X-ray diffraction show four satellites measurements between the major reflections of the tetragonal crystal structure. This indicates the presence of a modulated superstructure with a modulation of a period of five unit cells. Such modulated structure is called as 10M martensite. This

modulation can be described as the displacement of (110) planes in [1$\bar{1}$0] direction of austenite in a way that after ten atomic planes, (110) plane is back at the same position (figure 1.6). In many off- stoichiometric $Ni_{50}Mn_{50-y}X_y$ (X = Ga, In, Sn and Sb) alloys, different modulated structures (7M, 10M, 14M monoclinic) and 4O orthorhombic martensite structures have been reported depending on the "y" concentration [21–24]. Figure 1.6 shows some examples.

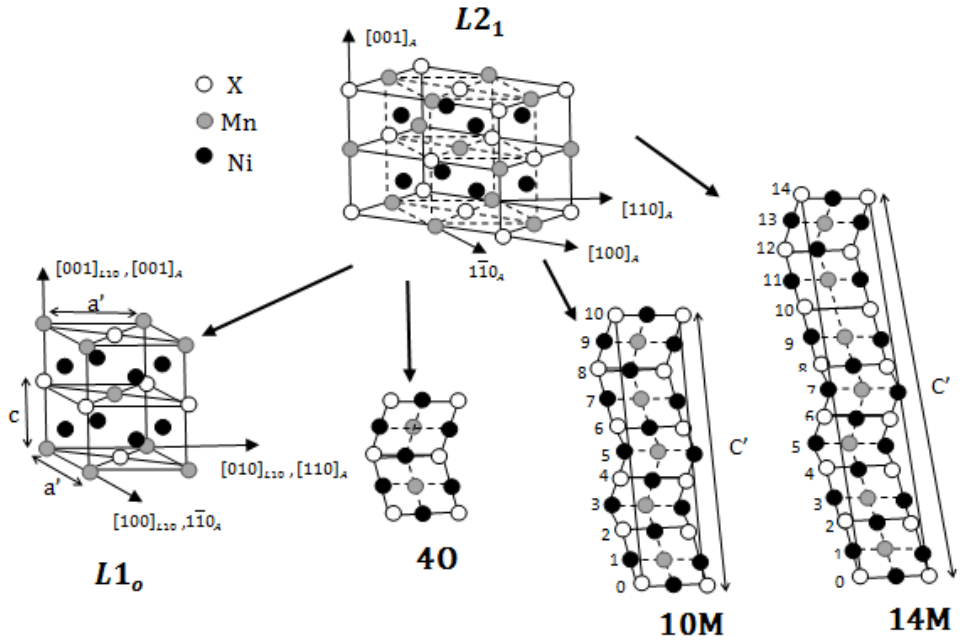

Fig. 1.6. $L2_1$ austenite, non-modulated $L1_0$, modulated martensite structures (10M, 14M monoclinic and 4O orthorhombic) in $Ni_{50}Mn_{50-y}X_y$ (X = Ga, In, Sn and Sb) alloys [25, 26].

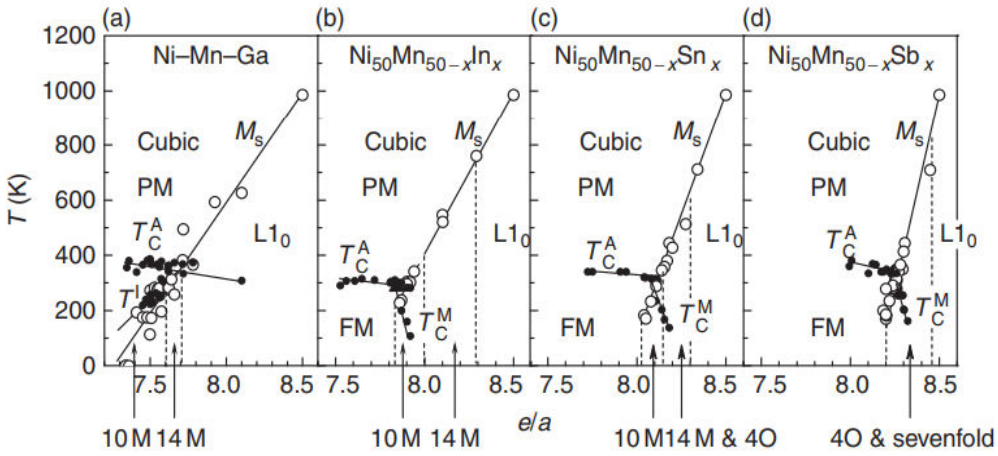

Fig. 1.7. Phase diagrams for Ni-Mn-X alloys, where a) X = Ga, b) X = In, c) X = Sn and d) X = Sb. Dotted lines represent the separations of different structures [27].

The stability of each martensitic phase depends upon the composition of the alloy and correlates with the e/a atom concentration [27–29]. The magnetic and structural transformation temperatures are plotted in figure 1.7 as a function of e/a atom ratio for the different Ni-Mn based Heusler alloys (T_C^A and T_C^M are represented as the Curie temperatures of the austenite and martensite phases respectively and M_s is the martensite start temperature).

1.2.1 Magnetic properties

The magnetism in these alloys mostly relies in the Mn atoms and depends on the inter-atomic distance between Mn-Mn atoms. The inter-atomic distances between the Mn atoms are reduced due to the lower crystallographic symmetry of the martensite phase, which usually gives rise to the anti-ferromagnetic coupling between the atoms. Thus the magnetic properties strongly change during the martensitic transformation [30–33]. According to Clausius-Clapeyron equation, the application of an external magnetic field (H) changes the MT temperatures (T_M):

$$\frac{dT_M}{dH} = -\mu_o \frac{\Delta M}{\Delta S} \qquad 1.2$$

where, T_M is the MT temperature, ΔM is the magnetization change and ΔS is the entropy change linked to the MT. For the transformation from austenite to martensitic phase, $\Delta S < 0$. Therefore, the shift of T_M to higher or lower temperatures depend upon the sign of ΔM. In the case of meta-magnetic shape memory alloys, the transformation occurs from ferromagnetic austenite to a weakly magnetic martensitic phase. Thus a huge drop in the magnetization at MT is observed, which lowers the T_M, under the application of magnetic field (see figure 1.8). On the other side, the application of magnetic field in the martensitic phase close to the martensitic transformation, can lead to the magnetic field induced reverse transformation [6, 34–38]. The magnetic field induction of the MT leads to other wide range of multi-functional properties like caloric effects [6, 8, 29, 42], magneto-resistivity [43–45], exchange bias [46] etc. These properties make these materials promising candidates for the applications like magnetic actuated devices, magnetic refrigeration technology and spintronic devices. In particular, and taking into account the objectives of the present work, let's focus on the understanding of the fundamental concepts related to the magnetocaloric effect.

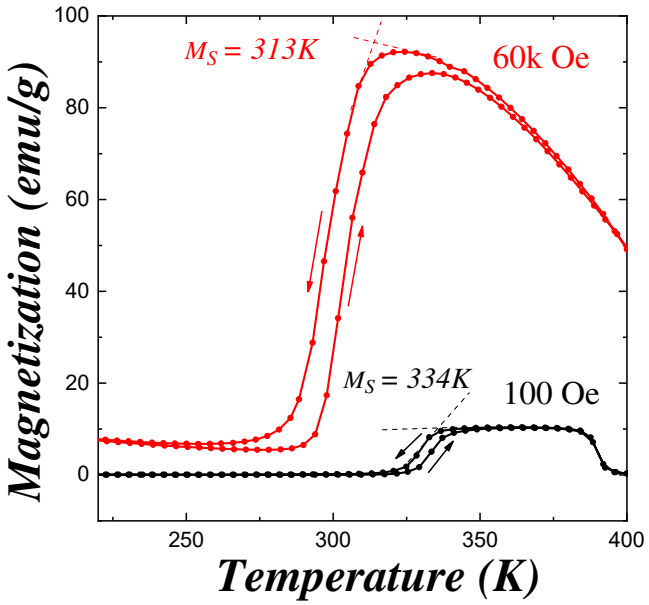

Fig. 1.8. Temperature dependence of magnetization under different magnetic fields for a $Ni_{45}Co_5Mn_{36.7}In_{13.3}$ alloy.

1.2.2 Magnetocaloric effect (MCE)

Discovered in 1881 by Warburg in iron [47], this effect is defined as the change in the magnetic entropy and the temperature of a magnetic materials under the application of a magnetic field. All magnetic materials intrinsically possess the MCE; however, the intensity of the effect depends on the properties of each material. The origin of the MCE can be better understood by the thermodynamic considerations, relating entropy and temperature to the magnetic variables like magnetization and magnetic field. The coupling of the magnetic sub-lattice to the applied field H, gives the variation in the magnetic entropy change [48]. The total entropy of a magnetic material can be written as the sum of the magnetic entropy (S_m), lattice entropy (S_{lat}) and the electronic entropy (S_e) [49, 50]:

$$S\,(p,T,H) = S_m\,(p,T,H) + S_{lat}\,(p,T,H) + S_e\,(p,T,H) \qquad 1.3$$

where, entropy is the function of temperature (T), applied field (H) and pressure (p). The entropies S_{lat} and S_e are independent of the magnetic field and S_m depends strongly on the magnetic field. In a closed system, the differential of the total entropy is given by:

$$dS\,(p,T,H) = \left(\frac{\partial S}{\partial P}\right)_{T,H} dp + \mu_o \left(\frac{\partial S}{\partial H}\right)_{p,T} dH + \left(\frac{\partial S}{\partial T}\right)_{p,H} dT \qquad 1.4$$

In the isobaric and isothermal condition (dp, $dT = 0$), equation 1.4 becomes:

$$dS\,(p,T,H)_{p,T} = \mu_o \left(\frac{\partial S}{\partial H}\right)_{p,T} dH \qquad 1.5$$

The total entropy, in this case, only varies with the magnetic field. According to the Maxwell relation, the field derivative of the entropy and the temperature derivative of the magnetization can be related as:

$$\left(\frac{\partial M}{\partial T}\right)_H = \left(\frac{\partial S}{\partial H}\right)_T \qquad 1.6$$

The heat capacity (C) can be expressed as the $C = \frac{dQ}{dT}$, where dQ is the quantity of heat change with the temperature change dT of the system. According to the second law of thermodynamics,

$$C = T\,\frac{dS}{dT} \qquad 1.7$$

Under isobaric and adiabatic conditions, using equation 1.6 and 1.7, equation 1.4 becomes:

$$dS\,(T,H) = \frac{C\,(T,H)}{T}\,dT + \left(\frac{\partial M\,(T,H)}{\partial T}\right)_H dH \qquad 1.8$$

From this equation, the entropy change can be easily calculated from measurable parameters. The entropy change in equation 1.8 is considered total entropy change, where lattice and electronic contributions are assumed to be contained by the value of C. The MCE by the S-T diagram is represented in figure 1.9. In the figure, the black and orange curves represent the variation in entropy and temperature under different magnetic fields. The magnetic field changes in a way that either $H_2 > H_1$, or $H_1 = 0$ *and* $H_2 > 0$. With the higher magnetic field, the magnetic contribution to the entropy changes due to the increment in the magnetic order of the alloy. The magnetic field can be varied isothermally or adiabatically. Under the adiabatic conditions ($dS = 0$), in a reversible process, a variation in the ΔT_{ad} is noted (see figure 1.9). Thermodynamically, for the isobaric and adiabatic conditions, equation 1.4 becomes:

$$-\mu_o \left(\frac{\partial S}{\partial H}\right)_T dH = \left(\frac{\partial S}{\partial T}\right)_H dT \qquad 1.9$$

Rearranging equation 1.9:

$$dT = -\mu_o \left(\frac{\partial S}{\partial H}\right)_T \left(\frac{\partial T}{\partial S}\right)_H dH \qquad 1.10$$

Using equations 1.6 and 1.8 in 1.10:

$$dT = -\mu_o \left(\frac{T}{C}\right)\left(\frac{dM}{dT}\right)_T dH \qquad 1.11$$

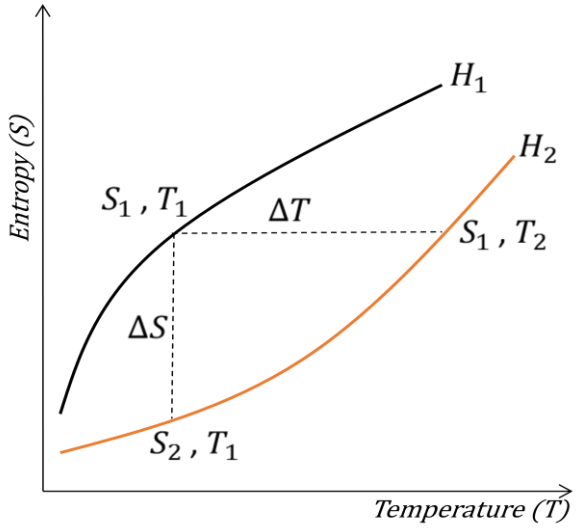

Fig. 1.9. Schematic representation of MCE showing variation in entropy and temperature of a material under magnetic field.

The integral of equation 1.11 becomes:

$$\Delta T_{ad} = -\mu_o \int_{H_1}^{H_2} \left(\frac{T}{C}\right)\left(\frac{dM}{dT}\right)_T dH \qquad 1.12$$

where, H_1 and H_2 are initial and final magnetic fields, respectively. On the other hand, in the case of isothermal conditions ($dT = 0$), in the magnetic field produces a change in the entropy of the system (ΔS_{iso}). Thermodynamically, ΔS_{iso} can be expressed by integrating equation 1.7:

$$\Delta S_{iso} = \int_{H_1}^{H_2} \left(\frac{\partial M}{\partial T}\right)_H dH \qquad 1.13$$

Therefore, the MCE can be represented by the magnitudes of either of ΔS_{iso} and ΔT_{ad}. During first order transitions, the variation in the entropy with the temperature must show discontinuity. The schematic representation of such first order transition is shown in figure 1.10. At MT temperature, a jump in the entropy is seen due to the presence of latent heat [51, 52]. The path for austenite to martensite transformation is also shown in the figure.

Under $H = 0$, MT takes place at $T_{H=0}$, however, with the application of magnetic field ($H > 0$), MT temperature shifts to higher values ($T_{H>0}$). Isothermal entropy change $\Delta S_{iso} = S_2 - S_1 < 0$ and adiabatic temperature change $\Delta T_{ad} = T_2 - T_1 > 0$. Such conditions with $\Delta S_{iso} < 0$ and $\Delta T_{ad} > 0$, refers to the conventional MCE. Ferromagnetic Ni-Mn-Ga system is a typical prototype for the conventional MCE and has been extensively studied [53–55]. Large ΔS up to -18J/kgK have been reported for $Ni_{52.6}Mn_{23.1}Ga_{24.3}$ alloy under 50kOe magnetic field.

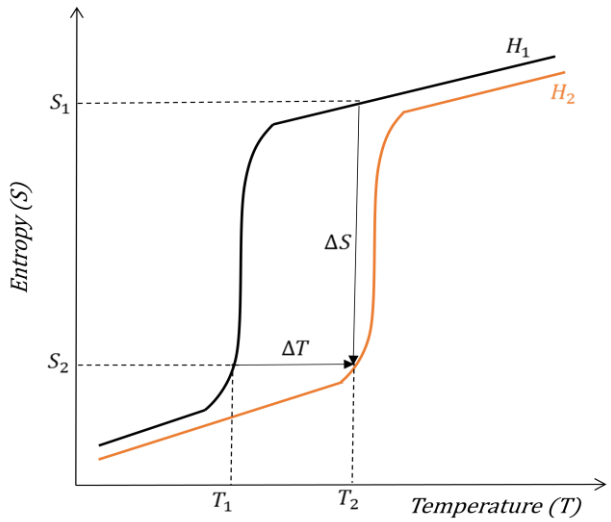

Fig. 1.10. Schematic representation of MCE showing variation in entropy and temperature of a material under magnetic field H = 0 and H > 0 during first-order MT.

On the other hand, in meta-magnetic shape memory alloys, the application of magnetic-field adiabatically, lowers the MT temperature. This can cause material to release heat in a way that [56] $\Delta S_{iso} > 0$ and $\Delta T_{ad} < 0$. These conditions refer to *inverse magneto-caloric effect.* The MCE in Ni-Mn based systems with In, Sn, Sb have also been widely studied [6, 7, 56–59] which show inverse MCE. For $Ni_{50}Mn_{50-x}Sn_x$ alloy system, the change in magnetic entropy for x =15 was reported to be around $15 Jkg^{-1}K^{-1}$ and for x= 13, $18 Jkg^{-1}K^{-1}$ at the field of 5T [6]. A high value of MCE effect ($\Delta S= 13 Jkg^{-1}K^{-1}$) for Ni-Mn-In alloy has been reported by Oikawa et al. which is comparable to the other MCE materials like $Gd_5Si_2Ge_2$ alloy [60].

Langevin first demonstrated the reversible temperature change by magnetizing a paramagnet [61]. Later on, paramagnetic salts were utilized for adiabatic demagnetization to achieve low temperatures [62–64]. Debye [62] and Giauque [63] first suggested the practical use of this effect by adiabatic demagnetization, to reach the temperatures lower than that of liquid helium. In today's world, MCE is considered to be the alternative technology for refrigeration. The magnetic refrigeration is energy-efficient, cost-effective and environment friendly promising technology instead of the conventional vapor-cycle refrigeration technology [65, 66]. Most of the refrigeration systems existing today still use the ozone-depleting liquid refrigerants. On the other hand, magnetic refrigeration technology uses solid refrigerants and common heat transfer fluids with no effects on the environment. The complete replacement of the conventional cooling systems is still a long shot. Currently, with the existing magnetic materials, higher efficiencies can be realized with high magnetic fields (above 5T). In order to get materials

operating under lower fields of about 2T and still showing large MCEs, more research and work has to be done.

1.2.3 Tuning the magneto-structural properties

Multi-functional properties (MCE, MFIMT, super-elasticity etc…) in Ni-Mn based Heusler alloys occur due to the presence of thermoelastic MT. In order to optimize the functional properties, it is important to have a good control of the parameters that affect the martensitic transformation and in particular, control the MT temperature (T_{MT}) and the Curie temperature (T_C). Both parameters determine the temperature range where the multi-functional features may be applied. The three main parameters are composition, atomic order and microstructure.

a) Composition

The main factor affecting the T_{MT} has been presented as the composition of the alloy [9, 14, 29, 67–69]. It has been shown that the transformation temperatures strongly depend upon the X species and on the valence electron to atoms (e/a) ratio in Ni-Mn-X alloys. The shifts around tens of Kelvins in both T_{MT} and T_C with slightly varying the composition can be clearly seen in figure 1.7. Therefore, the parameters T_{MT} and T_C and hence the magneto-structural properties may be adjusted in accordance with the needed specification by selecting the composition of the alloy. As previously mentioned, Ni-Mn-Ga is the only composition that exhibit MT in the stoichiometry. In the stoichiometric compositions for Ni-Mn-X (X = In, Sn), no martensitic transformation occurs and T_c = 350K. However, in the off-stoichiometric compositions $Ni_{50}Mn_{50-y}X_y$ (X = In, Sn) replacing the X atoms by Mn atoms, increases the values of T_{MT} while T_C decreases. With increasing X concentration up to 15%, the alloys begin to display MT. The compositions $Ni_{50}Mn_{37}In_{13}$, $Ni_{50}Mn_{37}Sn_{13}$ and $Ni_{50}Mn_{40}Sn_{10}$ have been studied extensively as they exhibit MT just above the room temperature, which is appropriate for many functional properties. For example, T_{MT} lying near to the room temperature is necessary for functional household refrigerators. The alloy with composition $Ni_{50}Mn_{36}In_{14}$ exhibit MT slightly lower than the room temperature. However, this system has been studied intensely since it exhibits high inverse-MCE at the MT. Nevertheless, for the alloys far away from the stoichiometry with the addition of excessive Mn atoms, the overall magnetism of the alloy reduces. This occurs due to the smaller spacing between Mn-Mn atoms and hence introduction of anti-ferromagnetic exchange coupling between the Mn atoms [9]. Therefore, another way of tuning the magneto-structural properties of the alloys is the doping of the alloy with a transition element. The modification in the alloy composition can lead to high MCE values. For instance, Ni atoms can be substituted for another transition element like Co by 3-5%. This increases the T_C and the magnetic moment of the austenite while decreasing the T_{MT} [70]. The addition of 3d element like

Co replacing Ni atoms reduces the magnetic coupling in the martensite state to almost paramagnetic state. Thus larger magnetization drops with large MCE [58, 69, 71]. For the Ni-Mn-In alloys, the doping of Co also greatly enhances the meta-magnetic properties of the alloys. Other than the large magneto-resistivity and large inverse MCE being the extraordinary properties of this Ni-Co-Mn-In composition, the advantages like not containing any rare earth or toxic elements, easy fabrication, super-elastic deformation, high machining [72] etc. makes this composition very promising for application point of view. Kainuma et al. calculated the magnetic entropy change for Ni-Mn-In-Co system at 292K using Maxwell equations in the fields of 20Oe and 70kOe around 15.2 and 28J/kgK [73]. The values of large magnetic entropy changes with $30Jkg^{-1}K^{-1}$, $32Jkg^{-1}K^{-1}$ and $34Jkg^{-1}K^{-1}$ have been achieved so far by the Co doping for Ni-Mn-Co-In[74], Ni-Mn-Co-Sn [75] and Ni-Mn-Co-Sb [76] respectively. In the composition $Ni_{49.8}Co_{1.2}Mn_{33.5}In_{15.5}$, large reverse magnetic entropy change (ΔS_m) of 14.6J/kgK has been found with the 7M modulated martensitic structure and a broad range of operating temperature (18K) under 5T field [77].

b) Atomic order

The influence in the atomic order is also one of the ways to tune the magneto-structural properties of the alloys. The atomic order is related to the occupancy of the lattice site and its subsequent electronic structure in the crystal lattice, which can be modified by the heating treatments. The thermal treatment could be either quenching the alloy from high temperatures or post-quench ageing. For instance, the exchange interactions between Mn atoms in their regular 4a sites are ferromagnetic. However, with addition of excess Mn atoms occupying 4b sites may alter the overall exchange interactions in the lattice. For instance, for high atomic disordering, high number of Mn atoms in the 4b sites that couple anti-ferromagnetically with the ones at 4a sites. Hence, the reduced net magnetic moment of the alloy. With higher long-range order, Mn atoms reoccupy their own lattice sites and couple ferromagnetically with the other Mn atoms. Hence, increase in the net magnetic ordering of the alloy and higher T_c. The relation between the atomic order and exchange interactions due to the lattice site occupancy has been established by the works of V. Sánchez-Alarcos and group in Ni-Mn-Ga alloy [19]. In their work, the variation in the atomic-order was achieved by the means of thermal treatments. In contrast, in Ni-Mn-Sn and Ni-Mn-Sb alloys, the extraordinarily high stability of austenite $L2_1$ structure makes it impossible to change the atomic order by thermal treatments [20]. The changes in the T_{MT} and T_c in Ni-Mn-In alloy with the variation in the long-range atomic order due to thermal treatments has been studied by Recarte el.al [78]. With the increase in the atomic order, the magnetic character of the austenite is enhanced. Consequently, a lower T_{MT} and higher T_c were observed. In $Ni_{52.6}Mn_{26.7}Ga_{20.7}$ and $Ni_{52}Mn_{34}In_{14}$ compositions with high e/a ratio, the change in degree of

atomic order only affects the T_c, whereas T_{MT} remains unaffected [32]. The change in T_c (lower for higher long-range atomic disordering) has been associated with the excessive number of Mn atoms in the 4b sites due to atomic disordering. In this case, MT occurs between paramagnetic austenite to paramagnetic martensite. It has been reported that variations in the atomic order through thermal treatments affect the T_{MT} in a way that depends on the magnetic character of the austenite and martensite phases. The variation in T_{MT} is seen only if at least one of the phases is magnetically ordered. Since, there is no magnetically ordered state involved in the MT (para-to-para transition), the change in degree of atomic order does not affect the T_{MT}. They conclude that the increase in the long-range atomic ordering stabilizes the phase with higher magnetic moment [32].

c) Microstructure

The modification in microstructural parameters like vacancies, internal stresses, anti-phase boundaries, grain size, etc. may lead to the modifications in the inter-atomic distances, atomic order or composition. This, in turn, may lead to the tuning of the magneto-structural properties of the alloy. As mentioned earlier, in Ni-Mn-Sn and Ni-Sn-Sb alloys, the $L2_1$ austenite structure is extremely stable and the atomic order is therefore hardly changeable by the means of thermal treatments [20]. The change in the microstructure appears to be the only way to modify the functional properties in these alloys. One of the simplest and most popular ways to change the microstructure is by mechanical milling and subsequent thermal treatments. The effect of the mechanical milling and the subsequent recovery thermal treatments onto the grain size and internal stresses has been extensively studied [79–85]. In $Fe_{20}Cr_{80}$ and Co_2Ge alloys, the spin-glass like behaviors have been synthesized by the means of ball milling for longer times [86, 87]. The origin of such behavior, however, is still unknown. A recent TEM study on $MnAu_2Al$ Heusler alloy reports that the plastic deformation induced by the milling methods generates dislocations that lead to the occurrence of the low energy anti-phase boundaries (APBs) [88]. The formation of such APBs may help understanding the glassy-behavior at low temperatures. APBs tend to reverse the magnetic moment near the dislocations and reduce the overall magnetization of the alloy. In Ni-Mn based alloys, the introduction of lattice strain and degradation of MT characteristics as a result of mechanical milling have been widely studied and reported [80, 81, 83–85, 89– 94]. Both MT and magnetic properties of Ni-Mn-Sn and Ni-Mn-In alloys are very sensitive to even slight microstructural distortions even when there is no resulting change in the atomic disorder. In Ni-Mn-Sn alloys, short milling time are sufficient to induce changes in the magneto-structural characteristics of the alloy [81]. With milling of only 90s, the $L2_1$-B2 disordered structure changes to simple cubic B2 structure. The formation of point defects lead to the internal stresses which in fact, increases with increasing milling time

[81]. This occurs due to the reduced ferromagnetic interactions causing smaller magnetization change at the MT and hence lower MCE. On the other hand, in Co doped Ni-Mn-Sn alloy, the introduction of defects by soft milling/hand crushing have reported to enhance the multi-functional properties of the alloy [92]. The enhancement in the MCE (ΔS_{iso}) in the milled samples has been associated with the increased intrinsic entropy change, where the defects increase the vibrational contribution to the total entropy change. Hence, higher total entropy change and higher MCE. The effect of milling in Ni-Mn-Ga has been thoroughly studied by Tian et al. [91]. Their study reports that no change in T_c and MT temperature as a result of milling is seen. However, a significant suppression in the MT characteristics and Curie Transition with increase in milling time due to higher lattice strains has been reported, which reduces the ferromagnetic nature of the martensite and total magnetic moment of the alloy. Moreover, change in atomic ordering with change in lattice parameters followed by a contraction of a and expansion of c parameter has been observed. This atomic disordering has been associated with the buildup of high density of overlapping and intersecting APB planes as a result of movement of imperfect dislocations. Annealing for recovery at 873K, however, restores the atomic ordering of the alloy, annihilating the dislocations, APBs and vacancies via diffusion [91]. Similarly, Peruman et al. report the increase in lattice strain resulting from internal stresses and defects including vacancies, dislocations, grain boundaries as a result of milling [89, 90]. Annealed particles show an improved ferromagnetic order with increase in the saturation magnetization with increasing annealing temperature. Even though it is well know that the elastic energy term is greatly affected by the grain size and state of internal stresses, less research has been done on the examination of the MT and its magnetic properties at smaller sizes that are on the cusp of the nano-scale [95]. Despite the fact that experiments have demonstrated super-elasticity in SMAs with sizes ranging from 30nm to 150μm [96–98], which is still above the critical size. In this regard, it has been proposed that the SMA nano-particles exhibit non-hysteretic super-elasticity below their critical size resulting from continuous lattice distortion between the parent and the product phase attributed to the surface effect [99]. On the other hand, many studies on SMAs show that the increasing the milling time not only induces defects and internal stresses but also leads to the amorphization of the alloy [85, 87, 89, 100–102]. The ball-milling-induced amorphization of the alloy can be attributed to the high-speed collision during milling resulting in generation of defects, anti-side disorder, grain boundaries, vacancies, etc.[101]. The amorphous phase can arise as a result of these defects, which can stabilize the ordered nature of the lattice and increase the free energy of the system [103]. To our knowledge, no such amorphization has been reposted in Ni-Mn-In-Co SMAs. The major part of the present framework is based on the study of effect of the mechanical milling on the

magneto-structural properties of Ni-Mn-In-Co alloys, which will be discussed in detail in next chapters.

1.3 Ni-Mn-In-Co alloys

Ni-Mn-In-Co alloys are meta-magnetic SMAs in which the ferromagnetic austenite transforms to a weakly magnetic martensite (see section 1.2) leading to a high change in magnetization ΔM during the MT. This high ΔM therefore, opens up the possibility to induce a reversible MT by the means of an external magnetic field and consequently leads to certain interesting properties like magnetic field induced strain (MFIS) and a giant inverse MCE values. For instance, a spark plasma sintered Ni-Mn-In-Co alloy has been reported to exhibit a MFIS as high as 14% [104] and a large value of MCE of ΔS_m= 30J\kgK has been reported for a Ni-Mn-In-Co single crystal [105].The substitution of 3d element like Co have reported to enhance the meta-magnetic properties of these alloys [69, 105–108]. The addition of Co in Ni-Mn based alloys have reported to enhance the magnetism in the austenite and reduce the magnetism in the martensite phase. This consequently leads to larger of ΔM values and thus larger MFIMT temperature shifts [106, 109]–112]. Nayak et al. report that the increase in the Co concentration in Ni-Mn-Sb Heusler alloys result in lower transformation temperatures and a rise in the MCE which is attributed to a significant increase in the ∂M/ ∂T with Co doping [110]. Huang et al. also report the high-performance Co doped Ni-Mn-Sn alloy for room temperature magnetic refrigeration, where transformation temperatures were brought down by Co substitution and a large ΔM is achieved due to enhanced ferromagnetic exchange interactions in the parent phase due to Co doping [111]. A large refrigeration capacity of 251J/kg was also reported at room temperature under 50kOe magnetic field. The neutron diffraction analysis on Ni-Mn-Sn Heusler alloys at 5K show that the Mn moments couple anti-ferromagnetically in $Ni_{50}Mn_{33}Sn_{17}$ alloys, whereas the substitution of Co result a change in the magnetic structure, which leads to the ferromagnetic alignment in the Mn moments in $Ni_{45}Co_5Mn_{33}Sn_{17}$ [112]. The spin density maps obtained by neutron studies on Co doped Ni-Mn-In alloys reveal the factors responsible for enhanced ferromagnetic interactions [113]. The maps show that the Co atoms that replace the Ni atoms in the 8c sites tend to couple ferromagnetically with the Mn atoms in the 4a and 4b sites, which results in the enhanced net ferromagnetic coupling and hence enhanced magnetism in these alloys. The studies on$Ni_{50}MnIn$, $Ni_{45}Co_5MnIn$, and $Ni_{42.5}Co_{7.5}MnIn$ alloys show that while the transformation temperature of the alloy with the same In composition decrease, the Curie temperature of the parent phase significantly increases by Co doping [114]. Kainuma et al. also report that the addition of Co to the Ni-Mn-In alloys increase the Curie temperature and saturation magnetization in these alloys [106]. They also report the huge stresses over 100MPa

under the magnetic field of 70kOe. Karaca et al. report a large transformation strain of around 6% in $Ni_{45}Mn_{36.5}In_{13.5}Co_5$ [115]. A large reversible MCE has been reported in a $Ni_{49.8}Mn_{33.5}In_{15.5}Co_{1.2}$ alloy with a 7-layered modulated monoclinic martensite structure with ΔS_m= 14.6J\kgK under a magnetic field of 50kOe [116].

The entropy change during the MT can be controlled by long-range atomic order in these alloys [117, 118]. As mentioned above, the degree of atomic order can be modified by subsequent thermal treatments via high temperature quenching or under the appropriate ageing process. In Ni-Mn-In-Co quaternary alloys, the MT temperature decreases and Curie temperature increases with quenching temperature T < 900K, whereas above this temperature, an opposite behavior is observed, contrary to ternary Ni-Mn-In alloys [117, 119]. Thus the entropy change at the MT increases up to T < 900K, similar to ternary alloys, and slightly decreases further. The study suggests that the difference in the behavior of these quaternary and ternary alloys for different quenching temperatures could be related to the retained degree of atomic order at high temperatures where the ordering process is assisted by the higher vacancy concentrations. Moreover, the neutron studies reveal that the $L2_1$ atomic order decreases on heating above 700K. The study also suggests that the appropriate way to tune the atomic order in Ni-Mn-In-Co alloys appears to be an "in-situ" post-quench ageing treatments, where the evolution of the entropy change is similar to the ternary Ni-Mn-In alloys. However, the influence of atomic order on the MT in quaternary alloys is much lower than in the ternary ones subjected to the same thermal treatments [117, 120, 121]. Under the appropriate ageing process, it is possible to control the entropy change of a single alloy from 40 to 5J/kgK. This amplifies the possibilities to tune the functional properties of these alloys for application purpose.

1.3.1 Drawbacks

As previously mentioned, it is possible to modify the transformation temperature, magnetic properties and MT characteristics of Ni-Mn based Heusler alloys through compositional modifications, doping, and heat treatments. The goal is to fine-tune the multi-functional properties by modifying MT and its characteristics. Despite their promising features, Ni-based Heusler alloys possess poor mechanical properties, which include brittleness and fragility, hindering their development for practical devices and applications. Thus, efforts have been made over the last decade to improve the mechanical properties of these alloys, as it is crucial for the development of functional elements based on Ni-based Heusler compounds.

Over the past few years, various alternatives have been explored to overcome the limitations of bulk materials, including the use of ribbons [122], foams [123], and films made of alloys, as

well as embedding shape memory particles in a polymer matrix [124, 125]. The approach to use fine particles instead of bulk materials as an active material has been proven to control the brittleness and fragility of these materials [126–129]. As a result, utilizing micro-particles and powdered samples as active elements is becoming increasingly popular as an effective method for addressing the defective mechanical properties [127, 130–132] of these materials. The method of production of Ni-Mn based Heusler alloys is of utter importance. The most common used technique, which is simple and cost effective, is mechanical grinding (ball-milling). However, this technique has shown to induce defects, local stresses, dislocations etc., which affects the martensitic transformation acutely and the associated properties with it [16, 80, 93–95]. Many studies have been performed in order to examine the features that are affected by ball-milling. The residual stresses induced by the production of fine powders leads to stabilization of the martensite far above the martensitic transformation and the irreversibility of the martensitic transformation [83, 133]. The degradation of the martensitic transformation and larger hysteresis linked to it are also one of the results of induction of local stresses and strain induced by milling process [83, 134]. The long range atomic order that highly influence the transformation temperatures, Curie temperature and other magnetic properties of the Ni-Mn-Sn and Ni-Mn-In alloys [18, 20, 135] remains unaffected by the milling process [32]. However, the variation of atomic-order by quenching or the thermal treatments shifts the transformation temperatures up to 100K [78]. Therefore, by the combined effort of milling, quenching and thermal treatments, it is possible to optimize the properties of these materials. Furthermore, recent studies have suggested that shape memory alloy nano-particles may exhibit non-hysteretic behavior below a certain size [99], making them promising option for simultaneously improving mechanical behavior and related multi-functionalities. Although using powdered Ni-based Heusler alloys offers unique advantages, like controlling defects, local stresses, internal strains, and dislocations, it becomes crucial in this regime since they directly influence the MT [95, 136, 137]. Thus, controlling the microstructure becomes even more essential to improve the multi-functional properties of micro-particles and films. Recent studies have shown that by controlling the microstructure, it is possible to fine-tune the MT and related multi-functional properties [20, 138, 139]. Thus, powdered samples may overcome the main drawback of the bulk samples; however, they introduce other issues that need to be considered in micro and nano-scale systems.

To sum up, when it comes to taking advantage of the versatile characteristics associated with the appearance of MT in Ni-based Heusler alloys, reducing the size of the active components is becoming a successful method or overcoming the undesirable mechanical properties that are present in the bulk alloys. However, as previously mentioned, in the micro/nano-scale,

imperfections in the structure and state of the material can significantly affect the overall structural and magnetic properties. Therefore, it is important to thoroughly examine defects, local stresses, and the impact of strains in order to fully understand the effect of these imperfections on MT. By doing so, we can better adjust the structural and magnetic properties in Ni-Mn based Heusler alloys for more widespread use in various applications.

1.4 MSMA/polymeric composites

To circumvent the intrinsic brittleness of the bulk, composites constructed from polymer matrix with meta-magnetic shape memory powder alloys (where the polymer provides integrity and the alloy provides functionality) have recently been proposed and developed [124, 125, 140–142]. Several additive manufacturing processes, which are currently being investigated as an alternative for the elaboration of diverse and complex geometric shape memory alloys-based devices, also require a controlled powder production [143–145]. Metal 3D printing has a lot of potential for creating intricate structures for many uses. For instance, the enhanced heat exchangers for MCE applications made possible by additive printing include complicated geometries that increase the thermal conductivity up to by 100% when compared to a conventional construction [146]. However, the existence of undesired phases, issues with oxidation, corrosion, and internal stress that weaken the piece [147] show the inherent challenges associated with the rapid melting and cooling rates in printing process. Several strategies have been put up to address these issues, including production of polymer composites, thin films and melt spin method [124, 140, 148, 149]. For instance, Ni-Mn-Ga polymeric composite with particle size below 45µm obtained by spark erosion exhibit significantly larger hysteresis than the pure polymer control sample [150]. Moreover, spark-eroded Ni-Mn-Ga powders embedded in epoxy resin are shown to enhance the ductility and shape memory properties of the powder [140] and improve the formability of the alloys and reduce the ac eddy current losses [151]. Polymeric composites with MSMA particles have been studied in mainly Ni-Mn-Ga alloy system with the approach to maximize the damping capacity of the alloy [125, 152, 153]. Glock et al. report the increase in the damping characteristics in Ni-Mn-Ga polycrystalline particles embedded in the epoxy system Araldite LY 3297 and Aradur 3298 [152]. Feuchtwanger et al. [150] also report the increase in the damping potential with increased hysteresis and hence, higher energy loss in a Ni-Mn-Ga composite than a pure PU matrix, due to the twin boundary motion in the Ni-Mn-Ga particles. Recently, composites of Ni-Mn-Ga particles distributed in a soft silicone matrix were reported to attain 4% magnetic field induced reversible strains [154, 155].

Magnetic soft composites where the magnetic fillers are embedded into the soft polymer matrices have attracted a huge interest due to their potential use in soft robotics [156], biomedical devices [157–159], morphable electronics [160, 161] etc. Such composites usually contain fillers that are operational under the external stimuli of temperature [162, 163], magnetic field [164, 165], electric field [166], light [167–169] or humidity [170]. The fillers could be in the form of nano/micro particles, wires, polymer chains or fibers that can cause the matrix to respond mechanically for a variety of physical behaviors and controllable qualities [171–174]. The most popular active material for incorporating magnetic activity on 3D printed polymeric devices is nano-particles of ferrites. Magnetic soft composites, also known as magnetically responsive soft materials, are among the stimuli-sensitive soft materials that display unrestricted, quick, and reversible actuation and movement with multiple degrees of freedom under remote magnetic fields. The development of high power density actuators using magnetically responsive soft materials offers new opportunities in the realms of soft robotics and biomedicine [157, 175–182]. Different magnetically responsive soft materials with precisely programmed shape transformation [183, 184], magnetic resonance [185], locomotion [186, 187], and remote heat generation [188] can be made by integrating different kinds of magnetic fillers with soft matrices. The applied magnetic field may modify magnetically sensitive soft materials to perform different functions by having customizable magnitude, direction, and distribution. This significantly increases the application possibilities of material systems. Additionally, a variety of materials, including air, water, and the human body, are permeable to magnetic fields. Due to their particular application potential in minimally invasive surgery and medication delivery, magnetic soft composites can be maneuvered in small and constrained locations. In the biomedical field, Titanium based alloys have been widely employed for bone replacement treatments, due to its biocompatibility and mechanical properties. However, the prosthetics made of titanium based alloys have a number of drawbacks, including stress shielding and recurrent pain [189]. The composite PLA-PCL with TiO_2, which mimics the cancellous bone if PLA/PCL is added in a 3:1 ratio, is a better alternative for bone replacement and grafting operations [159]. In addition, exposure of polymer blends to the UV-radiation may lead to the photo-oxidation of the material, which leads to the breaking of the polymer chains by producing free radicals and reducing molecular weights [190, 191]. The incorporation of TiO_2 to the polymer matrix acting as a UV-stabilizer or UV-absorber, and decreasing the tensile strength with lower elongation at break [192]. Magnetic polymer composites have also been fabricated for bonding and 3D printing of permanent magnets by embedding MnAlC magnetic particles in polyethylene matrix [193] and $SrFe_{12}O_19$ (8wt%) particles and NdFeB (6.6wt%) in ethylene ethyl acrylate matrix [194]. No deterioration

in the permanent magnetic properties of the particles has been observed after the synthesis of the magnetic composite. Song et al. proposes a novel approach to reprogram the magnetization profile in a soft magnetic composite [195] by manipulating the ferromagnetic particles configurations via solid-liquid phase transition of the polymer encasing the particles. This approach allows free programming of the magnetization in the elastomeric base material and the material can be converted into a programmed structure as many times as required. In light of this, this form of soft magnetic composite with reprogrammable magnetization pattern might be useful obtaining a reconfigurable material system for a variety of applications like biomedical engineering, soft robotics, etc. Recent works on Magnetocaloric materials using 55wt% of the $(La,Ce)(Fe,Mn,Si)_{13}$-H particles embedded in poly-lactic acid matrix as the feedstock for the extrusion for Fused Deposition Modeling (FDM) show that MCE properties of the particles are not altered during the whole process [196]. However, the concentration of the polymer in the composite mixture reduces the functionality of the particles in the polymer matrix. In order to improve that, the composition of the polymer must be carefully selected..

One of the important factors to fabricate the polymeric-composites is the selection of the appropriate polymer matrix. Many polymers like ethylene ethyl acrylate (EEA), polyethylene (PE), polybutylene terephthalate (PBT), acrylonitrile butadiene styrene (ABS), poly-lactic acid (PLA), poly-ξ-caprolactone (PCL) etc. have been efficiently used as a polymer matrix [193, 194, 196–199]. The advantages of polymers generally includes being lightweight, easy to process, minimal water absorption, high electrical resistivity, high voltage breakdown strength, corrosion resistance, and most crucially, low cost. However, as long as heat management is crucial to the effectiveness, longevity, and dependability of magnetocaloric devices, thermal conduction in polymers becomes a difficult issue. Since the polymer matrix separates the thermally conductive fillers and serves as a thermal barrier, limiting the thermal conduction channel, the thermal conductivity of the polymer is especially crucial at low filler loadings. The main challenge to achieve the high thermal conductivity in polymeric composites is the creation of a continuous filler network. On the contrary, network development typically occurs at high levels of filler loading, which can result in poor mechanical qualities, poor processability and expensive costs [200, 201]. In the presented work, a mixture of PLA and PCL blends has been used to fabricate the polymeric composites. For the creation of high filling-factor composites for MCE applications, PCL and PLA are ideal options due to their low melting point and excellent ductility close to room temperature. Moreover, the use of micro/nano-particles of functional material into the PLA/PCL blend is a promising alternative to the bulk material to address different shortcomings like brittleness [27, 36, 69, 202–204]. Moreover, sophisticated 3D functional elements might be created utilizing inexpensive printers and printable polymer

composites, which would also eliminate the need to further post-printing heat treatments. In fact, choosing the right polymer can allow for the creation of novel materials with functionalized features based on meta-magnetic shape memory alloys for biomedical applications [205–208]. In the next section, the polymers used for such path, in order to obtain functional composites have been thoroughly discussed.

1.4.1. PCL and PLA Polymers

Polymers like polyethylene, polypropylene and polystyrene are being successfully used in today's world in almost every household for almost every other use. The omnipresence and the ceaseless demand for these materials require producing them on a huge scale. However, in order to satisfy material needs, there is still a strong desire to comprehend these materials and enhance their qualities. Although the polymers are increasingly being used to address a variety of issues, the development of new materials must definitely have a far greater emphasis on control, mainly of the molecular weight distribution and the polymer architecture. Numerous products, including coatings, adhesives, engineering and structural materials, packaging and textiles, among others, utilize polymers. The ability to include specific qualities through the thoughtful design of the (mainly organic) molecules from which the chains are constructed is a crucial component of the success and adaptability of these materials.

There exist innumerous sorts of polymers for innumerous uses. The two main polymers used in this present study to carry out the optimization of the powdered particles are polylactic acid (PLA) and poly-ξ-caprolactone (PCL). PLA and PCL are biodegradable **polyester compounds** that are created from organic, regenerative materials like sugarcane or corn starch [209–211]. Polyesters are polymers created by a condensation process between monomers in which ester groups are formed to connect the molecules together. The overall structure of the esters, which nearly always connect an organic alcohol to a carboxylic acid, is shown as:

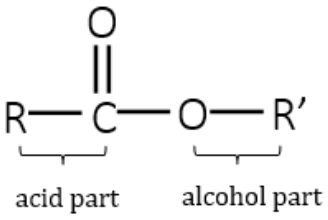

where, R and R' are any organic combining groups. Polyethylene terephthalate, polycarbonate, degradable polymers, alkyds and unsaturated polymers are some of the most common industrial polyesters. PLA and PCL fall into the degradable category of the polyesters along with the poly-glycolic acid (PGA) and poly-2-hydroxybutyrate (PHB), as well as their copolymers. The molecular structure of the PLA and PCL are described as:

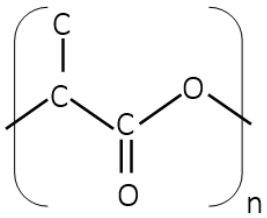

Poly-lactic acid (PLA)

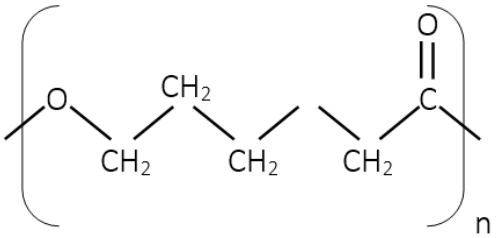

Poly-ξ-caprolactone (PCL)

These are prepared by ring-opening polymerization of the cyclic esters by acid catalysis. Micro-organisms or water can be used to degrade the ester groups that bind the monomers. Thus, these polymers are very useful in the medicinal applications since the breakdown products are natural metabolites. Since these polymers shrink when heated, these may also be utilized as shrink-wrap material in packaging [212–214]. Medical grade PLA is still a popular material for many medical applications, such as bone fixation [215] and tissues engineering [216], thanks to its fully biodegradable nature, well documented biocompatibility with the human body, high stiffness brought on by the relatively high glass transition temperature (T_g) [217–223]. In fact, the mechanical properties and the processing characteristics of each of a polymer play a vital role in the final required product and need further improvements.

a) PLA properties

One of the most significant advantages of PLA is its biodegradability. PLA's ability to biodegrade into water and carbon dioxide under controlled conditions makes it an attractive alternative to traditional petroleum-based plastics, which can take hundreds of years to degrade. PLA's biodegradability also makes it an excellent choice for disposable products such as food packaging and utensils, where waste reduction is a top priority. PLA is also known for its transparency, making it ideal material for packaging applications where product visibility is essential. Additionally, PLA has excellent mechanical properties, including high stiffness, strength, and impact resistance, which makes it suitable for various manufacturing applicatios.PLA has been extensively researched for its use in medical applications due to its ability to be absorbed by the human body and its compatibility with the human tissue. Medical products such as screws, sutures, and delivery systems have been developed using PLA-based

materials [224]. Researchers have focused on developing resorbable polymers for bone plate applications in order to reduce the stress-shielding effect and promote gradual healing. Resorbable composites, which can be reinforced with various materials such as calcium phosphate-based glass fibers and non-resorbable materials like carbon and polyamide fibers (in a way that PLA maintains its mechanical properties with time) [225], are also being explored. While resorbable composites prostheses have the advantage of not requiring a second operative procedure, concerns remain regarding the long-term effects of resorbed products and bio-stable or slowly eroding fibers in living tissues [225]. In addition to being used for medical devices, PLA fibers have also found success as resorbable sutures and in textile applications such as non-woven textiles for clothing. Micro- and nano-particles made from PLA are also being studied as potential drug delivery systems due to their degradability and low toxicity [226, 227]. Porous PLA scaffolds are also being explored as potential matrices for tissue and organ reconstruction, with various manufacturing techniques being developed for their production [226, 228].

PLA packaging is known for its mechanical properties and its considered a suitable material for packaging, being the most widely used biodegradable packaging material in the market, compared to polystyrene and PET [224, 229]. However, high cost of PLA limits its initial use in high-value applications, such as food beverage containers, rigid thermoforms, coated papers and films. Danone (France) is one of the first companies to use PLA as a packaging material, primarily for yogurt cups in the German market. Over the past decade, the use of PLA as a packaging material has increased cross Europe, Japan and the US, particularly for short shelf life products such as fruits and vegetables. PLA can be used for various packaging applications, such as containers, drinking cups, salad cup, water bottles, blister packages and wrapping for sweets, among others. PLA is also used in compostable yard bags to promote composting programs, and new applications such as cardboard or paper coatings are being pursued, especially in the fast-food industry. However, to expand the market for PLA, its limitations must be addressed.

One of the significant drawbacks of PLA is its relatively low heat resistance compared to traditional petroleum-based plastics [230, 231]. Due to the low melt tension, PLA's processing characteristics for blow molding are not particularly excellent. Peroxide, isocyanate and other additives might therefore be used to modify the melt's elongation viscosity since they can create cross-linked structures [232]. An efficient and effective filler for PLA that has been used in various studies is Nano-size clay, which overcome the high thermal distortion temperatures of PLA [233]. Brittle behavior and poor impact strength are the main mechanical characteristics that cause the most significant problems in the use of PLA. Recently, PLA was even combined

with synthetic rubbers to increase the impact strength while keeping in mind the limitation that only a small amount of petroleum-based ingredients may be used to maintain its biodegradable nature [234]. Recently, the authors tried to develop materials that might be used in actual applications while yet maintaining their biodegradable capabilities as well as improving its brittleness and toughness by acting as plasticizers [159, 235–243].

b) PCL properties

PCL has been extensively studied for its unique mechanical properties, ability to blend with polymers and biodegradability. Its physical, thermal and mechanical properties are determined by its molecular weight and degree of crystallinity, which also affect its biodegradation capability under physiological conditions. PCL is hydrophobic, semi-crystalline polymer that is easily soluble and processable due to its low melting temperature and exceptional blend compatibility. It has gained significant attention in the biomedical field due to its biocompatibility and biodegradability, making it a promising candidate for the development of controlled drug delivery systems, long-term implants, and scaffolds for tissue engineering and repairing [244, 245]. PCL has received certification from the FDA for use in a range of medical devices and drug-delivery applications, but only a few have been commercialized or translated to clinical studies. Recently, there has been growing interest in the use of PCL as a green material or biomaterial for various applications. PCL's superior rheological and visco-elastic properties make it easy to manufacture and shape into a wide range of biodegradable devices, making it suitable for medical applications like wound dressing, contraception, and dentistry [246]. PCL is also gaining attention in non-medical fields such as environment, packaging and food [247, 248]. PCL's interesting bio-friendly features make it a promising candidate for use in combination with biopolymers; enable tailorable degradation kinetics and mechanical properties, ease of shaping and the controlled delivery of drugs. PCL formulations have been prepared by self-assembly to form micro-/nanomicellar hydrogel structures after copolymerization, improving the encapsulation of bioactive molecules and drugs [249–251].

The tissue engineering approach involves creating porous scaffolds that need to provide suitable conditions for cells to grow and function optimally, which requires careful selection of polymers that can degrade at a suitable rate and exhibit intrinsic biocompatibility with cells. Aliphatic polyesters like PCL are attractive to use in such technology due to their ability to gradually degrade and support physiological loads until tissue formation is complete [252, 253]. Processing techniques must be chosen to confer tunable porosity and mechanical properties that can produce the most appropriate biological response to the PCL scaffold. Moreover, PCL has high permeability to small drug molecules and does not generate an acidic environment during

degradation, making it suitable for long-term delivery systems [254, 255]. However, its poor solubility in water can hinder drug release mechanisms. Recent advances in drug formulations using innovative colloidal vectors have improved the performance of drug delivery systems by increasing solubility (by solubilizing agents) and allowing for more efficient dispersion of drugs in PCL matrices [249]. Additionally, studies have shown that PCL/polyolefin blends can be a viable solution for food packaging, as enzymatic degradation of the can occur if viscosity and formulation are properly designed [256]. Porous PCL film, which increase the surface exposed to enzymatic degradation and also increase permeability to gaseous or vapor species, have also been studied [257].

PCL is semi-crystalline polyester with a rubbery amorphous phase at ambient temperature. The density of the PCL polymer is around 1.15g/cc with grass transition temperature (T_g) approximately ~60°C, and melting temperature (T_m) between 55-70°C, whereas for PLA density is around 1.24g/cc with T_g around 53°C and T_m around 153°C. PCL possess low melting and glass transition temperatures, high toughness and rubbery characteristics. Additionally, it is more thermally stable than PLA, raising the possibility that adding PCL to PLA may increase both its toughness/stiffness and thermal stability as well as the improved brittleness [258]. Therefore, combining this biodegradable polymer with PLA leaves the material with higher impact strength compared to neat PLA [259–261].The aim of this study is to achieve 3D printable filament wires with optimum magnetic response due to the meta-magnetic shape memory particles. The advantage of PLA/PCL blends is that these can be easily molded when heated, which makes these suitable for 3D printing applications.

1.4.2 3D Printing

Three-dimensional (3D) printing, also known as additive manufacturing, has revolutionized the way we produce and design objects. The technique involves building a 3D object layer by layer, using a digital model as blueprint. It allows for the creation of complex and lightweight structures that are difficult to produce using traditional manufacturing methods. The growth of 3D printing has been mainly in the prototype manufacturing sector, with actual production still at a lower level. However, there has been significant increase in the adoption of 3D printing in the medical, automotive, aerospace, food and engineering industries [262–268]. The compound annual growth rate of 3D printing in these industries is predicted to increase significantly by 2026. Among many materials that can be used for 3D printing, polymers have attracted significant attention due to their wide range of applications, low cost, and ease of processing [269–271]. The most commonly used polymers in 3D printing are thermoplastics, which can be melted and reshaped multiple times. Arcylonitrile butadiene styrene (ABS) and PLA are two of

the most widely used thermoplastics in 3D printing due to their cost, ease of processing and availability [272–275]. Other thermoplastics such as polyamide (PA), polyethylene terephthalate (PET) and polycarbonate (PC) have also been used for 3D printing. There are various types of 3D printing methods available, such as Stereo lithography (SLA), Selective Laser Sintering (SLS), Laminated object Manufacturing (LOM), Solvent Cast Direct Writing (SC-DW), and Fused Deposition Modeling (FDM). Among these, FDM is the most widely used method for 3D printing of polymers. While it has some limitations, such as slow printing speed, restricted print dimensions, and rough surface finish, it offers many benefits, including cost-effectiveness and can produce objects with a high degree of accuracy and detail. FDM involves melting a thermoplastic filament feedstock and extruding it layer by layer to build the object [276]. The filament feedstock for 3D printing can be a single polymer, polymer blends, or composite materials with a base polymer and filler materials like metals, ceramics, and carbon, depending on the intended application. For instance, researchers have combined ABS and multi-walled carbon nano-tubes to create filament for FDM feedstock [277]. Also, composites by combining Fe_2O_3 particles with PLA as feedstock filament for FDM were developed to print PLA-based magnetic polymer filaments [278]. A lot of research has been conducted to study the behavior of these polymers during printing and the mechanical performance of FDM printed parts under tensile, flexural and impact loading [279–288]. The use of FDM can significantly improve the thermal conduction of polymers, which is critical to the performance and lifetime of devices.

1.5 Objective and structure of thesis

The main objective of this thesis is to obtain 3D printable polymer-composites embedded with meta-magnetic shape memory micro-particles with optimum magneto-structural properties for magnetocaloric applications. A well known $Ni_{45}Co_5Mn_{36.7}In_{13.3}$alloy has been to obtain micro-particles. The route to obtain micro-particles from the bulk is hand-crushing/ball-milling, which induces large plastic deformation and internal stresses, which may have a significant impact on the magneto-structural properties of the alloys. Therefore, a deep understanding and analysis of the role of the defects onto the MT and multi-functional properties of these alloys is very important. The thesis work has been presented in six chapters.

- A broad introduction to the key ideas is given in Chapter 1, along with a list of the most important previous works and references related to the actual work.
- Chapter 2 contains the working mechanisms of the experimental techniques employed in this work. Characterization techniques like DSC, XRD, SQUID, SEM have been

presented briefly. A summary of the synthesized samples are also described in the chapter.

The main results obtained during the research work are presented in Chapter 3, 4 and 5.

- In Chapter 3, the influence of mechanical grinding/ball-milling on the microstructural and magnetic properties of $Ni_{45}Co_5Mn_{36.7}In_{13.3}$ alloy is presented. The bulk alloy was first subjected to soft-milling/hand crushing and then to ball milling. A thorough study of the effect of deformation on the different structural phases (austenite and martensite) has been presented.
- Chapter 4 studies the possible correlation between particle size and magneto-structural properties of milled micro-particles. The magneto-structural properties of the micro-particles previously analyzed have been studied separately for different particle size ranges. In particular, the characteristics of the martensitic transformation, the saturation magnetization and microstructural parameters such as the internal strains and crystallite size have been analyzed for particles within specific size ranges and coming from different milling times
- In Chapter 5, we provide a route to fabricate composites materials for MCE applications from the optimized micro-particles. A variety of 3D printed objects have been presented using flexible 3D printable polymer-composite wires. Various combinations of polymers and micro-particles concentrations have been tried in order to obtain 3D printable wires with optimum MCE response.
- Finally, the main conclusions established from this research work have been given.

Chapter 2

Experimental Techniques

The research work carried out in this doctoral thesis is basically of an experimental nature. This chapter provides a brief summary of the various experimental techniques and equipments used during the development of the present work. Different specific techniques have been used concerning the synthesis of materials, magnetic and structural characterization and analysis of their functionality. In some cases, such a standard X-ray diffraction or DSC, the equipment is available in the laboratory at the University, while in others, such as neutrons or synchrotron X-ray diffraction techniques, the measurements were carried out in large facilities. In any cases, the learning of these techniques, the control of the instrumental conditions and the correct interpretation of the results has been one of the main tasks throughout this thesis.

2.1 Powder elaboration

2.1.1 Arc melting furnace

An Edmund Buhler MAM-1 arc furnace was used in order to obtain polycrystalline samples from pure elements (figure 2.1). Arc-melting furnace is very common technique to melt the metals to obtain alloys. Ni, Mn, In, and Co high purity elements were melted to obtain polycrystalline samples with stoichiometry of $Ni_{45}Co_5Mn_{36.7}In_{13.3}$. The masses of the elements in the stoichiometric ratio are measured carefully and placed in the metal chamber. The melting is performed in a refrigerated copper crucible by introducing an arc discharge by inducing the voltage difference between a tip and Wolframium stick attached inside the chamber. The handle above the chamber controls the direction of the arc and it hits the elements right from the above. The temperatures up to 4000K can be acquired that ensures the fusion of all the elements. Constant water current is attached with the crucible in order to avoid the overheating of the constituents. The chamber is filled with Argon atmosphere by purging it for several times to ensure a pure Argon environment. This ensures the prevention from oxidation and a suitable environment for electric discharge to take place. The melting process has been performed for six to eight times to improve the homogeneity of the resulting ingot. This droplet shaped ingot is cleaned after each melting to ensure the oxide free bulk alloy. The ideal mass that can/should be produced is between 15-20gms. The higher masses are also feasible to produce up to 35-40gms, however, the quality and homogeneity of the ingot is reduced.

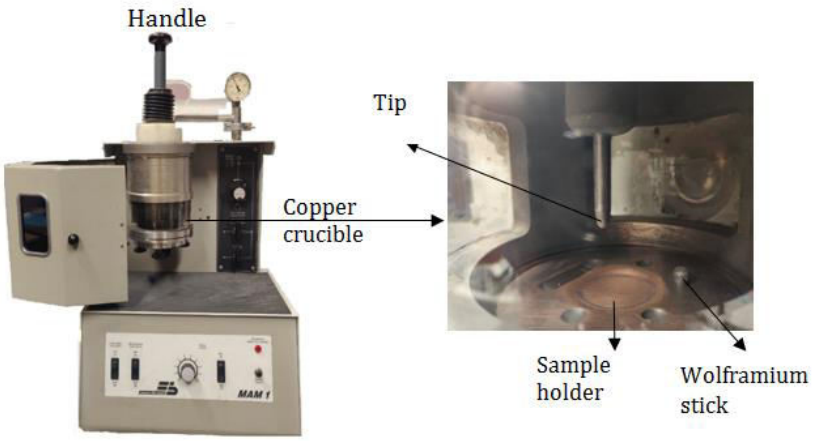

Fig. 2.1. Arc furnace Edmund Bühler MAM-1.

2.1.2 Thermal treatments

A long thermal treatment under high temperature is necessary post-synthesis of the ingot to further ensure the homogenization. Since the crucible chamber is refrigerated by water, its temperature is lower than that of the melted ingot. As a result, the solidification of the ingot becomes directional and non-homogeneous (from the edges to the center). Therefore, post-annealing process at high temperature is very necessary to ensure the homogenization. The annealing temperature has to be selected, depending on the melting temperature of the alloy system. In the case of $Ni_{45}Co_5Mn_{36.7}In_{13.3}$ composition, the lowest melting point of the alloy is around 1200-1300K. Therefore, the annealing was performed at 1073K for 24hrs. This treatment improves the homogeneity by allowing the atomic diffusion provided by the thermal energy at high temperatures. The long-range atomic order at room temperature and hence the martensitic transformation can be modified just by selecting the cooling route of the ingot (previously explained in Chapter 1). Slow cooling from the high temperatures in a controlled atmosphere or a controlled quenching from high temperatures are usually performed thermal treatments in these kinds of alloys. The used vertical furnace is shown in figure 2.2. The alloy is placed hanging tied to a Kanthal Wire (a ferrite iron-chromium-aluminum (FeCrAl) alloy with excellent heat resistance), in a vertical quartz tube. This vertical tube runs through the furnace and is connected to argon supply and a rotary vacuum pump. An inert atmosphere is achieved by purging the tube multiple times and filling with the argon, in order to avoid any kind of oxidation. The sample is hanging by a pin kept horizontally in such a way that the sample falls once the pin is removed. This furnace was also used for annealing treatments (873K for 30 minutes) to remove deformation induced defects (see later) or change the atomic order.

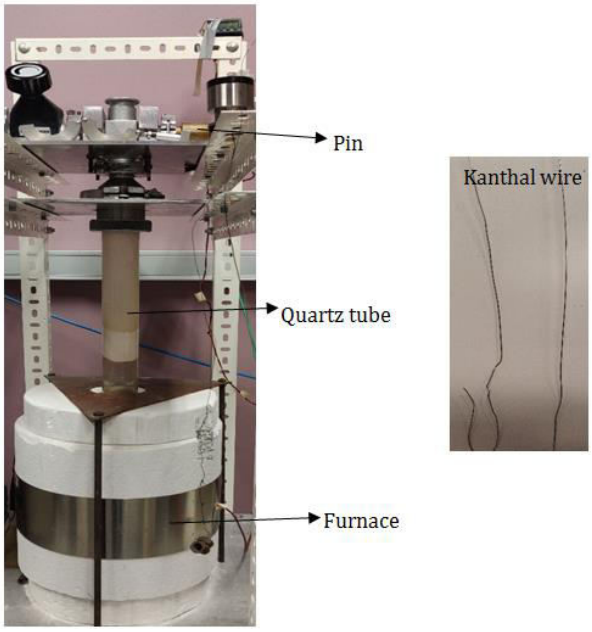

Fig. 2.2. Vertical furnace used for quenching and annealing treatments.

2.1.3 Mechanical treatments (milling)

Mechanical treatments, in particular hand crushing and ball milling, are used to obtain micro-particles which will be introduced in polymers (see later) to get functionalize and 3D printable composites. A key point is the understanding of the properties linked to the deformed microstructure. The first treatment the sample goes through is hand-crushing using agate mortar (figure 2.3a). The idea is to obtain smaller particles by soft crushing first to facilitate the ball milling process. Moreover, a controlled deformation needs to be introduced as an initial step. The further decrease in the particle size is achieved by ball-milling. Ball milling is the most used grinding technique that is used to induce deformation, or to mix or grind or blend materials like ceramics, paints or metals. In the present case, Retsch planetary ball mill PM-100 has been used, which consists of a cylindrical container and the tungsten carbide milling balls. The planetary motion with 300rpm in which the cylindrical container rotates (with the collisions of the milling balls with the material and the balls itself) have a great impact on the material by changing the structure and physical properties of the material as well as reduction in the size of the particles. The number of the tungsten carbide balls (around 10mm diameter) to add while milling is decided by the volume of the powder (5:1- ball to powder ratio), which, in the end, controls the properties of the final product. The ball mill used in this research work does not have any chamber that allows any inert atmosphere or a temperature controller. Due to the multiple collisions between the balls, particles and the cylindrical chamber, the temperature of

the system increases. This, consequently, leads to the risks of oxidation. To overcome this problem, the chamber is filled with nitrogen gas using glove box chamber. A few drops of methanol were added before closing the chamber tightly.

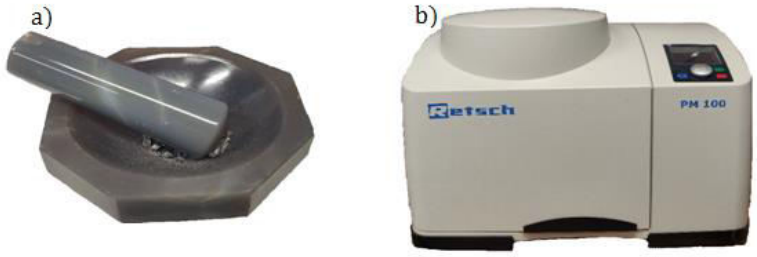

Fig. 2.3. a) Agate-mortar, b) Retsch planetary ball-mill PM 100.

In addition to this, the milling process is carried out in intervals, by interrupting the process every 5 minutes after each 5 minutes of milling. This helps to avoid the overheating of the chamber. The influence of the deformation on the microstructure and the magneto-structural properties has been studied in the hand-crushed and ball-milled powders in the next chapters. The obtained powders are sieved in order to study the correlation between the particle size and the degree of deformation. The sieves ranging from 100μm to 10μm have been used to filter the different particle sizes. The maximum milling time used to obtain smaller particles is up to 15 minutes. The particle size up to 25μm has been achieved by milling time of 15 minutes.

2.2 Synthesis of composites

In order to obtain printable composites, different compositions of PLA and PCL polymers have been mixed with different concentrations of magnetic particles. The technology developed for the production and the subsequent analysis of composites has been optimized throughout the development of this thesis. Therefore, this particular issue related to the synthesis procedure used to produce the magnetic polymer compounds will be presented and discussed in detail in section 5.2 of Chapter 5.

2.3 Characterization techniques

Various techniques have been used for the microstructural and magnetic characterization of the different samples. This section briefly describes the most relevant techniques to obtain the results shown in the following chapters. It is worth mentioning that in all cases, the chemical composition of the bulk alloy was verified by EDS (see below) before any further analysis or

procedure. The average composition has been estimated measuring the compositions in the various regions of the sample.

2.3.1 Differential Scanning Calorimetry (DSC)

Differential scanning calorimetry is a thermal characterization technique that measures the difference between the amount of heat needed to raise the temperature of the sample and the reference (during heating and cooling ramps or for isothermal measurements). The temperature is varied linearly with time in a way that the sample and the reference are at same temperature at all times. The amount of heat required keeping the sample and the reference at same temperature varies as the sample undergoes any kind of first or second order phase transition or chemical reaction during any thermal cycle. Such deviations provide the information about the phase transitions during thermal cycles and their corresponding enthalpies and the characteristic temperatures. In first order phase transitions (like the martensitic transformation or ordering processes), two possible processes are generally witnessed: i) an exothermic process, where the energy is released to the environment by the sample and lower heat flow required than in the reference. ii) an endothermic process, where energy is absorbed by the sample from the environment and higher heat flow than in the reference. The corresponding peaks are obtained during these processes.

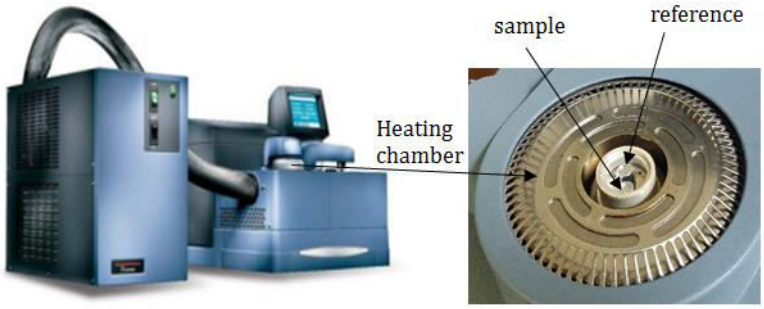

Fig. 2.4. Differential Scanning Calorimeter Q-100 DSC, TA Instruments.

A commercial DSC Q TA100 calorimeter was used for all the calorimetric measurements in this thesis work (figure 2.4). This DSC apparatus includes a heating chamber with two pans for the measurement, one for the sample and the other for the reference. The temperature of the sample and the reference are controlled by a thermocouple and a thermal resistance connected to the pans. This chamber is under a nitrogen gas environment that reduces the risks of oxidation and a better thermal conductivity. Different temperature control systems, enables the calorimeter to perform the measurements between 90K to 1000K ranges. For instance, the Liquid Nitrogen Cooling System (LNCS) allows covering the low temperature ranges from 90K to 673K. Based

on air compression refrigeration, Finned Air Cooling System (FACS) system allows the measurements from the room temperature up to 1000K. However, in the present work, the most used system for almost all of the research work is Refrigerated Cooling System (RCS), based on vapor compression, which allows measuring the heat exchanges from 180K to 673K.

In order to obtain the thermodynamic parameters, a previous calibration of the baseline and cell-constant is required. Firstly, two consecutive measurements are performed with the empty chamber and with two identical sapphire disks are placed in the sample and reference pans. The cell constant is determined through the latent heat of an Indium sample. In our case, is measured and the heat exchange with corresponding enthalpies are calculated. Once calibrated, the analysis provide the information about the presence or absence of martensitic transformation as well as the transformation temperatures, the corresponding enthalpy changes during the forward and reverse transformation, Curie temperature etc. For instance, figure 2.5 shows an example of the result obtained from the DSC instrument. The arrows represent the heating and cooling directions. The ramps are set at 10K/min heating-cooling rates. During cooling, an exothermic peak between 272K and 320K represents the forward/direct martensitic transformation (FMT) from austenite to martensite. On the other hand, during heating, an endothermic peak between 300K and 345K represents the reverse martensitic transformation (RMT) from martensite to austenite. The temperatures M_s, M_f represent the initial and final temperatures of the martensitic phase, whereas A_s, A_f represent the initial and final temperatures of the parent austenite phase transition. These temperatures are indicated by the intersection of the tangents of the baseline and start and final of the peaks obtained. The shoulder type curve in the baseline around 367K indicates the Curie temperature. The peak maximum are represented as T_M^{for} and T_M^{rev}, which are the martensitic transformation temperatures during FMT and RMT respectively. The difference in the peak temperatures during FMT and RMT gives the thermal hysteresis during the transformations $\left(\Delta T = T_m^{rev} - T_m^{for}\right)$.

The heat flow or the change in enthalpy (ΔH) during the transformation is calculated as the area under the peak. The entropy change (ΔS) during the transformation is calculated as:

$$\Delta S = \frac{\Delta H}{T_M} \quad (J/kgK) \qquad 2.1$$

where, T_M is the transformation/peak temperature during MT. In addition, the other factors affecting the magnetic and structural properties like recrystallization, atomic ordering, and appearance of secondary phases can also be detected and analyzed by DSC.

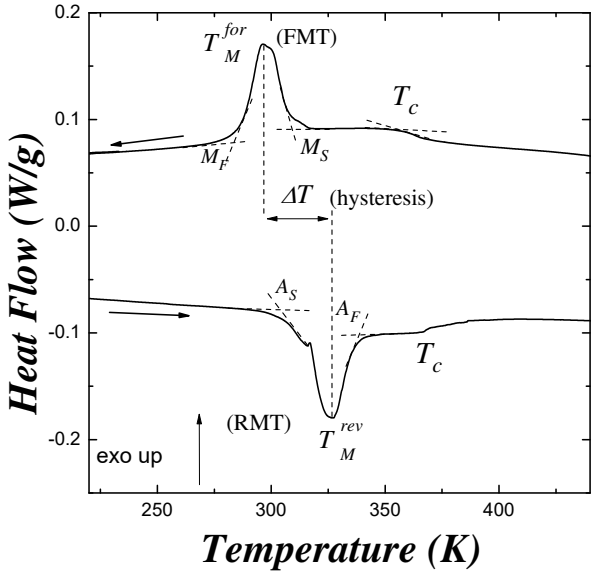

Fig. 2.5. Typical DSC thermogram with the critical temperatures obtained using tangent method for a $Ni_{45}Co_5Mn_{36.7}In_{1.3}$ bulk alloy.

2.3.2 Superconducting Quantum Interference Device (SQUID)

The SQUID magnetometer is a very sensitive device that was used to analyze the magnetic properties of the samples. By covering a broad temperature range from 1.5K to 300K and magnetic fields from -7T to 7T, this device allows the study of the magnetic susceptibility (χ) and magnetization (M) of the magnetic materials. This magnetometer consists of a superconducting loop with two Josephson junctions (see figure 2.6) [289]. With a specific threshold value of electric current, the electrons flow through these junctions by quantum tunneling. Any change in an external magnetic field should not affect the magnetic flux (Φ) contained within the superconducting loop, since it should be constant (since any variation in the external magnetic field produces a current in the ring that neutralizes the flux change). To offset the change in flux, the magnetic field causes a current (J) to flow through the loop. Any changes in Φcause changes in J, since the electric current J is defined as:

$$J \propto sin\emptyset \, cos\left(\frac{e\emptyset}{h}\right) + \frac{2V}{R} \qquad 2.2$$

where, $\emptyset$ is the phase difference in the wave-functions characterizing the quantum behavior of Cooper pairs that produce superconductivity at end of each junction, V is the potential difference and R is the resistance of the junction. If in the setup shown in the figure 2.6 we apply a bias current to the superconducting ring and, due to the presence of the sample, the external field increases in such a way that the critical current of the junctions is exceeded,

oscillations will be observed in the output voltage. The flux change brought by the magnetic sample can be calculated by counting the oscillations, as there is an increase of one quantum flux during each oscillation. The changes in the magnetic field linked with even one quantum flux can be measured by sensitive SQUID magnetometer, irrespective of the large absolute values of the magnetic field. In the present work, Quantum Design MPMS XL-7 SQUID was used for most of the magnetic characterization (figure 2.7). The measurements were performed: *i*) by keeping the temperature constant and analyzing the variation of the magnetization (*M*) with the magnetic field (*H*) and *ii*) by keeping the magnetic field constant and analyzing the variation in the magnetization with the temperature (*T*). The chosen temperature range in this work was mostly from 10K to 400K with field ranging from 100Oe to 6T.

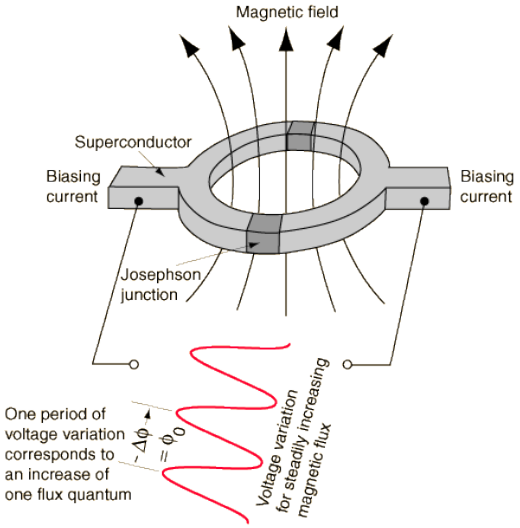

Fig. 2.6. Schematic representation of a SQUID magnetometer.

A typical curve generated by the temperature variation of the magnetization at 100Oe magnetic field for a $Ni_{45}Co_5Mn_{36.7}In_{13.3}$ alloy is shown in figure 2.8. The arrows show the direction of heating and cooling ramps. Cooling from 400K leads to the FMT with the characteristic temperatures M_s and M_f. The huge change in magnetization from austenite to martensitic phase shows the meta-magnetic behavior of the alloy, where transition occurs from ferromagnetic austenite to weakly magnetic martensite. While heating, RMT occurs and characteristic temperatures A_s and A_f are shown in the figure 2.8. Heating up to 400K, a fall in the magnetization around 367K is the Curie temperature (T_c) associated with the ferro-to-para transition in the austenite.

Fig. 2.7. Quantum Design MPMS XL-7 SQUID magnetometer.

.

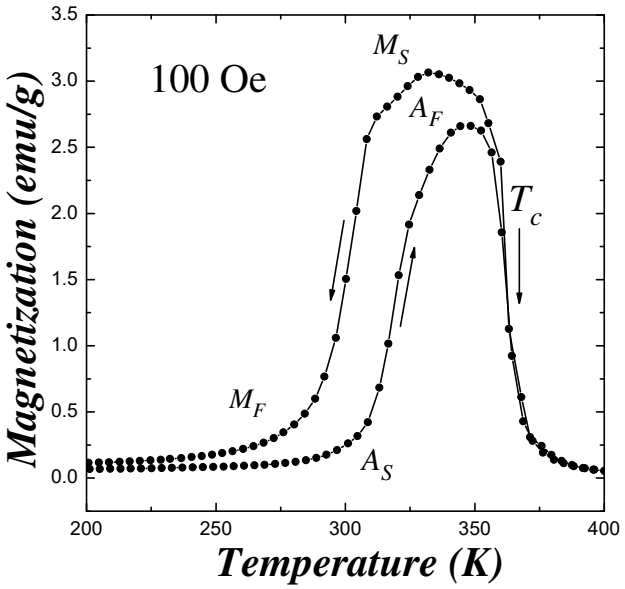

Fig. 2.8. Temperature dependence of magnetization under 100Oe applied field for the $Ni_{45}Co_5Mn_{36.7}In_{13.3}$ bulk alloy.

The Magnetocaloric effect (MCE) can be evaluated from the magnetization curves M(T) measured at different magnetic fields by using this formula:

$$\Delta S = (T,H) - (T,0) = \int_0^H \left(\frac{\partial M}{\partial T}\right) dH \qquad 2.3$$

where S is the entropy [51]. If raising the magnetic field increases the MT temperature, then magnetic solid heats up, while $\Delta S < 0$ (ferromagnetic materials, conventional MCE). On the other hand, if rising magnetic field lowers the MT temperature (higher magnetic order), the magnetic solid release the heat, while $\Delta S > 0$ (meta-magnetic materials, inverse MCE).

2.4 Structural analysis

The effect of the milling on the microstructural properties of the alloys has been analyzed mainly by X-ray and neutron diffraction and Scanning electron microscopy (SEM).

2.4.1 Scanning Electron Microscope (SEM)

A SEM produces images scanning the sample surface with a highly focused electron beam. In this process, electrons interact with the atoms to produce signals that reveal the topography, morphology, composition and crystallographic information of the object. The position of the beam and the signal being detected are combined to create a picture. A schematic representation of SEM is shown in figure 2.9. The electron source is equipped with a filament cathode that thermionically emits an electron beam. Due to its high melting point, low vapor pressure and inexpensive price, tungsten filaments are usually used. Tungsten wire is heated by the current and emitted electrons are accelerated to the anode. Lanthanum hexaboride (LaB_6) cathode or Field emission guns (FEG) are also other types of emitters that are used for electron emission. The beam travels through electromagnetic fields and lenses, which focus the beam down toward the sample.

The scanning coils guides the beam in a way that it scans the surface of the given sample in a raster way. The diameter or spot size of beam at the sample is determined by the final aperture lens, which is situated below the scanning coils. When the incident beam makes contact with the surface of the sample, it produces signals in the form of Secondary electrons (SE), Auger electrons, Backscattered electrons (BSE), Characteristic X-rays, Cathodoluminescence (see figure 2.10). Various signal detectors capture the emitted signals and transform them into digital images that can be seen on a screen. For example, Energy dispersive spectrometer (EDS/EDX) captures X-rays and turns them into a pattern of intensity *vs* frequency as shown in figure 2.11. The different peaks correspond to the energy levels of the different electronic transitions associated to the atoms present in the sample. Large peak intensities imply high concentration of the corresponding element. The EDX technique is used to identify the elemental composition of the specimen and allow the mapping of the different elements across the sample. These mapping creator composition dependent images of the sample surface.

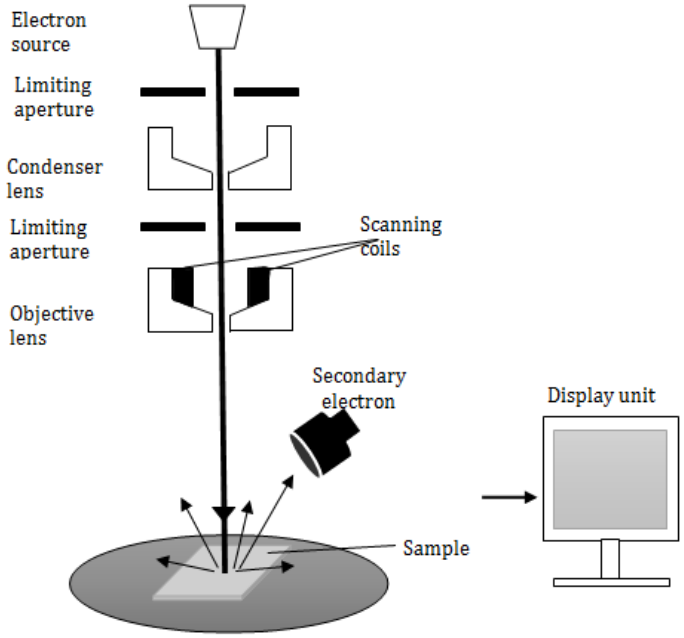

Fig. 2.9. Basic construction of SEM.

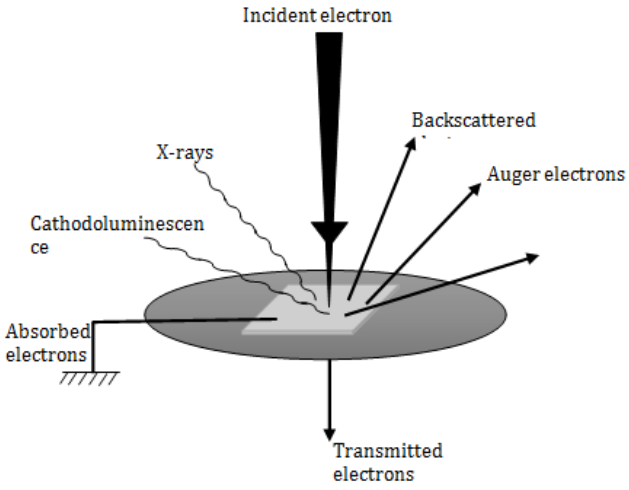

Fig. 2.10. Emission of various electrons and electromagnetic waves from the specimen.

On the other hand, BSE and SE are most commonly used for imaging of the specimen. The BSEs are emitted from the deeper parts of the specimen and are sensitive to the atomic number. The elements with the higher atomic number appear brighter in the image. The SE originate from surface regions providing topography information. A Joel JSM-5610LV system has been used during this thesis for the microstructural characterization.

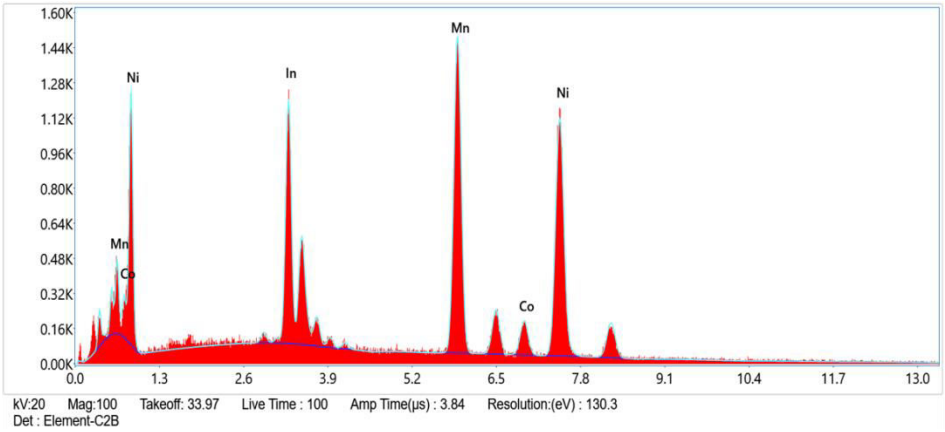

Fig. 2.11. SEM/EDX results output for $Ni_{45}Co_5Mn_{36.7}In_{13.3}$ alloy.

2.4.2 Diffraction

The elastic scattering of particles like photons, electrons, neutrons with a crystalline solid, give rise to the phenomenon of diffraction. In crystallographic terms, the scattering vector can be defined as $Q = k - k'$, being k, the incident wave vector and k', the scattered wave vector. The modulus of the both wave vectors is $1/\lambda$, where λ is the radiation wavelength. Bragg's law gives the diffraction condition:

$$n\lambda = 2d_{hkl}\sin\theta \qquad 2.4$$

where, (hkl) is the family of planes, d is the inter-planar distance and θ is the angle between the incident beam and atomic planes. The Bragg's law can be useful to determine the values of "d" and consequently about the crystallographic unit cell.

According to the Ewald construction (see figure 2.12), the Bragg's condition (with a maxima in a particular diffraction direction) can only occur if the scattering vector **Q** is a reciprocal lattice vector and its arrow head locates in the Ewald sphere of radius $|k| = 1/\lambda$. Consequently, **Q** is perpendicular to the diffracting (hkl) family of planes with the modulus $\mathbf{Q} = 2\sin\theta/\lambda$.

On the other side, the intensity of the diffracted peaks is proportional to the square modulus of the structured factor:

$$F(\boldsymbol{Q}) = \sum_{j=1}^{N} a_j e^{i2\pi Q.r_j} \qquad 2.5$$

where, j represents the different N atoms in the unit cell, r_j is the atomic position of the j atoms and a_j is the atomic scattering factor. In the present research work, powdered samples are used and therefore, considering the powder as a large amount of single crystals randomly oriented, the diffracted beams form a geometrical structure (as shown in figure 2.13) widely known as Debye-Scherrer cones.

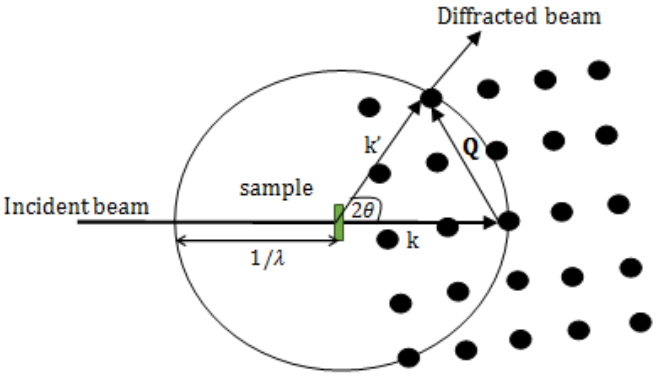

Fig. 2.12. Schematic representation of Ewald's sphere.

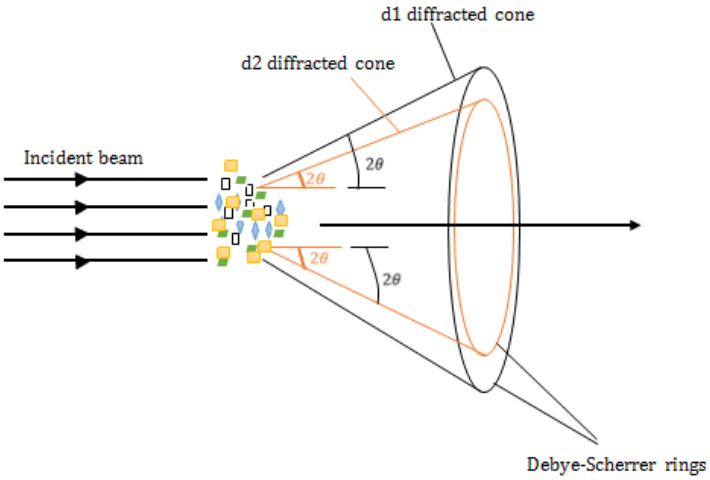

Fig. 2.13. Powder diffraction showing different Debye-Scherrer cones due to different diffraction conditions.

A standard diffraction pattern is obtained measuring the intensity of beams with a linear detector along a transversal direction (in texture free sample all directions are equivalent). An example of such diffractogram is shown in the figure 2.14. The positions of the peak are determined by

the parameters of the unit cell, whereas the intensities of the reflections can be calculated from the expression:

$$I = C \frac{J_{hkl} A_{hkl} F_{hkl}^2}{L} \quad 2.6$$

where C is the constant which varies with the instrument (depending upon the wavelength of the radiation, the intensity of the beam, the density and the dimensions of the specimen, the window detector size), J_{hkl} is the multiplicity of the hkl plane, L is the Lorentz factor, F_{hkl} is the structure factor, A_{hkl} is the absorption factor.

- J_{hkl} - The multiplicity is related to the number of equivalent planes participating in the intensity of the peaks.
- A_{hkl} - Takes into account absorption effects
- F_{hkl} - The position of the atoms in the unit cell is described in the structure factor.
- L – The geometry and polarization of the beam is accounted by the Lorentz-Polarization factor.

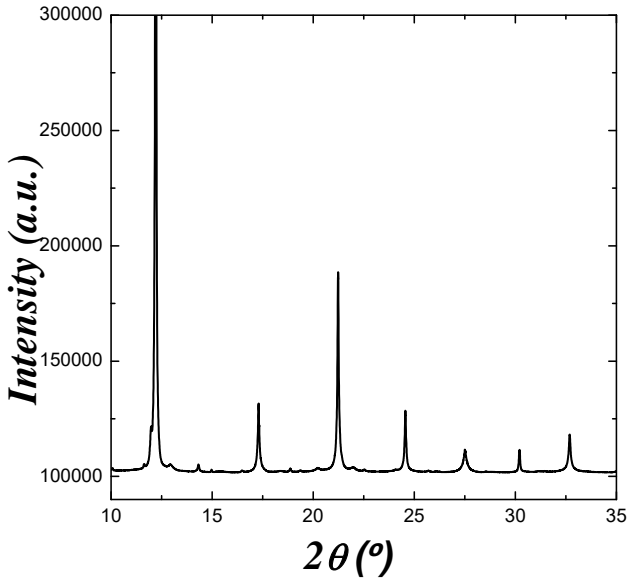

Fig. 2.14. Typical powder diffractogram for austenite phase in $Ni_{45}Co_5Mn_{36.7}In_{13.3}$ powdered alloy.

2.4.2.1 Rietveld refinement

The Rietveld refinement method has been used to analyze the spectra obtained by powder diffraction [83, 117, 138, 290–293]. The Rietveld method is based on the analysis of the complete profile of the diffraction pattern considered as a set of intensities for each angular position 2θi (i = 1....N). No prior correction is made to the observed diagram. All the

information contained in the powder diagram is parameterized in a mathematical model so that the square of the difference between the experimental data (y_i) and the calculated data ($y_{c,i}$) is minimized. The function to minimize is written as:

$$\chi^2 = \sum_{i=1}^{n} w_i \{ y_i - y_{c,i}(\beta) \}^2 \quad 2.7$$

where, i is the number of observations, y_i and $y_{c,i}$ are the observed and calculated intensities at step i, respectively and w_i is $1/\sigma^2$, where σ is the experimental observation variance.

The model to describe the function $y_i(2\theta)$, which represents the diffraction intensity at each angular position and fully defines the diffraction spectrum, is based on the expression:

$$Y_{i_{calculada}} = \sum_{\phi} c_{\phi} \sum_{k} I_{\phi k} \, \Omega(2\theta_i - 2\theta_{\phi k}) + b_i \quad 2.8$$

Being:

ϕ : Labels a given crystallographic phase and ranges from 1 to the number of phases present

k : Bragg reflection that can contribute to an observation "i"

c_ϕ : ϕ phase scale factor. Allow to determine the fraction of each phase

$I_{\phi k}$: Intensity of the reflection k of the phase ϕ

$\Omega(2\theta_i - 2\theta_{\phi k})$: Value of the function $\Omega(x)$ normalized to unity and chosen to describe the individual profile of a Bragg reflection at position $2\theta i$ due to the reflection ϕ_k situated in the $2\theta_{\phi k}$ position.

b_i : Background at position $2\theta i$

Each functions I, Ω and b are calculated based on models that depend on a series of parameters. These parameters, together with the scale factor (c_ϕ), are refined in order minimize the difference between experimental and calculated spectra.

Among the different factors that enable to assess the goodness of the fit, the Weighted R-pattern factor (R_{wp}) has been used:

$$\text{Weighted R-pattern factor } (R_{wp}) = \sqrt{\frac{\sum w_i |y_i - y_{c,i}|^2}{\sum w_i |y_i|^2}} \quad 2.9$$

Information about the micro-strains (linked to dislocations or anti-phase domains) and crystallite size can also be provided by the careful analysis of the broadening of the reflection

peaks. The Pseudo-Voigt approximation is vastly used when it comes to analyze microstructural aspects (average grain size and strain). The pseudo-Voigt function, *pV(x)*, is a linear combination of the Lorentzian and Gaussian function:

$$pV(x) = \eta L'(x) + (1 - \eta)\, G'(x) \qquad 2.10$$

with same Full Width Half Maxima, FWHM ($H_L = H_G$ = H), instead of two different parameters. These two functions are weighted by the parameter η, whose values range between 0 and 1. The profile shifts towards pure Gaussian or pure Lorentz when η approaches 0 or 1, respectively.
The integral width (β_S) of any particular reflection peak due to size effect can be related to the average volume of those crystallites size by using the Scherrer's formula:

$$\langle D \rangle_V = \frac{\lambda}{\beta_S \cos\theta} \qquad 2.11$$

It is worth mentioning here that the 'particle size' characterization in the powdered samples does not necessarily directly correspond with the 'crystallite size'. In fact, the perceived size of the coherent domains is not proportional to their physical dimensions. In order to correlate the apparent sizes for distinct Bragg's reflections, the crystallites are normally assumed spheres. The strain, however, depends on a different way with the diffraction angle.

The maximum strain, *e*, can be directly related to the integral width (β_D) of a reflection by due to strain effect:

$$e = \frac{\beta_D}{4\, tan\theta} \qquad 2.12$$

Alternative to the Rietveld refinement, Le Bail method can also be used to refine crystallite size and strain. This method does not take into account the structure factor and the intensity of the peaks are also adjustable parameters.

2.4.2.2 X-ray diffraction

In the present work, laboratory Powder X-ray diffraction technique (PXRD) and synchrotron PXRD techniques have been employed to characterize the microstructure of the powdered samples. The laboratory PXRD instrument used in this work is a Siemens Diffractometer D5000 with CuKα radiation (wavelength λ =1.54Å) in Bragg-Brentano configuration working at room temperature. The powder, beam source and the detector are placed forming a circle where the sample is at the center and source and the detector are at a same distance from the sample (figure 2.15).

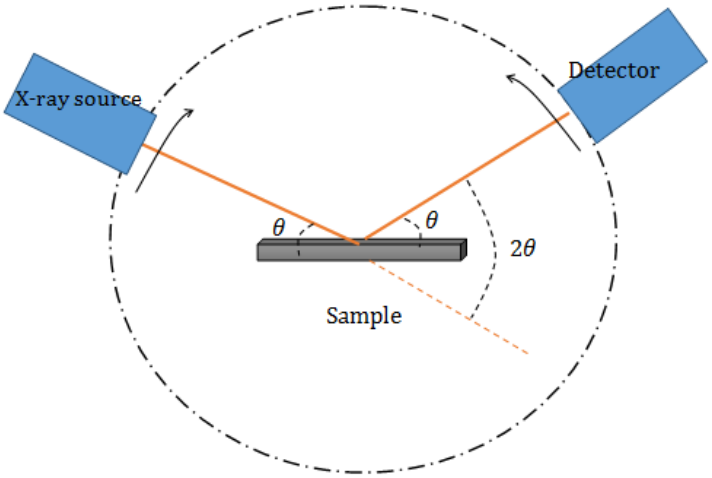

Fig. 2.15. Schematic Bragg-Brentano geometry.

In this geometry, well-focusing contemplation occurs when the angle between the incident ray and the sample surface is equal to the angle between the diffracted ray and sample surface (θ). The beam source and the detector move around the specimen in a circle to analyze the intensity of the dispersed beam and acquire the diffraction peaks [294]. The X-ray source is a vacuum tube (see figure 2.6) in which electrons flow from cathode to the anode (a Cu target in our case), due to a voltage difference. The interaction of electrons with the anode leads to fluorescence and emission of characteristic X-rays photons. The most commonly used metal targets are Cu with a wavelength of 1.52Å and Mo with 0.72Å.

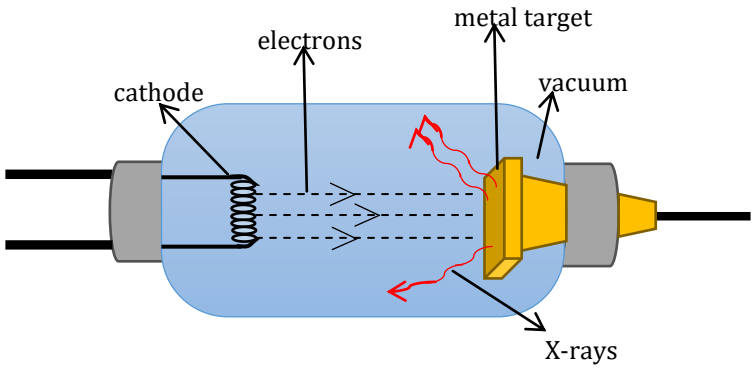

Fig. 2.16. Schematic representation of X-rays production in an X-ray tube.

High resolution PXRD experiments were performed at ALBA synchrotron, Barcelona, Spain, using a BL04-MPSD beamline. This instrument provides the high photon flux that allows a

quick data collection and also permits temperature during the experiments. The energies offered in this beamline range from 8 to 50keV. In order to avoid energy absorption by our samples, the energy of the beam was limited to 28keV. This beamline (figure 2.17) uses a double Si crystal in (111) direction orientation in a monochromator that selects the wavelength of a particular strong and highly focused X-ray beam. The sample holder uses a capillary tube (capillaries of 0.5m and 0.7mm were used) that is placed horizontally. The configuration of the equipment is set in Debye-Scherrer configuration, in transmission mode. In order to average out the potential textures of the sample, the capillaries spin around its longitudinal axis during the time of the measurements. A cryostream is attached to the equipment with nitrogen gas to vary the temperature during the measurements from 80K up to 500K. Measurements at higher temperatures (up to 900°C) are also possible by employing the FMB Oxford hot air blower. The two potential detectors can be used to carry out the diffraction experiments: a Mythen detector with six modules to acquire a rapid data or a MAD 26 detector with an array of analyzer crystals to acquire the data with high resolution. In our case, Mythen detector was used with the Oxford cryostream to vary the temperature of the sample.

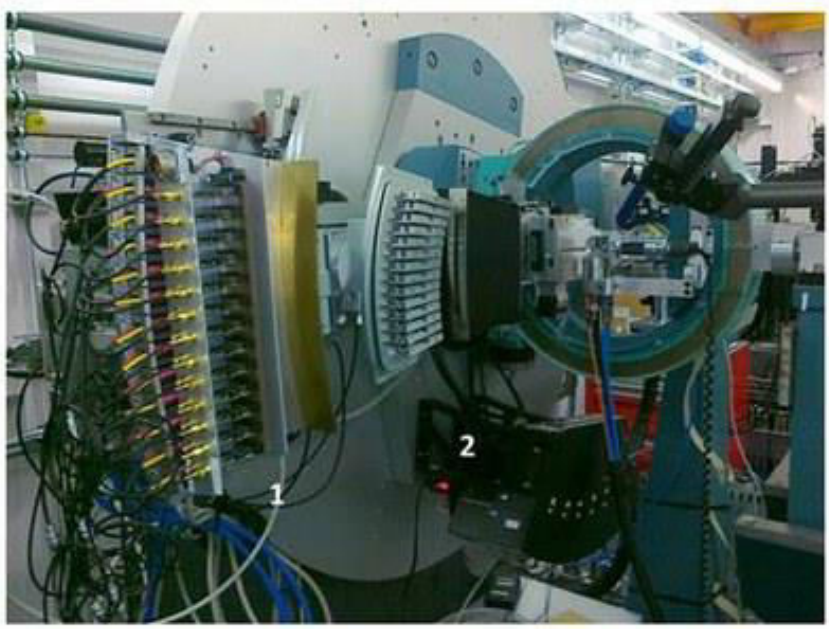

Fig. 2.17. Illustration of BL04-MPSD ALBA synchrotron.

2.4.2.3 Neutron diffraction

A neutron is a heavy particle with the mass closer to that of proton. The neutron does not normally exist in free form; instead, it decomposes into a proton, an electron and an anti-neutrino. A neutron uses the strong nuclear force to interact with the nuclei and electromagnetic

force to interact with the magnetic moments of the crystal atoms. Numerous characteristics of neutrons make them very beneficial for applications where X-rays are insufficient. Neutrons can replace or in fact compliment X-rays in the following situations:

- Neutrons can examine the structural and dynamical characteristics of the alloys. The energies of the neutrons (around 25meV) are on the same scale as the thermal excitations in solids and liquids. Moreover, the wavelength of the neutrons (around 1.8Å) is on the same scale as the inter-atomic distances in the alloys.
- Neutrons can penetrate the matter more deeply than the X-rays, since it has no charge and consequently shows a weak interaction with the matter. This facilitates the use of various environments, such as cryostats, furnaces, or pressure cells, as well as the study of large bulk materials. The disadvantage is that large samples are required.
- Neutrons scatter from magnetic structures or magnetic field gradients due to the neutron magnetic moment. While spin-polarized neutrons scattering can provide the information about the direction of the atomic magnetic moments, the periodicity and magnitude of the magnetic order are studied using unpolarized neutrons.
- The neutron scattering cross section varies in a random way even between different isotopes of the same element. Therefore, neutrons can be used to distinguish between elements with similar electronic density (undistinguishable by X-ray diffraction) or light isotopes. This is crucial for hydrogen in particular since it is nearly undetectable by X-rays.
- The nuclei of atoms where the scattering of neutrons mainly occurs, can be considered as a point diffraction center. As a result, the scattering length/fermi length, b, which is the scattering amplitude of neutrons, is constant in the reciprocal space and does not decay with Q. This makes neutrons especially suitable for precise structural analysis, since they can detect extremely small atomic displacements.

Neutron diffraction measurements have been performed using D1B powder diffractometer located at ILL, Grenoble, France. The ILL facility is based on a conventional fission reactor where a intense and continuous stream of neutrons is created (in opposition to a spallation reactor where a pulsed beam of neutrons is produced). The monochromator and the sample are the two sites in these instruments where the direction of the neutrons is deflected. So this instrument is also known as two-axes spectrometer. Neutrons arrive at monochromator after passing through the neutron guide. The monochromator determines which neutron wavelength will reach the sample. This instrument has a $^3He/CF_4$ position sensitive detector made up of a

system of 1280 wires and several electrodes that covers a 2θ range of 128°. Seven pyrolytic graphite monochromator crystals focusing onto the position of the sample produce a flux of 7.9106ncm^{-2}s^{-1}. Using a Ge monochromator, a second wavelength of 1.28Å is produced. Depending upon the goal of the analysis, different environment for the sample can be selected. In this thesis, all the experiments were carried out at λ = 1.28Å, since this wavelength enables recording a great number of diffraction peaks in the available detector angular range. A schematic representation of D1B diffractometer at ILL, Grenoble, France is shown in figure 2.18.

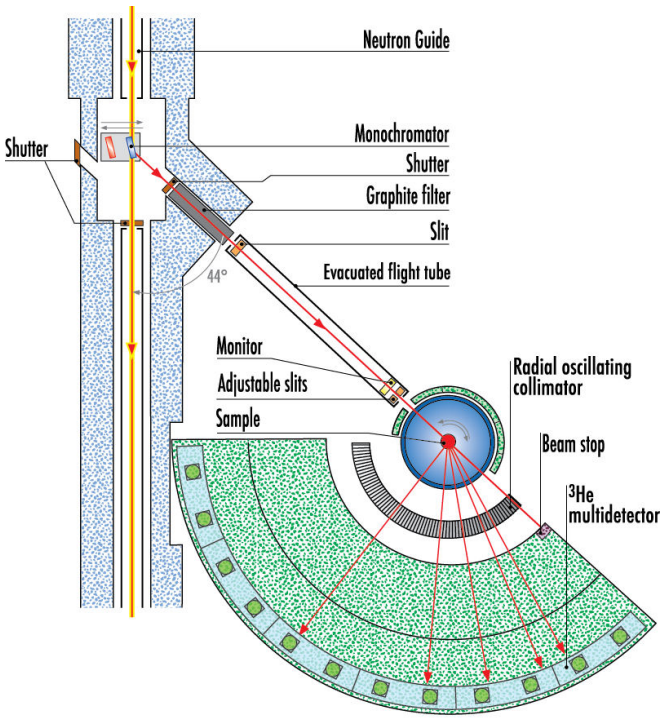

Fig. 2.18. Schematic representation of D1B powder neutron diffractometer at ILL, Grenoble, France.

Chapter 3

Mechanical milling and deformation induced martensite stabilization

3.1 Introduction

This chapter presents a study on the influence on mechanical milling on the magneto-structural properties of $Ni_{45}Co_5Mn_{36.7}In_{13.3}$ meta-magnetic shape memory alloy (MMSMA). The relative stability between the structural phases has been analyzed in samples deformed by hand crushing and ball milling, both in martensite and in austenite, from calorimetry, magnetometry and X-ray diffraction measurements. Apart from a significant decrease on the transforming fraction and the saturation magnetization in austenite, a huge stabilization of the martensite phase has been observed as a result of mechanically-induced plastic deformation, along with the formation of different martensite structures. The stabilization process and the magnetic features of the martensite phase have been fully characterized. A simple model based on the effect of magnetic entropy contribution to the driving force for the reverse martensitic transformation (RMT) has been proposed to explain the peculiar observed destabilization temperature.

3.1.1 Motivation and objectives

As mentioned in chapter 1, the embedding of small articles into a polymer appears as one of the most interesting alternatives to the use of bulk material. It could lead not only to an enhancement of the formability and the mechanical consistency of MMSMA but also to the obtaining of complex geometries through 3D printing if printable polymers are used. The production, characterization and optimization of the MMSMA particles are the necessary first step towards the development of any polymer/MMSMA composite. Mechanical grinding is a simple method to produce micro-particles from a bulk material. Nevertheless, the high energy involved in the milling process induces large plastic deformation and a high density of microstructural defects which may affect considerably the magneto-structural properties of the alloys [16, 79, 81, 82, 84, 91–93, 292, 295, 296]. The influence of mechanically-induced defects on the magneto-structural properties has been widely studies in Ni-Mn-Ga and Ni-Mn-Sn

systems [79–85, 297, 298]. Typically, the grain size reduction and the presence of defects and internal stresses induced by milling degrade the martensitic transformation (MT) and the magnetic properties, which can be then partially restored upon microstructural recovery processes brought by subsequent annealing treatments [84, 92, 292]. In ternary Ni-Mn-Sn alloys, it has been found that even though no atomic disorder is induced by milling, the anti-phase boundaries (APBs) linked to dislocations promote the anti-ferromagnetic coupling of Mn, thus resulting in a significant decrease in the saturation magnetization [84]. In Co-doped Ni-Mn-Sn alloys, in turn, the mechanically induced defects do not change the ferromagnetic coupling between Mn atoms and just cause a net reduction in the magnetic moments [85]. However, apart from some preliminary studies on the effect of hard deformation in ternary Ni-Mn-In alloys [16, 100] and a previous work on mechanical alloying [299], no similar systematic study has been performed up to now to analyze the effect of milling in Ni-Mn-In-Co alloys.

From both fundamental and applied points of view, the stabilization of the martensite is one of the most important effects taking place as a result of deformation. This effect, which is mainly manifested as an increase of the reverse MT temperature of the deformed martensite with respect to the thermal martensite, is typically attributed to changes in the stored internal elastic energy associated to reorientation deformation as well as to the pinning of the interfaces by defects created during deformation [300, 301]. Stabilization effects have been observed and widely studied in several non-magnetic shape memory alloy systems such as NiTi [300, 302–306], Cu-Al-Ni [307], Cu-Al-Zn [308, 309] and Cu-Al-Be [301], both in single-crystal and polycrystalline alloys subjected to cold deformation and pre-strains. On the contrary, this phenomenon has been scarcely reported in magnetic shape memory alloys. In fact, deformation-induced martensite stabilization has only been found after mechanical training of Co-Ni-Ga, Ni-Mn-Ga and Ni-Mn-Sn single crystals [310, 311] and in some Mn-rich alloys [83, 296]. Nevertheless, the occurrence of martensite stabilization as a result of milling-induced deformation has not been explored, or at least reported, up to now in Ni-Mn-In-Co alloys.

On the basis of the above, the main objective of this chapter is the study of the influence if mechanical milling on the structural and magnetic properties of a $Ni_{45}Co_5Mn_{36.7}In_{13.3}$ MMSMA. In order to do so, the MT characteristics, the appearing crystallographic structures and their saturation magnetization and magnetic susceptibility, and microstructural parameters such as the internal strains and crystallite sizes, have been determined and analyzed in samples milled in both austenite and in martensite and subjected to different milling times and several post-milling thermal treatments.

3.1.2 Chapter Organization

The experimental results shown in the following section are divided in three sections. First, the elaborated bulk alloy that will be subjected to milling is fully characterized. Then, in order to analyze the possible influence of the initial state of the bulk alloy, the results on the milled powders are shown separately depending on whether the bulk was milled in martensite or in austenite. In the former case, an initial exhaustive characterization of samples subjected to soft hand-crushing is carried out, followed by the comparative analysis of the powders obtained after sever ball-milling (15 and 45 minutes milling time). In the case of the samples milled in austenite, furthermore, a complete study of the magnetic properties of the structural phases appearing after milling is also shown. Finally, a brief summary of the obtained results and the main conclusions coming of it are presented at the end of chapter.

3.2 Experimental Results

3.2.1 Bulk alloy

A bulk $Ni_{45}Mn_{36.7}In_{13.3}Co_5$ alloy was elaborated from high purity elements by arc melting under protective Ar atmosphere. The as-cast ingot was homogenized at 1073K during 15h and then quenched into iced water. The composition was analyzed by EDS. Figure 3.1 shows the DSC thermograms obtained on a heating-cooling thermal cycle at a rate of 10K/minute for the temperature range 200K to 473K. In the region between 272K and 345K, an exothermic peak and an endothermic peak can be observed during cooling and heating, respectively, linked to the respective occurrence of the forward martensitic transformation (FMT) and reverse martensitic transformation (RMT). The temperature of the peak maxima linked to the FMT and RMT lie around T_m^{for}= 296K (neat RT) and T_m^{rev} = 327K, respectively, showing the expected thermal hysteresis$\left(\Delta T = T_m^{rev} - T_m^{for}\right)$ inherent to the first order character of the MT.

It is worth noting that the RMT is just below RT, what favors the magnetic-filed induction of MT (MFIMT) at RT under low magnetic fields, being this the optimal situation for most practical applications [6, 43, 68, 312, 313]. The enthalpy changes (ΔH) at the MT are ΔH_{for} = 8.1J/g and ΔH_{rev} = 8.7J/g for the FMT and RMT, respectively, with the associated entropy changes (estimated as $\Delta S = \Delta H/T_m$) ΔS_{for} = 20.5J/kgK and ΔS_{rev} = 20.1J/kgK. The slightly higher value of ΔS at RMT can be attributed to the higher value of the magnetic contribution (ΔS_{mag}) counterbalancing the vibrational one, just as explained in chapter 1. The λ-jump in the baseline that appears above the MT temperature, showing no thermal hysteresis, can be ascribed to the

ferromagnetic to paramagnetic transition taking place in austenite at the Curie temperature (T_c= 367K).

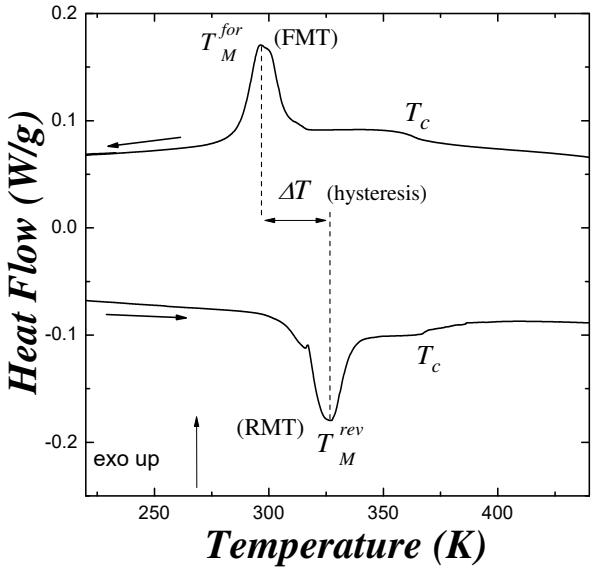

Fig. 3.1. DSC thermogram performed on the as-quenched bulk alloy.

Magnetic measurements have also been performed to confirm this point using SQUID magnetometry. Figure 3.2 shows the measurement obtained for the as-quenched alloy under an applied field of 100Oe. The magnetization at high temperatures is almost null, as corresponds to the paramagnetic state of the austenite and then a sharp increase is observed on cooling below the Curie temperature T_c = 367K. The subsequent huge drop in the magnetization on further cooling indicates the MT from austenite (ferromagnetic) to martensite (weakly magnetic), thus confirming the meta-magnetic character of the alloy. The first order nature of the martensitic transition is indeed confirmed by the thermal hysteresis between cooling and heating curves. The jump in magnetization above the MT around T_c, in turn, lies at the same temperature on heating and on cooling.

As explained in Chapter 1, the long-range atomic order in Ni-Mn-In-Co can be easily modified by means of various thermal treatments [17, 78, 119]. In particular, the quenching from high temperatures (above the B2-$L2_1$ ordering temperature) leads to a disordered state with lower atomic order degree than the maximum equilibrium value allowed by stoichiometry, which, in turn, can be obtained upon a slow enough cooling from high temperatures (ordered state). Bearing this in mind, and with the aim of shifting MT down below the MT (so that the alloy is in austenite state at RT), a part of the elaborated bulk was annealed for one hour at 1073K and then slowly cooled to RT. Figure 3.3 shows the DSC thermogram obtained in heating-cooling

the slowly cooled ordered bulk sample between 200K and 450K. It can be seen that, in effect, the MT lies below RT, with T_m^{rev} = 275K.

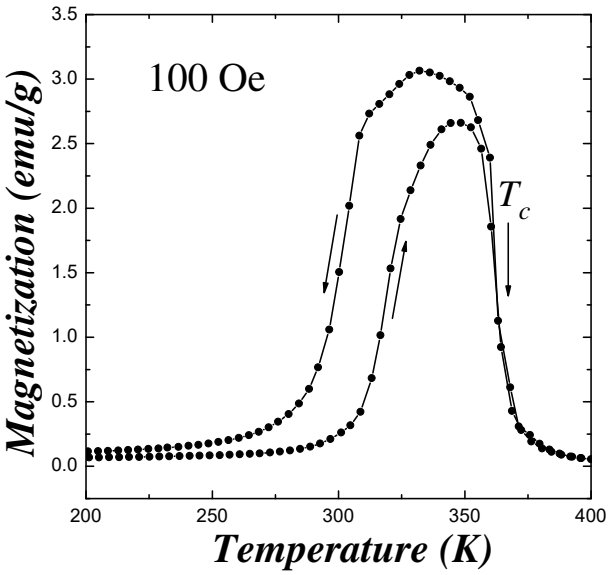

Fig. 3.2. Temperature dependence of magnetization under 100Oe applied field for the AQ bulk sample.

The shift of the martensitic transformation to lower temperatures in the ordered alloy can be attributed to the stabilization of the structural phase with higher magnetic moment as a consequence of the enhancement of the ferromagnetic coupling between the Mn atoms in the L21 structure, as proposed in previous works on Ni-Mn-Ga and Ni-Mn-In alloys [32]. The shift of the MT to lower temperatures also makes the area below the peaks be significantly smaller in the ordered sample, as long as it leads to an increase in the magnetic contribution to entropy, ΔS_{mag}, opposing the vibrational one, ΔS_{vib}, and thus resulting in a lower total entropy change ΔS_{tot} [314]. Moreover, a slight increase in T_c with respect to the as-quenched alloy is also observed for the slow-cooled sample, due to increase of the net magnetic moment of the alloy because of the ordering process.

The as-quenched disordered sample shows the RMT above RT while RMT is below RT in the slow-cooled ordered sample, in such a way that the elaborated alloy could be in martensite or in austenite at RT depending on the thermal treatment. This made it possible to carry out the milling process, which is performed at RT, both in austenite and in martensite phases. Let us start with the study when deformation is performed in martensite.

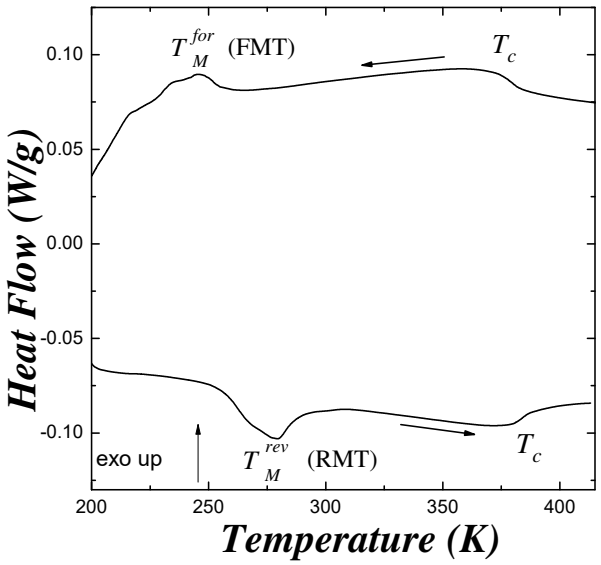

Fig.3.3. DSC thermogram for slowly cooled bulk alloy.

3.2.2 Milling in martensite

Ball-milling is a vigorous technique and may produce microstructural defects and severe plastic deformation that can even lead to the amorphization of the alloy [85]. The control of the particle deformation is of crucial importance since it determines the functional properties for subsequent applications. In previous works in similar Ni-Mn-Sn-Co alloys, reduction in the particle size is achieved after milling times up to 45 minutes, whereas higher milling times leads to the agglomeration of particles [85]. Thus, no longer milling times than 45 minutes has been applied in the present study. In fact, in order to avoid undesirable effects such as amorphization and particles agglomeration, the micro-particles obtained from a soft hand-crushing (HC, Hand Crushing) of the bulk alloy on an agate mortar have been first studied as a preliminary stage. Then, the particles will be milled for 15 and 45 minutes in order to analyze and compare the effect of a more severe deformation.

3.2.2.1. Hand-crushing

Figure 3.4a shows the DSC thermograms for Milled-in-Martensite Hand-Crushed powders (MM^{HC}). The first heating ramp up to 473K from the RT (shown by the red line), is followed by a cooling-heating cycle between 473 K and 200 K (black lines). It is worth noting, that during the first RMT, a jerky peak with burst-like behavior can be seen 60K above than in the first RMT in bulk (shown in figure 3.1). However, in the second heating ramp, the T_M^{rev}coincides

with that of bulk alloy (shown in figure 3.4b) and the serrated shape is no longer observed in the transformation peak, which recovers the smooth shape.

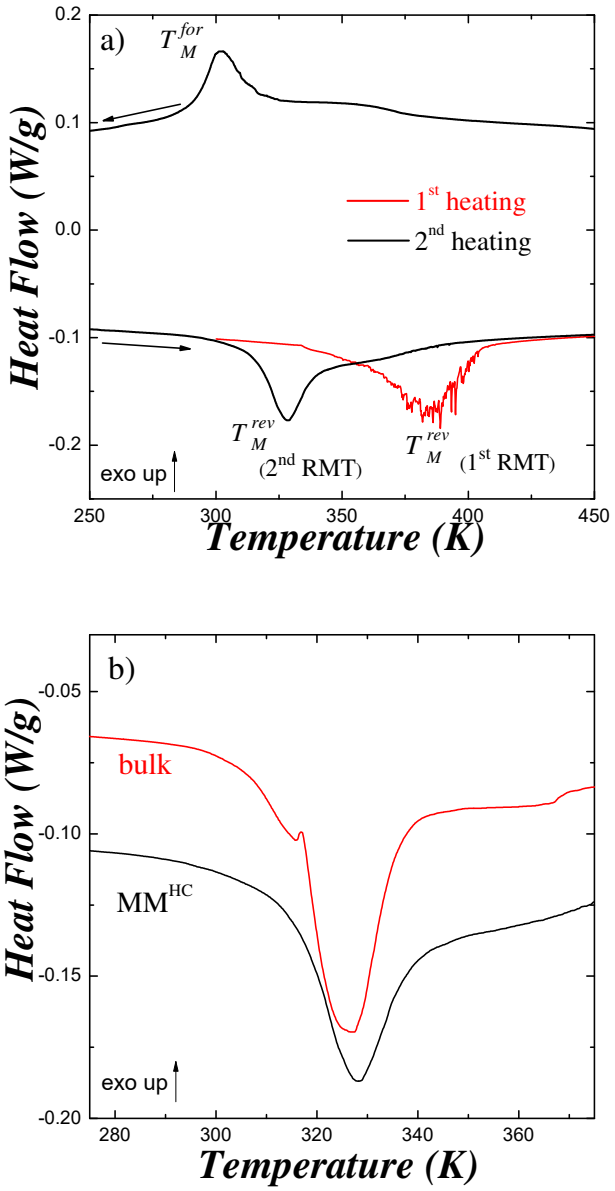

Fig. 3.4. a) DSC thermogram on the first heating (red line) and subsequent cooling-heating cycle (black line) for the MM^{HC} sample, b) Detail of the peaks linked to the second RMT in both MM^{HC} and the bulk sample.

Apart from its jerky behavior, the first RMT spreads over a much wider temperature range than the second RMT, with the corresponding enthalpy change also being significantly greater in the

former (see Table 3.1). The shift in the transition temperature, burst-like behavior and the broadening of the transformation peak point to a martensite stabilization [308].

Sample	1st heating (Stabilized)				2nd cycle				
	As (*K*)	T_M^{rev} (*K*)	*ΔH* (*J/g*)	*ΔS* (*J/kgK*)	*As* (*K*)	T_M^{rev} (*K*)	T_M^{for} (*K*)	*ΔH* (*J/g*)	*ΔS* (*J/kgK*)
MM^{HC}	333	383	13.0	33.9	300	328	300	8.0	24.3

Table 3.1. Austenite start temperature (A_S), peak maximum temperature (T_M^{rev}), enthalpy change (ΔH) and entropy change (ΔS) at the first and second RMT of the studied samples.

Martensite stabilization is a widely reported phenomenon. Similar behaviors have been indeed observed on different shape memory alloys subjected to quenching or pre-straining treatments [300–307, 309–311]. On one hand, numerous studies in shape memory alloys subjected to martensite aging show a martensite stabilization phenomenon evidenced by a shift of the A_s temperature [311, 315–317]. In this aspect, Otsuka et al. proposed that the martensite stabilization after martensite aging was a consequence of the effect of the short-range atomic reconfiguration of defects on the austenite Gibbs free energy [315]. Alternatively, martensite stabilization has also been found to appear as a consequence of pre-deformation in shape memory alloys [300, 304]. The strain-induced martensite stabilization has been associated with the relaxation of elastic strain energy upon deformation. Likewise, the pinning of the interfaces by mechanically induced defects [309], or the deletion of nucleation spots [318] have also been postulated to explain the shift in the transformation temperatures during the first RMT in pre-strained alloys. Similarly, the broadening of the transformation peaks over a temperature range with the increase of the enthalpy change has been related to the non-chemical irreversible energy contributions coming from frictional forces related to the presence of defects [303]. Thus, as reported in NiTi and Cu-based alloys [300, 303, 307], the higher is the plastic deformation (and consequently the amount of associated microstructural defects), the larger the expected stabilization. Similar behaviors have been observed on different shape memory alloys subjected to quenching or prestraining treatments[300–307, 309–311]. This stabilization effect has been attributed to the pinning of the interfaces through irreversible dissipative process [308, 309]. However, the stabilization effect disappears in further thermal cycles due to the

elimination of those defects by sufficient heating and/or by the development of a distinct, defect free martensitic structure [302]. This explains the behavior in the figure 3.4a during second RMT. In any case, it is worth mentioning that in spite of the large number of investigations on the mechanical properties, and in particular on the mechanical milling, of Ni-Mn based [17, 85, 93, 203, 319, 320], this is the first observation of a mechanically-induced martensite stabilization phenomenon in these alloys.

The crystallographic structure has been analyzed by high-resolution X-ray powder diffraction measurements carried out at Alba Synchrotron, using BL04-MPSD beamline with a wavelength of 0.4508Å. The diffractograms performed in martensite at 150K are shown in figure 3.5a. The measurements have been performed in two following states: i) before first RMT (stabilized martensite), ii) after first RMT (retransformed/destabilized martensite). The clear difference in the reflection peaks appearing in the respective diffractograms evidences different crystallographic structures. Such difference becomes more evident in the low-angle region shown in figure 3.5b. In effect, the structural refinement confirm that the stabilized martensite displays a tetragonal structure with I4/mmm space group, whereas the destabilized martensite shows a monoclinic structure with P2/m space group, typically observed in Ni-Mn-In-Co alloys [69, 125, 203]. The crystallographic parameters for both martensites at 150K (cell parameters, fractions, strains etc…) determined by Rietveld refinement for both martensites are shown in Table 3.2.

On the other hand, no other structure is visible in the diffractograms, demonstrating the absence of any relevant precipitated phase after grinding. The presence of non-modulated tetragonal structures has been previously reported in ternary Ni-Mn-In alloys subjected to severe deformation by high-pressure torsion of 8GPa [321], in grinded $Mn_2Ni_{1.34}Sn_{0.32}Co_{0.34}$ and in Ni-Mn-In-Co ribbons obtained from melt-spinning technique [296]. This, and the present observation, seems to indicate that the non-modulated tetragonal structure would accommodate better the mechanically-induced stresses than the thermally-induced modulated structures. The cell dimensions of the tetragonal structure may help to accommodate the internal stresses induced by plastic deformation (large misfit with austenite), whereas the cell parameters of monoclinic structure would result in a lower misfit of the austenite cell, encouraging self-accommodation during thermoelastic MT [322]. In any case, there is a significant difference in comparison with NiTi, Cu-based alloys or even grinded $Mn_2Ni_{1.34}Sn_{0.32}Co_{0.34}$ powders, since in all these cases the crystal structure of the martensite remained the same and did not vary after subsequent heating above the RMT.

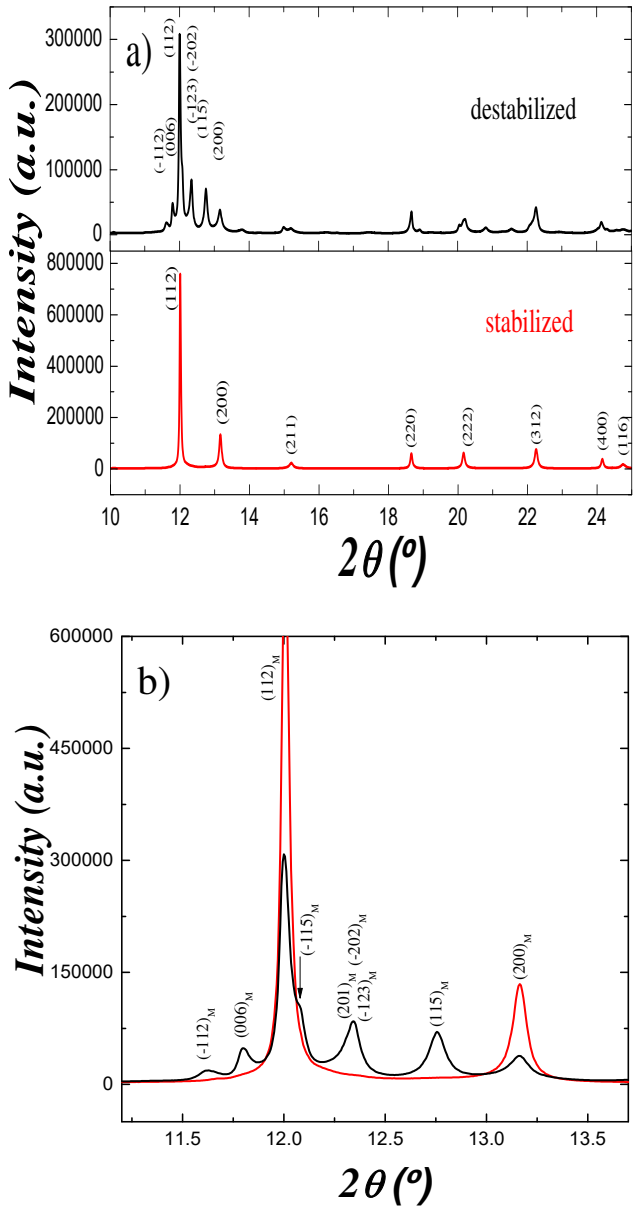

Fig. 3.5. (a) X-rays diffractograms at 150 K in the stabilized and destabilized martensite of the MM^{HC} sample. (b) Detail of the diffractograms on the 11º - 14º region.

Sample	430 K				150 K (stabilized)		150 K (destabilized)			
	a (Å)	F_{Mart} (%)	*Strain* (‰)	*Size* (Å)	*a* (Å)	*c* (Å)	*a* (Å)	*b* (Å)	*c* (Å)	*β* (º)
MM^{HC}	5.984	8.8	2.9	170	3.932	6.815	4.326	5.562	13.174	94.0

Table 3.2. Lattice parameters of the austenite (430 K), stabilized and destabilized martensites (150 K), volume fraction of deformed non-transforming martensite and microstructural parameters (internal strains and crystallite size) of the austenite obtained from Rietveld refinement.

- Magnetic properties

Magnetic measurements have also been performed on the MM^{HC} samples to determine the sequence of magneto-structural transformations and to analyze influence of milling on the magnetic properties. The temperature dependence of magnetization on heating from RT up to 400K and on subsequent cooling-heating between 400K and 150K under a low applied magnetic field of 100Oe is shown in figure 3.6a. During the first heating ramp, the magnetization values are almost negligible at RT, which is in agreement with the presence of weakly magnetic martensite. During heating, the reverse transition from martensite to ferromagnetic austenite around 330K causes the magnetization to grow. However, as a consequence of the occurrence of ferro-to-para transition at the Curie temperature of austenite (T_c^a), indeed overlapped to the first RMT, the magnetization quickly diminishes thus cancelling the magnetization rise. After heating upto 400K, the huge increase in the magnetization corresponding to T_c^a be clearly observed on cooling, followed on further cooling by the magnetization jump linked to the first FMT. This behavior is in agreement with the results shown by DSC measurements. So, right after the milling, the presence of stabilized martensite at RT is evidenced by low M values, and upon subsequent heating and cooling from 400K, the higher M values confirm the appearance of austenite and the corresponding disappearance of the stabilized martensite, just as observed by DSC. After the first heating up to 400K, the magnetization behavior resembles that of the bulk alloy (see figure 3.2), with jumps in the magnetization associated with the both magnetic ferro-to-para transition at T_c^a and the reversible MT.

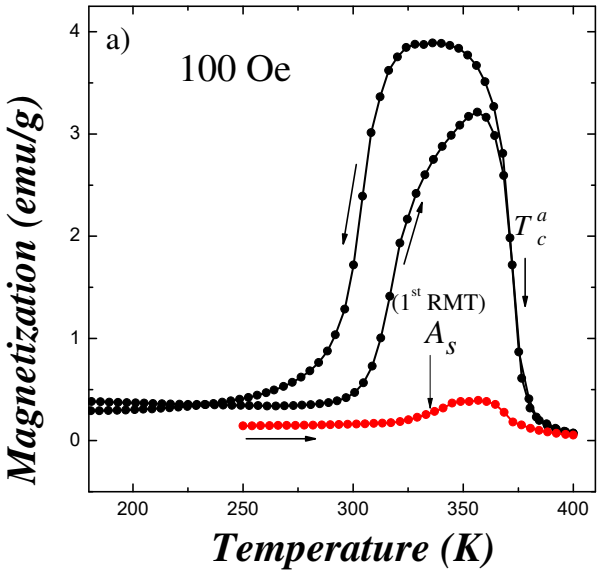

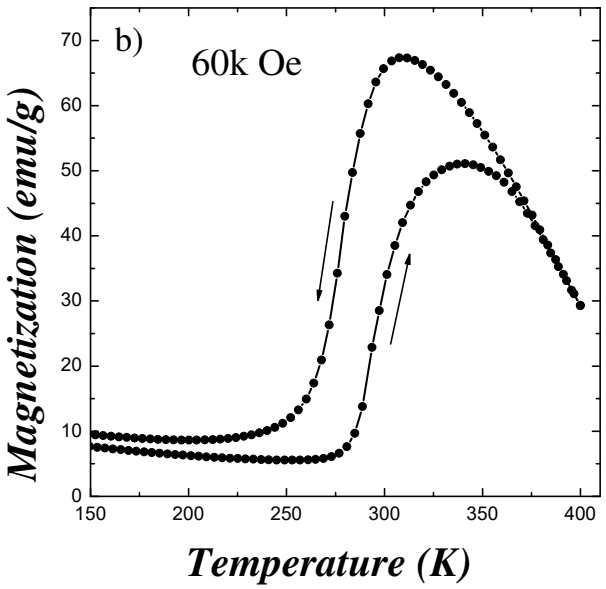

Fig. 3.6. (a) Temperature dependence of magnetization of the MM^{HC} sample under 100 Oe applied magnetic field, on heating from RT up to 400 K and on subsequent cooling-heating between 400 K and 150 K, b) M(T) under 60 kOe.

As shown in figure 3.6b, the application of a 60kOe magnetic field shifts the MT to lower temperatures (around 25K), in such a way that an almost complete RMT may be magnetically-induced at RT (compare figures 3.6a and 3.6b). This demonstrates the potential applicability of the produced micro-particles for room-temperature applications based on MFIMT effect.

On the other hand, the magnetic properties of the tetragonal (stabilized) and the monoclinic (destabilized) martensites under high magnetic field were also studied. The field dependence of magnetization at 10K for stabilized and destabilized martensites are shown in figure 3.7. The magnetization values at 60kOe for the both samples are similar, but the approach to the saturation of the stabilized phase is slower (harder) than the destabilized one. This could be due to either or both the intrinsic different magnetic anisotropy of the different crystallographic structures or the high local stresses caused but a higher concentration of crystalline defects in the stabilized martensite. In this latter case, the partially elimination of defects after heating above the first RMT could lead to a slightly smaller density of defects in the destabilized martensite and consequently, to a reduction on the magnetic anisotropy of the monoclinic martensite.

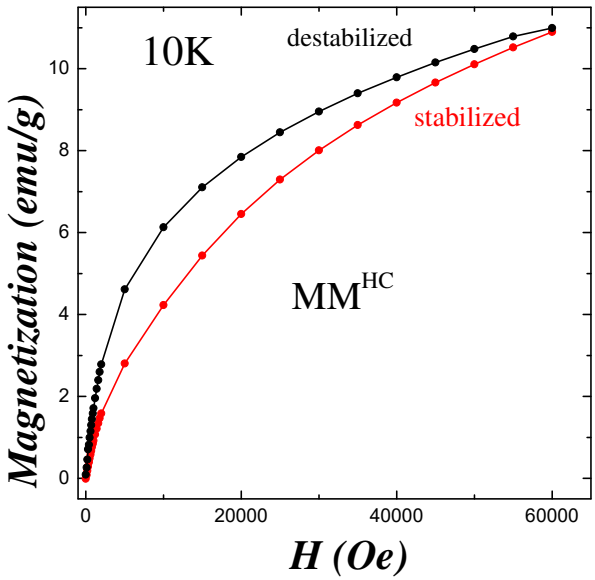

Fig. 3.7. Magnetization at 10 K as a function of the applied field, in the as-milled state (stabilized martensite) and after heating above the first RMT (destabilized martensite).

3.2.2.2 Ball-milling

After the analysis for MM^{HC} powders, two samples extracted from the initial as-quenched bulk alloy were subjected to a 15 minutes and 45 minutes ball milling at RT (hereafter called as MM^{15} and MM^{45} samples, respectively) and characterized to investigate the influence of a higher degree of deformation on the martensite stabilization process and on the magnetic properties. DSC measurements were firstly performed to detect the corresponding MT. For the sake of clarity, the DSC thermograms obtain upon first heating the three as-milled samples up to 473K are shown in figure 3.8a and the subsequent cooling-heating curve are shown separately in figure 3.8b. By comparing both figures, it can be seen that the first RMT occurs at substantially greater temperatures than the second RMT, pointing again to significant martensite stabilization, as observed in the MM^{HC} powders. For the first time, the austenite start temperature A_s highly increases with the increase of the milling time (figure 3.8a). Similar behaviors have been reported in Cu-Al-Ni alloys, where the increase in the A_s with the increasing plastic deformation has been attribute to the stored elastic strain energy [300, 305]. Despite the fact that A_s highly evolves with the milling time, there is almost no evolution neither in the peak maximum temperature (shown as T_M^{1RMT} in figure 3.4a) nor in the austenite finish temperature A_f, irrespective of the milling time. This remarkable matter will be discussed in more detail in the next section.

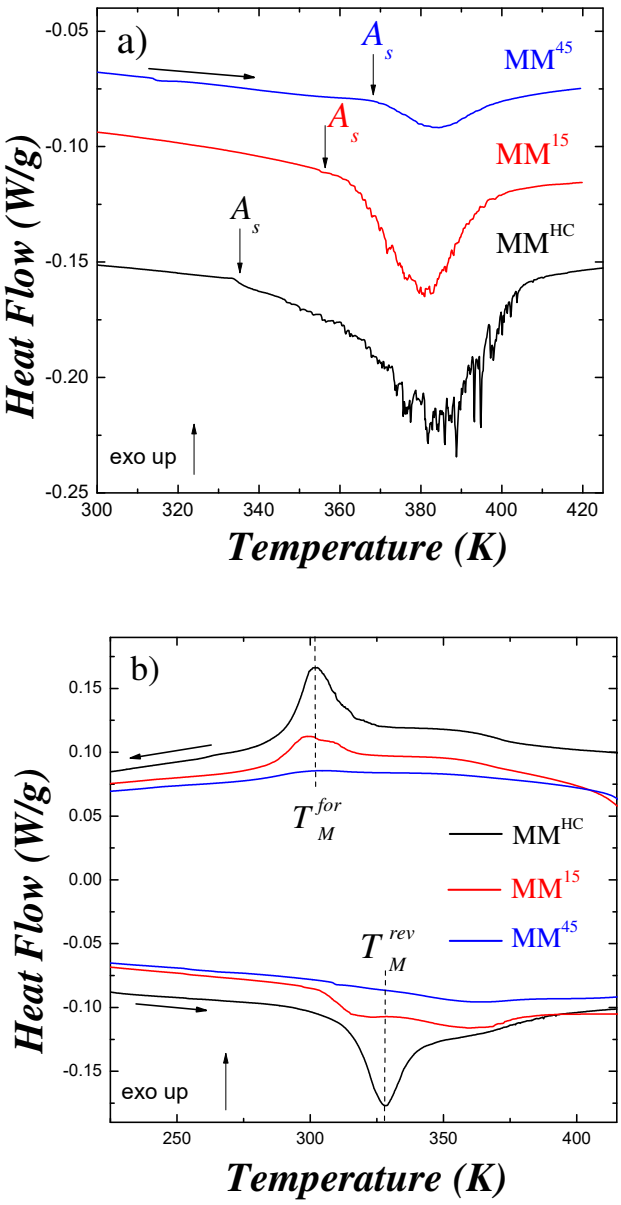

Fig.3.8. DSC thermograms on the MM^{HC}, MM^{15} and MM^{45} samples. (a) First heating ramp and (b) cooling-heating cycle after destabilization.

It is striking that the width and height of the transformation peaks linked to the initial RMT drop dramatically as the milling time increases, while the burst-like jerky behavior gradually diminishes (smoother peaks). Such disappearance of the jerky behavior can be ascribed to the decrease of the size of the martensite variants as a consequence of the particle size reduction, as previously reported in Cu-based alloys [309]. On the other hand, the decrease in the peaks area (and hence in the associated ΔH- see table 3.3), which is even more pronounced in the second RMT, points an increasing presence of highly deformed non-transforming regions. In this

respect, the volume fraction of transforming austenite has been estimated by comparing the enthalpy change at the second RMT of the milled samples with that of bulk alloy, assuming a complete MT in the latter. The calculated transforming fraction are 90%, 38% and 12% for the MM^{HC}, MM^{15} and MM^{45} samples, respectively, confirming a high degradation of the MT as a result of milling. A similar degradation of the transformation has been recently reported in Ni-Mn-Sn-Co alloys (though not related to stabilized maretnsite, but to 'standard' MT) subjected to similar milling treatments [85], such degradation being related to an increasing amount of amorphous-like non-transforming regions.

Sample	**1st heating (Stabilized)**				**2nd cycle**				
	As (K)	***T_M^{rev} (K)***	***ΔH (J/g)***	***ΔS (J/kgK)***	***As (K)***	***T_M^{rev} (K)***	***T_M^{for} (K)***	***ΔH (J/g)***	***ΔS (J/kgK)***
MM^{HC}	333	383	13.0	33.9	300	328	300	8.0	24.3
MM^{15}	355	383	7.4	19.3	297	323	299	3.0	9.3
MM^{45}	367	385	1.5	3.9	298	325	300	1.1	3.4

Table 3.3. Austenite start temperature (A_S), peak maximum temperature (T_M^{rev}), enthalpy change (ΔH) and entropy change (ΔS) at the first and second RMT of the MM^{HC}, MM^{15} and MM^{45} samples.

Once the as-milled samples are heated above the first RMT, destabilization occurs and the self-accommodating thermally-induced martensite regains its characteristics. Thus, during the second RMT, the A_s is restored for all milling times [300]. In this regard, it is worth noting that the entropy change linked to the second RMT is abnormally lower than that of the first FMT. This is in agreement with a larger influence of the irreversible positive frictional contribution to the ΔS_{tot} at the MT due to the defects induced by the milling process [5]. The enthalpy and entropy change during the transformation, and the transformation temperatures during the second RMT are given in Table 3.3. The heat flow and ΔS during the first RMT and second RMT are observed to be diminishing drastically, as seen in figure 3.8b and table 3.3, respectively. The transformation temperature of the second MT, in turn, remains constant, which implies that the long-range atomic order and the alloy composition are not altered as a result of the ball-milling [17, 32].

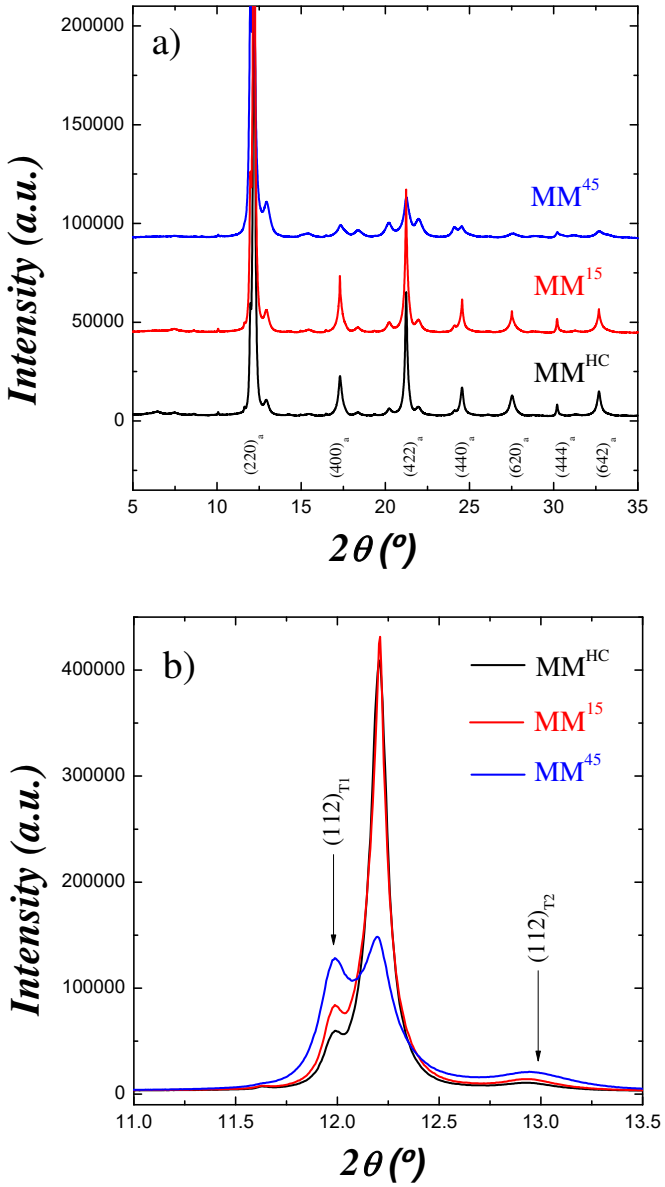

Fig. 3.9. a) X-rays diffractogram at 430 K (above first RMT) for the MM^{HC}, MM^{15} and MM^{45} samples (main reflections of the cubic $L2_1$ austenitic structure are indicated). (b) Detail of the low angle region.

X-ray diffraction measurements were performed to analyze the appearing crystal structures, the long-range atomic order variation and the microstructural evolution taking place as a consequence of the milling treatments. The X-ray diffraction patterns for MM^{HC}, MM^{15} and MM^{45} samples at 430K (in austenite) just above the first RMT are shown in figure 3.9a. The Rietveld refinement of the three diffractograms confirms the predominant presence of austenitic cubic $L2_1$ structure with almost the same lattice parameters. However, the presence of some

diffraction peaks corresponding to the tetragonal martensite at 430K have also been detected, as may be clearly seen in the low-angle region shown in figure 3.9b, where the intensity of the martensitic (112) and (121) reflections increase with milling time.

Sample	430 K				150 K (stabilized)		150 K (destabilized)			
	a (Å)	F_{Mart} (%)	*Strain* (‰)	*Size* (Å)	*a* (Å)	*c* (Å)	*a* (Å)	*b* (Å)	*c* (Å)	*β* (º)
MM^{HC}	5.984	8.8	2.9	170	3.932	6.815	4.326	5.562	13.174	94.0
MM^{15}	5.985	14.4	3.1	132	3.931	6.812	4.320	5.557	13.183	94.1
MM^{45}	5.985	34.6	8.6	73	3.932	6.812	4.318	5.554	13.194	94.0

Table 3.4. Lattice parameters of the austenite (430 K) and the stabilized and destabilized martensites (150 K), volume fraction of deformed non-transforming martensite and microstructural parameters (internal strains and crystallite size) obtained from Rietveld refinement.

The volume fractions of cubic austenite at 430K, estimated after Rietveld refinement, are 90%, 85.6% and 65.4% for MM^{HC}, MM^{15} and MM^{45}, respectively. The obtained fraction agrees perfectly with the value estimated from DSC in the case of the MM^{HC} sample, what means that the non-transforming regions in this sample must consist of deformed tetragonal martensite. Nevertheless, considerably higher transforming fractions are obtained for the MM^{15} and MM^{45} samples with respect to the corresponding DSC values, so the degradation of the MT cannot be entirely ascribed to the presence of retained martensite in these cases but to other contributions. In this sense, it is worth noting that the substantial decrease in the intensity and the broadening of the reflection peaks of the milled samples, pointing out a very high increase of internal stresses and reduction in particle size, as indeed confirmed from the Reitveld fit of the diffractograms (see table 3.4). In fact, the almost complete disappearance of the diffraction peaks in the MM^{45} case suggest a partial amorphization of the alloy, in agreement with the results in Ni-Mn-Sn-Co alloy [85].

The X-ray diffraction pattern of MM^{HC}, MM^{15} and MM^{45} samples at 150K in the stabilized and destabilized states are shown in figure 3.10. Again, the diffractograms are very similar for all three samples, both in the stabilized and destabilized states. In particular, the stabilized state displays in all cases a non-modulated tetragonal I4/mmm martensite with almost identical lattice parameters, although a minor fraction of modulated martensite is detected in MM^{15} sample

particles. Likewise, the destabilized martensite (figure 3.10b) also displays the same modulated monoclinic P2/m structure. Therefore, it seems that, irrespectively of the milling time and the deformation degree, the as-milled deformed martensites always show a tetragonal structure deformation degree, whereas the usual "thermally-induced" monoclinic structure appears after the first reverse MT.

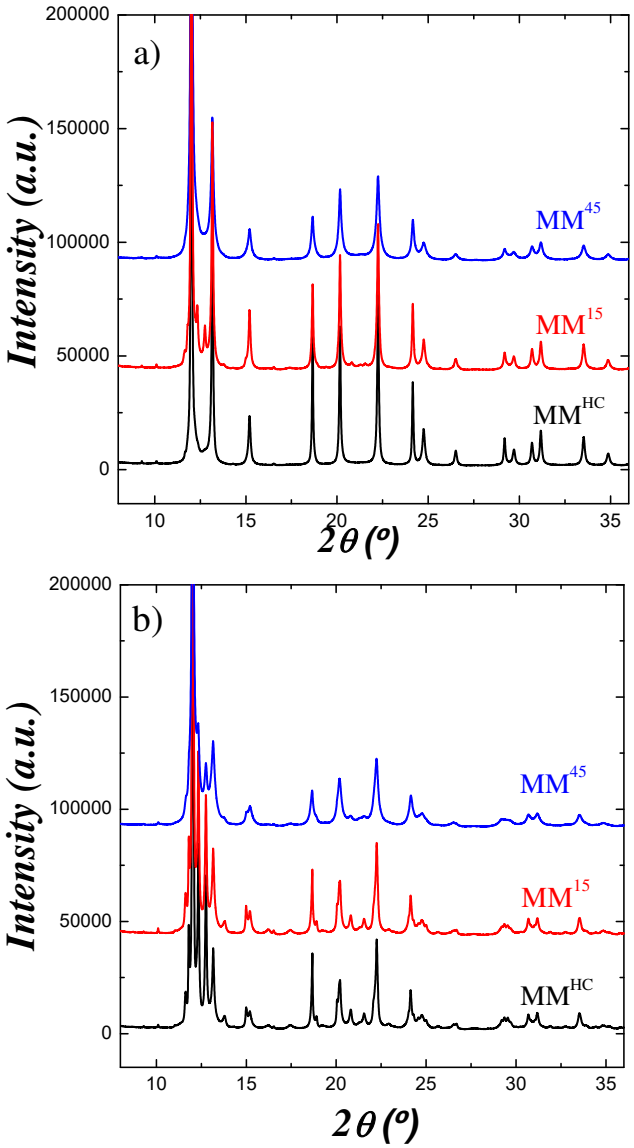

Fig. 3.10. X-rays diffractogram at 150 K for the MM^{HC}, MM^{15} and MM^{45} samples, a) in the stabilized state b) and after destabilization.

- **Magnetic properties**

The temperature dependences of magnetization of the MM^{HC}, MM^{15} and MM^{45} samples (after destabilization) under 100Oe and 60kOe magnetic fields are shown in figure 3.11. The low-field measurements confirm that the MT temperatures do not evolve with milling time. However, a

slight decrease in the Curie temperature can be indeed observed. A similar trend in T_c has been recently observed in $Ni_{1.8}Mn_{1.8}In_{0.4}$ grinded powders, the shift in T_c being associated to the diminished ferromagnetic exchange interaction in cubic austenite regions that did not transform due to the deformation [83]. Figure 3.11b shows the temperature dependence of the high-field magnetization (60kOe). As it occurred in the MM^{HC} sample, the MT shifts to lower temperatures in MM^{15} and MM^{45}, being the shift almost the same in the three samples. It is especially worth noting the high decrease of magnetization that takes place above the MT with the increasing milling time, while no significant variation is observed below the MT. To better illustrate this, the magnetization value at 350K under 60kOe magnetic field is shown in figure 3.11c. The magnetization hugely decreases with increase of milling time, showing an almost linear dependence. The degradation of high-field magnetization (similar to the saturation magnetization) as a result of milling can be quantified just by taking again the value in the bulk as a reference. It is obtained the magnetization values in the MM^{HC}, MM^{15} and MM^{45} samples correspond to the 90%, 60% and 22%, respectively, of the bulk magnetization. In the case of MM^{HC} sample, the value is in perfect agreement with the transforming fraction obtained from both DSC and X-ray measurements, so the magnetization value can be ascribed to the presence of weak magnetic martensite above RT. On the other hand, the discrepancy between the percentages obtained from magnetization, DSC and X-ray measurements in both MM^{15} and MM^{45} samples suggests that the highly deformed non-transforming regions must be weakly magnetic in nature.

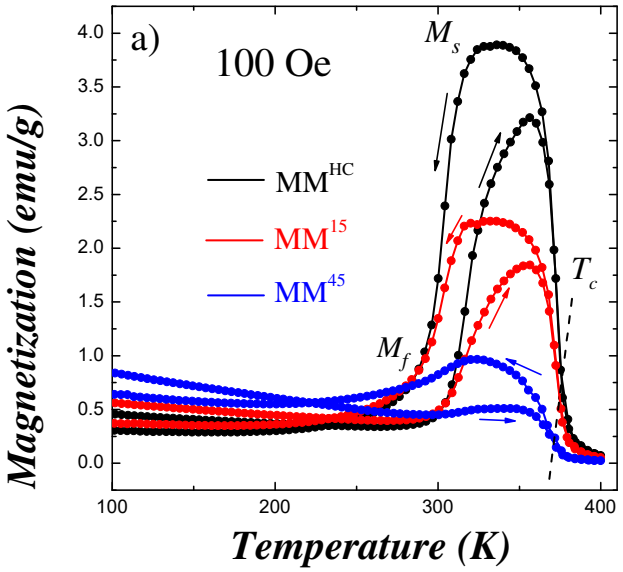

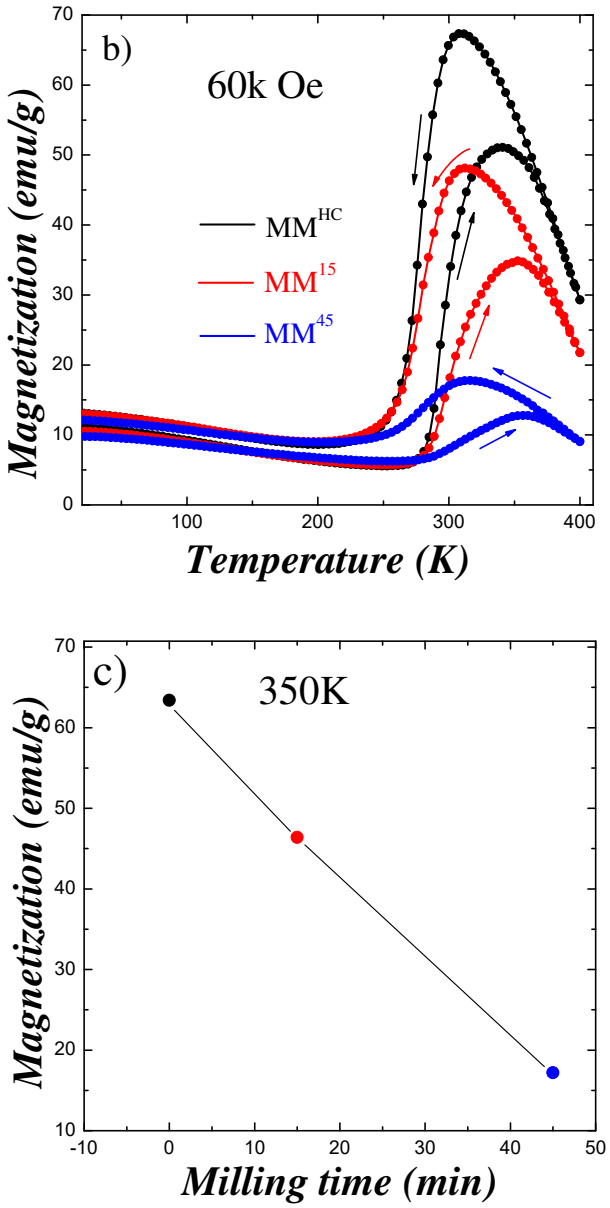

Fig. 3.11. Temperature dependence of magnetization, after destabilization, for the samples milled in martensite, under (a) 100Oe and (b) 60kOe applied magnetic fields (c) magnetization under 60kOe at 350K, as a function of the milling time

The field dependence of the magnetization in martensite at 10K for stabilized and destabilized MM^{15} and MM^{45} powders, are presented in the figure 3.12. The maximum magnetization at 60kOe in stabilized and destabilized states are similar but not the same, unlike it occurred in the MM^{HC} samples (figure 3.6c). The trend in the *M(H)* curves seem to indicate that as soon as the deformation increases, higher fields are required in the stabilized state to achieve similar

magnetization than in the destabilized one. The stabilized phase is clearly more difficult to be magnetized. Again, the different crystallographic structures in both states and the high local stress caused by crystalline defects in the stabilized phase should be at the origin of this phenomenon. Nevertheless, longer milling times (figure 3.12b) lead to a reduction of the magnetization values in the stabilized MM^{45} powders. This fact could be due to the presence of small fractions of amorphous-like regions with a little bit lower magnetization. Assuming this, the quantity of amorphous regions (which are out of equilibrium) and the internal stresses would be reduced (and the defect configuration changed) after the first RMT, thus leading to a consequent recovery of the magnetization value.

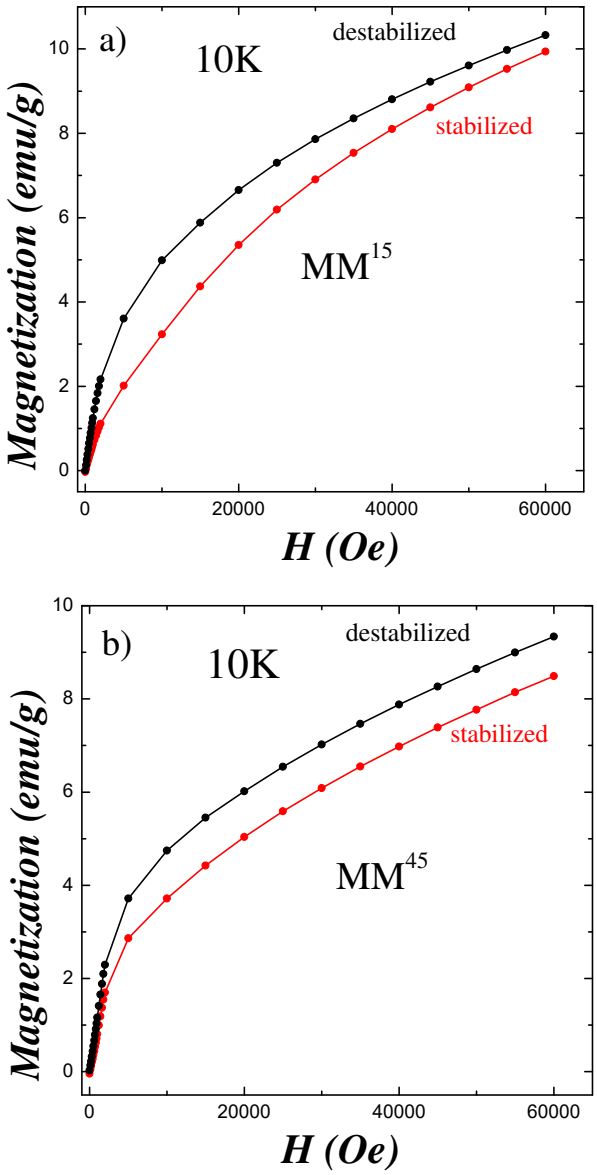

Fig.3.12. Magnetization at 10K as a function of the applied field, in the stabilized martensite and after heating above the first RMT (destabilized martensite) for a) MM^{15} and b) MM^{45}.

3.2.3 Milling in austenite

The milled in martensite has consistently showed the presence of non-transforming (martensite and/or amorphous-like) regions induced by the grinding process, as also found in Ni-Mn-Sn-Co alloys [85]. Nevertheless, in the present case a huge martensite stabilization has been observed, while no stabilization at all was reported in the Ni-Mn-Sn-Co case. Taking into account that one of the main difference between both cases is the structural state of the alloy during milling (our Ni-Mn-In-Co was milled in martensite whereas the Ni-Mn-Sn-Co alloy was milled in austenite). Moreover, taking into consideration the different mechanical properties of both phases, the slow-cooled ordered bulk alloy has been subjected to an identical milling process (just hand-crushing) in order to analyze the possible differences. In this case, since the alloy was in austenite at RT, the nomenclature is MA^{HC} for the hand-crushed powders.

Figure 3.13 shows the initial DSC measurements for the MA^{HC} sample. A very large shift of T_M^{rev} around 100K above the first RMT in the bulk alloy (see figure 3.3) can be clearly seen. The nature of the peak for the MA^{HC} sample is similar to that in the MM^{HC}, with a broadening of the transformation and a burst-like behavior during the first heating cycle. After heating the alloy to complete the first RMT, the stabilization disappears and the transformation characteristics resemble that of the bulk. Again, as it occurred in MM^{HC} sample, during the second heating ramp the T_M^{rev} coincide with that of the bulk alloy (shown in figure 3.3) and the serrated shape is no longer observed in the transformation peak. Interestingly, in spite of the initial bulk alloy at RT is in austenite, the characteristics of the first RMT after grinding suggests that the as-crushed powders are in martensite phase. So, despite the sample was crushed in austenite, a mechanical induction of the martensite and a subsequent huge martensite stabilization is observed. The induction of MT as a consequence of an applied mechanical stress has been widely reported and analyzed in many previous works on shape memory alloys [323, 324]. In particular, the stabilization of the martensite due to internal stresses can be explained in terms of Clausius-Clapeyron equation:

$$\frac{dT_M}{dP} = \frac{\Delta V}{\Delta S} \qquad 3.1$$

where, ΔV and ΔS are the volume and entropy change at MT and P is the hydrostatic pressure. Different stress contributions (σ_{ij}) may play similar role than P on controlling the transformation temperature T_M. Due to the lower volume of martensitic phase [42, 325], the internal stresses stabilizes the martensite, just as it occurs in the conventional pressure (stress) induced MT. It is worth noting that the MT transformation temperature during second RMT in the MM^{HC} sample is 50K higher than in the MA^{HC} (see table 3.5), but the maximum of the peak during the first

RMT (T_M^{rev}) takes place at approximately the same temperature in both samples, coinciding in turn with the Curie temperature. Such peculiar coincidence will be analyzed later.

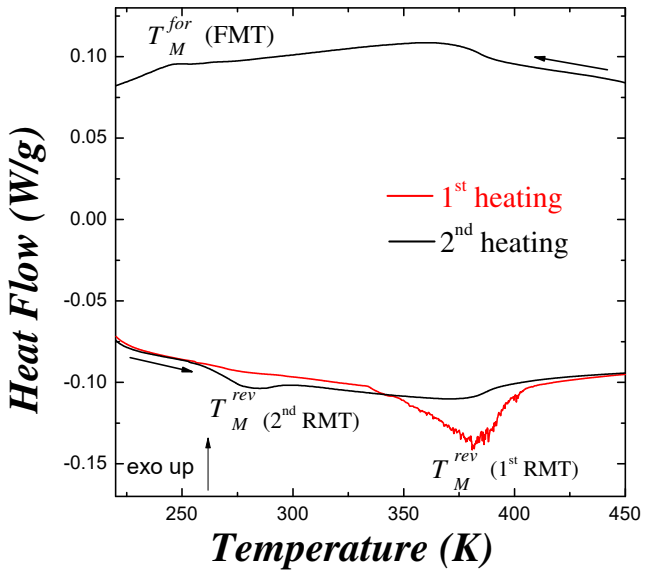

Fig. 3.13. DSC thermogram on the first heating run and subsequent cooling-heating cycle for the sample grinded in austenite (MA^{HC}).

Sample	1st heating (Stabilized)				2nd cycle				
	As (K)	T_M^{Rev} *(K)*	*ΔH (J/g)*	*ΔS (J/kgK)*	*As (K)*	T_M^{Rev} *(K)*	T_M^{For} *(K)*	*ΔH (J/g)*	*ΔS (J/kgK)*
MM^{HC}	333	383	13.0	33.9	300	328	300	8.0	24.3
MA^{HC}	333	383	8.6	22.4	254	278	246	1.4	5.0

Table 3.5. Austenite start temperature (A_S), peak maximum temperature (T_M^{rev}), enthalpy change (ΔH) and entropy change (ΔS) at the first and second RMT of the MM^{HC} and MA^{HC} samples.

The crystal structure for the MA^{HC} powders has been analyzed by the X-ray diffraction. Figure 3.14 shows the diffractograms obtained both at 430K and at 150K (for both stabilized and destabilized martensites). The structural refinement confirm that the stabilized martensite displays again a non-modulated $L1_0$ tetragonal structure whereas a modulated monoclinic structure appears on the further cooling after destabilization, just as it occurred in the MM^{HC} samples. Therefore, the tetragonal structure appears not only as a result of deformation of the martensitic variants in martensite phase but also during the stress-induction of martensite from

austenite. So, the tetragonal structure seems to accommodate the internal stresses better than the monoclinic one, no matter the previous state of the milled sample. Likewise, the diffraction peaks at 430K correspond to a cubic austenitic $L2_1$ structure with a small amount of tetragonal martensite, as in the MM^{HC} sample. In the present case, the volume fraction of retained martensite is 6.5% and the internal strains are around 1.3% (see table 3.6), which indicate a lower degree of deformation compared with the sample milled in martensite. In any case, it should be stressed that in spite of the degree of deformation is higher in the MM^{HC} (with similar grinding process), the disordered quenched alloy is more interesting from the RT application based on the magnetic field induced MT since it lies just above RT.

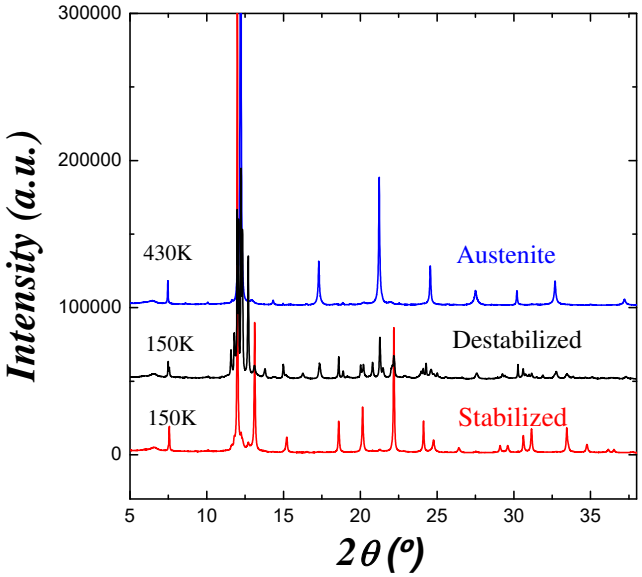

Fig. 3.14. X-rays diffractogram for the MA^{HC} sample at 430 K (austenite) and at 150 K in both the stabilized and the destabilized states.

Internal stresses associated to plastic deformation induced by milling are behind the observed stabilization of martensite. When plastic deformation takes place, it causes the stored elastic strain fields to relax, thus destroying the restoring force for the reverse MT. In addition, the enormous number of produced defects (dislocations, vacancies, antiphase boundaries…) acts as obstacles to the interface motion, resulting in the martensite pinning. In many studies, the changes in the configurational order by aging and thermal treatments (leading to the reduction of the martensite phase free energy) has been considered as the source of the stabilization process [308, 326].

Sample	430 K				150 K (stabilized)		150 K (destabilized)			
	a (Å)	F_{Mart} (%)	*Strain* (‰)	*Size* (Å)	*a* (Å)	*c* (Å)	*a* (Å)	*b* (Å)	*c* (Å)	*β* (º)
MM^{HC}	5.984	8.8	2.9	170	3.932	6.815	4.326	5.562	13.174	94.0
MA^{HC}	5.992	6.5	1.3	304	3.944	6.807	4.328	5.579	13.190	93.8

Table 3.6. Lattice parameters of the austenite (430K) and the stabilized and destabilized martensites (150K), volume fraction of deformed non-transforming martensite and microstructural parameters (internal strains and crystallite size) obtained from Rietveld refinement.

However, in the present example, the absence of such atomic order fluctuations caused by the mechanical milling allows us to dismiss this scenario. The plastic deformation produced in the powders milled in martensite or in austenite is preceded (or, at least, accompanied) by reorientation of martensite variants. The development of suitable habit planes between martensite and austenite in detwinned martensite requires more energy (increase in A_s), which in turn, raises the nucleation barrier for austenite. As recently hypothesized to explain the difference in the degree of stability between mechanically deformed Ni-Mn-Sn and Ni-Mn-Ga single crystals, the degree of stabilization could depend on the twinning stress [311]. The lower twinning stress in Ni-Mn-Ga alloys leads to martensite stabilization just by 1K temperature shift, whereas in Ni-Mn-Sn alloys it leads up to 26K due to higher twinning stresses. The absence of such stabilization effect in several SMA systems like Ni-Mn-In, Ni-Mn-Sn or Ni-Mn-Sn-Co [16, 81, 82, 84, 92, 292], even after subjecting to similar grinding/milling process, can be thought to be related to a lower of lower twinning stresses than in our Ni-Mn-In-Co alloy [203]. This system, in fact, show a large martensitic plasticity, despite their high brittleness [327]. On the other hand, in other works the concentration of Mn has been proposed to be responsible for such stabilization process [83]. However, the Mn concentration of the investigated alloys is similar to that of the most alloys that do not show stabilization. Therefore, the concentration of Mn cannot be responsible of the huge stabilization observed in our case.

Due to the modifications to the thermodynamic equilibrium conditions caused by the deformation, an overheating (increase in A_s) providing an additional driving force for the twin-boundary motion is required so that the first RMT can proceed. The driving force for the MT can be written as $\Delta G \approx -\Delta S\, \Delta T$, where the total entropy change has mainly magnetic and vibrational contribution, $\Delta S = \Delta S_{vib} + \Delta S_{mag}$. The vibrational and magnetic entropy

contributions to the total entropy change has been previously evaluated using the Debye and Bragg-Williams approximations [328, 329]. Just below the Curie temperature, the evolution of both the entropy contributions during the MT is shown in the figure 3.15. Above 250K (close to the Debye temperature), the vibrational contribution is positive and nearly constant. However, the negative magnetic contribution increases almost linearly up to a maximum at the Curie temperature. As a result, overall entropy rises with temperature. This justifies the larger entropy change during the first RMT (see table 3.1) with higher transformation temperature near T_c compared to the second RMT. At T_c, the magnetic contribution goes to zero and the vibrational entropy gives the total contribution to the total entropy. As a result, immediately below T_c, a maximum driving force ΔG_{max} for the MT is expected, which becomes unbalanced once the forces inhibiting the RMT are surpassed.

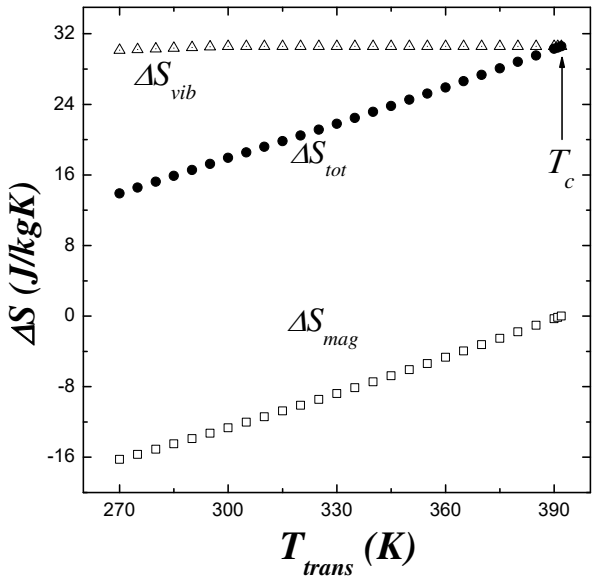

Fig. 3.15. Evolution of vibrational and magnetic entropy contributions (ΔS_{vib} and ΔS_{mag}) and the total entropy change (ΔS) at the MT as a function of the transformation temperature.

This proposed model is consistent with the presented results. The alloy has been exposed to different milling times, different degrees of plastic deformation and various thermal treatments resulting in a wide range of stable MT temperatures. However, for all the different cases, the irreversible instability vanishes (A_f for RMT)near the Curie temperature, similar to what has been reported in grinded $Mn_{50}Ni_{33.5}Sn_8Co_{8.5}$ powders [6]. Therefore, the Curie temperature T_c could be considered as a maximum temperature where mechanically stabilized martensite can exist in a meta-stable state.

3.2.3.1 Magnetic characterization of the martensitic phases

- **High field magnetization**

The magnetization *M(H)* curves corresponding to the MA^{HC} powders at 10K in both stabilized and destabilized martensite are shown in figure 3.16. Unlike MM^{HC} powders, the magnetization at 60kOe for the both states is quite distinct. The approach to saturation, in turn, appears to be very similar, though the magnetization is always smaller in the stabilized sample than in the destabilized one. This behavior is opposite to that observed in MM^{HC} powders, where the magnetization values at 60kOe were similar for stabilized and destabilized while showing a clear difference in the saturation trajectory. From the above results, the difference between the internal stress level in the samples milled in austenite and in martensite could be a factor responsible for such a varying behavior. Under this scenario, the lower internal stresses induced in the MA^{HC} would not be high enough to induce a strong magnetic anisotropy being able to make the approach to saturation harder. The crystallographic anisotropy seems to play a minor role since both martensites are different but the approach to saturation is similar.

The magnetization at 10K for MA^{HC} sample (20-25emu/g) is considerably higher than in MM^{HC} (8-10emu/g). On one hand, the long-range atomic order is higher in the alloy milled in austenite, so the different Mn-Mn distance may do the overall magnetization of martensite be higher than in the disordered alloy.

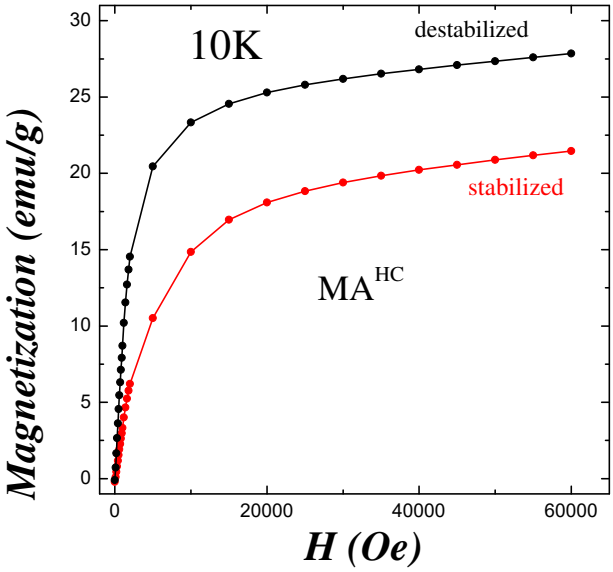

Fig. 3.16. *M(H)* for MA^{HC} for stabilized (black line) and destabilized martensite (red line).

On the other hand, the presence of small quantities of austenite (not transformed to martensite during milling) at 10K could also contribute the higher magnetization in the destabilized state.

Destabilization induces a reduction in the internal stresses and can also increase the magnetization but the large magnetization increase (with respect to MM^{HC}) points to a larger fraction of austenite (see reflection around 28°C in figure 3.14 corresponding to austenite). Therefore, although milling-induced deformation induces an almost complete transformation to martensite (stabilized), the subsequent thermally-induced martensite on cooling (destabilized) seems to be not so complete.

- **Low field magnetization**

The low magnetic moment of martensite with respect to austenite in Ni-Mn-In-Co alloys are usually explained as a consequence of coexistence of ferromagnetic and anti-ferromagnetic interactions, favored by the changes in the inter-atomic distances brought by the MT [330]. To better understand the true nature of the two both martensite structures, further magnetic analysis are necessary. In this respect, the temperature dependence of magnetization at low magnetic fields (i.e. 100Oe) can give information about the magnetic character of the tetragonal and monoclinic martensite phases. In the present chapter, such study has been only performed in the MA^{HC} sample, as it comes from an ordered state and hence the evolution of atomic order can be disregarded as a contribution factor. In particular, the analysis has been performed from ZFC-FC curves at 100Oe obtained in both martensitic structures; the sample is firstly cooled in the absence of magnetic field, then a magnetic field of 100Oe is applied and the magnetization is measured during a heating ramp (ZFC) followed by subsequent cooling (FC). The existence of well-controlled stabilized and destabilized states in the present case, allow analyzing the evolution of the martensitic magnetism in two different situations; a tetragonal structure with high stresses and a particular defect configuration (stabilized) and a monoclinic phase produced on cooling from a retransformed state (destabilized). The atomic order is the same in both cases, and due to the low temperature required to retransform the alloy; the density of defects is probably similar.

a) Stabilized Martensite (tetragonal structure)

ZFC-FC curves for the stabilized MA^{HC} sample are shown in figure 3.17a. Above T_c = 380K, the sample is paramagnetic and the MT start temperature on cooling is around M_s = 340K. Figure 3.17b shows the ZFC-FC magnetization versus temperature corresponding to the bulk alloy (without deformation) and after crushing (low temperature region of figure 3.17a). A clear difference can be observed in the low temperature region: whereas the difference between FC and ZFC curves in the as-crushed samples is evident, such difference in bulk nearly disappears. A maximum in the ZFC curve at T_f (around 80K) in the milled sample can be well identified.

Different mechanisms, i.e. super-spin glasses, super-paramagnetism, reentrant spin glasses or anti-ferromagnetism have been proposed to explain this kind of behavior [16, 331, 332]. The bulk sample does not show the presence of such a maximum (at least it is much less pronounced). Besides, deformation makes the global magnetization (DC magnetic susceptibility) increase. Anyway, results in figure 3.17b seem to indicate that the mechanism responsible for this peak at T_f could be also related (the effect is clearly enhanced) to the deformation and therefore, to the microstructural defects created during the milling process.

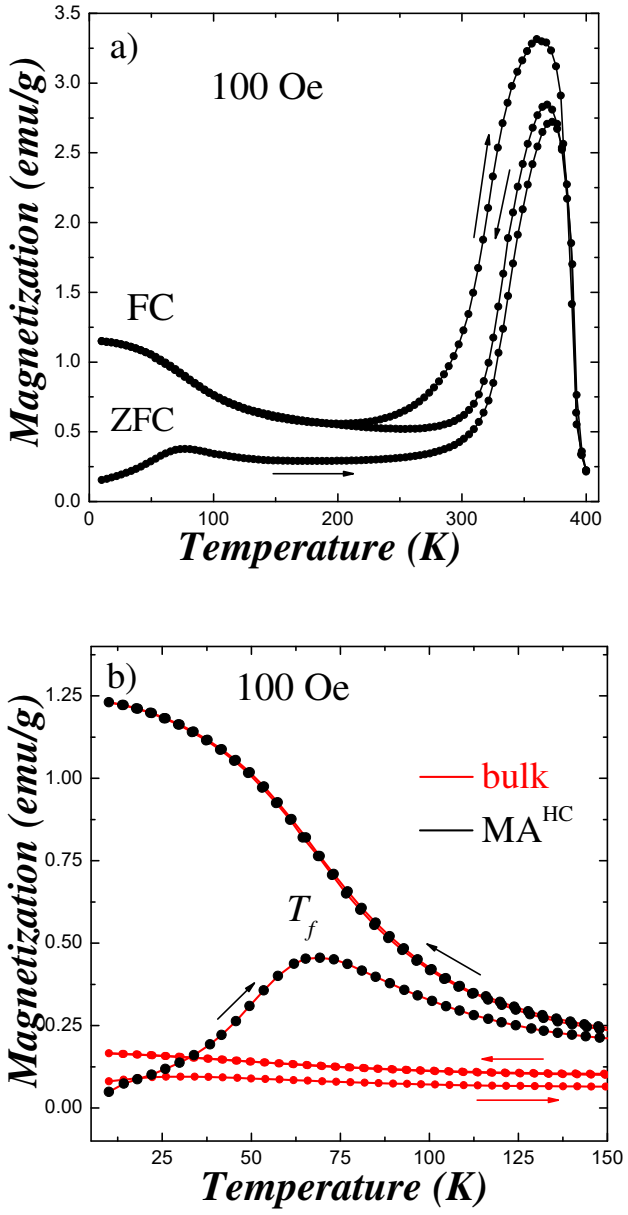

Fig. 3.17. a) ZFC-FC *M(T)* measurement at 100Oe for MA^{HC} sample, b) Detailed low-temperature region.

The presence of the peak at T_f points to a spin-glass like behavior. The spin-glass is considered to be a magnetically frustrated state where spins are frozen under a freezing temperature in random directions [333–335]. The magnetic frustration, randomness of the spins and the mixed interactions are the main ingredients for the spin-glass systems. Since spin-glass states are meta-stable, these are very sensitive to the history of the magnetic field and temperature as demonstrated by the irreversibility in the ZFC and FC curves at low temperatures.

In order to understand the irreversibility in the magnetic curves, the frequency dependence of the AC susceptibility was also measured. Figure 3.18 shows the real part of the susceptibility curves (dispersion) for four different frequencies 2Hz, 20Hz, 200Hz and 1000Hz, under a H = 3.5Oe oscillating magnetic field. Increasing the frequency, the magnitude of susceptibility decreases and the maximum of the peak T_f shift to higher temperatures (see table 3.7). The frequency dependence of T_f has been first analyzed using the Mydosh parameter (ϕ). The Mydosh parameter gives the shift in the T_f, per decade of the frequency change:

$$\phi = \frac{\Delta T_f}{T_f \Delta \log_{10} f} \qquad 3.2$$

where T_f is the peak temperature of the maximum in the ZFC curve at the corresponding AC frequency (f). T_f is called as the spin-freezing temperature.

The Mydosh parameter helps to understand the mechanism responsible of the process taking place in this temperature range [333, 334]:

- $\phi \leq 0.08$ indicates that the nature of the process correspond to a canonical spin-glass (randomly oriented isolated magnetic moments).
- Values of ϕ in the range $0.08 \leq \phi \leq 0.2$ correspond to cluster spin-glass.
- $\phi \geq 0.2$ corresponds to a super-paramagnetic system.

Using equation 3.2, the obtained value of ϕ is around 0.012, which suggests the presence of canonical-spin glass system in our samples. The presence of such canonical spin-glass system has also previously been reported in ball-milled Ni-Mn-In alloys [299, 331]. To confirm this point, a dynamic scaling theory (critical slowing-down law, CSDL) has been used. According to this theory, the relaxation time τ ($\tau = 1/f$) corresponding to the measured frequency follows the law:

$$\tau = \tau_o \left(\frac{T_f}{T_g} - 1\right)^{-zv} \qquad 3.3$$

where τ_o is the relaxation time constant for flipping of a single spin entity, T_g is the magnetic glass transition temperature when the frequency approach to zero ($T_g = T_f$ as $f \to 0$) and zv is a critical exponent. The temperature dependence of the relaxation time is shown in figure 3.19, where the fitting is performed using:

$$ln\,\tau = ln\,\tau_o - zv\,ln\left(\frac{T_f}{T_g} - 1\right) \qquad 3.4$$

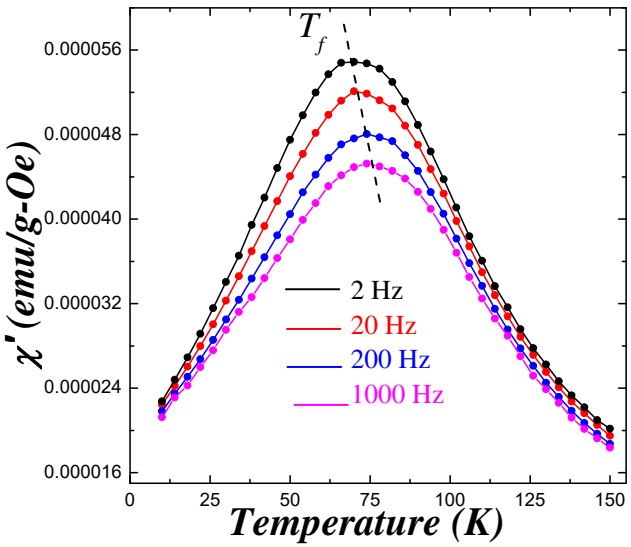

Fig. 3.18. Temperature variation of real (χ') part of as susceptibility at different frequencies for stabilized MA^{HC} powders.

Frequency (*Hz*)	T_f **(*K*)**
2	71.4
20	72.6
200	73.5
1000	74.0

Table 3.7. Values of peak temperature T_f, for different frequency measurements for stabilized MA^{HC} powders.

The values of frequency and the temperature used are given in table 3.7. The fitting of the equation 3.4, yields T_g= 67K, τ_o = 2.54*10^{-13} and zv = 8.3, which agrees with an atomic spin-

glass mechanism. The values of τ_o and zv for a typical canonical spin-glass system is around 10^{-13}-10^{-6} and 4-12, respectively [333, 335].

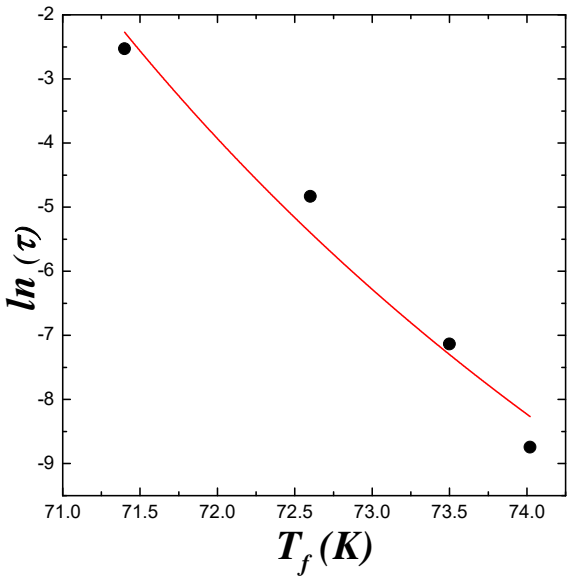

Fig. 3.19. Best fit of the equation 3.5 with the temperature dependence of the observation time for stabilized MA^{HC} powders.

In order to further understand the magnetic glassy behavior at low temperatures, the frequency dependence of peak temperature (T_f) in the AC susceptibility measurements are usually analyzed as well by other different approaches:

$$\text{Neel-Arrhenius Law} \qquad \tau = \tau_o \exp\left(\frac{E_a}{k_B T_f}\right) \tag{3.5}$$

$$\text{Vogel Fulcher Law (VFL)} \qquad \tau = \tau_o \exp\left(\frac{E_a}{k_B (T_f - T_o)}\right) \tag{3.6}$$

where, k_B is the Boltzmann constant, T_o is the Vogel-Fulcher parameter that takes into account the interaction between atoms or clusters and E_a is the activation energy. The Neel-Arrhenius approach is a particular case of Vogel-Fulcher Law where the interaction parameter T_o between atoms or clusters is neglected. The logarithm of both sides of equation 3.6 yields:

$$ln\,\tau = ln\,\tau_o + \left(\frac{E_a}{k_B (T_f - T_o)}\right) \tag{3.7}$$

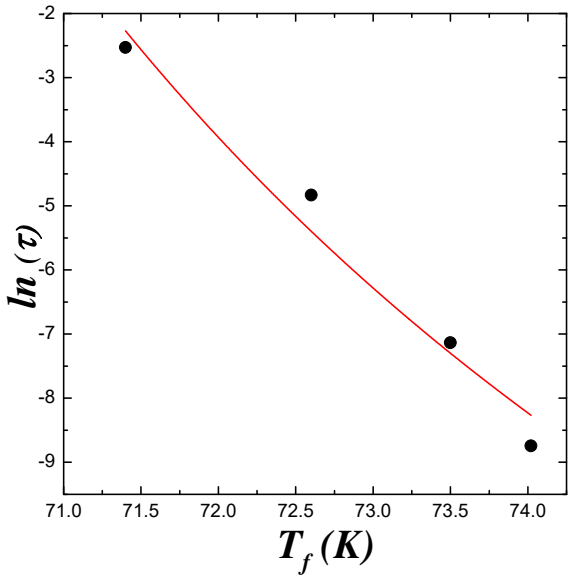

Fig. 3.20. *ln* τ vs T_f data fitted to the Vogel-Fulcher law for stabilized MA^{HC} powders

The fit to the VFL shown in figure 3.20 yields T_o = 68 and E_a/k_B = 242.27K, which is reasonable for the canonical spin-glass system [331, 336]. T_o has been related in several studies to the interaction between the cluster in cluster-spin glasses or the magnetic moments in the canonical systems [337–339]. The non-zero values of T_o implies the existence of significant interaction between the magnetic moments. In case of T_o = 0, the systems indicates the presence of non-interacting spins/clusters and the VFL approaches to the Neel- Arrhenius law which is primarily valid for super-paramagnetic systems.

The distinction between the cluster system and canonical system can also be made using the Tholence Criterion, which is $[T_f - T_o]/T_f$. The value of this coefficient is ≤ 0.1 for canonical spin-glasses and ≥ 0.5 for cluster spin-glass system [340, 341]. In the present case, this coefficient being < 0.1, also suggests a canonical spin-glass mechanism. Thus, previous results strongly suggest the presence of canonical spin-glass system.

b) Destabilized Martensite (monoclinic structure)

In order to study the possible influence of the microstructure (different crystallographic structure, stresses, defects etc.) on the spin-glass, similar measurements were performed for the destabilized martensite. Figure 3.21 represents the ZFC-FC at 100Oe for stabilized (red curve) and destabilized states (black curves).

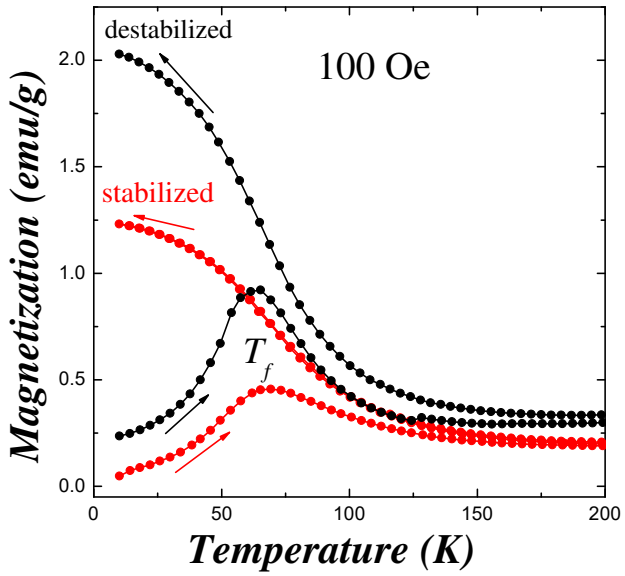

Fig. 3.21. ZFC-FC *M(T)* measurement at 100Oe for stabilized and destabilized martensite for MA^{HC} powders.

The T_f for destabilized sample is similar to that of the stabilized one in the DSC measurements. On the other hand, the magnetization of the stabilized state is lower than the destabilized one. This difference point to a higher internal stress level present in the stabilized martensite. The reorientation of martensite variants induced by deformation may lead to incoherent interfaces resulting in higher stress levels. After the first RMT, the stabilization disappears and the resultant martensite shows a better coherency between the interfaces resulting in a lower stress levels. The reduction of the internal stress seems to increase the global susceptibility of the alloy. Besides, the thermal treatment involved during destabilization should not be able to modify the density of dislocations created during deformation. Nevertheless, the movement of the interfaces (austenite/martensite or variants) can modify their configuration and probably their distribution.

The nature of the glassy-system for the destabilized martensite was also studied by the frequency dependence of the magnetic susceptibility measurements at low temperatures. The increment in T_f with the frequency observed in table 3.8 occurs like in the stabilized state but values are slightly higher (compare table 3.7 with table 3.8).

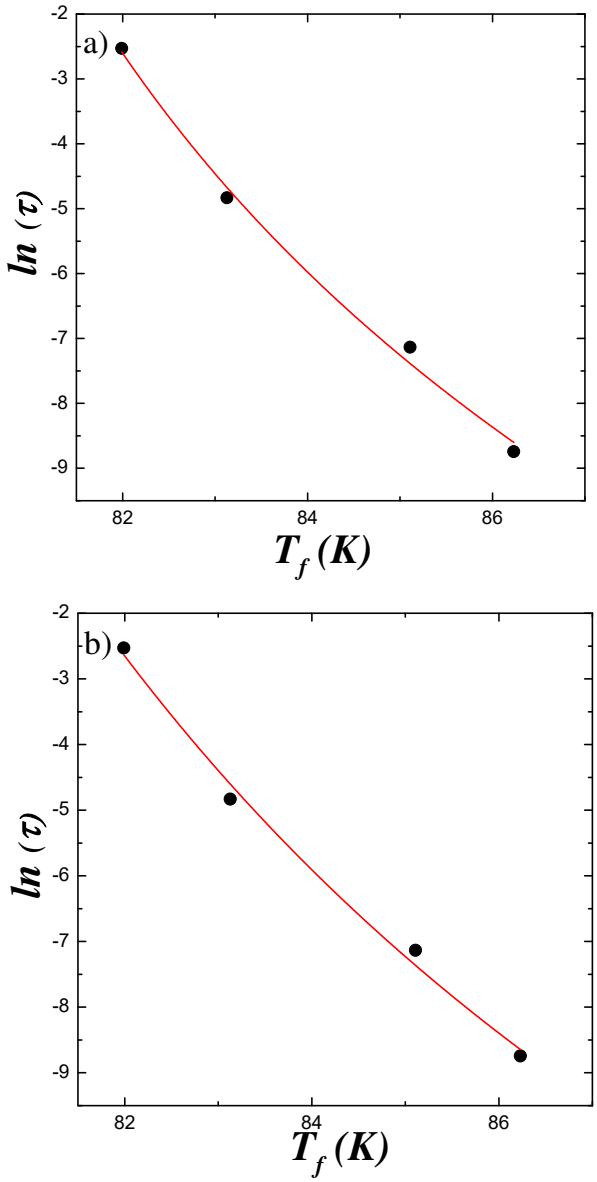

Fig. 3.22. a) Best fit of the equation 3.5 with the temperature dependence of the observation time for destabilized MA^{HC} powders, b) $ln\ \tau$ vs T_f data fitted to the Vogel-Fulcher law for destabilized MA^{HC} powders.

The Mydosh parameter for the destabilized powders is around 0.013, which again indicates the presence of a canonical system just as the stabilized martensite. The fittings of the temperature dependence of the relaxation time using CSDL and VFL using equations 3.4 and 3.6, respectively, is shown in figure 3.22. The fittings to the CSDL yields T_g = 78K, τ_o = $1.52*10^{-12}$ and zv = 8.26. The VFL yields T_o = 69 and E_a/k_B = 315.46K. The values obtained again suggest the presence of canonical spin-glass system. The comparison between the values for both stabilized and destabilized states is shown in table 3.9.

Frequency (Hz)	T_f *(K)*
2	81.99
20	83.13
200	85.11
1000	86.23

Table 3.8. Values of peak temperature T_f, for different frequency measurements for destabilized MA^{HC} powders.

Thus, it appears that the nature of the spin-glass system does not change due to the difference in microstructure in the martensite (tetragonal induced by plastic deformation or "thermally-induced" monoclinic). In any case, plastic deformation seems to enhance the spin-glass behavior as shown in figure 3.17b. The general behavior of the curves suggests that deformed samples have ferromagnetic regions locate in the APBs and paramagnetic-like state surrounding the APBs. It also seems that the paramagnetic regions change to a canonical spin-glass below T_f. The larger T_g observed in the destabilized state could be then associated with the degree of plastic deformation [342]. Nevertheless, the difference in the magneto-crystalline anisotropy for the two different microstructural states (seen figure 3.6c) could play an important role to understand the shift in the freezing temperature. Although the present results give some hint on the origin of glassy-behavior, the true mechanism controlling the effect needs an exhaustive and more detailed analysis.

	Stabilized	**Destabilized**
ϕ	0.012	0.013
τ_o	2.54E-13	1.52E-12
T_g	67.5	78.03
Zv	8.3	8.26
E_a/k_B	242.27	315.46
T_o	68.3	69.04

Table 3.9. Values obtained by best fit of the equation 3.5 and 3.7 for stabilized and destabilized powders for MA^{HC} samples.

3.3 Conclusions

The effect of the deformation induced by the grinding process and different milling times has been studied in the $Ni_{45}Mn_{36.7}In_{13.3}Co_5$ alloy. The main conclusions deduced from this chapter are as follows:

- The grinding process leads to the drastic deterioration of the MT characteristics. The degradation in the magneto-structural properties is associated with the milling-induced highly deformed non-transforming regions. The volume of such regions increase with the time of milling in a way that it could lead even to the amorphization of the alloy.
- The stabilization of martensite due to induced deformation by grinding has been reported for the first time in these alloys. The shift in transformation temperatures reach up to 100K and have been observed irrespective of the initial phase at RT (austenite or martensite). The stabilization is probably linked with higher twinning stresses present in the Ni-Mn-In-Co alloys.
- The martensite induced by deformation have been documented to be distinct than the thermally induced. The stabilized martensite is found to possess a non-modulated tetragonal structure (I4/mmm), whose smaller lattice parameters accommodates the generated internal stresses better than the thermally induced modulated monoclinic structure (P2/m).
- The destabilization during the first RMT completes at temperatures (A_f) around the Curie temperature independently of the deformation degree. The maximum RMT driving forces occur at T_c linked to a maximum entropy change (no magnetic contribution). Therefore, T_c represents a high temperature limit to mechanically induce the martensite phase.
- The presence of spin-glass like systems with canonical nature has been documented in the both stabilized martensite and destabilized martensite state with considerable interaction between the spins. Nevertheless, their characteristics are independent of the stabilization state. The internal stresses play a key role in the global magnetic difference between stabilized and destabilized states.

Chapter 4

Correlation between particle size and magneto-structural properties of milled micro-particles

4.1 Introduction

In this chapter, the magneto-structural properties of the $Ni_{45}Co_5Mn_{36.7}In_{13.3}$ micro-particles obtained from ball milling have been studied separately for different particle size ranges. In particular, the characteristics of the martensitic transformation, the saturation magnetization and microstructural parameters such as the internal strains and crystallite size have been analyzed for particles within specific size ranges and coming from different milling times. A similar very high degradation of both the MT and the austenite magnetization has been observed both with the increasing milling time and, for each selected milling time, with the decreasing particle size. Such behavior has been analyzed and explained as a consequence of the increasing amount of retained martensite and the highly deformed non-transforming regions appearing because of the milling induced deformation. From the comparison between particles within the same size range and different milling times, a direct correlation between the particle size and the magneto-structural properties of the micro-particles could have been demonstrated. The improvement, through thermal treatments, of the functional properties of those micro-particles suitable for the elaboration of the printable filaments has been also explored.

4.1.1 Motivation and Objectives

This chapter is focused on obtaining the $Ni_{45}Co_5Mn_{36.7}In_{13.3}$ micro-particles to be used as fillers in printable polymeric matrices for magnetic refrigeration applications. Such particles must fulfill two main requirements; the particle size must be compatible with the printer nozzle and they must show good enough Magnetocaloric response. However, as mentioned in chapter 1, the reduction of particle size by means of ball milling is always accompanied by plastic deformation and the induction of a large amount of microstructural defects, which may highly affect the functional properties of the alloys. Typically, the achieved particle size is lower the longer the

milling time, but, in turn, the detrimental effects of milling become interestingly striking with the milling time [80, 343, 344]. Post-milling thermal treatments may result in a partial recovery of the MT and the austenite magnetization [83, 343–346], but in the case of severe milling, residual effects and plastic deformation may persist even after high temperature annealing [347]. A comprise between particle size and milling time is therefore needed, and it will depend on the required functionality.

As shown in the previous chapter, a significant drop in the enthalpy change during the MT and a strong reduction in the saturation magnetization are observed in the $Ni_{45}Co_5Mn_{36.7}In_{13.3}$ powders milled for 15 minutes. Similarly, previous works on Ni-Mn-Sn-Co alloy are subjected to exactly same ball milling process (same equipment, spinning rate, number and type of balls…) also show a large reduction on both the transforming volume fraction and the ferromagnetic exchange interaction for milling times longer than 15 minutes [344]. In both cases, the presence of a considerable amount of highly deformed amorphous-like regions, along with the retention of martensite above the MT temperature, is behind the observed structural and magnetic degradation. On the contrary, a much lower degradation (just related to the appearance of a small fraction of retained martensite) is observed on the corresponding samples after a soft hand crushing. Unfortunately, the inherent limited particle downsizing and the lack of repeatability with same outcome make this grinding method be not suitable for the production of functional micro-particles. However, it is worth recalling that the powders resulting from ball milling show a non-homogeneous size distribution [344] and hence micro-particles within similar size range could be obtained from different milling times. Thus, small particles (though a small amount) could be obtained from alloys subjected to short milling times. For a later use of the particles selected in this way, a comparative analysis of the magneto-structural properties of the micro-particles with the same size but coming from different milling times should be performed. Nevertheless, no study in this respect has been carried out in MSMAs up to now. Undertaking such study is the main objective of the present chapter.

From the above, and with the aim of obtaining micro-particles with acceptable MCE features in a controlled manner, the $Ni_{45}Co_5Mn_{36.7}In_{13.3}$ powders obtained after ball milling for short milling times (below 15 minutes) have been studied. First, the MT and the saturation magnetization have been analyzed as a function of milling time to evaluate the net effect of milling. Then, for each milling time, the particles have been sieved into different size intervals and a comparative analysis of the magneto-structural and microstructural parameters of the particles within the same size range have been performed. The MCE and the refrigerating cooling power in those particles suitable for embedding into printable polymeric filaments have been estimated.

4.1.2 Chapter Organization

The experimental results shown below are presented in two main parts. In the first part, the net effect of milling on the MT and the saturation magnetization is evaluated for milling times up to 15 minutes. In particular, both the degradation of the MT as a consequence of milling and the frictional contribution linked to the defects created during the milling process are analyzed from the enthalpy and entropy changes at the MT. In the second part, the possible correlation between particle size and magneto-structural properties is explored from the comparison between the micro-particles within the same size interval but coming from the extreme analyzed situations: soft hand crushing and ball milling for 15 minutes. The MCE is quantified for each particle size and the effect of post-milling annealing treatment on the microstructural recovery and the MCE is also analyzed. Finally, the viability of the studied powders as active part in the production of polymeric composites for magnetic refrigeration applications is evaluated.

4.2 Experimental Results

A new bulk $Ni_{45}Co_5Mn_{36.7}In_{13.3}$ alloy is used in the present chapter. The alloy was also elaborated from high purity elements by arc melting under protective Ar atmosphere, homogenized at 1073K during 15h and slow cooled. The composition was checked by EDS. Samples extracted from bulk ingot were subjected either to soft hand crushing or to ball milling in order to obtain small micro-particles. As reported in previous chapter, all the as-milled samples showed huge martensite stabilization, regardless of the milling method and the milling time. In order to remove the stabilized martensite and therefore achieving a stable initial state, all the as-milled powders were preliminarily heated up to 450K, just above the first reverse martensitic transformation (RMT), before any other measurement.

4.2.1 Influence of milling time

Different pieces taken from the bulk ingot were subjected to hand crushing (0 minutes milling) or to ball milling for 1, 2, 3, 5, 7, 10 and 15 minutes. The so obtained powders will be hereafter referred to as M0, M1, M2, M3, M5, M7, ML10 and ML15 samples, respectively. The MT taking place in the samples has been first analyzed from DSC measurements. Figure 4.1 shows the thermograms obtained on a heating-cooling thermal cycle at a rate of 10K/minute for the temperature range 200K to 473K. The exothermic and endothermic peaks corresponding to FMT and the RMT, respectively, can be clearly seen between 300K and 350K. The para-ferromagnetic transition is also detectable as a non-hysteretic shoulder around 390K. As it occurred in the

previous chapter, the lack of evolution of the transformation temperatures with milling time suggest a null impact of milling on the long-range atomic order.

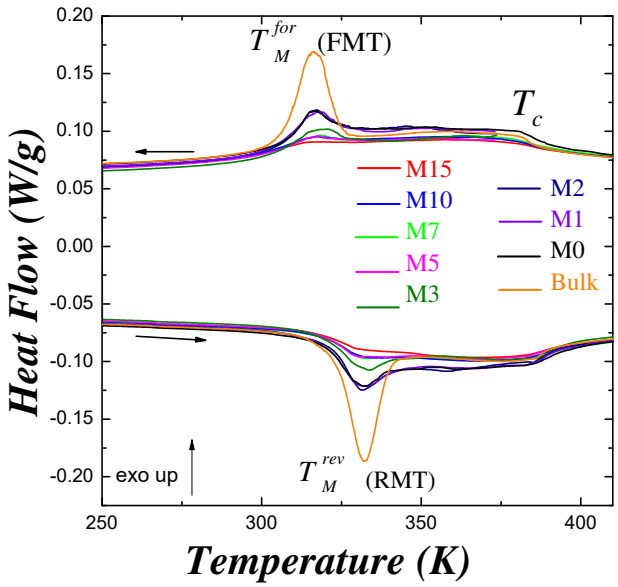

Fig. 4.1. DSC thermogram for the bulk sample and the milled powders.

The MT peaks become noticeably smaller and slightly broader as the milling time increases, showing a considerable degradation of the MT as a result of milling. The highest peak reduction takes place just after hand-crushing, and then a further gradual decrease of the peak intensity is observed with the increase of milling time. The degradation of the MT upon milling can be assumed to be linked to both the presence of retained martensite and the existence of heavily deformed non-transforming regions. The volume fraction of the alloy undergoing MT in each sample has been calculated by comparing the enthalpy change at the FMT with that of the bulk alloy (ΔH^{bulk} = 7.7J/g), assuming the transforming fraction to be 100% in the latter. The evolution of transforming fraction with the milling time is shown in Figure 4.2. It is worth noting that the impact of hand crushing on the MT is much higher in this case (with just a 35% transforming fraction for M0 sample) than in the previous chapter, where almost no variation was observed in the hand-crushed sample (MM^{HC}) with respect to the corresponding bulk (see Figure 3.4b). This evidences the different efficiency of hand crushing in both cases, in line with the above mentioned lack of repeatability of the manual grinding. The transformation fraction does not evolve for milling times up to two minutes, and just an abrupt decrease is observed after three minutes milling, followed by a further smooth decrease. It is also worth noting that the transformation fraction in M15 sample is just 5%, whereas the sample milled for 15 minutes

studied in previous chapter showed a 38%. Therefore, it seems that the ball milling also, and not only the hand crushing suffer from a clear lack of repeatability with respect to outcome.

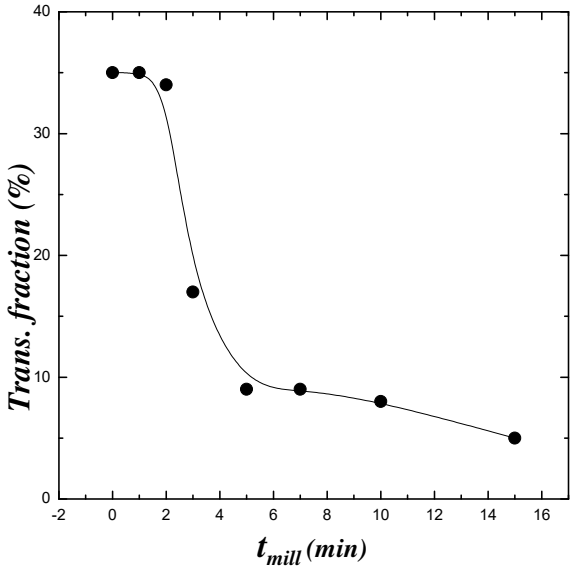

Fig. 4.2. Transforming fraction of the milled sample, estimated from the enthalpy change at the MT.

In section 3.2.2.2, the influence of a frictional contribution to the entropy change at the MT was inferred from the higher ΔS value at the FMT with respect to RMT in the sample subjected to 15 minutes milling. The transforming fraction as a function of milling times is plotted in figure 4.2b. The origin of such contribution would on the interaction between interphases and defects induced by milling [348]. Under an ideal scenario, where the frictional contribution is insignificant, the total entropy change can be thought of as the contribution of the vibrational and magnetic terms

$$\Delta S_{tot} = \Delta S_{vib} + \Delta S_{mag} \quad 4.1$$

neglecting the electronic term [348]. A stronger magnetic contribution opposing the vibrational one should be anticipated in the FMT (with respect to the RMT), which is closer to the Curie temperature, as long as the magnetic term is directly connected to the magnetization change at MT. Thus, the difference in entropy between the forward and reverse MTs (in absolute values), therefore, should be always negative. That is, $\Delta S^o_{for} < \Delta S^o_{rev}$, where the superscript refers to the ideal situation (free of frictional terms) [348]. On the other hand, the mobility of interphases throughout the MT depends on their interaction with defects. Such interaction modifies the entropy change through a frictional term (ΔS_{fr}) which is always negative (exothermic process during both the FMT and RMT). Therefore, the net entropy change at FMT can be written as:

$$\Delta S_{for}(-) \approx \Delta S^{0}_{for}(-) + \Delta S_{fr}(-) \quad 4.2$$

And for the RMT:

$$\Delta S_{rev}(+) \approx \Delta S^{0}_{rev}(+) + \Delta S_{fr}(-) \quad 4.3$$

The net entropy change should be positive (+) for the FMT and negative (-) for the RMT. The difference between the FMT and RMT entropy changes can give the information about the frictional contribution. Such contribution has been evaluated in the milled powders from the analysis of the entropy change values obtained from thermograms ($\Delta S = \Delta H/T_M$). The difference between the entropy changes at the FMT and the RMT, normalized to the forward entropy change to prevent volume defects (that is, the normalized difference, ND) is shown in figure 4.3 where longer times data taken from [348] have been included. For shorter milling times (below 15 minutes), ND is negative, however it becomes positive for longer times as shown by the red points in figure 4.3.

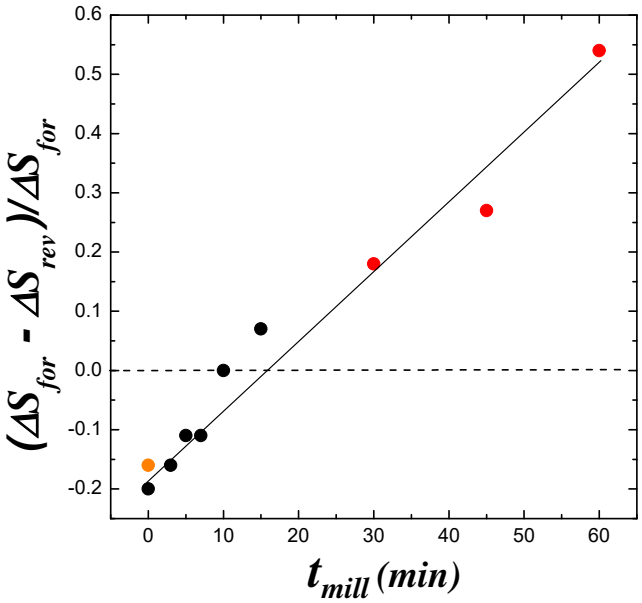

Fig. 4.3. Normalized difference between entropy change at the forward and reverse MT, Red points: data from[348]. Orange point: bulk sample.

The frictional entropy contribution from this normalized difference (ND) can be easily estimated:

$$ND = \frac{|\Delta S_{for}| - |\Delta S_{rev}|}{|\Delta S_{for}|} \approx \frac{|\Delta S^{o}_{for}| - |\Delta S^{o}_{rev}| + 2|\Delta S_{fr}|}{|\Delta S^{o}_{for}| + |\Delta S_{fr}|} \quad 4.4$$

And therefore,

$$|\Delta S_{fr}| \approx \frac{|\Delta S^{o}_{for}|(ND-1)+|\Delta S^{o}_{rev}|}{2-ND} \qquad 4.5$$

Thus, assuming that ΔS^{o}_{for} and ΔS^{o}_{rev} correspond to the entropy change at the FMT and RMT of the undeformed bulk sample respectively, the percentage of the frictional contribution ($\Delta S_{fr}/\Delta S^{0}$) can be directly calculated. The evolution of the corresponding fraction is plotted in figure 4.4 as a function of milling time. As expected, the frictional term rises with the increase of milling time, suggesting an increase in the generated number of microstructural defects. In particular, the frictional contribution reaches values higher than 10% after 15 minutes milling, which means a considerable decrease in the net entropy change at the RMT, and therefore, in the highest attainable MCE effect.

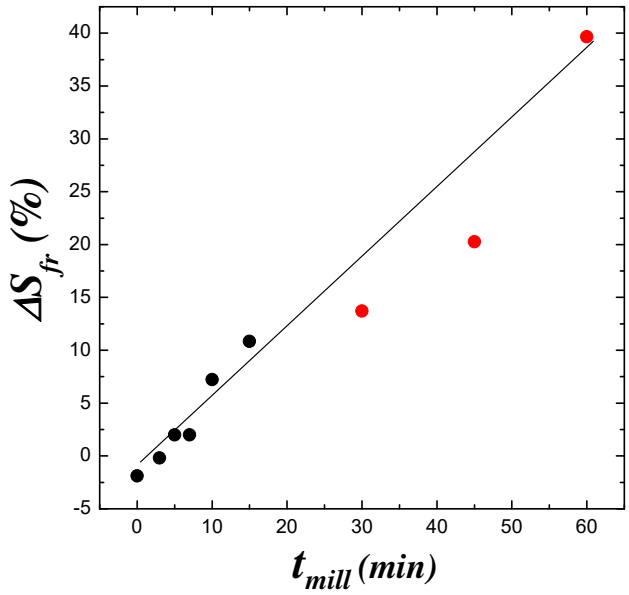

Fig. 4.4. Frictional entropy term as a function of the milling time Red points: data from[348].

The presence of the milling-induced microstructural defects and plastic deformation also affects the magnetic properties. Figure 4.5 shows the field dependence of magnetization for the two extreme cases, that is, the hand crushed (M0) and the sample milled for 15 minutes (M15). The high-field magnetization in austenite (350K) diminishes with increase on milling time whereas almost no variation is observed in martensite (10K), in agreement with the results shown in section 3.2.2.2. As explained there, the observed behavior could be attributed to the presence of

either retained martensite or almost paramagnetic highly deformed regions. Nevertheless, the net magnetization values are different from the corresponding values obtained in the previous chapter for a similar sample subjected to the same milling process (see Figure 3.11), so, as expected, the lack of repeatability inferred from the estimated transforming fraction also affects the magnetic properties. Therefore, the milling time does not seem to be in itself an adequate parameter to quantatively assess the impact of milling. In this regard, the particle size, which can be assumed to be somewhat related to the achieved degree of deformation, will be explored as an alternative parameter.

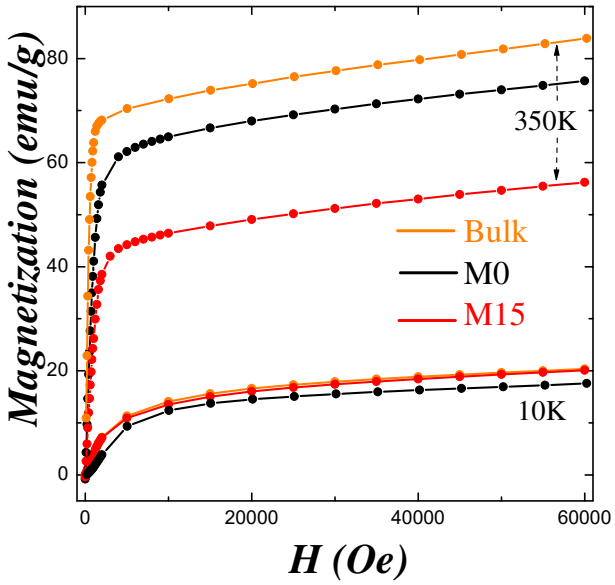

Fig. 4.5. Field dependence of magnetization at 350K (austenite) and 10K (martensite) for the bulk alloy and the as-crushed and 15 minutes milled samples.

4.2.2 Correlation between particle size and magneto-structural properties

Since the elaborated micro-particles are ultimately intended to be used as magnetic active material in 3D printable composite filaments, the particle size is expected to highly condition the mechanical consistency and therefore, the highest filling factor of the composite. In anticipation of the final printability of the material might be optimized by certain particle size (or size ranges), the eventual variation of the magneto-structural properties with the particle size should also be studied. In order to do so, the powders obtained after milling have been sieved into different size ranges and then analyzed separately. In particular, the MCE has been estimated for each size

range to analyze the possible influence of the particle size on the final functionality of the material. The analysis has been performed in the particles obtained from soft hand-crushing and from 15 minutes ball-milling, the less and most severe milling treatments carried out in this chapter, respectively. The characteristics of the particles within the same size range but coming from each mechanical treatment has been also comparatively analyzed in the search of a quantative relationship between magneto-structural properties and particle size.

4.2.2.1 Soft milling

The analysis of the MT and the magnetic properties as a function of particle size was first performed on the M0 sample obtained after hand-crushing, which, as shown in the previous section (and as expected) showed the lowest degree of deformation among the studied milled samples. The as-grinded powders were sieved into three different particle size intervals: large particles (100μm < φ < 400μm), medium particles (63μm < φ < 100μm) and small particles (φ < 63μm), denoted hereafter as $M0_L$, $M0_M$ and $M0_S$ samples, respectively. Figure 4.6 show the DSC thermograms obtained on the three as-grinded samples on heating from RT up to 450K (Figure 4.6a) and on subsequent cooling-heating between up to 450K and 250K (Figure 4.6b). It is worth noting the striking resemblance of these thermograms to those in Figure 3.8, some of which corresponding to samples subjected to ball milling for different milling times. With respect to the first RMT, the austenite start temperature A_S highly increases with the decrease of particle size while both the peak high and the burst-like jerky behavior clearly diminish, just as it occurred with the increase of milling time. Likewise, the area below the peaks at the MT taking place after destabilization (Figure 4.6b) clearly decreases on decreasing the particle size, again in accordance with the behavior observed on increasing the milling time.

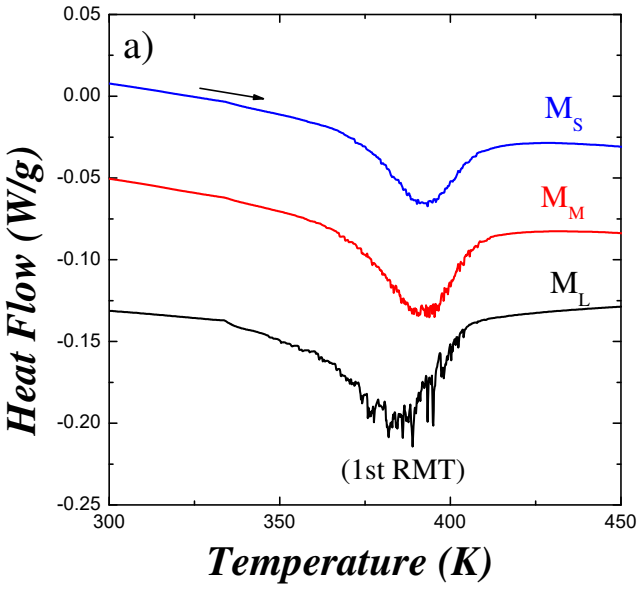

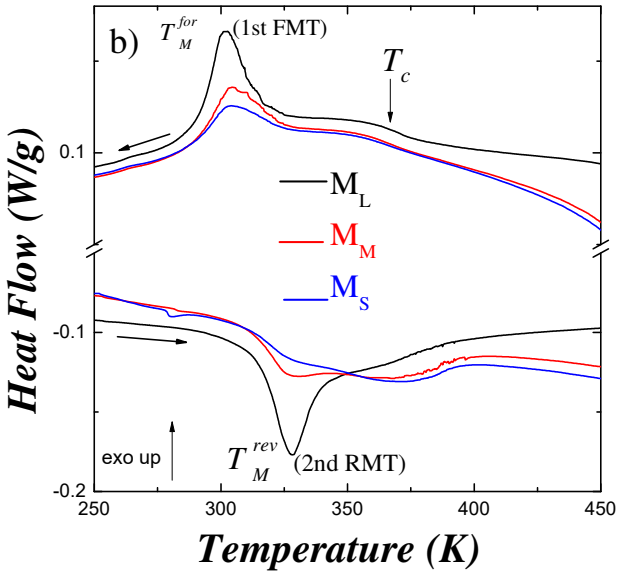

Fig.4.6. DCS thermogram for $M0_L$, $M0_M$ and $M0_S$ samples a) on heating the as-grinded samples, b) on subsequent cooling-heating cycle after destabilization.

Moreover, it can be also seen that the DSC peaks linked to the second RMT becomes lower than the respective peaks at the first FMT as the particle size is reduced (for instance, the 2nd RMT is hardly detectable in the $M0_S$ sample, while the 1st FMT is clearly distinguished) which, a is explained above, would be in agreement with a higher frictional contribution to ΔS in the smaller particles. The similar degradation of the MT with decreasing particle size and increasing milling time seems to point out that the degree of mechanically-induced deformation could be intrinsically linked to the particle size, and therefore, the behavior observed in the milled samples in the previous section would just reflect the different particle-size distribution obtained after each milling time.

The transformation temperatures and the enthalpy change values at the first FMT are shown in table 4.1. The decrease in the enthalpy change linked to the particle size distribution evidences a decrease of the volume of the fraction undergoing the MT. By comparing the enthalpy change at the MT with that in the bulk alloy, where a 100% transforming fraction is assumed ($\Delta H_{bulk}^{1FMT} = 7.7 J/g$), the estimated corresponding transforming fractions are 83%, 55% and 42% for $M0_L$, $M0_M$ and $M0_S$ samples, respectively. If we compare these values with those obtained from respective DSC measurements in both the MM_{HC} (previous chapter) and the unsieved M0 (previous section) samples, that is 90% and 35% respectively, it might be concluded that the

MM_{HC} powders are mainly composed of large particles whereas the unsieved M0 is, in turn, composed of very small particles.

Sample	T_M (K)	ΔH (J/g)	T_C (K)	M_{60kOe} (AMM/kg)	
	1st FMT	1st FMT		10K (mart)	343 K (aust)
M_L	301	6.4	373	10.7	61.7
M_M	304	4.3	373	10.5	40.8
M_S	305	3.3	373	11.6	31.7

Table 4.1. MT temperature (peak maximum), enthalpy changes at the 1st FMT, Curie temperature and magnetization values under 60kOe (both in austenite and in martensite) after retransformation.

In order to elucidate the origin of the degradation of the MT on reducing the particle size, X-ray diffraction measurements were performed on the sieved powders. Figure 4.7 shows the diffractograms obtained at 400K (after destabilization) on the three samples. From the mere analysis of the peaks positions, the same cubic $L2_1$ structure with almost the same lattice parameter is obtained in all cases, alongside with a small quantity of additional martensitic phase. As shown in table 4.2, the fraction of austenite in the sample, estimated from integrated intensity of the corresponding peaks in the diffractograms, decreases with the decrease on the particle size in a similar way as it occurred on increasing the milling time (see table 3.4). In particular, it is worth noting the austenite volume fraction in the $M0_L$ sample is around 90%, almost the same as in the MM_{HC} sample. From our previous hypothesis, this would again indicate that the MM_{HC} sample mainly consist of large particles (above 100 μm), as indeed concluded from DSC measurement. Nevertheless, the considerable discrepancy between the transforming fractions estimated from DSC (83%, 55% and 42%) and from XRD (90%, 82% and 77%) measurements, indicates that the degradation of the MT (that is, the decrease of the enthalpy change) cannot be exclusively ascribed to the presence of martensite above A_f. The lack of any other structural phase in the diffractograms and the fact that the discrepancy becomes higher as the particle size decreases suggest the presence of highly-deformed amorphous-like regions linked to the microstructural defects induced in the powders, just as it occurred in the previous chapter.

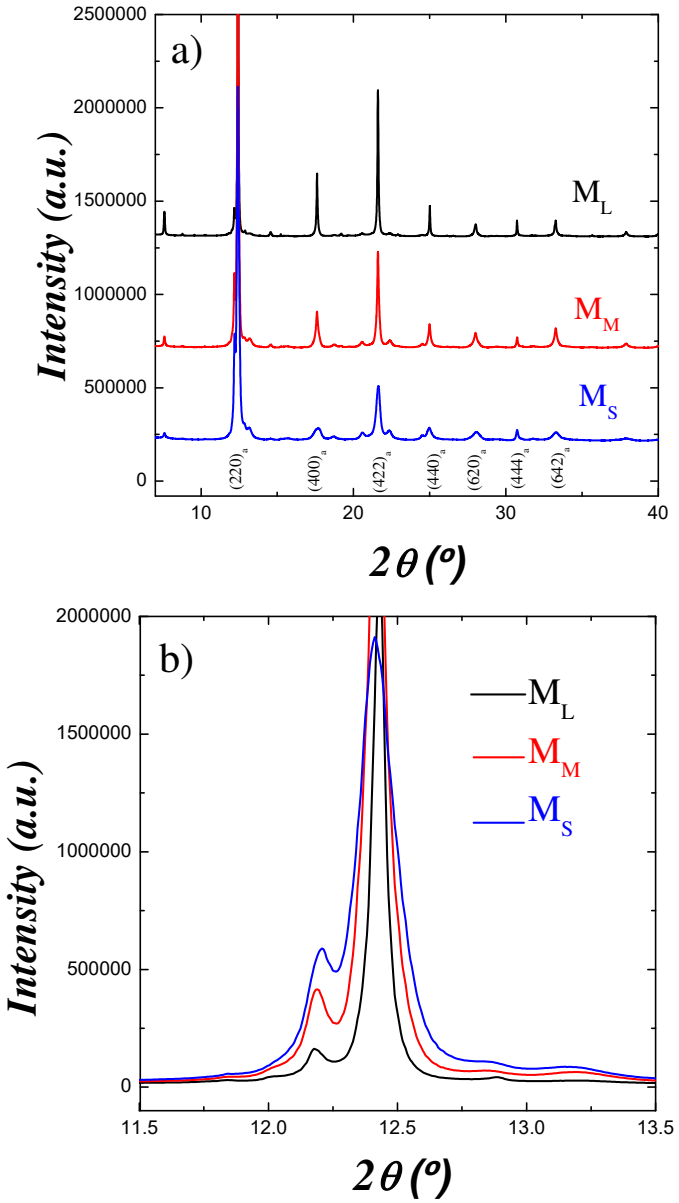

Fig. 4.7. a) X-ray diffraction measurements at RT in the as-milled powders for M_L, M_M and M_S particles, b) Detail of the low angle region.

The increasing amount of such defects on reducing the particle size would be behind both the decrease in the intensity and the broadening of the reflection peaks observed in the diffractograms (highlighted in Figure 4.7b). As a way of quantifying the impact of milling on the microstructure, the internal strains and the crystallite size in the three samples have been determined from the Lebail fit of the diffractograms. The obtained values are shown in table 4.2 and plotted in figure 4.8 as a function of the average particle size (estimated from optical

microscopy). The internal strains are much larger for smaller particles, thus reflecting a higher milling-induced plastic deformation in these powders than in the larger particles. Accordingly, the crystallite size decreases with the decreasing particle size.

Sample	Average particle size (μm)	Austenite ($L2_1$) (%)	Microstrains (‰)	Crystallite size (Å)
M_L	430 ± 80	90	3.6	170
M_M	80 ± 10	82	22.4	140
M_S	30 ± 10	77	23.1	130

Table 4.2. Particle size (estimated from optical microscopy), lattice parameters, internal strains and coherent diffracting size (determined from the Scherrer formula) for the M_L, M_M and M_S samples.

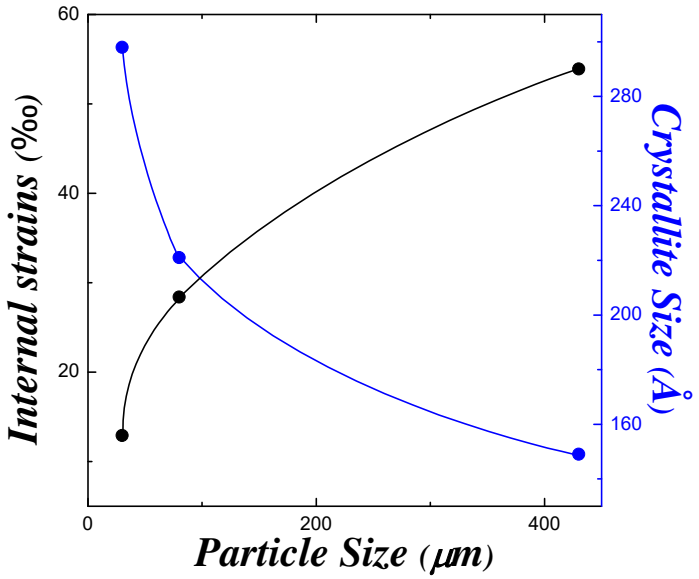

Fig. 4.8. Internal strains and crystallite size as a function of particle size.

The presence of paramagnetic martensite above A_f and the large internal strains in the powders should affect the magnetic properties of the particles. In order to analyze an eventual relationship between magnetism and particle size, high-field magnetization measurements have been performed in the three samples. The *M(H)* curves are obtained in the martensite state (10K) and in the austenite state (343K) are shown in figure 4.9. The high-field magnetization highly varies in austenite with the particle size, whereas almost no variation is observed in martensite. The obtained magnetization values are shown in table 4.1. Bearing in mind the low saturation magnetization of the weakly magnetic martensite phase, both the absence of variation

in martensite and the large magnetization decrease in austenite can be partly explained as a consequence of presence of non-transforming martensite, whose saturation magnetization is expected to be similar to that in the transforming martensite. However, it can be seen that the magnetization at 343K in the $M0_S$ sample is around half that in the $M0_L$, which does not agree with the respective fractions of austenite at this temperature (see table 4.2). Therefore, it can be inferred that the saturation magnetization of the above mentioned amorphous-like regions also present at the particles, must be similar to that of the martensitic phase.

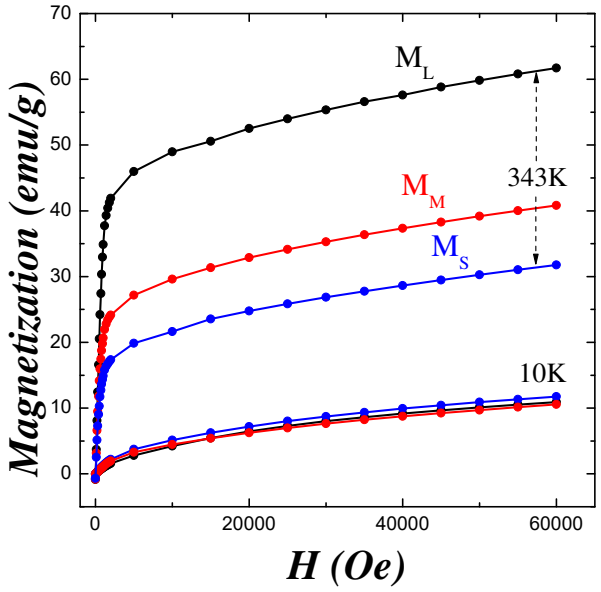

Fig. 4.9. Magnetization *M(H)* curves for as-crushed samples at 10K and 343K.

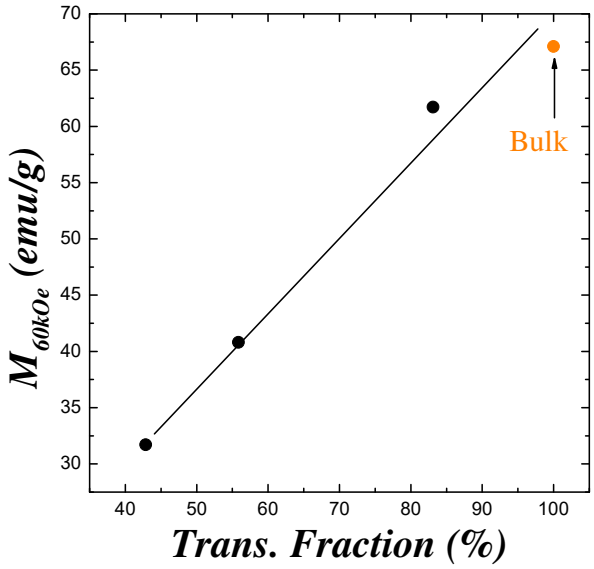

Fig. 4.10. Correlation between the high-field magnetization and the fraction of material undergoing MT.

The relationship between the degradation of the MT and the magnetic properties becomes evident if we plot the high-field magnetization as a function of the transforming fraction estimated from DSC measurements, as shown in figure 4.10. In effect, an almost perfect linear dependence is observed, which seem to confirm the proposed direct correlation between particle size and degree of deformation in the milled powders.

- Magnetocaloric effect

The final objective of this work is the production of composites with good enough MCE to be used in heat exchangers for magnetic refrigeration. In order to analyze the influence of the grinding induced deformation on the functional properties of the alloy, the magnetocaloric effect has been evaluated on the three powder samples. The MCE, which can be defined as the isothermal entropy change, ΔS_{iso}, caused by the application of a magnetic field, H, has been calculated from a set of zero-filed-cooled thermo-magnetization curves $M(T)$ (measured on heating under different magnetic fields, ranging from 100Oe to 60kOe), following the expression:

$$\Delta S_{iso} = S(T,H) - S(T,O) = \int_0^H \left(\frac{\partial M}{\partial T}\right)_H dH \qquad 4.6$$

Figure 4.11shows the magnetically-induced isothermal entropy change as a function of both temperature and applied magnetic field. An inverse MCE ($\Delta S_{iso} > 0$) is observed associated to the MT, together with a direct MCE at high temperatures linked to second order magnetic transition (in all cases the maximum values are obtained under the highest magnetic field). A significant decrease of the MCE is observed with the decrease of the particle size, as expected from the corresponding decrease in the fraction of transforming martensite.

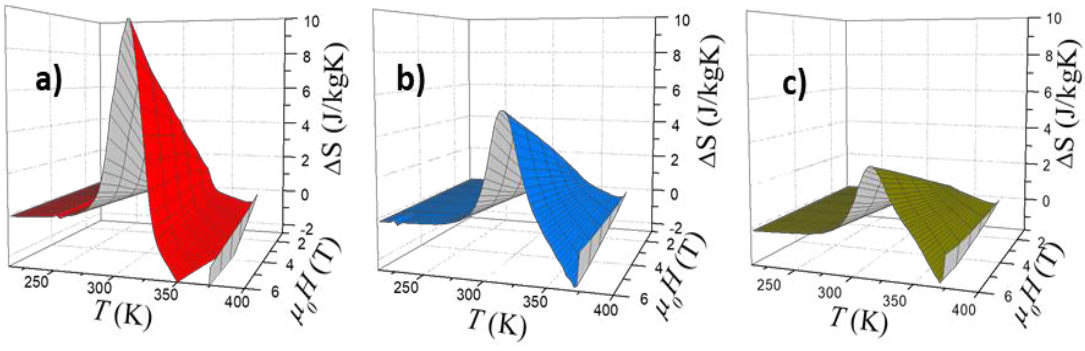

Fig. 4.11. Isothermal magnetically-induced entropy change as a function of temperature and applied magnetic field for the three powdered samples (a) $M0_L$, (b) $M0_M$ and (c) $M0_S$.

The maximum MCE obtained in both the bulk and the powder samples are compared in figure 4.12 as a function of temperature. In the bulk sample, ΔS_{iso} reaches a high value of 20J/kgK at the MT temperature, which is close to the highest values reported in Ni-Mn-In-Co alloys. The MCE values in the grinded samples, in turn, are much lower, being the maximum ΔS_{iso} in the $M0_L$ sample, almost half that in the bulk. However, it is worth noting that the MCE peaks around the MT get broader as the particle size decrease, presumably due to the broadening of the MT temperature range as a consequence of the reduction of the particle size and the associated increase in the internal strain [292]. Hence, even though the MCE values are considerably lower than in the bulk, the broad temperature range is covered by the MT in the milled samples results in a broad associated entropy peak (ΔT).

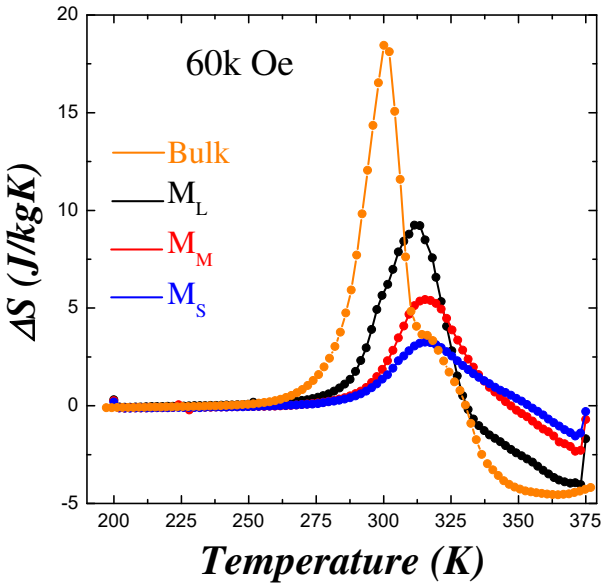

Fig. 4.12. Magnetically-induced entropy change at 60kOe as a function of temperature for the bulk alloy and the micro-particles.

Such a defects-induced broadening gives rise to a quite large relative cooling power, RCP, which is the main performance metric to rank magnetocaloric materials as long as it represents the maximum amount of the thermal energy that can be transferred between cold (T_{cold}) and hot (T_{hot}) sources in a thermodynamic cycle [349]. The RCP can be estimated by:

$$RCP = \int_{T_{cold}}^{T_{hot}} \Delta S_{iso}(T) dT \qquad 4.7$$

where, T_{cold} and T_{hot} define the temperature application range and are evaluated from the lower and higher temperatures defined by the Full Width at Half Maxima (T_{FWHM}) of the $\Delta S_{iso}(T)$ peak. The calculated RCP values are shown in table 4.3. For instance, the RCP value for $M0_L$ sample is

quite large, indeed comparable to that in the bulk. In this sense, the grinding-induced micro-particles can be considered as good preliminary candidates for magnetic refrigeration applications at the micro-scale. In any case, as will be exposed later, it should be recalled that these obtained maximum MCE values are expected to be considerably improved after annealing treatments.

Samples	RCP (J/kg)
Bulk	288
M_L	240
M_M	145
M_S	102

Table 4.3. Relative Cooling Power for the different samples.

4.2.2.2 Hard milling

The martensitic transformation and the magnetic properties of the micro-particles have been also analyzed as a function of the particle size in the powders obtained after 15 minutes ball milling, that is, in particles subjected to a more severe milling than the hand-crushed powders. In fact, from results in section 4.2.1, a much higher degree of plastic deformation is indeed expected in the M15 particles. The as-milled powders were this time sieved into four different particle size intervals: small particles: ($\varphi < 63\mu m$), medium particles: ($63\mu m < \varphi < 100\mu m$), large particles: ($100\mu m < \varphi < 400\mu m$) and very large particles: ($\varphi > 400\mu m$), denoted hereafter as $M15_S$, $M15_M$, $M15_L$ and $M15_{XL}$, respectively. The new fourth size interval was included to discern the contribution of the largest particles, which would be regarded as almost bulk samples. The DSC thermograms (on cooling-heating after destabilization) and *M(H)* curves obtained on the different size ranges are shown in figure 4.13. The peak high and therefore the enthalpy change at the MT, decreases with the reduction of particle size, just as it occurred in M0 sample (see figure 4.6). The transforming fractions are estimated again from the comparison with the enthalpy change in the bulk alloy are 84%, 56% and 46% and 35% for $M15_{XL}$, $M15_L$, $M15_M$ and $M15_S$ samples, respectively. It is worth noting that in the case of "S" and "M" particles, whose size range is narrower and the same for both M0 and M15 samples, the transforming fraction is quite similar in both samples, in spite of the very different milling treatment. From the observed decrease of the enthalpy change at the MT on reducing the particle size, the very small DSC peak observed on the unsieved M15 sample (see figure 4.1)

would confirm that this sample mainly consist of very small particles, most of which below 63µm.

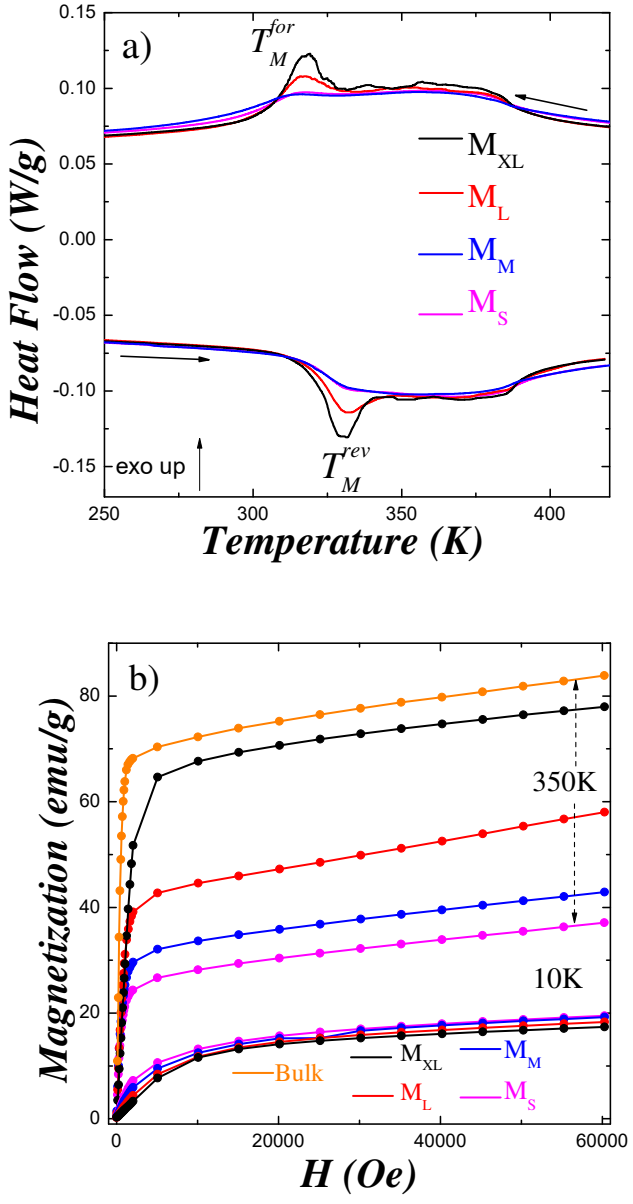

Fig. 4.13. a) DSC thermograms , b) magnetic-field dependence of magnetization for the powders with different particle size, obtained from the 15 minutes milled sample.

On the other hand, the evolution of magnetization with the particle size shown in figure 4.13b is also similar to that in the M0 powders, the values for the "S" and "M" particles being almost the same both in the hand-crushed and in the M15 samples (see figure 4.9). Again the observed decrease of the high-field magnetization in austenite and the lack of evolution in martensite are

compatible with the increasing amount of both non-transforming martensite and highly-deformed amorphous-like regions.

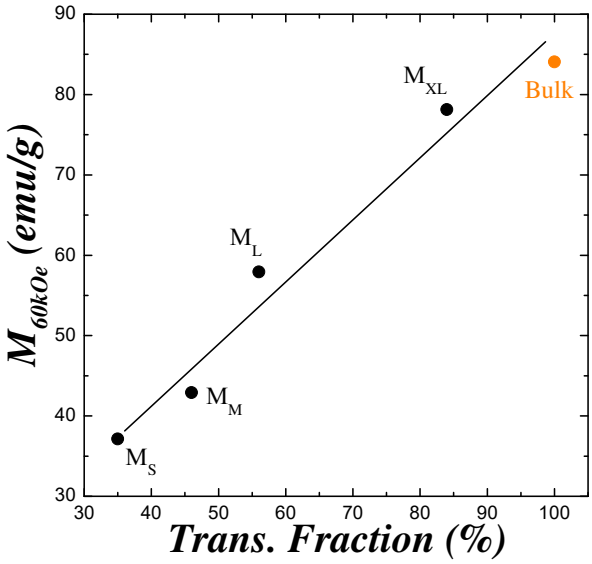

Fig. 4.14. Magnetization at 60kOe in austenite as a function of the transforming fraction for the powders with different particle size (obtained from the 15 minutes milled sample).

4.2.2.3 Same particle size from different milling time

The parallel evolution of the MT characteristics and the magnetic properties on varying the particle size and in particular the similar ΔH and magnetization values obtained for each size range (irrespectively of the milling time), point to a close relationship between milling-induced deformation and particle size. The particle size seems to be then the most accurate parameter to assess the impact of milling, as long as the average behavior of the unsieved as-milled powders appears as just a mere consequence of different size distributions achieved after each milling time. This point has been analyzed from the comparison between the magneto-structural properties of the "M" particles (63µm < φ < 100µm) coming from the soft hand-crushing and from the more severe 15 minutes ball milling. Apart from being the narrowest studied size range (hence with the lowest intrinsic particle size dispersion), this is the most suitable range for the production of printable 3D composites since (a) particles are compatible with the standard printer nozzles, (b) particles above 100µm are presumably too large to generate homogeneous and ductile enough printable wires, and (c) particles below 63µm exhibit weak magnetic response, which may compromise the functionality of the material. Figure 4.15 shows the DSC thermograms (on cooling-heating after destabilization) and the *M(H)* curves at 350K obtained in

the $M0_M$ and the $M15_M$ samples, alongside with the measurement corresponding to the bulk sample. It can be seen that, in effect, the enthalpy change at the MT and the austenite magnetization are almost same in both the samples in spite of very different milling intensity, thus confirming the proposed closed correlation between particle size and milling-induced plastic deformation.

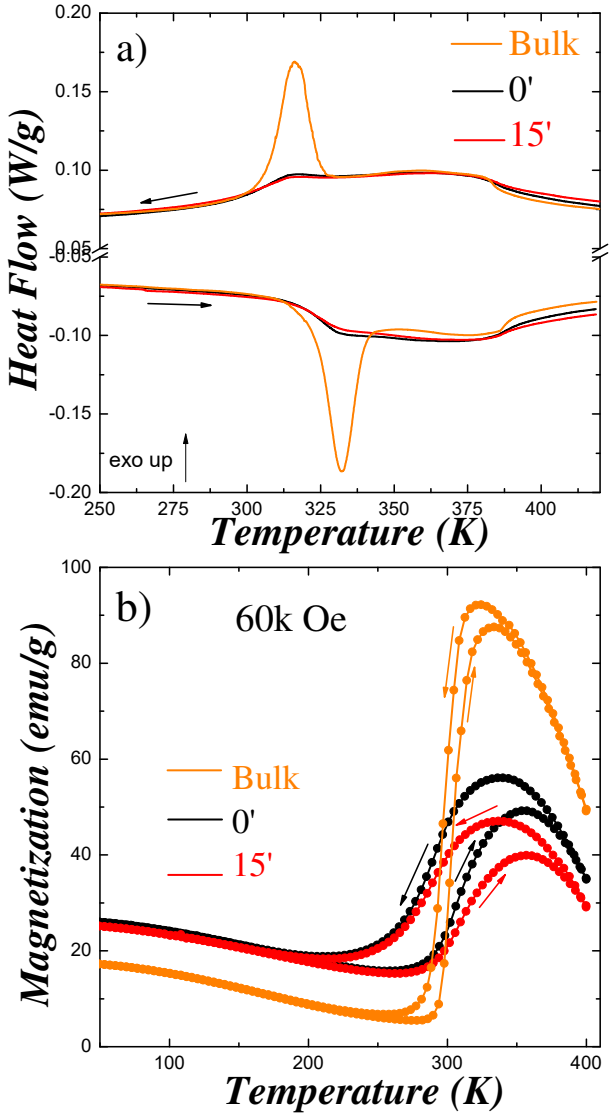

Fig. 4.15. a) DSC thermograms, and b) magnetic-field dependence of magnetization for the $M0_M$ and $M15_M$ powders.

Since the analyzed size interval ranges from 63µm to 100µm, the slight differences observed in the curves for the $M0_M$ and $M15_M$ powders could be attributable to a small difference in the distribution of the sizes inside the respective samples. This fact has been checked from Scanning Electron Microscopy (SEM) observations. The obtained micrographs and the particle size histograms calculated from it, are shown in figure 4.16. The obtained histograms indeed reveal a

slight variation in the size distribution between both samples. In particular, the $M0_M$ sample consists of larger particles in average than the $M15_M$ samples, which contains more particles below 80µm. Such a small difference in the size distribution, in turn, result in small differences on the amount of non-transforming martensite and the internal strains present in each sample, as revealed by XRD measurements performed in both samples.

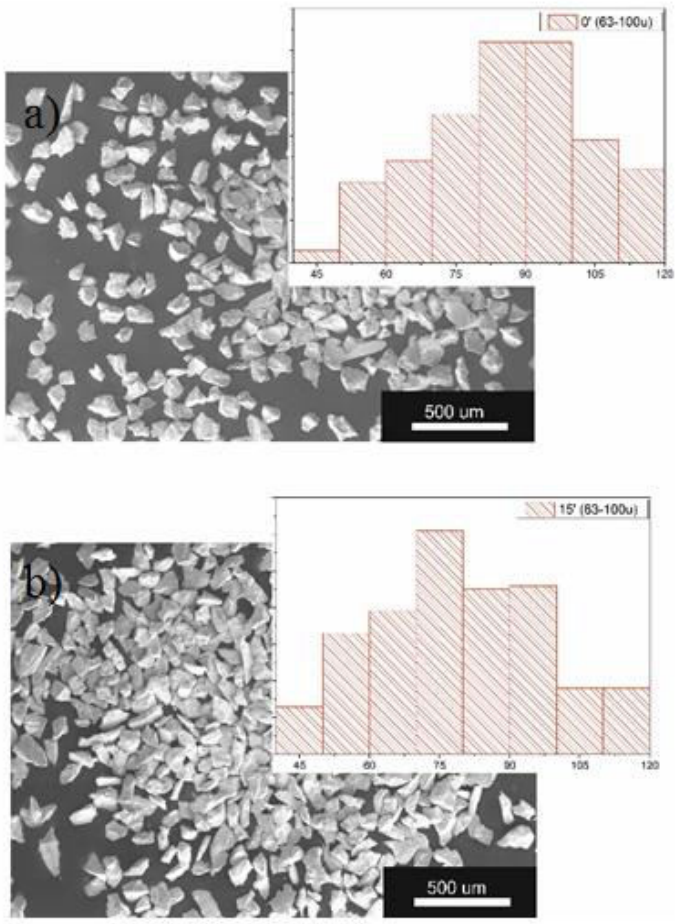

Fig. 4.16. SEM micrographs and particle-size histograms on the $M0_M$ and $M15_M$ powders.

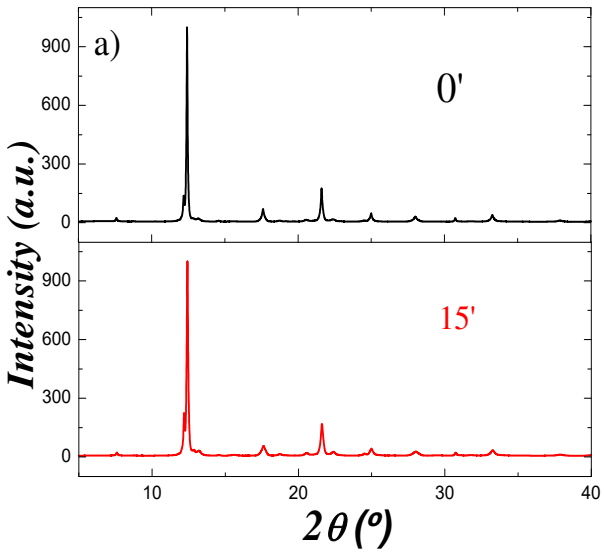

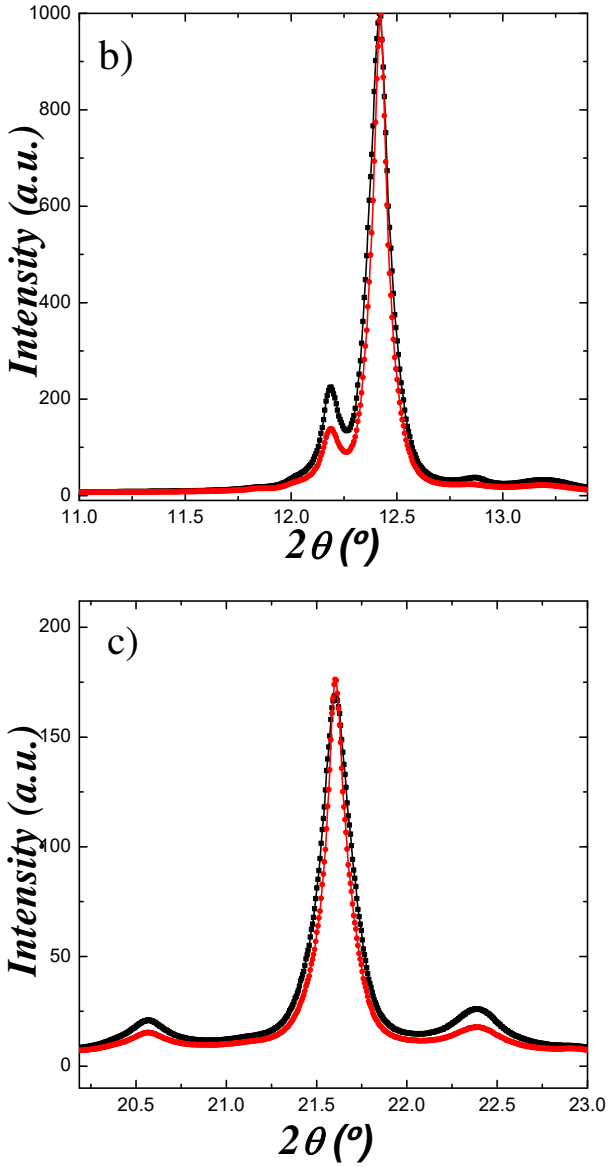

Fig. 4.17. X-ray diffractogram at 400K (black dots), calculated (red line), and the difference between experimental and calculated diffractogram (blue line) for the 0´, 15´; the green marks indicate the Bragg reflections.

Figure 4.17 shows the XR diffractograms obtained at 400K, which confirm the predominance of the austenite cubic $L2_1$ structure together with the presence of a small amount of martensitic phase. As shown in figure 4.17b, the intensity of the reflection peaks linked to the retained martensite is slightly higher in the $M15_M$ sample than in the $M0_M$ sample. Likewise, the austenite peak is slightly broader in the $M15_M$ sample (see figure 4.17c), which is compatible with a higher value of internal strains. So, all the analyzed measurement is in line with an intimate relationship between particle size and degree of milling-induced deformation, which is fulfilled regardless of the milling duration. This means that particles of the same size must exhibit the same magneto-

structural features irrespectively of the milling time. Even though a more detailed work (for which more and narrower particle sizes should be analyzed) is obviously required to establish a quantitative correlation between the particle size and the magneto-structural properties of the powders obtained after milling. The present finding is particularly intriguing from an applied point of view, since it implies that specific MT and magnetization properties may be attained by selecting particles with particular sizes, regardless of the milling process (hand crushing or ball milling), milling duration or even milling equipment.

- Microstructure recovery

As widely reported in the literature, the MT characteristics and the magnetic properties of the as-milled MSMA particles may be significantly enhanced after high temperature annealing treatments leading to microstructural recovery [83, 296, 343, 345, 346]. In order to explore this point, the particles between 63µm and 100µm were subjected to a 150 minutes annealing treatments at 873K. Such a relatively low temperature was chosen for the first attempt to avoid the risk of oxidation.

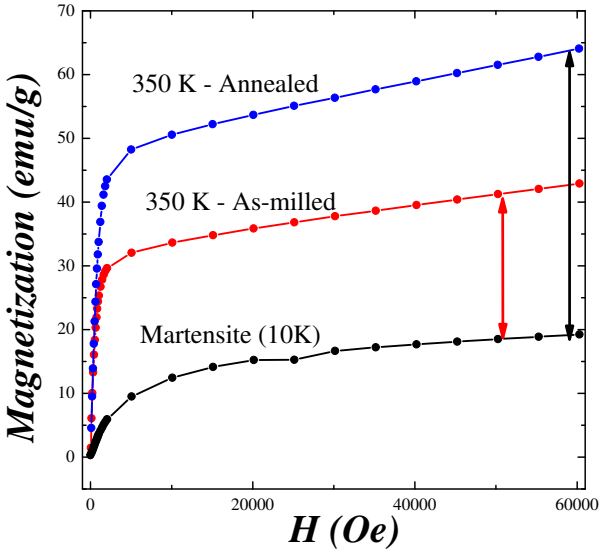

Fig. 4.18. Magnetic-field dependence of magnetization of the particles lying on the 63µm < φ < 100µm range, after annealing.

Figure 4.18 shows the comparison between the high-field magnetization at 350K in the as-milled samples and after annealing. It can be seen that the magnetization at 60KOe, M_{60kOe}, experiences a rise around 50% while the magnetization in martensite remains almost unaffected, which results in a ΔM in the annealed sample twice that in the as-milled state. Therefore, a considerable improvement in the MCE should be expected after annealing.

Finally, the MCE has also been assessed in the annealed powders. Figure 4.19 displays the isothermal entropy change as a function of both temperature and applied magnetic field. A maximum $\Delta S_{iso} \approx 8$J/kgK for the annealed powders in 63 < μm < 100 size range has been obtained under a 60kOe magnetic field. This entropy change is considerably higher than that obtained in as-milled powders with the same particle size ($\Delta S_{iso}^{as-mill} \approx 5.5$J/kgK, see figure 4.12). A direct second order MCE ($\Delta S_{iso} < 0$) linked to the Curie temperature can also be observed. Due to the large ΔS_{iso} and the relatively wide MT temperature range, the calculated RCP = 300J/kg is similar to that found in the bulk alloy. Therefore, it can be concluded that selecting the particle size after milling (independently of the milling time) and performing subsequent annealing treatments seem to be an efficient procedure to get controlled powders, suitable for the production of composites for magnetic refrigeration.

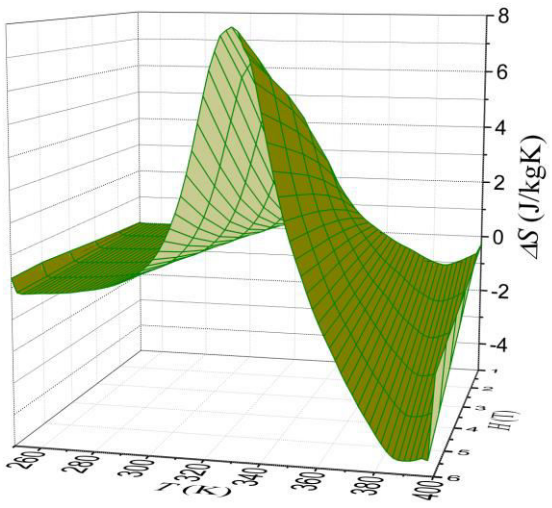

Fig. 4.19. Isothermal magnetically-induced entropy change as a function of temperature and applied magnetic field for the particles between 63μm and 100μm after annealing.

4.3 Conclusions

- The milling strongly affects the MT characteristics: increasing the milling time implies a deterioration of the MT and a large reduction in austenite magnetization caused by an increase in the amount of severely deformed non-transforming martensite.
- The magnetic properties of martensite are barely affected by deformation.

- The frictional entropy term related to the martensitic transformation and consequently the number of intrinsic defects increase with the milling time. The correlation between internal strain/stresses and microstructure has been evaluated.
- Particles with the same size exhibit the same transformation enthalpy and magnetization regardless of the milling time, demonstrating a clear relationship between particle size and deformation intensity. From an applied point of view, regardless of the ball milling process (hand crushing, ball milling equipment, milling duration etc.) precise MT and magnetization properties may be attained selecting particular particle sizes.
- Selecting the particle size after milling and performing low temperature annealing treatments is an efficient procedure to get controlled powders with properties comparable to that of bulk.
- The particles show similar RCP values than the bulk and seem to be suitable for the production of composites for magnetic refrigeration.

Chapter 5

Production of 3D printable MSMA-polymeric composites

5.1 Introduction

This chapter presents a preliminary study on the fabrication routes for 3D printable magnetic composites for magnetic refrigeration applications. In the seek for materials exhibiting both good printability and high magnetocaloric response, different composite materials have been elaborated from the inclusion of selected Ni-Mn-In-Co micro-particles on different printable polymers. In particular, PCL, PLA and PCL-PLA polymer blends has been explored as polymeric matrix. From the analysis of the effect of the micro-particles on the thermal stability and the processability of the composite, the most suitable polymers combination and the particle concentration optimizing the functionality of the composite have been estimated. A promising printable composite with filler loading as high as 80% (weight) in a pure PCL matrix has been successfully produced, from which a honeycomb 3D piece has been printed as a proof-of-concept for a heat-exchanger.

5.1.1 Motivation and objectives

For any magnetic-refrigeration application, the design of well-controlled geometries of heat exchangers is crucial to obtain a good performance and efficiency in the heat transference between the active material and the surroundings [350, 351]. Unfortunately, in the case of MSMA, the poor mechanical properties of the MMSMA bulk alloys make very difficult the machining of pieces with complex geometries from the bulk. In order to overcome this problem, powdered MSMA micro-particles can be inserted in polymeric matrices, in such a way that the polymer gives structural integrity and formability while the particles provide magneto-thermal functionality. Moreover, if the polymers are printable thermoplastics, the composite material could be used to feed a standard FDM 3D printer, whose relatively low extruding temperatures avoid the possible deterioration of the physical properties of the particles (contrary to what

occurs in Selective Laser or Electron Beam Melting techniques used for direct 3D printing of metallic materials).

Polymers have the advantage of good processability, but their inherent low thermal conduction becomes a challenging problem, as long as thermal management is critical to the performance, lifetime, and reliability of magnetocaloric devices. The thermal conductivity of the polymer is particularly important at low filler loadings, since the polymer matrix acts as a thermal barrier between conductive fillers and thus limits the thermal conduction pathway. In this respect, Poly-ξ-caprolactone (PCL) and Poly-lactic acid (PLA) showing low melting point and high ductility close to ambient temperature, are good candidates for the development of high filling-factor composites for MCE applications [352, 353]. The embedding of large amount of micro-particles in the matrix polymer, in turn, may lead to a worsening of the mechanical properties and the processability that could hinder both the extrusion of filaments and the subsequent printing process.

The aim of this chapter is to obtain a MSMA/polymer composite filament with a high proportion of functional particles, which is able to feed standard and cheap FDM 3D printers. In order to do so, different combinations of PCL and PLA and different concentrations of micro-particles have been tested. First, the thermal properties of both polymers have been analyzed to evaluate the miscibility between them. Then, the composites have been produced by solution phase inversion method, mixing different amounts of Ni-Mn-In-Co micro-particles in the diluted polymers. The thermal and magnetic properties of the elaborated composites have been analyzed from DSC/TGA and SQUID measurements, whereas the microstructure has been evaluated from SEM observations. The composites with the highest particle concentration compatible with and admissible mechanical consistency have been extruded in filaments, whose printability has been also tested. Finally, a 3D piece has been printed as a proof of-of-concept for a heat-exchanger.

5.1.2 Chapter Organization

The experimental results in this chapter are presented in two main parts. The first one is devoted to the synthesis, thermal characterization and optimization of the polymer matrix from mixtures of PLA and PCL. The second part is focused on the elaboration of MSMA/polymer composites from the dispersion of ball-milled Ni-Mn-In-Co micro-particles on the polymer matrix. Several composites with different PCL/PLA fractions and various particle concentrations are studied in order to optimize the particle filling load. Finally, the thermal properties and the good

printability of the best obtained composite, elaborated from the embedding of 80% (weight) particles on pure PCL matrix, are shown at the end of chapter.

5.2 Experimental Results

As explained above, PLA and PCL polymers were tried as polymer matrix because of its expected high filling factor. Furthermore, these two polymers are compatible with most of the standard FDM printers.

5.2.1 Polymer matrix

As mentioned above, the low thermal conductivity of the polymeric matrix is a drawback for magnetic refrigeration. However, the use of a homogeneous distribution of metallic particles in the polymer and the subsequent increase of the effective heat-transference surface could counterbalance the low conductivity of the polymer. Furthermore, the possibility of building-up devices with high surface to volume ratio may counterbalance the low conductivity of the polymer and make 3D-printed composite structures be even more efficient (from the point of view of heat transfer) than a piece of bulk material with standard shape.

5.2.1.1 Heat-transfer simulation

The suitability of the use of PCL and PLA polymers for the development of heat-exchangers has been preliminary analyzed from numeric calculations. In particular, finite-element simulations (collaborative study with Isaac Royo, Department of Mathematics, UPNa) have been performed to compare the heat transfer process of a standard cubic shape piece of pure active material (MSMA) with that of composite wires containing MSMA particles in various concentrations and different types of polymers as matrix. The volume of active material was kept constant for both geometries, so the length of the wire varies depending upon the diameter and the particle concentration. The transfer rate will depend on the length of the wire, type of material, percentage of particles and quality of cooling/heat transfer to the medium. The simulations describe a situation in which the active material has an initial temperature different from that of the polymer matrix and the environment and calculates the dynamics of the thermal energy transference towards or from the surroundings. As an example, figure 5.1 shows the normalized heat transference as a function of time for a composite wire with PCL matrix and 50% volume fraction of functional particles and for the bulk MSMA piece. The results evidence that wires with MMSMA micro-particles in the PCL matrix transfer more energy per second (higher slope) than the bulk. Consequently, the simulations support the idea that geometries with high specific surface, obtained by 3D printing methods from printable polymer composites can be

more efficient than a standard metallic piece in terms of heat transference, despite the low thermal conductivity of the polymer matrix. These results encourage the fabrication of printable functional composites for magnetocaloric applications.

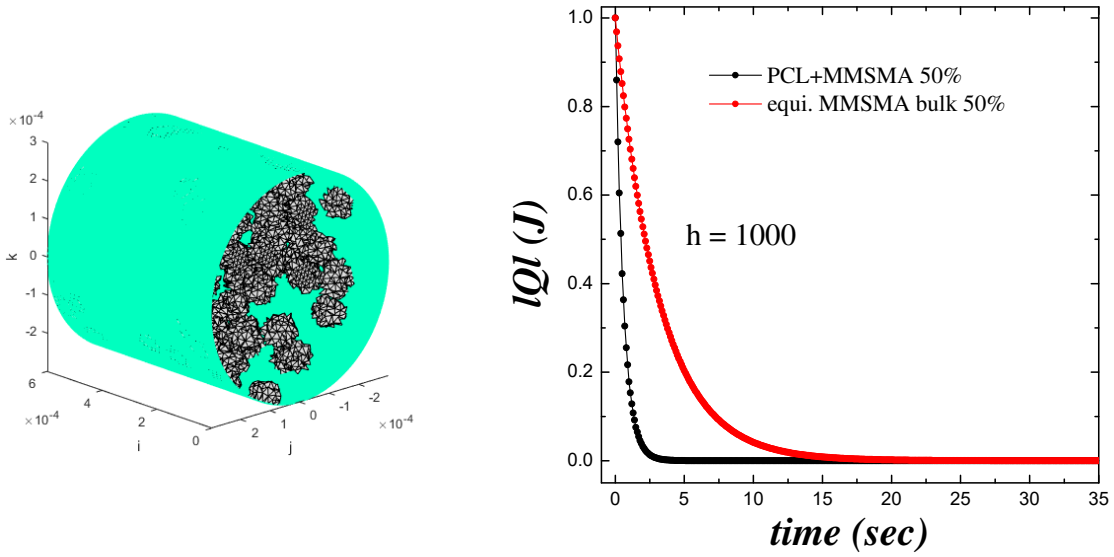

Fig. 5.1. Left) Wire geometry (50% in volume of particles), right) Heat transfer as a function of time for $Ni_{45}Co_5Mn_{36.7}In_{13.3}$ bulk (red line) and equivalent volume of particles embedded in PCL matrix (black line). Simulation condition: 0.6mm wire diameter, 50% volume particle, perfect refrigeration, environment = 20°C and initial temperature = 15°C.

5.2.1.2 Thermal analysis of PCL/PLA polymers

As explain in Chapter 1, the operating range of the polymer is limited by the melting temperature, above which the material loses its mechanical consistency. In order to determine the phase transformation taking place in the polymers to be used, DSC measurements have been analyzed in raw PLA and PCL polymers. Figure 5.2 shows the corresponding thermograms obtained on heating and cooling at the rate of 10K/min. In the case of PCL (figure 5.2a), the endothermic peak around 338K (ΔH^{PCL}_m= 68J/g) corresponds to the transformation from solid to liquid (viscous) phase associated to the melting point of PCL. The exothermic peak around 291K during cooling, is linked to the the crystallization of the polymer (ΔH^{PCL}_c= 51J/g). It is worth noting that intensity of the melting peak is quite lower on the second heating run, whereas the calculated melting enthalpy is (ΔH^{PCL}_m= 48J/g), very close to crystallization enthalpy on cooling.

The phase transformations in PLA are shown in figure 5.2b. The inflection in the baseline observed around 330K must correspond to the occurrence of the glass transition in the polymer, which indicates that some fraction of polymer was initially in amorphous state. The endothermic peak observed on further heating (around 440K) corresponds to the melting of the polymer (ΔH^{PLA}_{m}= 39J/g). Contrary to PCL, PLA does not show any crystallization process on cooling. When the cooling process is rapid enough to skip the crystallization process, the molecules arrange randomly giving rise to an amorphous state. However, an exothermic peak is indeed observed around 376K on the second heating run, linked to the cold crystallization of PLA. The cold crystallization (ΔH^{PLA}_{m}= 39J/g) occurs during heating above the glass transition as soon as the molecules gain mobility to rearrange in an ordered manner.

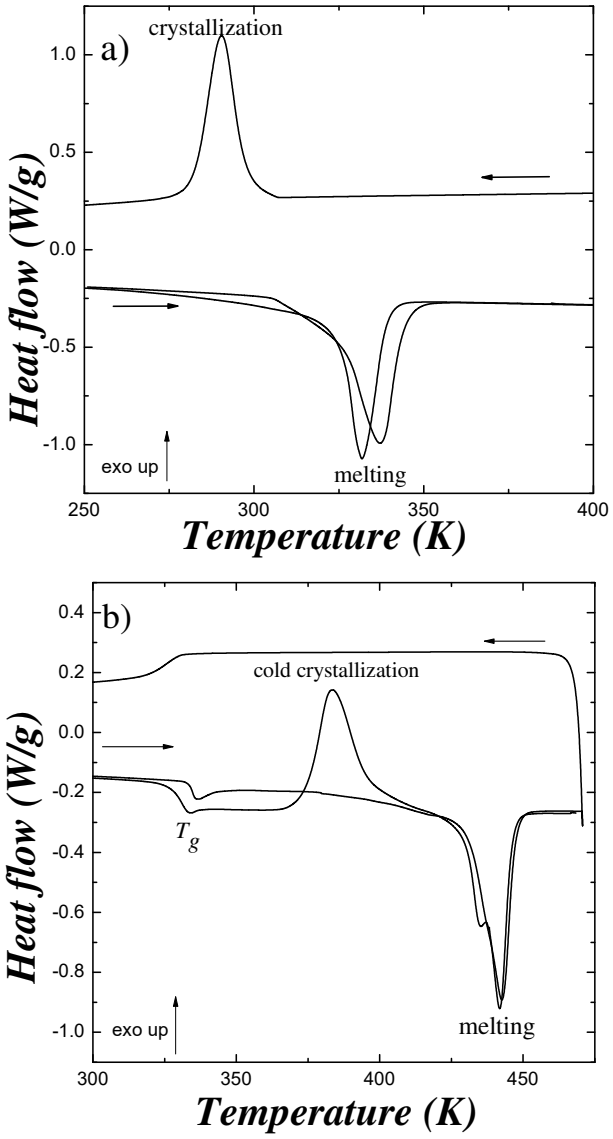

Fig. 5.2. DSC thermograms during heating and cooling ramps for a) PCL and b) PLA raw polymers.

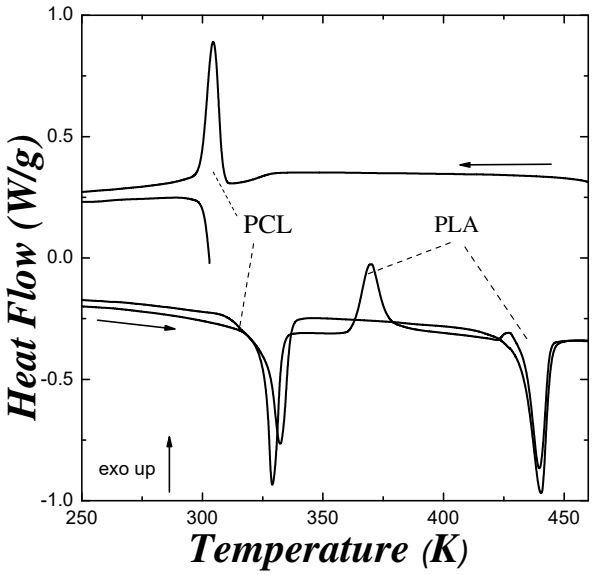

Fig. 5.3. DSC thermograms for a 50-50 (wt%) mixture of PCL and PLA.

Different mixtures of PLA and PCL have been used to carry out the fabrication of MSMA/polymer-composites. To evaluate the eventual interaction between the different polymers, the effect of presence of one polymer on the phase transformations taking place in the other one, has been analyzed from DSC measurements. As an example, figure 5.3 shows the thermograms obtained on a 50-50 (wt%) mixture of PCL and PLA. It can be seen that the melting and crystallization peak temperatures for both polymers remain unaffected, which suggests no interaction between the polymers. The same lack of interaction has been observed in all the analyzed mixtures, regardless of the polymer concentrations.

5.2.2 MSMA/polymer composites

Different composites have been elaborated from the dispersion of the ball-milled micro-particles analyzed in the previous chapters onto polymer matrices. On the seek for composites with high amounts of magnetically-active particles, the mechanical consistency, understood as the capacity of the material to be extruded in coiled wires, has been the primary criterion on the composite selection. The nomenclature of the elaborated composites has been set by keeping the concentration (in wt%) of PLA and PCL as a subscript, i.e. $P_{10\text{-}90}$ means a 10wt% of PLA and 90wt% PCL (the first number corresponding to PLA and the second to the PCL), and the particle concentration as a superscript.

5.2.2.1 Synthesis of the composite material

The production of the composites has been carried out by solution phase inversion method, which is frequently utilized to create porous polymeric structures [354–356]. This process involves transforming a liquid into a solid phase, upon exposure to the change in temperature and/or by inclusion of a solvent in which the polymers are insoluble, to aid their precipitation. This process is known as the non-solvent induced phase separation (NIPS) [357]. In this framework, Hexane is used a non-solvent that is directly combined with the stirring polymer solution.

The initial polymer mixture is obtained by first taking the PCL and PLA in raw forms as shown in figure 5.4 and combining one part (in mass) of the polymer mix with three parts of the dichloromethane (DCM).

Fig. 5.4. Raw polymers PCL, PLA, and c) mixing of PLA, PCL and DCM with magnetic stirrer.

The mixture is continuously stirred at room temperature (RT) until a viscous and translucent homogeneous liquid is obtained (figure 5.5).

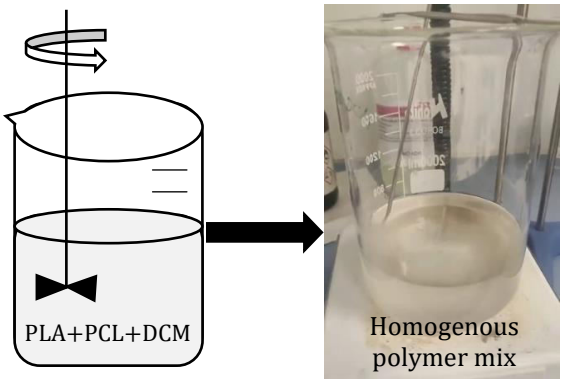

Fig. 5.5. Viscous translucent homogeneous polymer mix.

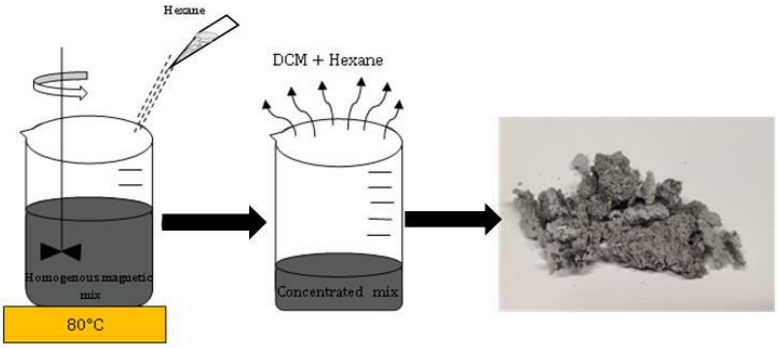

Fig. 5.6. Addition of MMSMA powders to the homogeneous polymer mix.

The micro-particles are then added to the mixture and stirring, and the temperature is elevated up to 313K (figure 5.6). At this point, the magnetic stirrer is replaced by a mechanical one to avoid magnetic agglomeration. After two hours of continuous stirring, a homogenous polymer-composite dark solution is achieved (the required time depends upon the quantity of the total solution, higher quantity might need longer time to obtain homogeneity).

In order to induce the solid-liquid phase separation, Hexane is incorporated to the dark solution (three times the total weight of the solution) and the temperature is again increased up to 353K (figure 5.7). DCM evaporates which increases the Hexane/DCM ratio and helps the precipitation process. This way, the precipitation of the composite occurs producing foam of polymeric matrix with homogeneously distributed micro-particles inside. The apparent porosity of the foam increase with the PLA/PCL weight ratio. The foam is then dried for an hour at room temperature (under vacuum) to remove any amount of non-solvent hexane and get a dry foam.

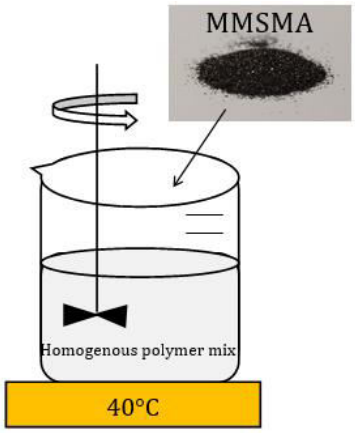

Fig. 5.7. Evaporation of the non-solvent Hexane for the concentrated mixture.

The dry foam is then transformed into wires using a Felfil Evo extruder (figure 5.8) that allow the increase in temperature to melt the foam. PLA and PCL polymers have different melting points and consequently the temperature of the extrusion is selected depending on the PLA/PCL weight ratio (the maximum available temperature is around 573K). This diameter of the extrusion nozzle is selected to be 1.75mm to ensure the 3D printability in standard 3D printers. The screw rotation speed is kept at 4-5rpm just to avoid the overheating of the motor.

The addition of the Ni-Mn-In-Co micro-particles (MP) may influence the phase transformations and the general behavior (porosity, brittleness etc...) of the polymers. Different compositions have been tested in order to optimize the final composite in terms of quality, texture, flexibility and magnetic response of the obtained wires. In all cases, the used MP size ranges between 25-60µm. When the particle concentration above 10wt%, the extruded wires become brittle and difficult to print except when using polymer mixtures with low PLA concentrations. Thus, just the results obtained on composites elaborated from pure PCL or from $PCL_{90wt\%}$-$PLA_{10wt\%}$ polymer matrix will be exposed. Using the previous nomenclature for the polymers, the composites are described with a superscript indicating the wt% of MP. Therefore, a $P_{20\text{-}80}{}^{90}MP^{10}$ represents a mixture of 90wt% of polymer (20wt% of PLA and 80wt% PCL) and a 10wt% of MP.

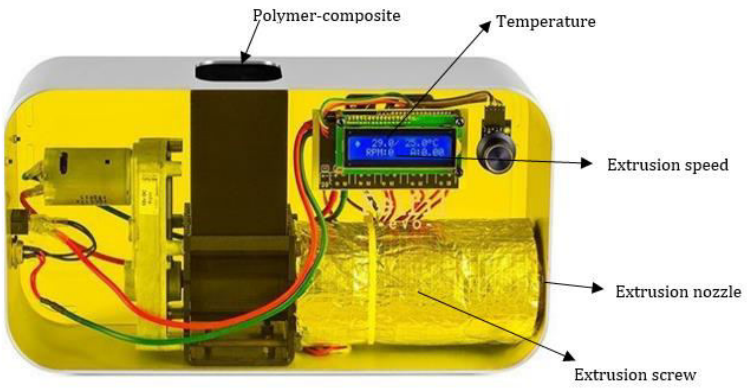

Fig. 5.8. Bundle Felfil Evo Spooler extruder.

It is worth highlighting that all the analyzed 90wt% PCL and 10wt% PLA composites result in a very malleable material showing no porosity and able to be extruded and 3D printed (see figure 5.9).

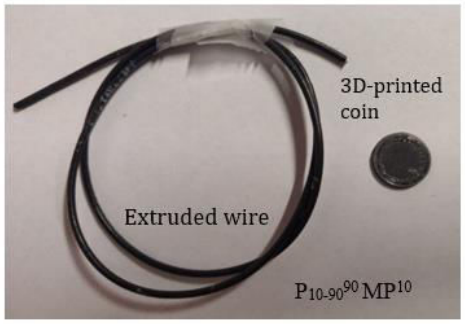

Fig. 5.9. Polymer-composite wire and 3D-printed coin with $P_{10\text{-}90}^{90}$-MP^{10} consisting PCL^{90}-$PLA^{10.}$

5.2.2.2 Thermal stability of PCL/PLA-based composites

As a preliminary study, the effect of the addition of a small amount of micro-particles (5% and 10%, wt.) on the thermal properties of the polymers has been analyzed. Figure 5.10 shows the DSC thermograms obtained on the$P_{10\text{-}90}$,$P_{10\text{-}90}^{95}$ $MP^{5}$and $P_{10\text{-}90}^{90}MP^{10}$ samples measured at a 10K/min heating and cooling rate in the temperature range 223 to 453K. The figure shows the crystallization and melting peaks for PCL and PLA polymers. The MT peak associated to the MP cannot be observed in the thermogram since it is overlapped to the melting peak for PCL, which also lies round the same temperature (323-333K). The presence of MP in the polymer clearly shifts the exothermic crystallization peak of the PCL on cooling. The detailed temperature region for crystallization in temperature range 273-323K in PCL is shown in figure 5.10b. By comparing with the neat polymer matrix, the crystallization peak (T_c) shifts to the higher temperatures (see table 5.1).

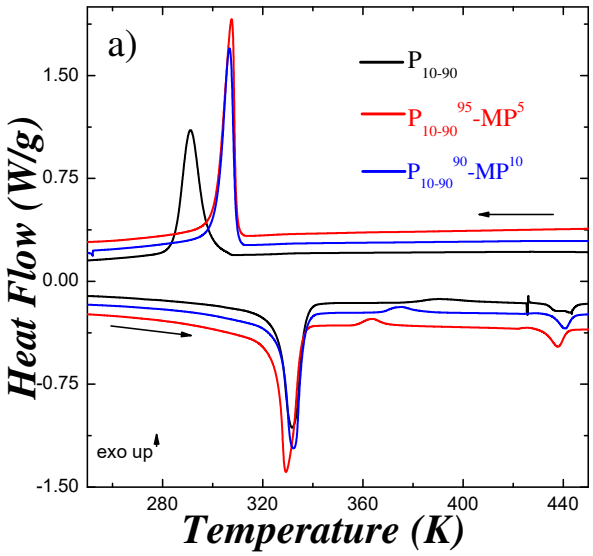

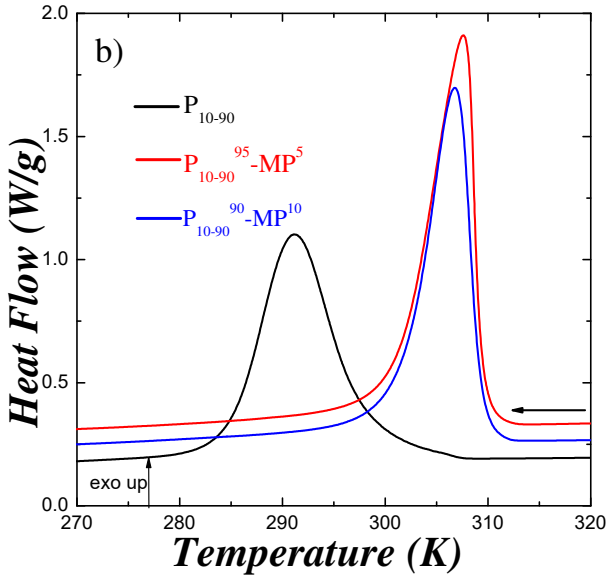

Fig. 5.10. a) DSC thermograms during heating and cooling ramps for $P_{10\text{-}90}$,(black line), $P_{10\text{-}90}{}^{95}MP^{5}$ (red line) and $P_{10\text{-}90}{}^{90}MP^{10}$(blue line), b) Detailed temperature region for crystallization peak for PCL.

This shift in T_c has been reported previously in nano-composites of Fe_3O_4 and graphene oxide with PCL [358–360], where the incorporated nano-particles (up to 1.5wt% for Fe_3O_4 and 3wt% in Fe_3O_4-graphene oxide) act as heterogeneous nucleating points that favor the crystallization in PCL. However, with increasing concentration of nano-particles, the values of T_c start decreasing, which is attributed to the strong interaction between molecular chains of PCL and Fe_3O_4 nano-particles that hinder the motion of PCL chains [360]. The higher T_c during cooling observed in the MP containing composites suggest a strong nucleating effect on the MP-polymer interface.

Samples	T_m^{PCL}	ΔH_m^{PCL}	T_c	ΔH_c	X_c^{PCL}
	(K)	*(J/g)*	*(K)*	*(J/g)*	*(%)*
$P_{10\text{-}90}$	331	50	291	47	40
$P_{10\text{-}90}{}^{95}$-MP^{5}	329	55	307	51	47
$P_{10\text{-}90}{}^{90}$-MP^{10}	330	55	306	50	48

Table. 5.1. Thermal properties of PCL during heating and cooling ramps with different MP concentrations.

The variation in the degree of crystallinity (X_c) of PCL with different MP concentration. X_c^{PCL}can be calculated by using the equation:

$$X_c^{PCL} = \frac{\Delta H_m^{PCL}}{(1-\varphi)\,\Delta H_o^{PCL}} 100\% \qquad 5.1$$

where, ΔH_m^{PCL} is the melting temperature of PCL, (1-φ) is the weight fraction of PCL and ΔH_o^{PCL} represents the theoretical enthalpy of fusion of pure crystalline PCL, which is 139J/g [361]. The calculated values of X_c^{PCL} are also given in table 5.1. The higher degree of crystallinity in $P_{10\text{-}90}{}^{90}$ MP^{10} and $P_{10\text{-}90}{}^{95}$ than in $P_{10\text{-}90}$, suggest the MP increases the diffusion ability of the molecular chains of PCL resulting in higher crystalline fraction [362, 363]. On the other hand, the values of melting temperature (T_m^{PCL}) slightly decreases for $P_{10\text{-}90}{}^{90}$ MP^5 and $P_{10\text{-}90}{}^{95}$ MP^{10} (see table 5.2) but in any case the changes are insignificant. This stable to stable phase transformation seems to be less susceptible to the presence of MP in the matrix.

On the other hand, the effect of the MP on the crystallization behavior of PLA has also been analyzed. Figure 5.11 represents the cold crystallization and melting peaks for PLA for $P_{10\text{-}90}$,$P_{10\text{-}90}{}^{95}$ MP^5 and $P_{10\text{-}90}{}^{90}MP^{10}$ (detailed temperature region taken from figure 5.9a). The degree of crystallinity of PLA was obtained by [362]

$$X_c^{PLA} = \frac{\Delta H_m^{PLA}}{(1-\varphi)\,\Delta Hm_o^{PLA}} 100\% \qquad 5.2$$

where, (1-φ) is the weight fraction of PLA and ΔHm_o^{PLA}= 93.6J/g is the melting enthalpy of the 100% PLA [362, 364].

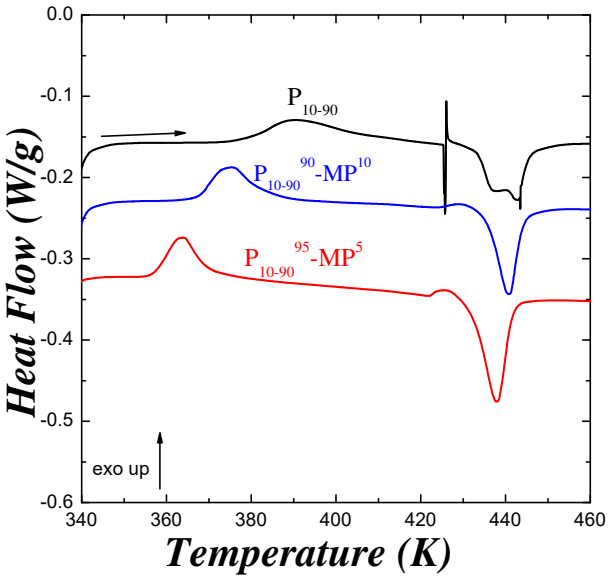

Fig. 5.11. Detailed temperature region for cold crystallization and melting peaks for PLA (heating) for $P_{10\text{-}90}$,$P_{10\text{-}90}{}^{95}$ $MP^5$and $P_{10\text{-}90}{}^{90}MP^{10}$samples.

The values of cold crystallization temperature (T_{cc}), melting temperature (T_m^{PLA}) and corresponding enthalpy changes (ΔH_{cc} and ΔH_m^{PLA}) are shown in table 5.2. The melting temperature T_m^{PLA} slightly decreases with the presence of MP. The lower value of T_{cc} for particle containing samples during heating, suggests again that the addition of micro-particles facilitate the crystallization. A similar behavior in T_{cc} has been reported previously in PLA polymer matrix where the addition of bamboo cellulose nano-whisker helps improving the crystalline properties of the composite [362]. The higher degree of crystallinity X_m^{PLA} in $P_{10\text{-}90}{}^{90}MP^{10}$ and $P_{10\text{-}90}{}^{95}MP^{5}$ than in $P_{10\text{-}90}$, again suggest that MP increases the diffusion ability of the molecular chains resulting in a higher crystalline fraction. Nevertheless, $P_{10\text{-}90}{}^{90}MP^{10}$ shows a lower crystalline fraction than, $P_{10\text{-}90}{}^{95}$ MP^5. Anyway, the low PLA fraction present and the lack of definition of the curve baseline in the sample make the estimation of the thermodynamic quantities (mainly enthalpies) very difficult.

Samples	T_m^{PLA}	ΔH_m^{PLA}	T_{cc}	ΔH_{cc}	X_c^{PLA}
	(K)	***(J/g)***	***(K)***	***(J/g)***	***(%)***
$P_{10\text{-}90}$	443	3	390	2.4	6
$P_{10\text{-}90}{}^{95}$-MP^5	437	5	364	2.6	27
$P_{10\text{-}90}{}^{90}$-MP^{10}	440	4	375	2.6	17

Table. 5.2. Thermal properties of PLA during heating and cooling ramps.

The high temperatures thermal stability of the polymer-composites has been analyzed by Thermo-gravimetric analysis (TGA). Figure 5.12 shows the TGA curves for the $P_{10\text{-}90}$, $P_{10\text{-}90}{}^{95}$ MP^5 and $P_{10\text{-}90}{}^{90}MP^{10}$ samples. The decomposition of the polymer-composites for all samples occurs between 573 and 693K due to the large-scale degradation of the polymer chains. However, it is worth noticing that for $P_{10\text{-}90}{}^{95}$ MP^5 and $P_{10\text{-}90}{}^{90}MP^{10}$, the thermal degradation take place at lower temperatures on increasing the amount of micro-particles. Hence, the addition of micro-particles seems to reduce the thermal stability of the polymer matrix. This effect has been explained previously assuming that particles act as catalyst causing a random pyrolysis of the molecular chains and accelerating the thermal decomposition [365, 366].

- **FILLING LOAD**

The mechanical consistency of different PCL/PLA composites elaborated with different particles concentration was analyzed on the basis of both visual and touch direct analysis (hard to quantify). After tens of trials (not shown here), it was confirmed particles concentrations above 10wt% while keeping constant the $PCL_{90wt\%}$-$PLA_{10wt\%}$ polymers ratio resulted in a critical increase of brittleness that made the material not adequate for 3D-printing.

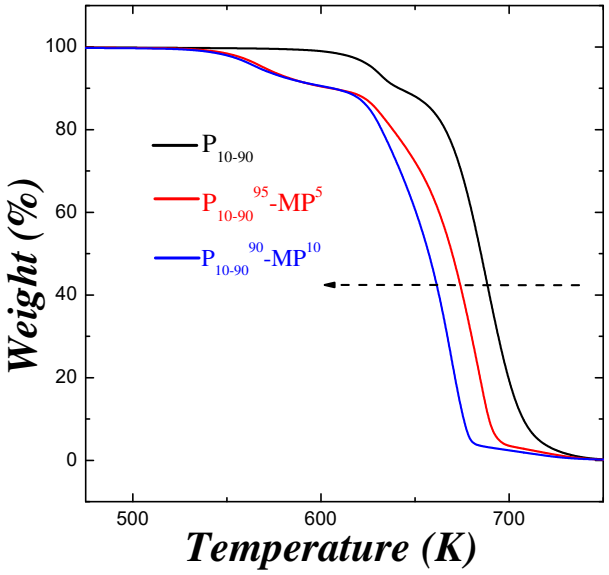

Fig. 5.12. TGA curves for $P_{10\text{-}90}$(black line), $P_{10\text{-}90}{}^{95}MP^{5}$(red line) and $P_{10\text{-}90}{}^{90}MP^{10}$(blue line) samples.

5.2.2.3 PCL-based composites

The removing of PLA from the polymer matrix, that is, the elaboration of pure PCL matrix, has been explored as an alternative to further increase the concentration of magnetic particles (better magnetic response), while keeping acceptable mechanical properties (in terms of printability). The particle concentration up to 80wt% has been successfully dispersed in PCL matrix obtaining apparent acceptable mechanical response. In fact, the obtained wires show very high flexibility and 3D printability. The distribution of MP in the matrix and the surface morphology of the polymer-composites have been analyzed by SEM observations. As an example, SEM images for $P_{0\text{-}100}{}^{50}MP^{50}$ wires are shown in figure 5.13. The surface morphology to the composites (figures 5.13a-c) show that micro-particles are well embedded in cavities surrounded by polymer matrix. This point to a robust interaction between micro-particles and polymer matrix. The higher magnification images (figure 5.13d, e) show that the MPs are homogeneously dispersed in the polymer-matrix.

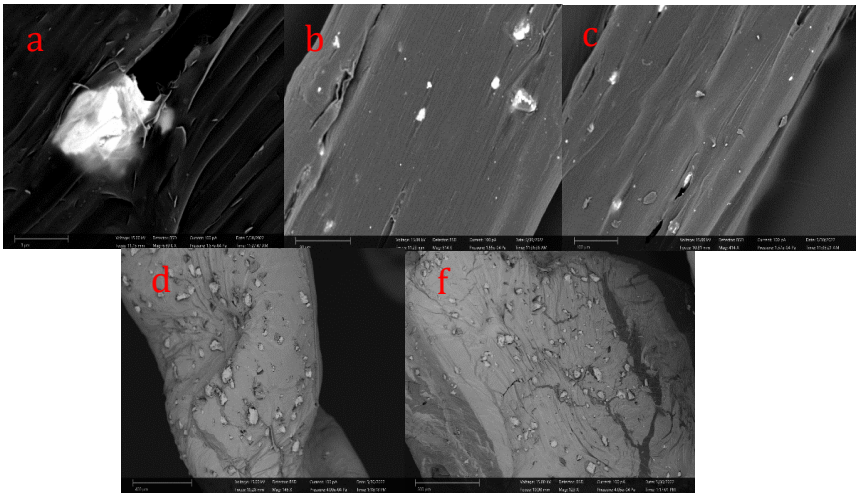

Fig. 5.13. SEM images of $P_{0\text{-}100}^{50}$-MP^{50} composites at different magnification.

5.2.2.3.1 High filling-load printable composite (80wt% particles)

As mentioned, composites with 80wt% particles and acceptable printability were obtained from the dispersion of particles in pure PCL. Nevertheless, in the case of the previously studied MSMA/PCL composites, an additional problem arose from the fact the MT in the used particles took place at approximately the same temperature as the melting of the polymer (compare figures 4.1 and 5.2). This implies that the composite will lose the structural integrity at working temperatures, thus hindering any possible practical application.

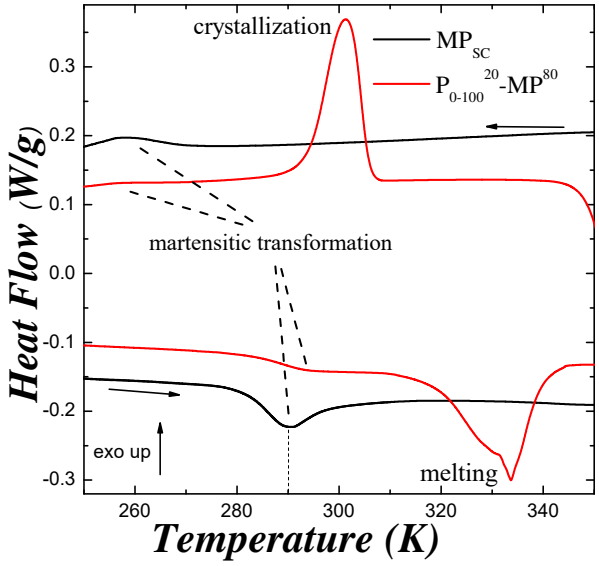

Fig. 5.14. DSC thermogram for ordered powdered alloy (black line) and $P_{0\text{-}100}^{20}$-MP^{80} (red line).

In order to overcome this setback, new composites were produced from powders sieved from the MA^{HC} samples studied in Chapter 3, whose MT take place well below the PCL melting point. Both the MT in the particles and the melting of the polymer in a $P_{0\text{-}100}{}^{20}MP^{80}$ composite can be clearly seen in the DSC thermograms shown in figure 5.14. In effect, the reverse martensitic transformation temperature in the particles lies around 40K below the melting point of PCL, in such a way that there is no overlapping at all.

- **Microstructure and thermal stability**

The distribution of sizes and geometry of the particles used for $P_{0\text{-}100}{}^{20}MP^{80}$ composite can be seen in the SEM images displayed in figure 5.15. The images show the morphological homogeneity and the arrangement of the particles in the PCL matrix. The mixture of small and large particles in the composite show that the smaller particles are located in the gaps between the bigger particles. Many studies involving metallic particles, soft magnetic materials, permanent magnet composites or concrete in the construction area report that such distribution of the particles along the composite leads to an increase in the packing fraction [197, 366–368]. In particular, Palmero et al. report slight increase in the magnetization values in the MnAlC-based permanent magnet composites by increasing the fine to coarse particle ratio [197]. Therefore, the observed particle-size distribution along the composite could be behind the high achieved filling factor.

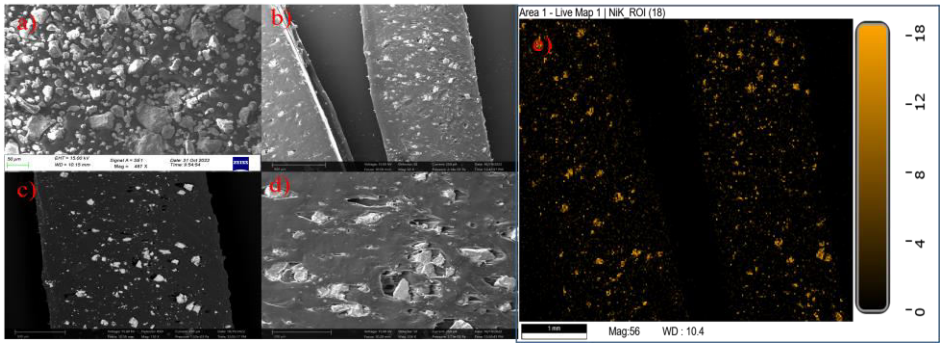

Fig. 5.15. SEM images of a) MP_{SC} of $Ni_{45}Co_5Mn_{36.7}In_{13.3}$ powder with particle size <100µm, b)-d) $P_{0\text{-}100}{}^{20}MP^{80}$wire at different magnifications, and e) dispersion of Ni element in composite wires.

The effect of such a high concentration of particles on the thermal stability of the $P_{0\text{-}100}{}^{20}MP^{80}$ has been analyzed by comparing the behavior of the composite with pure PCL polymer. Figure 5.16 shows the TGA curves for raw PCL and $P_{0\text{-}100}{}^{20}MP^{80}$. The thermal degradation in the $P_{0\text{-}100}{}^{20}MP^{80}$ composite takes place at lower temperature than in pure PCL, as it occurred for lower micro-particle concentration in previous cases (figure 5.12). On the other hand, the weight loss

in the $P_{0\text{-}100}{}^{20}MP^{80}$ occurs at lower temperatures than in the $P_{0\text{-}100}{}^{50}MP^{50}$ one, thus evidencing a considerable influence of the amount of particles on the thermal decomposition in the composites. In particular, the higher the concentration of micro-particles, the lower the evaporation temperature of the polymer matrix.

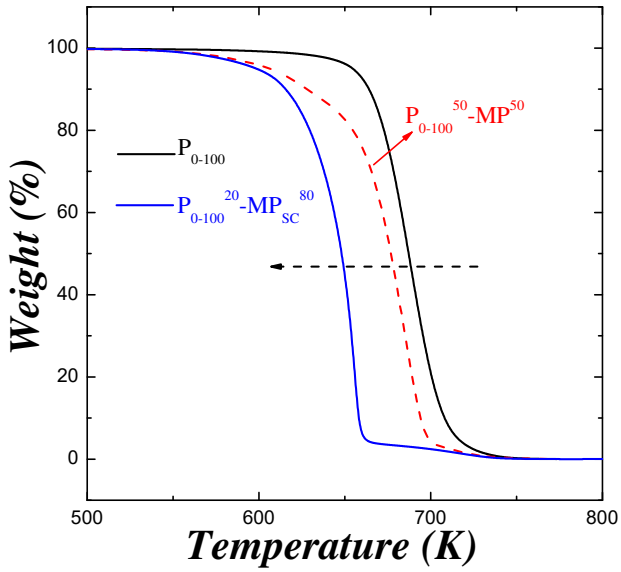

Fig. 5.16. TGA curves for $P_{0\text{-}100}$ (black line), $P_{0\text{-}100}{}^{50}MP^{50}$ (red dotted line) and $P_{0\text{-}100}{}^{20}MP^{80}$ (blue line) samples.

- **Magnetic response**

In order to assess the functionality of the elaborated composite, the magnetic properties have been also evaluated. Figure 5.17a, shows the *M(H)* magnetization curves at 343K for the milled micro-particles and the $P_{0\text{-}100}{}^{50}MP^{50}$ and $P_{0\text{-}100}{}^{20}MP^{80}$ composites. The saturation magnetization for the micro-particles is around 63 emu/g, whereas it decreases to 52 emu/g for $P_{0\text{-}100}{}^{20}MP^{80}$ (around 20%) and almost 50% for $P_{0\text{-}100}{}^{50}$-MP^{50} (~33emu/g). Obviously, the magnetization reduction is in perfect agreement with the fraction of non-magnetic polymer in the composite. Similar behaviors have been reported by Wang et al.. with composites of PCL-Fe_3O_4@graphene oxide [359], where the nano-composites exhibit a super-paramagnetic behavior. However, by increasing the concentration of MP, the magnetic properties can be improved.

Likewise, the influence of the micro-particle concentration on the functional properties (active magnetic refrigeration) of the composite has been evaluated by the estimation of the MCE. Figure 5.17b shows the isothermal entropy change (ΔS_{iso}) calculated from a set of zero-cooled

thermo-magnetization curves measured on heating under different magnetic fields. It has been calculated for fields ranging from 100Oe to 60kOe using equation [314]:

$$\Delta S_{iso} = S(T,H) - S(T,0) = \int_0^H \left(\frac{\partial M}{\partial T}\right)_H dH \qquad 5.3$$

The temperature dependence of the entropy change (60kOe) for free MP, $P_{0\text{-}100}{}^{50}MP^{50}$ and $P_{0\text{-}100}{}^{20}MP^{80}$ composites are shown in figure 5.17b.

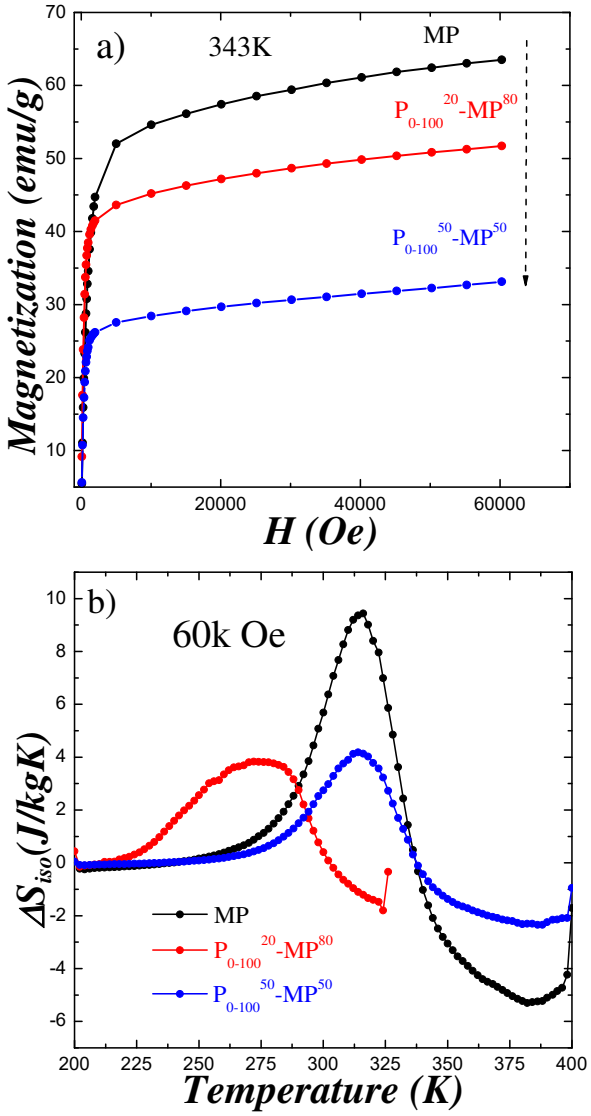

Fig. 5.17. a) M(H) curves at 70°C, b) Magnetically-induced entropy change at 60kOe as a function of temperature for free MP, $P_{0\text{-}100}{}^{20}MP^{80}$ and $P_{0\text{-}100}{}^{50}$-MP^{50} samples.

The ΔS_{iso} corresponding to the micro-particles reaches a maximum value of around 9.5J/kgK at martensitic temperature. The MCE in polymer-composites however is relatively much lower. For $P_{0\text{-}100}{}^{50}MP^{50}$ and $P_{0\text{-}100}{}^{20}MP^{80}$ composites, the MCE value is almost half (4.5J/kgK). On the other side, as previously stated (see chapter 4), the relative cooling power (RCP) is a primary

performance indicator to rank the MCM for active refrigeration. The RCP for MP, $P_{0\text{-}100}^{50}MP^{50}$ and $P_{0\text{-}100}^{20}MP^{80}$ composites are given in table 5.3. The reduction in the RCP is mainly linked to the reduction in the MP content. However,$P_{0\text{-}100}^{20}MP^{80}$ shows relatively higher RCP values than free MP.

Samples	*RCP* *(J/kg)*
$P_{0\text{-}100}^{0}$-MP^{100}	154
$P_{0\text{-}100}^{20}$- MP^{80}	171
$P_{0\text{-}100}^{50}$-MP^{50}	78

Table. 5.4. Refrigeration Cooling Power for different samples

The entropy change (under 60kOe) as a function of temperature for MP and $P_{0\text{-}100}^{20}MP^{80}$ are shown in figure 5.18. The RCP for MP is around 195J/kg and reduces by 13% to 171J/kg for $P_{0\text{-}100}^{20}MP^{80}$ composite. The decrease in RCP must be expected around 20% (polymer concentration). However, the wider peak for $P_{0\text{-}100}^{20}$-MP^{80} compensates the decrease in ΔS_{iso} and results in RCP relatively comparable to the MP. In this regard, the polymeric composites with high concentration of MP are seen to be promising candidates for magnetic refrigeration applications.

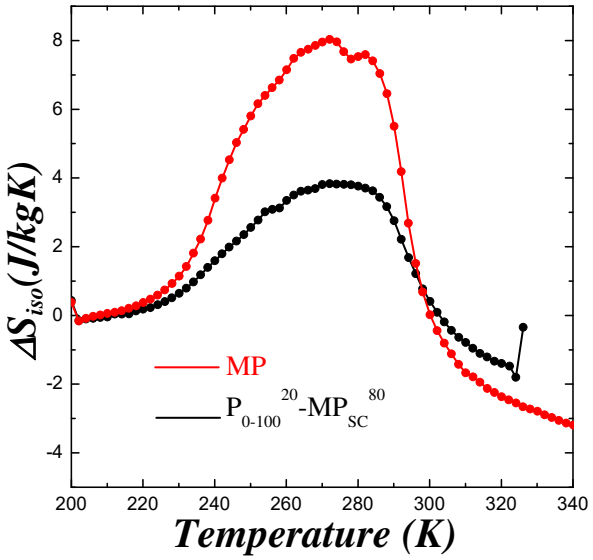

Fig. 5.18. Magnetically-induced entropy change at 60kOe as a function of temperature for MP and $P_{0\text{-}100}^{20}MP^{80}$.

- **3D printing**

Some simple objects have been successfully printed using the above wires with a commercial Artillery Sidewinder-X 3D printer. The nozzle used for printing is 0.6mm in diameter to ensure there is no clogging of the particle the tip of the nozzle (the maximum size of the particles is 0.006mm). The bed temperature has been kept constant at 303K to make ensure the printed layers have sufficient time to cool down. A relatively low printing speed (12.5mm/s) has been used to ensure the cooling of previous layers. The desired shape or form is designed by the CURA software, where the parameters like printing speed, filling density of the printed shape, thickness of each layer, etc. are adjusted and transferred to the printer. The printing temperature has been set at 473K. These parameters have been kept constant in all cases. Figure 5.19 show the obtained wires from $\mathbf{P_{0\text{-}100}^{50}MP^{50}}$ composites and some simple printed objects.

Fig. 5.19. Polymer-composite wire and 3D-printed objects with $P_{0\text{-}100}^{50}MP^{50}$.

The heat exchanger represents the active part of the magnetic refrigeration and therefore, their design is crucial to get a good effectiveness and performance. The development of the technology to produce heat exchanger in different geometries with large area/volume ratio and so a high capacity to remove or absorb heat is the final objective of this Ph.D. thesis. Numerous computational and experimental investigations have been conducted to optimize the MCM heat transfer regenerator geometry, including taking into account stacked thin parallel plates, micro-channels with various geometries, fin structures, woven screens, packed bed etc. [365, 369, 370]. A porous structure like honeycomb-like shape of a heat exchanger used in magnetic refrigeration provides several advantages over conventional designs [371]. Such structure allows for a greater surface area to be exposed to the working magnetic field, leading to better heat transfer efficiency. This, in turn, leads to faster cooling and heating times, making the system more energy efficient. The honeycomb shape also facilitates the removal of excess heat

from the system, which can help to prolong the lifespan of the materials used in the heat exchanger.

From the above, and as a colophon, figure 5.20 shows a proof-of-concept honey-comb/maze-like geometry printed from the produced $P_{0\text{-}100}^{20}$-MP^{80} composite. The successfully 3D printing from the elaborated magnetically-active composites open the door to the production of pieces with complex geometries with high interest in magnetic refrigeration applications.

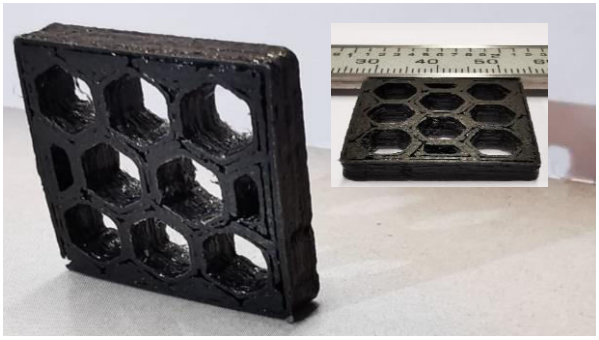

Fig. 5.20. Side view of the $POLY^{20}$-MP^{80} sample printed in a honey-comb like structure.

5.3 Conclusions

This chapter includes the morphological, thermal and magnetic studies of the Ni-Mn-In-Co MMSMA particles-composites. The main conclusions deduced from this chapter are:

- 3D-printable homogeneous magnetic composites have been successfully prepared by Solutions casting method using mixtures of PCL and PLA polymers.
- Small quantity of micro-particles enhances the crystallization process of the polymers. The micro-particles in the polymer matrix act as nucleating points that favor the crystallization process.
- Thermal stability of polymer reduces with increase in the micro-particle concentration probably due to the random pyrolysis of the molecular chains in the polymer.
- The magnetic properties of the polymer-composites improve with the higher concentration of MP embedded in the polymer-matrix.
- A homogeneous 3D-printable polymer-composite wire with micro-particle concentration up to 80wt%is achieved with higher RCP than the micro-particles itself, showing promising feature for the active magnetic refrigeration applications.

Main Conclusions

The objective of this study was to develop 3D printable polymeric composites for magnetic refrigeration utilizing Ni-Mn-In-Co shape memory alloys. Extensive experimentation and analysis were conducted to investigate the magnetic and structural properties of the composites. In conclusion, this thesis work successfully achieved the development of 3D printable magnetic composites for magnetic refrigeration applications based on the Magnetocaloric effect. By incorporating micro-particles with sizes compatible with standard 3D printer nozzles, the composites exhibited enhanced magnetocaloric effect and relative cooling power. The study also demonstrated the control of martensitic transformation and magnetic properties through precise selection of sizes, paving the way for tailored fabrication of magnetic composites. During the course of investigation, additional noteworthy findings emerged, which led to further specific conclusions described in the following:

- The martensite stabilization due to the induced deformation caused by grinding has been observed for the first time in these alloys, resulting in a shift in transformation temperatures by up to 100K, regardless of the initial phase (austenite or martensite) at room temperature. The martensite induced by deformation is distinct from thermally induced martensite. The stabilized martensite exhibits a non-modulated tetragonal structure (I4/mmm) with smaller lattice parameters that better accomodate the generated internal stresses compared to the thermally induced modulated monoclinic structure (P2/m). The destabilization of the martensite phase during the first reverse martensitic structure occurs around the Curie temperature, irrespective of the degree of deformation. Thus, the Curie temperature, marked by a maximum entropy change (with no magnetic contribution), represents an upper limit for mechanically induced martensite phase.
- Spin-glass-like systems with canonical behavior have been observed in both the stabilized and destabilized martensite states, indicating considerable interaction between the spins. However, the characteristics of these systems are independent of the stabilization state. Internal stresses play a crucial role in the overall magnetic differences between the stabilized and destabilized state.
- The grinding/milling process has a significant negative impact on the magnetic and structural properties of the material under investigation, leading to the deterioration of the martensitic transformation and a significant reduction in the magnetization of austenite. This deterioration is attributed to the formation of highly deformed non-

transforming martensite appear during milling. The volume of such regions increases with increasing milling time, and in extreme cases, it can even lead to the amorphization of the alloy. The frictional entropy term related to the martensitic transformation increases with milling time, indicating a correlation between internal stresses/strains and microstructure.

- Particles of same size exhibit similar transformation enthalpy and magnetization, regardless of the milling time. This demonstrates a clear relationship between particle size and degree of deformation. Therefore, a precise control of martensitic transformation and magnetization properties can be achieved by selecting specific particle sizes, regardless of the ball milling process employed.
- By selecting the particle size after milling and conducting low temperature annealing treatments, controlled powders with desirable properties comparable to those of the bulk material can be obtained. The particles show cooling power values comparable to the bulk material and are suitable for the production of composites for magnetic refrigeration applications.
- Homogeneous 3D-printable magnetic composites have been successfully prepared using a solution casting method and mixtures of PLA and PCL polymers. The addition of small quantity of the micro-particles enhances the crystallization process of the polymers by acting as nucleating agents. However, the thermal stability of the polymer decreases with an increase in micro-particle concentration, likely due to random pyrolysis of the molecular chains. The magnetic properties of the polymer composites improve with a higher concentration of micro-particles embedded in the polymer matrix.
- A homogeneous 3D-printed polymer composite object with micro-particle concentration up to 80% (weight) has been achieved, exhibiting a higher relative cooling power than the micro-particles alone. The described procedure proves to be suitable for active magnetic refrigeration applications and open new possibilities for efficient and customizable refrigeration systems.

Conclusiones Principales

El objetivo de este estudio ha sido desarrollar compuestos poliméricos imprimibles en 3D para refrigeración magnética utilizando aleaciones con memoria de forma de Ni-Mn-In-Co. Se ha llevado a cabo un amplio trabajo experimental para investigar las propiedades magnéticas y estructurales de los compuestos. En conclusión, a lo largo de la tesis se ha logrado con éxito el desarrollo de compuestos magnéticos imprimibles en 3D para aplicaciones de refrigeración magnética basadas en el efecto magnetocalórico. Se han incorporado micro-partículas con tamaños compatibles con las boquillas de las impresoras 3D estándar y los compuestos exhibieron un buen efecto magnetocalórico y un considerable poder de enfriamiento. El estudio también demostró que es posible el control de la transformación martensítica y de las propiedades magnéticas de las partículas a través de una selección precisa de tamaños, allanando el camino para la fabricación personalizada de compuestos magnéticos. Durante el curso de la investigación, surgieron resultados de interés, que llevaron a conclusiones adicionales más específicas y que describen a continuación:

- Se ha observado por primera vez la estabilización martensítica debida a la deformación inducida por molienda, lo que se traduce en un desplazamiento de las temperaturas de transformación de hasta 100K, independientemente de la fase presente al inicio de la molienda (austenita o martensita) a temperatura ambiente. La martensita inducida por deformación es distinta de la martensita inducida térmicamente. La martensita estabilizada tiene una estructura tetragonal no modulada (I4/mmm) con parámetros de red más pequeños que acomodan mejor las tensiones internas generadas en comparación con la estructura monoclínica modulada inducida térmicamente (P2/m). La desestabilización de la fase martensítica durante la primera transformación inversa ocurre alrededor de la temperatura de Curie, independientemente del grado de deformación. Por lo tanto, la temperatura de Curie, marcada por un cambio de entropía máximo (sin contribución magnética), representa un límite superior para la fase de martensita inducida mecánicamente.
- Se han observado la presencia de un comportamiento similar a un Spin-Glass canónico en los estados martensítico estabilizado y desestabilizado, con cierta interacción entre los spines. Sin embargo, las características de estos sistemas son independientes del estado de estabilización. Las tensiones internas juegan un papel importante en las diferencias magnéticas generales entre el estado estabilizado y desestabilizado.

- El proceso de molienda tiene un impacto negativo significativo en las propiedades magnéticas y estructurales del material, lo que lleva al deterioro de la transformación martensítica y a una reducción significativa en la magnetización de la austenita. Este deterioro se atribuye a la formación durante la molienda de martensitas deformadas que no transforman. El volumen de tales regiones aumenta con el aumento del tiempo de molienda y, en casos extremos, incluso puede conducir a la amorfización de la aleación. El término de entropía friccional relacionado con la transformación martensítica aumenta con el tiempo de molienda, lo que indica una correlación entre las tensiones/deformaciones internas y la microestructura.
- Partículas del mismo tamaño muestran una entalpía de transformación y una magnetización similar, independientemente del tiempo de molienda. Esto demuestra una clara relación entre el tamaño de partícula y el grado de deformación. Por lo tanto, se puede lograr un control preciso de las propiedades de magnetización y transformación martensítica seleccionando tamaños de partículas específicos, independientemente del proceso de molienda empleado.
- Seleccionando el tamaño de partícula después de la molienda y realizando tratamientos de recocido a baja temperatura, se pueden obtener polvos con propiedades comparables a las del material inicial. Las partículas muestran unos valores de potencia de enfriamiento comparables al material inicial y son adecuadas para la producción de compuestos para aplicaciones en refrigeración magnética.
- Se han preparado compuestos magnéticos imprimibles en 3D homogéneos utilizando un método denominado “solution casting” y mezclas de polímeros PLA y PCL. La adición de una pequeña cantidad de micro-partículas mejora el proceso de cristalización de los polímeros al actuar como agentes de nucleación. Sin embargo, la estabilidad térmica del polímero disminuye con el aumento de la concentración de micropartículas, probablemente debido a la pirólisis aleatoria de las cadenas moleculares. Las propiedades magnéticas de los compuestos poliméricos mejoran con una mayor concentración de micro-partículas en la matriz polimérica.
- Se ha logrado imprimir en 3D un objeto compuesto homogéneode polímero con una concentración de micro-partículas de hasta el 80 % (en peso) y con un poder de enfriamiento relativo mayor que el de las micro-partículas. Esto demuestra que el procedimiento desarrollado es adecuado para aplicaciones de refrigeración magnética y abre nuevas posibilidades para sistemas de refrigeración eficientes y personalizables.

List of publications by the author

The thesis work has yielded significant contributions, leading to the publication of several papers in international peer-reviewed journals:

- J. I. Pérez-Landazábal, V. Sánchez-Alarcos, V. Recarte, O. A. Lambri, F. G. Bonifacich, D. L.R. Khanna, I. Unzueta, J.A. García, F. Plazaola, J. López-García, M. Jimenez Ruiz, J.A. Rodríguez-Velamazán, and E. Cesari, "Influence of Structural Defects on the Properties of Metamagnetic Shape Memory Alloys" Metals, 10(9), (2020), 1131

- D.L.R. Khanna, V. S´ anchez-Alarcos, V. Recarte, and J.I. P´erez-Landazabal, "Correlation between particle size and magnetic properties in soft-milled $Ni_{45}Co_5Mn_{34}In_{16}$ powders" Intermetallics, 130, (2021), 107076

- V. Sánchez-Alarcos, V. Recarte, D.L.R. Khanna, J. López-García, and J.I. Pérez-Landazábal, "Deformation induced martensite stabilization in $Ni_{45}Mn_{36.7}In_{13.3}Co_5$ micro-particles" Journal of alloys and compounds, 870, (2021), 159536

References

[1] A. A. Likhachev and K. Ullakko, "Magnetic-field-controlled twin boundaries motion and giant magneto-mechanical effects in Ni-Mn-Ga shape memory alloy," *Physics Letters A*, vol. 275, no. 1, pp. 142–151, Oct. 2000, doi: 10.1016/S0375-9601(00)00561-2.

[2] J. W. Christian, G. B. Olson, and M. Cohen, "Classification of Displacive Transformations : What is a Martensitic Transformation ?," *J. Phys. IV France*, vol. 05, no. C8, pp. C8-C8-10, Dec. 1995, doi: 10.1051/jp4:1995801.

[3] P. Tong, D. C. C. Lam, and Q. P. Sun, "Department of Mechanical Engineering Hong Kong University of Science and Technology, Hong Kong, China," in *IUTAM Symposium on Mechanics of Martensitic Phase Transformation in Solids*, Springer Science & Business Media, 2013, p. 221.

[4] Fr. Heusler and F. Richarz, "Studien über magnetisierbare Manganlegierungen," *Z. Anorg. Chem.*, vol. 61, no. 1, pp. 265–279, Feb. 1909, doi: 10.1002/zaac.19090610121.

[5] T. Graf, C. Felser, and S. S. P. Parkin, "Simple rules for the understanding of Heusler compounds," *Progress in Solid State Chemistry*, vol. 39, no. 1, pp. 1–50, May 2011, doi: 10.1016/j.progsolidstchem.2011.02.001.

[6] T. Krenke, E. Duman, M. Acet, E.F. Wassermann, X. Moya, L. Mañosa, and A. Planes, "Inverse magnetocaloric effect in ferromagnetic Ni–Mn–Sn alloys," *Nature Mater*, vol. 4, no. 6, pp. 450–454, Jun. 2005, doi: 10.1038/nmat1395.

[7] T. Krenke, E. Duman, M. Acet, E.F. Wassermann, X. Moya, L. Mañosa, A. Planes, E. Suard, and B. Ouladdiaf, "Magnetic superelasticity and inverse magnetocaloric effect in Ni-Mn-In," *Phys. Rev. B*, vol. 75, no. 10, p. 104414, Mar. 2007, doi: 10.1103/PhysRevB.75.104414.

[8] V. K. Sharma, M. K. Chattopadhyay, R. Kumar, T. Ganguli, P. Tiwari, and S. B. Roy, "Magnetocaloric effect in Heusler alloys $Ni_{50}Mn_{34}In_{16}$ and $Ni_{50}Mn_{34}Sn_{16}$," *J. Phys.: Condens. Matter*, vol. 19, no. 49, p. 496207, Dec. 2007, doi: 10.1088/0953-8984/19/49/496207.

[9] T. Krenke, M. Acet, E. F. Wassermann, X. Moya, L. Mañosa, and A. Planes, "Martensitic transitions and the nature of ferromagnetism in the austenitic and martensitic states of Ni-Mn-Sn alloys," *Phys. Rev. B*, vol. 72, no. 1, p. 014412, Jul. 2005, doi: 10.1103/PhysRevB.72.014412.

[10] K. Ullakko, J. K. Huang, C. Kantner, R. C. O'Handley, and V. V. Kokorin, "Large magnetic-field-induced strains in Ni_2MnGa single crystals," *Appl. Phys. Lett.*, vol. 69, no. 13, pp. 1966–1968, Sep. 1996, doi: 10.1063/1.117637.

[11] R. Ranjan, S. Banik, S. R. Barman, U. Kumar, P. K. Mukhopadhyay, and D. Pandey, "Powder x-ray diffraction study of the thermoelastic martensitic transition in $Ni_2Mn_{1.05}Ga_{0.95}$," *Phys. Rev. B*, vol. 74, no. 22, p. 224443, Dec. 2006, doi: 10.1103/PhysRevB.74.224443.

[12] I. Dikshtein, V. Koledov, V. Shavrov, A. Tulaikova, A. Cherechukin, V. Buchelnikov, V. Khovailo, M. Matsumoto, T. Takagi, and J. Tani, "Phase transitions in intermetallic compounds Ni-Mn-Ga with shape memory effect," *IEEE Transactions on Magnetics*, vol. 35, no. 5, pp. 3811–3813, Sep. 1999, doi: 10.1109/20.800673.

[13] H.F. Wang, J.M. Wang, C.B. Jiang, and H.B. Xu, "Phase transition and mechanical properties of $Ni_{30}Cu_{20}Mn_{37+x}Ga_{13-x}$(x = 0–4.5) alloys," *Rare Met.*, vol. 33, no. 5, pp. 547–551, Oct. 2014, doi: 10.1007/s12598-013-0103-4.

[14] T. Krenke, M. Acet, E. F. Wassermann, X. Moya, L. Mañosa, and A. Planes, "Ferromagnetism in the austenitic and martensitic states of Ni-Mn-In alloys," *Phys. Rev. B*, vol. 73, no. 17, p. 174413, May 2006, doi: 10.1103/PhysRevB.73.174413.

[15] T. Krenke, "Untersuchung der martensitischen Umwandlung und der magnetischen Eigenschaften Mangan-reicher Ni-Mn-In-und Ni-Mn-Sn-Heusler-Legierungen," Duisburg, Essen, Univ., Diss., 2007.

[16] V. Sánchez-Alarcos, V. Recarte, J. I. Pérez-Landazábal, S. Larumbe, R. Caballero-Flores, I. Unzueta, J.A. García, F. Plazaola, and J.A. Rodríguez-Velamazán, "Mechanically induced disorder and crystallization process in Ni-Mn-In ball-milled alloys," *Journal of Alloys and Compounds*, vol. 689, pp. 983–991, Dec. 2016, doi: 10.1016/j.jallcom.2016.08.068.

[17] V. Sánchez-Alarcos, V. Recarte, J. I. Pérez-Landazábal, E. Cesari, and J. A. Rodríguez-Velamazán, "Long-Range Atomic Order and Entropy Change at the Martensitic Transformation in a Ni-Mn-In-Co Metamagnetic Shape Memory Alloy," *Entropy*, vol. 16, no. 5, Art. no. 5, May 2014, doi: 10.3390/e16052756.

[18] V. Sánchez-Alarcos, V. Recarte, J. I. Pérez-Landazábal, and G. J. Cuello, "Correlation between atomic order and the characteristics of the structural and magnetic transformations in Ni-Mn-Ga shape memory alloys," *Acta Materialia*, vol. 55, no. 11, pp. 3883–3889, Jun. 2007, doi: 10.1016/j.actamat.2007.03.001.

[19] V. Sánchez-Alarcos, J. I. Pérez-Landazábal, and V. Recarte, "Influence of Long-Range Atomic Order on the Structural and Magnetic Properties of Ni-Mn-Ga Ferromagnetic Shape Memory Alloys," *Materials Science Forum*, vol. 684, pp. 85–103, 2011, doi: 10.4028/www.scientific.net/MSF.684.85.

[20] V. Sánchez-Alarcos, J. I. Pérez-Landazábal, V. Recarte, I. Lucia, J. Vélez, and J. A. Rodríguez-Velamazán, "Effect of high-temperature quenching on the magneto-structural transformations and the long-range atomic order of Ni-Mn-Sn and Ni-Mn-Sb metamagnetic shape memory alloys," *Acta Materialia*, vol. 61, no. 12, pp. 4676–4682, Jul. 2013, doi: 10.1016/j.actamat.2013.04.040.

[21] V. A. Chernenko, C. Seguí, E. Cesari, J. Pons, and V. V. Kokorin, "Sequence of martensitic transformations in Ni-Mn-Ga alloys," *Phys. Rev. B*, vol. 57, no. 5, pp. 2659–2662, Feb. 1998, doi: 10.1103/PhysRevB.57.2659.

[22] J. Pons, V. A. Chernenko, R. Santamarta, and E. Cesari, "Crystal structure of martensitic phases in Ni–Mn–Ga shape memory alloys," *Acta Materialia*, vol. 48, no. 12, pp. 3027–3038, Jul. 2000, doi: 10.1016/S1359-6454(00)00130-0.

[23] V. V. Kokorin, V. V. Martynov, and V. A. Chernenko, "Stress - induced martensitic transformations in Ni2MnGa," *Scripta Metallurgica et Materialia*, vol. 26, no. 2, pp. 175–177, Jan. 1992, doi: 10.1016/0956-716X(92)90168-E.

[24] N. Lanska, O. Söderberg, A. Sozinov, Y. Ge, K. Ullakko, and V. K. Lindroos, "Composition and temperature dependence of the crystal structure of Ni–Mn–Ga alloys," *Journal of Applied Physics*, vol. 95, no. 12, pp. 8074–8078, Jun. 2004, doi: 10.1063/1.1748860.

[25] R. F. Hamilton, H. Sehitoglu, C. Efstathiou, and H. J. Maier, "Inter-martensitic transitions in Ni-Fe-Ga single crystals," *Acta Materialia*, vol. 55, no. 14, pp. 4867–4876, Aug. 2007, doi: 10.1016/j.actamat.2007.05.003.

[26] S. Aksoy, "Magnetic interactions in martensitic Ni-Mn based Heusler systems," Apr. 2010, Accessed: Oct. 31, 2022. [Online]. Available: https://www.osti.gov/etdeweb/biblio/21340401

[27] M. Acet, Ll. Mañosa, and A. Planes, "Chapter Four - Magnetic-Field-Induced Effects in Martensitic Heusler-Based Magnetic Shape Memory Alloys," in *Handbook of Magnetic Materials*, K. H. J. Buschow, Ed., Elsevier, 2011, pp. 231–289. doi: 10.1016/B978-0-444-53780-5.00004-1.

[28] Y. Jiang, Z. Li, Z. Li, Y. Yang, B. Yang, Y. Zhang, C. Esling, X. Zhao and L. Zuo, "Magneto-structural transformation and magnetocaloric effect in Mn-Ni-Sn melt-spun ribbons," *Eur. Phys. J. Plus*, vol. 132, no. 1, p. 42, Jan. 2017, doi: 10.1140/epjp/i2017-11316-1.

[29] M. Khan, I. Dubenko, S. Stadler, and N. Ali, "Magneto-structural phase transitions in $Ni_{50}Mn_{25}Sb_{25-x}$Heusler alloys," *J. Phys.: Condens. Matter*, vol. 20, no. 23, p. 235204, Apr. 2008, doi: 10.1088/0953-8984/20/23/235204.

[30] A. Planes, E. Obradó, A. Gonzàlez-Comas, and L. Mañosa, "Premartensitic Transition Driven by Magnetoelastic Interaction in bcc Ferromagnetic Ni_2MnGa," *Phys. Rev. Lett.*, vol. 79, no. 20, pp. 3926–3929, Nov. 1997, doi: 10.1103/PhysRevLett.79.3926.

[31] E. Şaşıoğlu, L. M. Sandratskii, and P. Bruno, "First-principles calculation of the intersub-lattice exchange interactions and Curie temperatures of the full Heusler alloys Ni_2MnX (X = Ga , In , Sn , Sb)," *Phys. Rev. B*, vol. 70, no. 2, p. 024427, Jul. 2004, doi: 10.1103/PhysRevB.70.024427.

[32] V. Sánchez-Alarcos, V. Recarte, J. I. Pérez-Landazábal, C. Gómez-Polo, and J. A. Rodríguez-Velamazán, "Role of magnetism on the martensitic transformation in Ni–Mn-based magnetic shape memory alloys," *Acta Materialia*, vol. 60, no. 2, pp. 459–468, Jan. 2012, doi: 10.1016/j.actamat.2011.10.026.

[33] X. Moya, L. Mañosa, A. Planes, T. Krenke, M. Acet, and E. F. Wassermann, "Martensitic transition and magnetic properties in Ni–Mn–X alloys," *Materials Science and Engineering: A*, vol. 438–440, pp. 911–915, Nov. 2006, doi: 10.1016/j.msea.2006.02.053.

[34] G. Porcari S. Fabbrici, C. Pernechele, F. Albertini, M. Buzzi, A. Paoluzi, J. Kamarad, Z. Arnold, and M. Solzi, "Reverse magneto-structural transformation and adiabatic temperature change in Co- and In-substituted Ni-Mn-Ga alloys," *Phys. Rev. B*, vol. 85, no. 2, p. 024414, Jan. 2012, doi: 10.1103/PhysRevB.85.024414.

[35] R. Kainuma, W. Ito, R. Y. Umetsu, K. Oikawa, and K. Ishida, "Magnetic field-induced reverse transformation in B2-type NiCoMnAl shape memory alloys," *Appl. Phys. Lett.*, vol. 93, no. 9, p. 091906, Sep. 2008, doi: 10.1063/1.2965811.

[36] R. Kainuma, Y. Imano, W. Ito, H. Morito, Y. Sutou, K. Oikawa, A. Fujita, K. Ishida, S. Okamoto, O. Kitakami, and T. Kanomata, "Metamagnetic shape memory effect in a Heusler-type $Ni_{43}Co_7Mn_{39}Sn_{11}$ polycrystalline alloy," *Appl. Phys. Lett.*, vol. 88, no. 19, p. 192513, May 2006, doi: 10.1063/1.2203211.

[37] J. Du, Q. Zheng, W. J. Ren, W. J. Feng, X. G. Liu, and Z. D. Zhang, "Magnetocaloric effect and magnetic-field-induced shape recovery effect at room temperature in ferromagnetic Heusler alloy Ni-Mn-Sb," *J. Phys. D: Appl. Phys.*, vol. 40, no. 18, p. 5523, Aug. 2007, doi: 10.1088/0022-3727/40/18/001.

[38] K. Oikawa, W. Ito, Y. Imano, Y. Sutou, R. Kainuma, K. Ishida, S. Okamoto, O. Kitakami, and T. Kanomata, "Effect of magnetic field on martensitic transition of $Ni_{46}Mn_{41}In_{13}$ Heusler alloy," *Appl. Phys. Lett.*, vol. 88, no. 12, p. 122507, Mar. 2006, doi: 10.1063/1.2187414.

[39] Y. Sutou, R. Kainuma, K. Ishida, and M. Taya, "Martensitic transformation behavior under magnetic field in Co-Ni-Al ferromagnetic shape memory alloys," in *Smart Structures and Materials 2003: Active Materials: Behavior and Mechanics*, SPIE, Aug. 2003, pp. 159–168. doi: 10.1117/12.484349.

[40] A. A. Cherechukin, I. E. Dikshtein, D. I. Ermakov, A. V. Glebov, V. V. Koledov, D. A. Kosolapov, V. G. Shavrov, A. A. Tulaikova, E. P. Krasnoperov, and T. Takagi, "Shape memory effect due to magnetic field-induced thermoelastic martensitic transformation in polycrystalline Ni-Mn-Fe-Ga alloy," *Physics Letters A*, vol. 291, no. 2, pp. 175–183, Dec. 2001, doi: 10.1016/S0375-9601(01)00688-0.

[41] T. Wada, Y. Liang, H. Kato, T. Tagawa, M. Taya, and T. Mori, "Structural change and straining in Fe–Pd polycrystals by magnetic field," *Materials Science and Engineering: A*, vol. 361, no. 1, pp. 75–82, Nov. 2003, doi: 10.1016/S0921-5093(03)00444-1.

[42] L. Mañosa, D. González-Alonso, A. Planes, E. Bonnot, M. Barrio, J.-Lluís Tamarit, S. Aksoy, and M. Acet , "Giant solid-state barocaloric effect in the Ni-Mn-In magnetic shape-memory alloy," *Nature Mater*, vol. 9, no. 6, Art. no. 6, Jun. 2010, doi: 10.1038/nmat2731.

[43] S. Y. Yu, Z. H. Liu, G. D. Liu, J. L. Chen, Z. X. Cao, G. H. Wu, B. Zhang, and X. X. Zhang, "Large magnetoresistance in single-crystalline $Ni_{50}Mn_{50-x}In_x$ alloys (x=14–16) upon martensitic transformation," *Appl. Phys. Lett.*, vol. 89, no. 16, p. 162503, Oct. 2006, doi: 10.1063/1.2362581.

[44] K. Koyama, H. Okada, K. Watanabe, T. Kanomata, R. Kainuma, W. Ito, K. Oikawa, and K. Ishida, "Observation of large magnetoresistance of magnetic Heusler alloy $Ni_{50}Mn_{36}Sn_{14}$ in high magnetic fields," *Appl. Phys. Lett.*, vol. 89, no. 18, p. 182510, Oct. 2006, doi: 10.1063/1.2374868.

[45] W. Ito, K. Ito, R. Y. Umetsu, R. Kainuma, K. Koyama, K. Watambe, A. Fujita, K. Oikawa, K. Ishida, and T. Kanomata, "Kinetic arrest of martensitic transformation in the NiCoMnIn metamagnetic shape memory alloy," *Appl. Phys. Lett.*, vol. 92, no. 2, p. 021908, Jan. 2008, doi: 10.1063/1.2833699.

[46] Y. B. Yang, X. B. Ma, G. Chen, J. Z. Wei, R. Wu, J. Z. Han, H. L. Du, C. S. Wang, S. Q. Liu, Y. C. Yang, Y. Zhang, J. B. Yang "Structure and exchange bias of $Ni_{50}Mn_{37}Sn_{13}$ ribbons," *Journal of Applied Physics*, vol. 111, no. 7, p. 07A916, Apr. 2012, doi: 10.1063/1.3672244.

[47] E. Warburg, "Magnetische Untersuchungen," *Ann. Phys.*, vol. 249, no. 5, pp. 141–164, 1881, doi: 10.1002/andp.18812490510.

[48] V. K. Pecharsky and K. A. Gschneidner Jr, "Magnetocaloric effect and magnetic refrigeration," *Journal of Magnetism and Magnetic Materials*, vol. 200, no. 1, pp. 44–56, Oct. 1999, doi: 10.1016/S0304-8853(99)00397-2.

[49] V. K. Pecharsky and K. A. Gschneidner, "Some common misconceptions concerning magnetic refrigerant materials," *Journal of Applied Physics*, vol. 90, no. 9, pp. 4614–4622, Nov. 2001, doi: 10.1063/1.1405836.

[50] A. M. Tishin, "Magnetocaloric effect in strong magnetic fields," *Cryogenics*, vol. 30, no. 2, pp. 127–136, Feb. 1990, doi: 10.1016/0011-2275(90)90258-E.

[51] V. K. Pecharsky, K. A. Gschneidner, A. O. Pecharsky, and A. M. Tishin, "Thermodynamics of the magnetocaloric effect," *Phys. Rev. B*, vol. 64, no. 14, p. 144406, Sep. 2001, doi: 10.1103/PhysRevB.64.144406.

[52] Y. I. Spichkin and A. M. Tishin, "Magnetocaloric effect at the first-order magnetic phase transitions," *Journal of Alloys and Compounds*, vol. 403, no. 1, pp. 38–44, Nov. 2005, doi: 10.1016/j.jallcom.2005.05.026.

[53] A. Aliev A. Batdalov, S. Bosko, V. Buchelnikov, I. Dikshtein, V. Khovailo, V. Koledov, R. Levitin, V. Shavrov, and T. Takagi, "Magnetocaloric effect and magnetization in a Ni–Mn–Ga Heusler alloy in the vicinity of magneto-structural transition," *Journal of Magnetism and Magnetic Materials*, vol. 272–276, pp. 2040–2042, May 2004, doi: 10.1016/j.jmmm.2003.12.1363.

[54] Z. Li, Yudong Zhang, C. F. Sánchez-Valdés, J. L. Sánchez Llamazares, Claude Esling, Xiang Zhao, and Liang Zuo, "Giant magnetocaloric effect in melt-spun Ni-Mn-Ga ribbons with magneto-multistructural transformation," *Appl. Phys. Lett.*, vol. 104, no. 4, p. 044101, Jan. 2014, doi: 10.1063/1.4863273.

[55] J. Marcos, L. Mañosa, A. Planes, F. Casanova, X. Batlle, and A. Labarta, "Multiscale origin of the magnetocaloric effect in Ni-Mn-Ga shape-memory alloys," *Phys. Rev. B*, vol. 68, no. 9, p. 094401, Sep. 2003, doi: 10.1103/PhysRevB.68.094401.

[56] P. A. Bhobe, K. R. Priolkar, and A. K. Nigam, "Room temperature magnetocaloric effect in Ni–Mn–In," *Appl. Phys. Lett.*, vol. 91, no. 24, p. 242503, Dec. 2007, doi: 10.1063/1.2823601.

[57] M. Khan, N. Ali, and S. Stadler, "Inverse magnetocaloric effect in ferromagnetic $Ni_{50}Mn_{37+x}Sb_{13-x}$ Heusler alloys," *Journal of Applied Physics*, vol. 101, no. 5, p. 053919, Mar. 2007, doi: 10.1063/1.2710779.

[58] Z. D. Han, D. H. Wamg, C. L. Zhang, H. C. Xuan, J. R. Zhang, B. X. Gu, and Y. W. Du, "The phase transitions, magnetocaloric effect, and magnetoresistance in Co doped Ni-Mn-Sb ferromagnetic shape memory alloys," *Journal of Applied Physics*, vol. 104, no. 5, p. 053906, Sep. 2008, doi: 10.1063/1.2975146.

[59] A. Ghosh and K. Mandal, "Effect of structural disorder on the magnetocaloric properties of Ni-Mn-Sn alloy," *Appl. Phys. Lett.*, vol. 104, no. 3, p. 031905, Jan. 2014, doi: 10.1063/1.4862431.

[60] V. K. Pecharsky, A. P. Holm, K. A. Gschneidner, and R. Rink, "Massive Magnetic-Field-Induced Structural Transformation in G d 5 G e 4 and the Nature of the Giant Magnetocaloric Effect," *Phys. Rev. Lett.*, vol. 91, no. 19, p. 197204, Nov. 2003, doi: 10.1103/PhysRevLett.91.197204.

[61] P. Langevin, "Magnétisme et théorie des électrons," *Ann. chim. et phys.*, no. 8, p. 203, 1905.

[62] P. Debye, "Einige Bemerkungen zur Magnetisierung bei tiefer Temperatur," *Annalen der Physik*, vol. 386, no. 25, pp. 1154–1160, 1926, doi: 10.1002/andp.19263862517.

[63] W. F. Giauque, "A Thermodynamic treatment of certain magnetic effects. A proposed method of producing temperatures considerably below 1° absolute," *ACS Publications*, May 01, 2002. https://pubs.acs.org/doi/pdf/10.1021/ja01407a003 (accessed Aug. 11, 2021).

[64] W. F. Giauque and D. P. MacDougall, "Attainment of Temperatures Below 1° Absolute by Demagnetization of $Gd_2(SO_4)_3.8H_2O$," *Phys. Rev.*, vol. 43, no. 9, pp. 768–768, May 1933, doi: 10.1103/PhysRev.43.768.

[65] K. A. Gschneidner Jr., V. K. Pecharsky, A. O. Pecharsky, and C. B. Zimm, "Recent Developments in Magnetic Refrigeration," *MSF*, vol. 315–317, pp. 69–76, Jul. 1999, doi: 10.4028/www.scientific.net/MSF.315-317.69.

[66] K. A. Gschneidner and V. K. Pecharsky, "Magnetocaloric Materials," *Annual Review of Materials Science*, vol. 30, no. 1, pp. 387–429, 2000, doi: 10.1146/annurev.matsci.30.1.387.

[67] Y. Sutou, Y. Imano, N. Koeda, T. Omori, R. Kainuma, K. Ishida, and K. Oikawa, "Magnetic and martensitic transformations of NiMnX(X=In,Sn,Sb) ferromagnetic shape memory alloys," *Appl. Phys. Lett.*, vol. 85, no. 19, p. 4358, 2004, doi: 10.1063/1.1808879.

[68] A. Planes, L. Mañosa, and M. Acet, "Magnetocaloric effect and its relation to shape-memory properties in ferromagnetic Heusler alloys," *J. Phys.: Condens. Matter*, vol. 21, no. 23, p. 233201, Jun. 2009, doi: 10.1088/0953-8984/21/23/233201.

[69] W. Ito, Y. Imano, R. Kainuma, Y. Sutou, K. Oikawa, and K. Ishida, "Martensitic and Magnetic Transformation Behaviors in Heusler-Type NiMnIn and NiCoMnIn Metamagnetic Shape Memory Alloys," *Metall and Mat Trans A*, vol. 38, no. 4, pp. 759–766, Jun. 2007, doi: 10.1007/s11661-007-9094-9.

[70] H. S. Liu, C. L. Zhang, Z. D. Han, H. C. Xuan, D. H. Wang, and Y. W. Du, "The effect of Co doping on the magnetic entropy changes in $Ni_{44-x}Co_xMn_{45}Sn_{11}$ alloys," *Journal of Alloys and Compounds*, vol. 467, no. 1, pp. 27–30, Jan. 2009, doi: 10.1016/j.jallcom.2007.11.137.

[71] H. C. Xuan, F. H. Chen, P. D. Han, D. H. Wang, and Y. W. Du, "Effect of Co addition on the martensitic transformation and magnetocaloric effect of Ni-Mn-Al ferromagnetic shape memory alloys," *Intermetallics*, vol. 47, pp. 31–35, Apr. 2014, doi: 10.1016/j.intermet.2013.12.007.

[72] J. Liu, T. Gottschall, K. P. Skokov, J. D. Moore, and O. Gutfleisch, "Giant magnetocaloric effect driven by structural transitions," *Nature Mater*, vol. 11, no. 7, Art. no. 7, Jul. 2012, doi: 10.1038/nmat3334.

[73] R. Kainuma, Y. Imano, W. Ito, Y. Sutou, H. Morito, S. Okamoto, O. Kitakami, K. Oikawa, A. Fujita, T. Kanomata, and K. Ishida , "Magnetic-field-induced shape recovery by reverse phase transformation," *Nature*, vol. 439, no. 7079, Art. no. 7079, Feb. 2006, doi: 10.1038/nature04493.

[74] D. Bourgault, J. Tillier, P. Courtois, D. Maillard, and X. Chaud, "Large inverse magnetocaloric effect in Ni45Co5Mn37.5In12.5 single crystal above 300 K," *Appl. Phys. Lett.*, vol. 96, no. 13, p. 132501, Mar. 2010, doi: 10.1063/1.3372633.

[75] L. Huang, D.Y. Cong, L. Ma, Z.H. Nie, M.G. Wang, Z.L. Wang, H.L. Suo, Y. Ren, and Y.D. Wang, "Large magnetic entropy change and magnetoresistance in a $Ni_{41}Co_9Mn_{40}Sn_{10}$ magnetic shape memory alloy," *Journal of Alloys and Compounds*, vol. 647, pp. 1081–1085, Oct. 2015, doi: 10.1016/j.jallcom.2015.06.175.

[76] A. K. Nayak, K. G. Suresh, and A. K. Nigam, "Giant inverse magnetocaloric effect near room temperature in Co substituted NiMnSb Heusler alloys," *J. Phys. D: Appl. Phys.*, vol. 42, no. 3, p. 035009, Feb. 2009, doi: 10.1088/0022-3727/42/3/035009.

[77] L. Huang, D. Y. Cong, L. Ma, Z. H. Nie, Z. L. Wang, H. L. Suo, Y. Ren, and Y. D. Wang, "Large reversible magnetocaloric effect in a Ni-Co-Mn-In magnetic shape memory alloy," *Appl. Phys. Lett.*, vol. 108, no. 3, p. 032405, Jan. 2016, doi: 10.1063/1.4940441.

[78] V. Recarte, J. I. Pérez-Landazábal, V. Sánchez-Alarcos, and J. A. Rodríguez-Velamazán, "Dependence of the martensitic transformation and magnetic transition on the atomic order in Ni-Mn-In metamagnetic shape memory alloys," *Acta Materialia*, vol. 60, no. 5, pp. 1937–1945, Mar. 2012, doi: 10.1016/j.actamat.2012.01.020.

[79] X. Wang, F. Sun, J. Wang, Q. Yu, Y. Wu, H. Hua, and C. Jiang, "Influence of annealing temperatures on the magneto-structural transition and magnetocaloric effect of $Ni_{40}Co_{10}Mn_{40}Sn_{10}$ powders," *Journal of Alloys and Compounds*, vol. 691, pp. 215–219, Jan. 2017, doi: 10.1016/j.jallcom.2016.08.253.

[80] P. Czaja, J. Przewoźnik, M. Fitta, M. Bałanda, A. Chrobak, B. Kania, P. Zackiewicz, A. Wójcik, M. Szlezynger, and W. Maziarz, "Effect of ball milling and thermal treatment on exchange bias and magnetocaloric properties of $Ni_{48}Mn_{39.5}Sn_{10.5}Al_2$ ribbons," *Journal of Magnetism and Magnetic Materials*, vol. 401, pp. 223–230, Mar. 2016, doi: 10.1016/j.jmmm.2015.10.043.

[81] A. L. Alves, E. C. Passamani, V. P. Nascimento, A. Y. Takeuchi, and C. Larica, "Influence of grain refinement and induced crystal defects on the magnetic properties of Ni50Mn36Sn14 Heusler alloy," *J. Phys. D: Appl. Phys.*, vol. 43, no. 34, p. 345001, Aug. 2010, doi: 10.1088/0022-3727/43/34/345001.

[82] E. C. Passamani, V.P. Nascimento, C. Larica, A.Y. Takeuchi, A.L. Alves, J.R. Proveti, M.C. Pereira, and J.D. Fabris, "The influence of chemical disorder enhancement on the martensitic transformation of the $Ni_{50}Mn_{36}Sn_{14}$ Heusler-type alloy," *Journal of Alloys and Compounds*, vol. 509, no. 30, pp. 7826–7832, Jul. 2011, doi: 10.1016/j.jallcom.2011.05.018.

[83] S. Singh, P. Kushwaha, F. Scheibel, H. P. Liermann, S. R. Barman, M. Acet, C. Felser, and D. Pandey, "Residual stress induced stabilization of martensite phase and its effect on the magneto-structural transition in Mn-rich Ni-Mn-In/Ga magnetic shape-memory alloys," *Phys. Rev. B*, vol. 92, no. 2, p. 020105, Jul. 2015, doi: 10.1103/PhysRevB.92.020105.

[84] I. Unzueta, J. López-García, V. Sánchez-Alarcos, V. Recarte, J. I. Pérez-Landazábal, J. A. Rodríguez-Velamazán, J. S. Garitaonandia, J. A. García, and F. Plazaola, "^{119}Sn Mössbauer spectroscopy for assessing the local stress and defect state towards the tuning of Ni-Mn-Sn alloys," *Appl. Phys. Lett.*, vol. 110, no. 18, p. 181908, May 2017, doi: 10.1063/1.4982630.

[85] J. López-García, V. Sánchez-Alarcos , V. Recarte, J.A. Rodríguez-Velamazán, I. Unzueta, J.A. García, F. Plazaola, P. La Roca, and J.I. Pérez-Landazábal, "Effect of high-energy ball-milling on the magneto-structural properties of a $Ni_{45}Co_5Mn_{35}Sn_{15}$ alloy," *Journal of Alloys and Compounds*, vol. 858, p. 158350, Mar. 2021, doi: 10.1016/j.jallcom.2020.158350.

[86] D. Martínez-Blanco, P. Gorria, A. Fernández-Martínez, M. J. Pérez, G. J. Cuello, and J. A. Blanco, "Spin-glass-like behaviour in ball milled Fe30Cr70 alloy studied by ac magnetic susceptibility," *Journal of Alloys and Compounds*, vol. 509, pp. S397–S399, Jun. 2011, doi: 10.1016/j.jallcom.2010.11.039.

[87] G. F. Zhou and H. Bakker, "Spin-glass behavior of amorphous ${\mathrm{Co}}_{2}$Ge synthesized by mechanical milling," *Phys. Rev. Lett.*, vol. 72, no. 14, pp. 2290–2293, Apr. 1994, doi: 10.1103/PhysRevLett.72.2290.

[88] E. E. Levin, D. A. Kitchaev, Y. M. Eggeler, J. A. Mayer, P. Behera, D. S. Gianola, A.Van der Ven, T. M. Pollock, and R. Seshadri, "Influence of plastic deformation on the magnetic properties of Heusler $MnAu_2Al$," *Phys. Rev. Mater.*, vol. 5, no. 1, p. 014408, Jan. 2021, doi: 10.1103/PhysRevMaterials.5.014408.

[89] K. V. Peruman, R. Chokkalingam, and M. Mahendran, "Annealing effect on phase transformation in nano structured Ni-Mn-Ga ferromagnetic shape memory alloy," *Phase Transitions*, vol. 83, no. 7, pp. 509–517, Jul. 2010, doi: 10.1080/01411594.2010.495554.

[90] K. Vallal Peruman, M. Mahendran, S. Seenithurai, R. Chokkalingam, R. K. Singh, and V. Chandrasekaran, "Internal stress dependent structural transition in ferromagnetic Ni-Mn-Ga nanoparticles prepared by ball milling," *Journal of Physics and Chemistry of Solids*, vol. 71, no. 11, pp. 1540–1544, Nov. 2010, doi: 10.1016/j.jpcs.2010.07.022.

[91] B. Tian, F. Chen, Y. Liu, and Y. F. Zheng, "Effect of ball milling and post-annealing on magnetic properties of $Ni_{49.8}Mn_{28.5}Ga_{21.7}$ alloy powders," *Intermetallics*, vol. 16, no. 11, pp. 1279–1284, Nov. 2008, doi: 10.1016/j.intermet.2008.08.002.

[92] V. Sánchez-Alarcos, J. López-García, I. Unzueta, J.I. Pérez-Landazábal, V. Recarte, J.J. Beato-López, J.A. García, F. Plazaola, and J.A. Rodríguez-Velamazán, "Magnetocaloric effect enhancement driven by intrinsic defects in a $Ni_{45}Co_5Mn_{35}Sn_{15}$ alloy," *Journal of Alloys and Compounds, 774 (2019) 586-592*, 2019.

[93] E. Matyja, K. Prusik, M. Zubko, G. Dercz, and K. Glowka, "Structure of the Ni-Co-Mn-In alloy obtained by mechanical alloying and sintering," *Journal of Alloys and Compounds*, vol. 801, pp. 529–535, Sep. 2019, doi: 10.1016/j.jallcom.2019.06.079.

[94] G. Cavazzini, F. Cugini, F. Puglielli, S. Fabbrici, D. Delmonte, G. Trevisi, L. Nasi, L. Righi, S. Ener, L. Pfeuffer, D. Koch, O. Gutfleisch, F. Albertini, and M. Solzi, "Effect of size and disorder on martensitic phase transition and thermal hysteresis in milled Ni-Mn-In-Co micro-particles," *Journal of Alloys and Compounds*, vol. 906, p. 164377, Jun. 2022, doi: 10.1016/j.jallcom.2022.164377.

[95] J. Ortín and A. Planes, "Thermodynamic analysis of thermal measurements in thermoelastic martensitic transformations," *Acta Metallurgica*, vol. 36, no. 8, pp. 1873–1889, Aug. 1988, doi: 10.1016/0001-6160(88)90291-X.

[96] S. M. Ueland, Y. Chen, and C. A. Schuh, "Oligocrystalline Shape Memory Alloys," *Advanced Functional Materials*, vol. 22, no. 10, pp. 2094–2099, 2012, doi: 10.1002/adfm.201103019.

[97] J. S. Juan, M. L. Nó, and C. A. Schuh, "Nanoscale shape-memory alloys for ultrahigh mechanical damping," *Nature Nanotech*, vol. 4, no. 7, Art. no. 7, Jul. 2009, doi: 10.1038/nnano.2009.142.

[98] K. Tsuchiya, M. Inuzuka, D. Tomus, A. Hosokawa, H. Nakayama, K. Morii, Y. Todaka, and M. Umemoto, "Martensitic transformation in nanostructured TiNi shape memory alloy formed via severe plastic deformation," *Materials Science and Engineering: A*, vol. 438–440, pp. 643–648, Nov. 2006, doi: 10.1016/j.msea.2006.01.110.

[99] Z. Zhang, X. Ding, J. Sun, T. Suzuki, T. Lookman, K. Otsuka, and X. Ren, "Nonhysteretic Superelasticity of Shape Memory Alloys at the Nanoscale," *Phys. Rev. Lett.*, vol. 111, no. 14, p. 145701, Sep. 2013, doi: 10.1103/PhysRevLett.111.145701.

[100] D. M. Liu, Z. H. Nie, Y. Ren, Y. D. Wang, J. Pearson, P. K. Liaw and D. E. Brown "Structural Transitions and Magnetic Properties of $Ni_{50}Mn_{36.7}In_{13.3}$ Particles with Amorphous-Like Phase," *Metall Mater Trans A*, vol. 42, no. 10, pp. 3062–3070, Oct. 2011, doi: 10.1007/s11661-011-0724-x.

[101] G. F. Zhou and H. Bakker, "Atomic disorder and amorphization of B2-structure CoZr by ball milling," *Scripta Materialia*, vol. 34, no. 1, pp. 29–35, Jan. 1996, doi: 10.1016/1359-6462(95)00467-X.

[102] L. Zhang, E. Brück, O. Tegus, K. H. J. Buschow, and F. R. de Boer, "The crystallization of amorphous Fe2MnGe powder prepared by ball milling," *Journal of Alloys and Compounds*, vol. 352, no. 1, pp. 99–102, Mar. 2003, doi: 10.1016/S0925-8388(02)01116-7.

[103] C. Suryanarayana, "Mechanical alloying and milling," *Progress in Materials Science*, vol. 46, no. 1, pp. 1–184, Jan. 2001, doi: 10.1016/S0079-6425(99)00010-9.

[104] J. Bai, D. Liu, J. Gu, X. Jiang, X. Liang, Z. Guan, Y. Zhang, C. Esling, X. Zhao, and L. Zuo "Excellent mechanical properties and large magnetocaloric effect of spark plasma sintered Ni-Mn-In-Co alloy," *Journal of Materials Science & Technology*, vol. 74, pp. 46–51, May 2021, doi: 10.1016/j.jmst.2020.10.011.

[105] D. Bourgault, J. Tillier, P. Courtois, D. Maillard, and X. Chaud, "Large inverse magnetocaloric effect in $Ni_{45}Co_5Mn_{37.5}In_{12.5}$ single crystal above 300 K," *Appl. Phys. Lett.*, vol. 96, no. 13, p. 132501, Mar. 2010, doi: 10.1063/1.3372633.

[106] R. Kainuma, Y. Imano, W. Ito, Y. Sutou, H. Morito, S. Okamoto, O. Kitakami, K. Oikawa, A. Fujita, T. Kanomata and K. Ishida "Magnetic-field-induced shape recovery by reverse phase transformation," *Nature*, vol. 439, no. 7079, Art. no. 7079, Feb. 2006, doi: 10.1038/nature04493.

[107] H. E. Karaca, I. Karaman, B. Basaran, Y. Ren, Y. I. Chumlyakov, and H. J. Maier, "Magnetic Field-Induced Phase Transformation in NiMnCoIn Magnetic Shape-Memory Alloys-A New Actuation Mechanism with Large Work Output," *Adv. Funct. Mater.*, vol. 19, no. 7, Art. no. 7, Apr. 2009, doi: 10.1002/adfm.200801322.

[108] T. Gottschall, K. P. Skokov, B. Frincu, and O. Gutfleisch, "Large reversible magnetocaloric effect in Ni-Mn-In-Co," *Appl. Phys. Lett.*, vol. 106, no. 2, Art. no. 2, Jan. 2015, doi: 10.1063/1.4905371.

[109] R. Kainuma, Y. Imano, W. Ito, H. Morito, Y. Sutou, K. Oikawa, A. Fujita, K. Ishida, S. Okamoto, O. Kitakami, and T. Kanomata "Metamagnetic shape memory effect in a Heusler-type $Ni_{43}Co_7Mn_{39}Sn_{11}$ polycrystalline alloy," *Appl. Phys. Lett.*, vol. 88, no. 19, p. 192513, May 2006, doi: 10.1063/1.2203211.

[110] A. K. Nayak, K. G. Suresh, and A. K. Nigam, "Giant inverse magnetocaloric effect near room temperature in Co substituted NiMnSb Heusler alloys," *J. Phys. D: Appl. Phys.*, vol. 42, no. 3, p. 035009, Jan. 2009, doi: 10.1088/0022-3727/42/3/035009.

[111] L. Huang, D. Y. Cong, H. L. Suo, and Y. D. Wang, "Giant magnetic refrigeration capacity near room temperature in $Ni_{40}Co_{10}Mn_{40}Sn_{10}$ multi-functional alloy," *Appl. Phys. Lett.*, vol. 104, no. 13, Art. no. 13, Mar. 2014, doi: 10.1063/1.4870771.

[112] R. Y. Umetsu, A. Sheikh, W. Ito, B. Ouladdiaf, K. R. A. Ziebeck, T. Kanomata, and R. Kainuma "The effect of Co substitution on the magnetic properties of the Heusler alloy $Ni_{50}Mn_{33}Sn_{17}$," *Appl. Phys. Lett.*, vol. 98, no. 4, p. 042507, Jan. 2011, doi: 10.1063/1.3548558.

[113] J. López-García, V. Sánchez-Alarcos, V. Recarte, J.I. Pérez-Landazábal, O. Fabelo, E. Cesari, and J.A. Rodríguez-Velamazán, "Routes for enhanced magnetism in Ni-Mn-In metamagnetic shape memory alloys," *Scripta Materialia*, vol. 167, pp. 21–25, 2019, doi: 10.1016/j.scriptamat.2019.03.025.

[114] W. Ito, Y. Imano, R. Kainuma, Y. Sutou, K. Oikawa, and K. Ishida, "Martensitic and Magnetic Transformation Behaviors in Heusler-Type NiMnIn and NiCoMnIn Metamagnetic Shape Memory Alloys," *Metall and Mat Trans A*, vol. 38, no. 4, pp. 759–766, Apr. 2007, doi: 10.1007/s11661-007-9094-9.

[115] H. E. Karaca, I. Karaman, A. Brewer, B. Basaran, Y. I. Chumlyakov, and H. J. Maier, "Shape memory and pseudoelasticity response of NiMnCoIn magnetic shape memory alloy single crystals," *Scripta Materialia*, vol. 58, no. 10, pp. 815–818, May 2008, doi: 10.1016/j.scriptamat.2007.12.029.

[116] L. Huang, D. Y. Cong, L. Ma, Z. H. Nie, Z. L. Wang, H. L. Suo, Y. Ren, and Y. D. Wang "Large reversible magnetocaloric effect in a Ni-Co-Mn-In magnetic shape memory alloy," *Appl. Phys. Lett.*, vol. 108, no. 3, Art. no. 3, Jan. 2016, doi: 10.1063/1.4940441.

[117] V. Sánchez-Alarcos, V. Recarte, J. I. Pérez-Landazábal, E. Cesari, and J. A. Rodríguez-Velamazán, "Long-Range Atomic Order and Entropy Change at the Martensitic Transformation in a Ni-Mn-In-Co Metamagnetic Shape Memory Alloy," *Entropy*, vol. 16, no. 5, Art. no. 5, May 2014, doi: 10.3390/e16052756.

[118] J. A. Monroe, I. Karaman, B. Basaran, W. Ito, R.Y. Umetsu, R. Kainuma, K. Koyama, and Y.I. Chumlyakov, "Direct measurement of large reversible magnetic-field-induced strain in Ni-Co-Mn-In metamagnetic shape memory alloys," *Acta Materialia*, vol. 60, no. 20, pp. 6883–6891, Dec. 2012, doi: 10.1016/j.actamat.2012.07.040.

[119] V. Recarte, J. I. Pérez-Landazábal, and V. Sánchez-Alarcos, "Dependence of the relative stability between austenite and martensite phases on the atomic order in a Ni-Mn-In Metamagnetic Shape Memory Alloy," *Journal of Alloys and Compounds*, vol. 536, pp. S308–S311, Sep. 2012, doi: 10.1016/j.jallcom.2011.11.053.

[120] V. Recarte, J. I. Pérez-Landazábal, V. Sánchez-Alarcos, and J. A. Rodríguez-Velamazán, "Dependence of the martensitic transformation and magnetic transition on the atomic order in Ni-Mn-In metamagnetic shape memory alloys," *Acta Materialia*, vol. 60, no. 5, Art. no. 5, Mar. 2012, doi: 10.1016/j.actamat.2012.01.020.

[121] V. Recarte, J. I. Pérez-Landazábal, and V. Sánchez-Alarcos, "Dependence of the relative stability between austenite and martensite phases on the atomic order in a Ni–Mn–In Metamagnetic Shape

Memory Alloy," *Journal of Alloys and Compounds*, vol. 536, pp. S308–S311, Sep. 2012, doi: 10.1016/j.jallcom.2011.11.053.

[122] J. L. Sánchez Llamazares, H. Flores-Zúñiga, D. Ríos-Jara, C. F. Sánchez-Valdes, T. García-Fernández, C. A. Ross, and C. García, "Structural and magnetic characterization of the intermartensitic phase transition in NiMnSn Heusler alloy ribbons," *Journal of Applied Physics*, vol. 113, no. 17, p. 17A948, May 2013, doi: 10.1063/1.4800836.

[123] M. Acet, "Magnetoelastic sponges," *Nature Mater*, vol. 8, no. 11, Art. no. 11, Nov. 2009, doi: 10.1038/nmat2551.

[124] J. Feuchtwanger, M. L. Richard, Y. J. Tang, A. E. Berkowitz, R. C. O'Handley, and S. M. Allen, "Large energy absorption in Ni–Mn–Ga/polymer composites," *Journal of Applied Physics*, vol. 97, no. 10, p. 10M319, May 2005, doi: 10.1063/1.1857653.

[125] J. Liu, N. Scheerbaum, S. Kauffmann-Weiss, and O. Gutfleisch, "NiMn-Based Alloys and Composites for Magnetically Controlled Dampers and Actuators," *Advanced Engineering Materials*, vol. 14, no. 8, pp. 653–667, 2012, doi: https://doi.org/10.1002/adem.201200038.

[126] M. Kohl, M. Gueltig, V. Pinneker, R. Yin, F. Wendler, and B. Krevet, "Magnetic Shape Memory Microactuators," *Micromachines*, vol. 5, no. 4, Art. no. 4, Dec. 2014, doi: 10.3390/mi5041135.

[127] S. V. Kumar, R. K. Singh, M. M. Raja, A. Kumar, S. Bysakh, and M. Mahendran, "Microstructure and nanomechanical properties of Mn-rich Ni–Mn–Ga thin films," *Intermetallics*, vol. 71, pp. 57–64, Apr. 2016, doi: 10.1016/j.intermet.2015.12.012.

[128] M. Schmitt, A. Backen, S. Fähler, and M. Kohl, "Freely movable ferromagnetic shape memory nanostructures for actuation," *Microelectronic Engineering*, vol. 98, pp. 536–539, Oct. 2012, doi: 10.1016/j.mee.2012.07.045.

[129] M. Kohl, D. Brugger, M. Ohtsuka, and T. Takagi, "A novel actuation mechanism on the basis of ferromagnetic SMA thin films," *Sensors and Actuators A: Physical*, vol. 114, no. 2, pp. 445–450, Sep. 2004, doi: 10.1016/j.sna.2003.11.006.

[130] C. A. Biffi and A. Tuissi, "Micro-processing of NiMnGa shape memory alloy by using a nanosecond fiber laser," *Optics & Laser Technology*, vol. 78, pp. 42–49, Apr. 2016, doi: 10.1016/j.optlastec.2015.10.008.

[131] M. Schmitt, A. Backen, S. Fähler, and M. Kohl, "Freely movable ferromagnetic shape memory nanostructures for actuation," *Microelectronic Engineering*, vol. 98, pp. 536–539, Oct. 2012, doi: 10.1016/j.mee.2012.07.045.

[132] M. Kohl, D. Brugger, M. Ohtsuka, and T. Takagi, "A novel actuation mechanism on the basis of ferromagnetic SMA thin films," *Sensors and Actuators A: Physical*, vol. 114, no. 2, Art. no. 2, Sep. 2004, doi: 10.1016/j.sna.2003.11.006.

[133] A. A. Prasanna and S. Ram, "Local strains, calorimetry, and magnetoresistance in adaptive martensite transition in multiple nanostrips of $Ni_{39+x}Mn_{50}Sn_{11-x}$($x \leq 2$) alloys," *Science and Technology of Advanced Materials*, vol. 14, no. 1, p. 015004, Mar. 2013, doi: 10.1088/1468-6996/14/1/015004.

[134] D. L. R. Khanna, V. Sánchez-Alarcos, V. Recarte, and J. I. Pérez-Landazábal, "Correlation between particle size and magnetic properties in soft-milled $Ni_{45}Co_5Mn_{34}In_{16}$ powders," *Intermetallics*, vol. 130, p. 107076, Mar. 2021, doi: 10.1016/j.intermet.2020.107076.

[135] V. Sánchez-Alarcos, J. I. Pérez-Landazábal, V. Recarte, J. A. Rodríguez-Velamazán, and V. A. Chernenko, "Effect of atomic order on the martensitic and magnetic transformations in Ni–Mn–Ga ferromagnetic shape memory alloys," *J. Phys.: Condens. Matter*, vol. 22, no. 16, p. 166001, Apr. 2010, doi: 10.1088/0953-8984/22/16/166001.

[136] K. V. Peruman, S. Vinodh Kumar, K. Pushpanathan, and M. Mahendran, "Structural and Martensitic Transformarion of bulk, disordered and nanocrystalline Ni_2MnGa alloys," *Funct. Mater. Lett.*, vol. 04, no. 04, pp. 415–418, Dec. 2011, doi: 10.1142/S1793604711002329.

[137] A. L. Roytburd, T. S. Kim, Q. Su, J. Slutsker, and M. Wuttig, "Martensitic transformation in constrained films," *Acta Materialia*, vol. 46, no. 14, pp. 5095–5107, Sep. 1998, doi: 10.1016/S1359-6454(98)00165-7.

[138] V. Sánchez-Alarcos, J. López-García, I. Unzueta, J.I. Pérez-Landazábal, V. Recarte, J.J. Beato-López, J.A. García, F. Plazaola and J.A. Rodríguez-Velamazán, "Magnetocaloric effect enhancement driven by intrinsic defects in a $Ni_{45}Co_5Mn_{35}Sn_{15}$ alloy," *Journal of Alloys and Compounds*, vol. 774, pp. 586–592, 2019.

[139] V. Sánchez-Alarcos, V. Recarte, J.I. Pérez-Landazábal, S. Larumbe, R. Caballero-Flores, I. Unzueta, J.A. García, F. Plazaola and J.A. Rodríguez-Velamazán, "Mechanically induced

disorder and crystallization process in Ni-Mn-In ball-milled alloys," *Journal of Alloys and Compounds*, vol. 689, pp. 983–991, Dec. 2016, doi: 10.1016/j.jallcom.2016.08.068.

[140] H. Hosoda, S. Takeuchi, T. Inamura, and K. Wakashima, "Material design and shape memory properties of smart composites composed of polymer and ferromagnetic shape memory alloy particles," *Sci. Technol. Adv. Mater.*, vol. 5, no. 4, p. 503, Jul. 2004, doi: 10.1016/j.stam.2004.02.009.

[141] M. Lahelin, I. Aaltio, O. Heczko, O. Söderberg, Y. Ge, B. Löfgren, S.-P. Hannula and J. Seppälä, "DMA testing of Ni–Mn–Ga/polymer composites," *Composites Part A: Applied Science and Manufacturing*, vol. 40, no. 2, pp. 125–129, Feb. 2009, doi: 10.1016/j.compositesa.2008.10.011.

[142] J. Liu, N. Scheerbaum, S. Weiß, and O. Gutfleisch, "Ni–Mn–In–Co single-crystalline particles for magnetic shape memory composites," *Appl. Phys. Lett.*, vol. 95, no. 15, p. 152503, Oct. 2009, doi: 10.1063/1.3249585.

[143] A. Mostafaei, P. Rodriguez De Vecchis, E. L. Stevens, and M. Chmielus, "Sintering regimes and resulting microstructure and properties of binder jet 3D printed Ni-Mn-Ga magnetic shape memory alloys," *Acta Materialia*, vol. 154, pp. 355–364, Aug. 2018, doi: 10.1016/j.actamat.2018.05.047.

[144] M. P. Caputo, A. E. Berkowitz, A. Armstrong, P. Müllner, and C. V. Solomon, "4D printing of net shape parts made from Ni-Mn-Ga magnetic shape-memory alloys," *Additive Manufacturing*, vol. 21, pp. 579–588, May 2018, doi: 10.1016/j.addma.2018.03.028.

[145] S. L. Taylor, R. N. Shah, and D. C. Dunand, "Ni-Mn-Ga micro-trusses via sintering of 3D-printed inks containing elemental powders," *Acta Materialia*, vol. 143, pp. 20–29, Jan. 2018, doi: 10.1016/j.actamat.2017.10.002.

[146] D. Jafari and W. W. Wits, "The utilization of selective laser melting technology on heat transfer devices for thermal energy conversion applications: A review," *Renewable and Sustainable Energy Reviews*, vol. 91, pp. 420–442, Aug. 2018, doi: 10.1016/j.rser.2018.03.109.

[147] J. D. Moore, D. Klemm, D. Lindackers, S. Grasemann, R. Träger, J. Eckert, L. Löber, S. Scudino, M. Katter, A. Barcza, K. P. Skokov and O. Gutfleisch, "Selective laser melting of La(Fe,Co,Si)$_{13}$ geometries for magnetic refrigeration," *Journal of Applied Physics*, vol. 114, no. 4, p. 043907, Jul. 2013, doi: 10.1063/1.4816465.

[148] A. Annadurai, A.K. Nandakumar, S. Jayakumar, M.D. Kannan, M. Manivel Raja, S. Bysak, R. Gopalan and V. Chandrasekaran, "Composition, structure and magnetic properties of sputter deposited Ni–Mn–Ga ferromagnetic shape memory thin films," *Journal of Magnetism and Magnetic Materials*, vol. 321, no. 6, pp. 630–634, Mar. 2009, doi: 10.1016/j.jmmm.2008.10.015.

[149] S. K. Wu, K. H. Tseng, and J. Y. Wang, "Crystallization behavior of r.f.-sputtered near stoichiometric Ni_2MnGa thin films," *Thin Solid Films*, vol. 408, no. 1, pp. 316–320, Apr. 2002, doi: 10.1016/S0040-6090(02)00134-7.

[150] J. Feuchtwanger, S. Michael, J. Juang, D. Bono, R. C. O'Handley, S. M. Allen, C. Jenkins and J Goldie; Ami Berkowitz, "Energy absorption in Ni-Mn-Ga-polymer composites," *Journal of Applied Physics*, vol. 93, no. 10, pp. 8528–8530, May 2003, doi: 10.1063/1.1557762.

[151] V. C. Solomon, D. J. Smith, Y. Tang, and A. E. Berkowitz, "Microstructural characterization of Ni-Mn-Ga ferromagnetic shape memory alloy powders," *Journal of Applied Physics*, vol. 95, no. 11, pp. 6954–6956, Jun. 2004, doi: 10.1063/1.1687204.

[152] S. Glock and V. Michaud, "Thermal and damping behaviour of magnetic shape memory alloy composites," *Smart Mater. Struct.*, vol. 24, no. 6, p. 065025, May 2015, doi: 10.1088/0964-1726/24/6/065025.

[153] J. Feuchtwanger, J. Aurrekoetxea, J. Zurbitu, J. L. Vilas, L. M. León, J. M. Barandiaran, H. Hosoda and V. A. Chernenko, "Impact Damping in NiMnGa/Polymer Composites," *Materials Transactions*, vol. 55, no. 3, pp. 629–632, 2014, doi: 10.2320/matertrans.M2013407.

[154] W.-T. Chiu, P. Sratong-on, M. Tahara, V. Chernenko, and H. Hosoda, "Large magnetostrains of Ni-Mn-Ga/silicone composite containing system of oriented 5M and 7M martensitic particles," *Scripta Materialia*, vol. 207, p. 114265, Jan. 2022, doi: 10.1016/j.scriptamat.2021.114265.

[155] P. Sratong-on, V. A. Chernenko, J. Feuchtwanger, and H. Hosoda, "Magnetic field-induced rubber-like behavior in Ni-Mn-Ga particles/polymer composite," *Sci Rep*, vol. 9, no. 1, Art. no. 1, Mar. 2019, doi: 10.1038/s41598-019-40189-2.

[156] L. Hines, K. Petersen, G. Z. Lum, and M. Sitti, "Soft Actuators for Small-Scale Robotics," *Advanced Materials*, vol. 29, no. 13, p. 1603483, 2017, doi: 10.1002/adma.201603483.

[157] M. Cianchetti, C. Laschi, A. Menciassi, and P. Dario, "Biomedical applications of soft robotics," *Nat Rev Mater*, vol. 3, no. 6, Art. no. 6, Jun. 2018, doi: 10.1038/s41578-018-0022-y.

[158] M. Sitti, “Miniature soft robots — road to the clinic,” *Nat Rev Mater*, vol. 3, no. 6, Art. no. 6, Jun. 2018, doi: 10.1038/s41578-018-0001-3.

[159] S. Nájera, M. Michel, J. Kyung-Hwan, and J. N. S. Kim, “Characterization of 3D printed PLA/PCL/TiO2 composites for Cancellous bone,” *J. Mater. Sci. Eng*, vol. 7, p. 417, 2018.

[160] D.-H. Kim, R. Ghaffari, N. Lu, and J. A. Rogers, “Flexible and stretchable electronics for biointegrated devices,” *Annual review of biomedical engineering*, vol. 14, no. 1, pp. 113–128, 2012.

[161] M. Amjadi, K.-U. Kyung, I. Park, and M. Sitti, “Stretchable, Skin-Mountable, and Wearable Strain Sensors and Their Potential Applications: A Review,” *Advanced Functional Materials*, vol. 26, no. 11, pp. 1678–1698, 2016, doi: 10.1002/adfm.201504755.

[162] Y. Mao, K. Yu, M. S. Isakov, J. Wu, M. L. Dunn, and H. Jerry Qi, “Sequential Self-Folding Structures by 3D Printed Digital Shape Memory Polymers,” *Sci Rep*, vol. 5, no. 1, Art. no. 1, Sep. 2015, doi: 10.1038/srep13616.

[163] A. Kotikian, R. L. Truby, J. W. Boley, T. J. White, and J. A. Lewis, “3D Printing of Liquid Crystal Elastomeric Actuators with Spatially Programed Nematic Order,” *Advanced Materials*, vol. 30, no. 10, p. 1706164, 2018, doi: 10.1002/adma.201706164.

[164] B. Jang, E. Gutman, N. Stucki, B. F. Seitz, P. D. Wendel-García, T. Newton, J. Pokki, O. Ergeneman, S. Pané, Y. Or and B. J. Nelson, “Undulatory Locomotion of Magnetic Multilink Nanoswimmers,” *Nano Lett.*, vol. 15, no. 7, pp. 4829–4833, Jul. 2015, doi: 10.1021/acs.nanolett.5b01981.

[165] W. Hu, G. Z. Lum, M. Mastrangeli, and M. Sitti, “Small-scale soft-bodied robot with multimodal locomotion,” *Nature*, vol. 554, no. 7690, Art. no. 7690, Feb. 2018, doi: 10.1038/nature25443.

[166] T. Li, G. Li, Y. Liang, T. Cheng, J. Dai, X. Yang, B. Liu, Z. Zeng, Z. Huang, Y. Luo, T. Xie, and W. Yang, “Fast-moving soft electronic fish,” *Science Advances*, vol. 3, no. 4, p. e1602045, Apr. 2017, doi: 10.1126/sciadv.1602045.

[167] S. Iamsaard, S. J. Aßhoff, B. Matt, T. Kudernac, J. J. L. M. Cornelissen, S. P. Fletcher and N Katsonis, “Conversion of light into macroscopic helical motion,” *Nature Chem*, vol. 6, no. 3, Art. no. 3, Mar. 2014, doi: 10.1038/nchem.1859.

[168] H. Shahsavan, A. Aghakhani, H. Zeng, Y. Guo, Z. S. Davidson, A. Priimagi and M. Sitti, “Bioinspired underwater locomotion of light-driven liquid crystal gels,” *Proceedings of the National Academy of Sciences*, vol. 117, no. 10, pp. 5125–5133, Mar. 2020, doi: 10.1073/pnas.1917952117.

[169] M. Li, X. Wang, B. Dong, and M. Sitti, “In-air fast response and high speed jumping and rolling of a light-driven hydrogel actuator,” *Nat Commun*, vol. 11, no. 1, Art. no. 1, Aug. 2020, doi: 10.1038/s41467-020-17775-4.

[170] A. Sydney Gladman, E. A. Matsumoto, R. G. Nuzzo, L. Mahadevan, and J. A. Lewis, “Biomimetic 4D printing,” *Nature Mater*, vol. 15, no. 4, Art. no. 4, Apr. 2016, doi: 10.1038/nmat4544.

[171] Y. Zhang, F. Zhang, Z. Yan, Q. Ma, X. Li, Y. Huang and J. A. Rogers, “Printing, folding and assembly methods for forming 3D mesostructures in advanced materials,” *Nat Rev Mater*, vol. 2, no. 4, Art. no. 4, Mar. 2017, doi: 10.1038/natrevmats.2017.19.

[172] X. Liu, J. Liu, S. Lin, and X. Zhao, “Hydrogel machines,” *Materials Today*, vol. 36, pp. 102–124, Jun. 2020, doi: 10.1016/j.mattod.2019.12.026.

[173] X. Kuang, J. Wu, K. Chen, Z. Zhao, Z. Ding, F. Hu, D. Fang and H. J. Qi, “Grayscale digital light processing 3D printing for highly functionally graded materials,” *Science Advances*, vol. 5, no. 5, p. eaav5790, May 2019, doi: 10.1126/sciadv.aav5790.

[174] R. Liu, X. Kuang, J. Deng, Y. Wang, A. C. Wang, W. Ding, Y. Lai, J. Chen, P. Wang, Z. Lin, H. J. Qi, B. Sun and Z. L. Wang, “Shape Memory Polymers for Body Motion Energy Harvesting and Self-Powered Mechanosensing,” *Advanced Materials*, vol. 30, no. 8, p. 1705195, 2018, doi: 10.1002/adma.201705195.

[175] S. Yim and M. Sitti, “Design and Rolling Locomotion of a Magnetically Actuated Soft Capsule Endoscope,” *IEEE Transactions on Robotics*, vol. 28, no. 1, pp. 183–194, Feb. 2012, doi: 10.1109/TRO.2011.2163861.

[176] H.-W. Huang, F. E. Uslu, P. Katsamba, E. Lauga, M. S. Sakar, and B. J. Nelson, “Adaptive locomotion of artificial microswimmers,” *Science Advances*, vol. 5, no. 1, p. eaau1532, Jan. 2019, doi: 10.1126/sciadv.aau1532.

[177] Y. Kim, G. A. Parada, S. Liu, and X. Zhao, “Ferromagnetic soft continuum robots,” *Science Robotics*, vol. 4, no. 33, p. eaax7329, Aug. 2019, doi: 10.1126/scirobotics.aax7329.

[178] M. Y. Khalid, Z. U. Arif, R. Noroozi, A. Zolfagharian, and M. Bodaghi, "4D printing of shape memory polymer composites: A review on fabrication techniques, applications, and future perspectives," *Journal of Manufacturing Processes*, vol. 81, pp. 759–797, Sep. 2022, doi: 10.1016/j.jmapro.2022.07.035.

[179] L. M. Bollig, P. J. Hilpisch, G. S. Mowry, and B. B. Nelson-Cheeseman, "3D printed magnetic polymer composite transformers," *Journal of Magnetism and Magnetic Materials*, vol. 442, pp. 97–101, Nov. 2017, doi: 10.1016/j.jmmm.2017.06.070.

[180] K. J. Merazzo, A. C. Lima, M. Rincón-Iglesias, L. C. Fernandes, N. Pereira, S. Lanceros-Mendez and P. Martins, "Magnetic materials: a journey from finding north to an exciting printed future," *Mater. Horiz.*, vol. 8, no. 10, pp. 2654–2684, Oct. 2021, doi: 10.1039/D1MH00641J.

[181] A. M. Schmidt, "Electromagnetic Activation of Shape Memory Polymer Networks Containing Magnetic Nanoparticles," *Macromolecular Rapid Communications*, vol. 27, no. 14, pp. 1168–1172, 2006, doi: 10.1002/marc.200600225.

[182] W. Zhao, Z. Huang, L. Liu, W. Wang, J. Leng, and Y. Liu, "Bionic design and performance research of tracheal stent based on shape memory polycaprolactone," *Composites Science and Technology*, vol. 229, p. 109671, Oct. 2022, doi: 10.1016/j.compscitech.2022.109671.

[183] Q. Ze *et al.*, "Magnetic Shape Memory Polymers with Integrated Multi-functional Shape Manipulation," *Advanced Materials*, vol. 32, no. 4, p. 1906657, 2020, doi: 10.1002/adma.201906657.

[184] J. Cui, T. Huang, Z. Luo, P. Testa, H. Gu, X-Z. Chen, B. J. Nelson and L. J. Heyderman, "Nanomagnetic encoding of shape-morphing micromachines," *Nature*, vol. 575, no. 7781, Art. no. 7781, Nov. 2019, doi: 10.1038/s41586-019-1713-2.

[185] K. Yang, L. Hu, X. Ma, S. Ye, L. Cheng, X. Shi, C. Li, Y. Li and Z. Liu, "Multimodal Imaging Guided Photothermal Therapy using Functionalized Graphene Nanosheets Anchored with Magnetic Nanoparticles," *Advanced Materials*, vol. 24, no. 14, pp. 1868–1872, 2012, doi: 10.1002/adma.201104964.

[186] E. Diller, S. Floyd, C. Pawashe, and M. Sitti, "Control of Multiple Heterogeneous Magnetic Microrobots in Two Dimensions on Nonspecialized Surfaces," *IEEE Transactions on Robotics*, vol. 28, no. 1, pp. 172–182, Feb. 2012, doi: 10.1109/TRO.2011.2170330.

[187] H. Lu, M. Zhang, Y. Yang, Q. Huang, T. Fukuda, Z. Wang and Y. Shen, "A bioinspired multilegged soft millirobot that functions in both dry and wet conditions," *Nat Commun*, vol. 9, no. 1, Art. no. 1, Sep. 2018, doi: 10.1038/s41467-018-06491-9.

[188] R. Mohr, K. Kratz, T. Weigel, M. Lucka-Gabor, M. Moneke, and A. Lendlein, "Initiation of shape-memory effect by inductive heating of magnetic nanoparticles in thermoplastic polymers," *Proceedings of the National Academy of Sciences*, vol. 103, no. 10, pp. 3540–3545, Mar. 2006, doi: 10.1073/pnas.0600079103.

[189] A. Besinis, T. De Peralta, and R. D. Handy, "The antibacterial effects of Ag, TiO2 and SiO2 nanoparticles compared to the Dental Disinfectant Chlorhexidine on Streptococcus mutans Using a Suite of Bioassays," *Nanotoxicology*, vol. 8, no. 1, pp. 1–16, 2014.

[190] E. Yousif and R. Haddad, "Photodegradation and photostabilization of polymers, especially polystyrene: review," *SpringerPlus*, vol. 2, no. 1, p. 398, Aug. 2013, doi: 10.1186/2193-1801-2-398.

[191] M. Kurzböck, G. M. Wallner, and R. W. Lang, "Black pigmented polypropylene materials for solar absorbers," *Energy Procedia*, vol. 30, pp. 438–445, Jan. 2012, doi: 10.1016/j.egypro.2012.11.052.

[192] K. Han and M. Yu, "Study of the preparation and properties of UV-blocking fabrics of a PET/TiO2 nanocomposite prepared by in situ polycondensation," *Journal of Applied Polymer Science*, vol. 100, no. 2, pp. 1588–1593, 2006, doi: 10.1002/app.23312.

[193] E. M. Palmero, J. Rial, J. de Vicente, J. Camarero, B. Skårman, H. Vidarsson, P. Larsson and A. Bollero, "Development of permanent magnet MnAlC/polymer composites and flexible filament for bonding and 3D-printing technologies," *Science and Technology of Advanced Materials*, vol. 19, no. 1, pp. 465–473, Dec. 2018, doi: 10.1080/14686996.2018.1471321.

[194] E. M. Palmero, D. Casaleiz, N. A. Jiménez, J. Rial, J. de Vicente, A. Nieto, R. Altimira and A. Bollero, "Magnetic-Polymer Composites for Bonding and 3D Printing of Permanent Magnets," *IEEE Transactions on Magnetics*, vol. 55, no. 2, pp. 1–4, Feb. 2019, doi: 10.1109/TMAG.2018.2863560.

[195] H. Song, H. Lee, J. Lee, J. K. Choe, S. Lee, J. Y. Yi, S. Park, J. W. Yoo, M. S. Kwon, and J. Kim, "Reprogrammable Ferromagnetic Domains for Reconfigurable Soft Magnetic Actuators," *Nano Lett.*, vol. 20, no. 7, pp. 5185–5192, Jul. 2020, doi: 10.1021/acs.nanolett.0c01418.

[196] Á. Díaz-García, J. Revuelta, L. M. Moreno-Ramírez, J. Y. Law, C. Mayer, and V. Franco, "Additive manufacturing of magnetocaloric (La,Ce)(Fe,Mn,Si)13–H particles via polymer-based composite filaments," *Composites Communications*, vol. 35, p. 101352, Nov. 2022, doi: 10.1016/j.coco.2022.101352.

[197] E. M. Palmero, D. Casalei, Javier de Vicente, B. Skårman, H. Vidarsson, Per-Olof Larsson, and A. Bollero. "Effect of particle size distribution on obtaining novel MnAlC-based permanent magnet composites and flexible filaments for 3D-printing," *Additive Manufacturing*, vol. 33, p. 101179, May 2020, doi: 10.1016/j.addma.2020.101179.

[198] G. S. Deshmukh, D. R. Peshwe, S. U. Pathak, and J. D. Ekhe, "Nonisothermal crystallization kinetics and melting behavior of poly(butylene terephthalate) and calcium carbonate nanocomposites," *Thermochimica Acta*, vol. 606, pp. 66–76, Apr. 2015, doi: 10.1016/j.tca.2015.03.008.

[199] A. J. Guerra, P. Cano, M. Rabionet, T. Puig, and J. Ciurana, "3D-Printed PCL/PLA Composite Stents: Towards a New Solution to Cardiovascular Problems," *Materials*, vol. 11, no. 9, Art. no. 9, Sep. 2018, doi: 10.3390/ma11091679.

[200] H. Chen, V. V. Ginzburg, J. Yang, Y. Yang, W. Liu, Y. Huang, L. Du, and B. Chen, "Thermal conductivity of polymer-based composites: Fundamentals and applications," *Progress in Polymer Science*, vol. 59, pp. 41–85, Aug. 2016, doi: 10.1016/j.progpolymsci.2016.03.001.

[201] S. Hwang, E. I. Reyes, K. Moon, R. C. Rumpf, and N. S. Kim, "Thermo-mechanical Characterization of Metal/Polymer Composite Filaments and Printing Parameter Study for Fused Deposition Modeling in the 3D Printing Process," *J. Electron. Mater.*, vol. 44, no. 3, pp. 771–777, Mar. 2015, doi: 10.1007/s11664-014-3425-6.

[202] K. Koyama, K. Watanabe, T. Kanomata, R. Kainuma, K. Oikawa, and K. Ishida, "Observation of field-induced reverse transformation in ferromagnetic shape memory alloy $Ni_{50}Mn_{36}Sn_{14}$," *Appl. Phys. Lett.*, vol. 88, no. 13, p. 132505, Mar. 2006, doi: 10.1063/1.2189916.

[203] H. E. Karaca, I. Karaman, B. Basaran, Y. Ren, Y. I. Chumlyakov, and H. J. Maier, "Magnetic Field-Induced Phase Transformation in NiMnCoIn Magnetic Shape-Memory Alloys-A New Actuation Mechanism with Large Work Output," *Adv. Funct. Mater.*, vol. 19, no. 7, pp. 983–998, Apr. 2009, doi: 10.1002/adfm.200801322.

[204] V. V. Khovaylo, T. Kanomata, T. Tanaka, M. Nakashima, Y. Amako, R. Kainuma, R. Y. Umetsu, H. Morito, and H. Miki, "Magnetic properties of $Ni_{50}Mn_{34.8}In_{5.2}$ probed by M\"ossbauer spectroscopy," *Phys. Rev. B*, vol. 80, no. 14, p. 144409, Oct. 2009, doi: 10.1103/PhysRevB.80.144409.

[205] M. Shahrezaee, M. Salehi, S. Keshtkari, A. Oryan, A. Kamali, and B. Shekarchi, "In vitro and in vivo investigation of PLA/PCL scaffold coated with metformin-loaded gelatin nanocarriers in regeneration of critical-sized bone defects," *Nanomedicine: Nanotechnology, Biology and Medicine*, vol. 14, no. 7, pp. 2061–2073, Oct. 2018, doi: 10.1016/j.nano.2018.06.007.

[206] Q. Yao, J. G. L. Cosme, T. Xu, J. M. Miszuk, P. H. S. Picciani, H. Fong, and H. Sun, "Three dimensional electrospun PCL/PLA blend nanofibrous scaffolds with significantly improved stem cells osteogenic differentiation and cranial bone formation," *Biomaterials*, vol. 115, pp. 115–127, Jan. 2017, doi: 10.1016/j.biomaterials.2016.11.018.

[207] S. Buscemi, V. D. Palumbo, A. Maffongelli, S. Fazzotta, F.S. Palumbo, M. Licciardi, C. Fiorica, R. Puleio, G. Cassata, L. Fiorello, G. Buscemi, and A.I. lo Monte, "Electrospun PHEA-PLA/PCL Scaffold for Vascular Regeneration: A Preliminary in Vivo Evaluation," *Transplantation Proceedings*, vol. 49, no. 4, pp. 716–721, May 2017, doi: 10.1016/j.transproceed.2017.02.017.

[208] R. M. Felfel, L. Poocza, M. Gimeno-Fabra, T. Milde, G. Hildebrand, I. Ahmed, C. Scotchford, V. Sottile, D. M. Grant and K. Liefeith, "In vitro degradation and mechanical properties of PLA-PCL copolymer unit cell scaffolds generated by two-photon polymerization," *Biomed. Mater.*, vol. 11, no. 1, p. 015011, Feb. 2016, doi: 10.1088/1748-6041/11/1/015011.

[209] H. Tsuji, H. Daimon, and K. Fujie, "A New Strategy for Recycling and Preparation of Poly(l-lactic acid): Hydrolysis in the Melt," *Biomacromolecules*, vol. 4, no. 3, pp. 835–840, May 2003, doi: 10.1021/bm034060j.

[210] A. J. Nijenhuis, D. W. Grijpma, and A. J. Pennings, "Lewis acid catalyzed polymerization of L-lactide. Kinetics and mechanism of the bulk polymerization," *ACS Publications*, May 01, 2002. https://pubs.acs.org/doi/pdf/10.1021/ma00050a006 (accessed Sep. 12, 2022).

[211] E. T. H. Vink, K. R. Rábago, D. A. Glassner, and P. R. Gruber, "Applications of life cycle assessment to NatureWorks™ polylactide (PLA) production," *Polymer Degradation and Stability*, vol. 80, no. 3, pp. 403–419, Jan. 2003, doi: 10.1016/S0141-3910(02)00372-5.

[212] J. Lunt, "Large-scale production, properties and commercial applications of polylactic acid polymers," *Polymer Degradation and Stability*, vol. 59, no. 1, pp. 145–152, Jan. 1998, doi: 10.1016/S0141-3910(97)00148-1.

[213] D. Garlotta, "A Literature Review of Poly(Lactic Acid)," *Journal of Polymers and the Environment*, vol. 9, no. 2, pp. 63–84, Apr. 2001, doi: 10.1023/A:1020200822435.

[214] L. Avérous and E. Pollet, "Biodegradable Polymers," in *Environmental Silicate Nano-Biocomposites*, L. Avérous and E. Pollet, Eds., in Green Energy and Technology. London: Springer, 2012, pp. 13–39. doi: 10.1007/978-1-4471-4108-2_2.

[215] M. Todo, S.-D. Park, T. Takayama, and K. Arakawa, "Fracture micromechanisms of bioabsorbable PLLA/PCL polymer blends," *Engineering Fracture Mechanics*, vol. 74, no. 12, pp. 1872–1883, Aug. 2007, doi: 10.1016/j.engfracmech.2006.05.021.

[216] T. Patr\'{\i}cio, A. Glória, and P. J. D. S. Bartolo, "Mechanical and biological behaviour of PCL and PCL/PLA scaffolds for tissue engineering applications," *Chemical Engineering Transactions*, vol. 32, pp. 1645–1650, 2013.

[217] L. Fambri and C. Migliaresi, "Crystallization and Thermal Properties," in *Poly(Lactic Acid)*, John Wiley & Sons, Ltd, 2022, pp. 135–151. doi: 10.1002/9781119767480.ch8.

[218] J. C. Middleton and A. J. Tipton, "Synthetic biodegradable polymers as orthopedic devices," *Biomaterials*, vol. 21, no. 23, pp. 2335–2346, Dec. 2000, doi: 10.1016/S0142-9612(00)00101-0.

[219] R. Auras, B. Harte, and S. Selke, "An Overview of Polylactides as Packaging Materials," *Macromolecular Bioscience*, vol. 4, no. 9, pp. 835–864, 2004, doi: 10.1002/mabi.200400043.

[220] A. R. Boccaccini, J. J. Blaker, V. Maquet, W. Chung, R. Jérôme, and S. N. Nazhat, "Poly(D,L-lactide) (PDLLA) foams with TiO2 nanoparticles and PDLLA/TiO2-Bioglass® foam composites for tissue engineering scaffolds," *J Mater Sci*, vol. 41, no. 13, pp. 3999–4008, Jul. 2006, doi: 10.1007/s10853-006-7575-7.

[221] L.-T. Lim, R. Auras, and M. Rubino, "Processing technologies for poly(lactic acid)," *Progress in Polymer Science*, vol. 33, no. 8, pp. 820–852, Aug. 2008, doi: 10.1016/j.progpolymsci.2008.05.004.

[222] K. Hamad, M. Kaseem, H. W. Yang, F. Deri, and Y. G. Ko, "Properties and medical applications of polylactic acid: A review," *Express Polym. Lett.*, vol. 9, no. 5, pp. 435–455, 2015, doi: 10.3144/expresspolymlett.2015.42.

[223] M. Murariu and P. Dubois, "PLA composites: From production to properties," *Advanced Drug Delivery Reviews*, vol. 107, pp. 17–46, Dec. 2016, doi: 10.1016/j.addr.2016.04.003.

[224] H. Tsuji, in: Y. Doi, and A. Steinbüchel, "Biopolymers. Polyesters III. Applications and commercial products," *Biopolymers*, vol. 4, pp. 129–178, 2002.

[225] S. Ramakrishna, J. Mayer, E. Wintermantel, and K. W. Leong, "Biomedical applications of polymer-composite materials: a review," *Composites Science and Technology*, vol. 61, no. 9, pp. 1189–1224, Jul. 2001, doi: 10.1016/S0266-3538(00)00241-4.

[226] A. Södergård and M. Stolt, "Properties of lactic acid based polymers and their correlation with composition," *Progress in Polymer Science*, vol. 27, no. 6, pp. 1123–1163, Jul. 2002, doi: 10.1016/S0079-6700(02)00012-6.

[227] A.-C. Albertsson and I. K. Varma, "Recent Developments in Ring Opening Polymerization of Lactones for Biomedical Applications," *Biomacromolecules*, vol. 4, no. 6, pp. 1466–1486, Nov. 2003, doi: 10.1021/bm034247a.

[228] S. Nájera, M. Michel, J. Kyung-Hwan, and J. N. S. Kim, "Characterization of 3D printed PLA/PCL/TiO_2 composites for Cancellous bone," *J. Mater. Sci. Eng*, vol. 7, p. 417, 2018.

[229] R. Auras, B. Harte, and S. Selke, "An Overview of Polylactides as Packaging Materials," *Macromolecular Bioscience*, vol. 4, no. 9, Art. no. 9, 2004, doi: 10.1002/mabi.200400043.

[230] K. Petersen, P. V. Nielsen, and M. B. Olsen, "Physical and Mechanical Properties of Biobased Materials Starch, Polylactate and Polyhydroxybutyrate," *Starch - Stärke*, vol. 53, no. 8, pp. 356–361, 2001, doi: 10.1002/1521-379X(200108)53:8<356::AID-STAR356>3.0.CO;2-7.

[231] C. Bastioli, "Global Status of the Production of Biobased Packaging Materials," *Starch - Stärke*, vol. 53, no. 8, pp. 351–355, 2001, doi: 10.1002/1521-379X(200108)53:8<351::AID-STAR351>3.0.CO;2-R.

[232] J. A. Cicero, J. R. Dorgan, J. Garrett, J. Runt, and J. S. Lin, "Effects of molecular architecture on two-step, melt-spun poly(lactic acid) fibers," *Journal of Applied Polymer Science*, vol. 86, no. 11, pp. 2839–2846, 2002, doi: 10.1002/app.11268.

[233] Y. Di, S. Iannace, E. D. Maio, and L. Nicolais, "Poly(lactic acid)/organoclay nanocomposites: Thermal, rheological properties and foam processing," *Journal of Polymer Science Part B: Polymer Physics*, vol. 43, no. 6, pp. 689–698, 2005, doi: 10.1002/polb.20366.

[234] E.-S. Park, H. K. Kim, J. H. Shim, H. S. Kim, L. W. Jang, and J.-S. Yoon, "Compatibility of poly(butadiene-co-acrylonitrile) with poly(L-lactide) and poly(3-hydroxybutyrate-co-3-hydroxyvalerate)," *Journal of Applied Polymer Science*, vol. 92, no. 6, pp. 3508–3513, 2004, doi: 10.1002/app.20356.

[235] T. Semba, K. Kitagawa, U. S. Ishiaku, and H. Hamada, "The effect of crosslinking on the mechanical properties of polylactic acid/polycaprolactone blends," *Journal of Applied Polymer Science*, vol. 101, no. 3, pp. 1816–1825, 2006, doi: 10.1002/app.23589.

[236] A. Ujcic, I. Fortelny, S. Krejcikova, E. Pavlova, J. Hodan, and M. Slouf, "Effects of thermal treatment and nucleating agents on crystallinity, toughness, and stiffness of PLA/PCL blends," *Express Polymer Letters*, vol. 16, no. 3, pp. 221–233, Mar. 2022, doi: 10.3144/expresspolymlett.2022.18.

[237] R. H. A. Haq, O. M. F. Marwah, M. N. A. Rahman, H. F. Haw, H. Abdullah, and S. Ahmad, "3D Printer parameters analysis for PCL/PLA filament wire using Design of Experiment (DOE)," *IOP Conf. Ser.: Mater. Sci. Eng.*, vol. 607, no. 1, p. 012001, Aug. 2019, doi: 10.1088/1757-899X/607/1/012001.

[238] Hindawi, "Plasticized Biodegradable Poly(lactic acid) Based Composites Containing Cellulose in Micro- and Nanosize." https://www.hindawi.com/journals/je/2013/329379/ (accessed Sep. 13, 2022).

[239] J. Urquijo, G. Guerrica-Echevarría, and J. I. Eguiazábal, "Melt processed PLA/PCL blends: Effect of processing method on phase structure, morphology, and mechanical properties," *Journal of Applied Polymer Science*, vol. 132, no. 41, 2015, doi: 10.1002/app.42641.

[240] B. Imre and B. Pukánszky, "Compatibilization in bio-based and biodegradable polymer blends," *European Polymer Journal*, vol. 49, no. 6, pp. 1215–1233, Jun. 2013, doi: 10.1016/j.eurpolymj.2013.01.019.

[241] H. Bai, C. Huang, H. Xiu, Y. Gao, Q. Zhang, and Q. Fu, "Toughening of poly(l-lactide) with poly(ε-caprolactone): Combined effects of matrix crystallization and impact modifier particle size," *Polymer*, vol. 54, no. 19, pp. 5257–5266, Aug. 2013, doi: 10.1016/j.polymer.2013.07.051.

[242] X. Zhao, H. Hu, X. Wang, X. Yu, W. Zhou, and S. Peng, "Super tough poly(lactic acid) blends: a comprehensive review," *RSC Advances*, vol. 10, no. 22, pp. 13316–13368, 2020, doi: 10.1039/D0RA01801E.

[243] H. Bai, H. Xiu, J. Gao, H. Deng, Q. Zhang, M. Yang, and Q. Fu, "Tailoring Impact Toughness of Poly(l-lactide)/Poly(ε-caprolactone) (PLLA/PCL) Blends by Controlling Crystallization of PLLA Matrix," *ACS Appl. Mater. Interfaces*, vol. 4, no. 2, pp. 897–905, Feb. 2012, doi: 10.1021/am201564f.

[244] L. S. Nair and C. T. Laurencin, "Prog. Polym. Sci.," 2007.

[245] J. L. Lowery, N. Datta, and G. C. Rutledge, "Effect of fiber diameter, pore size and seeding method on growth of human dermal fibroblasts in electrospun poly(ε-caprolactone) fibrous mats," *Biomaterials*, vol. 31, no. 3, pp. 491–504, Jan. 2010, doi: 10.1016/j.biomaterials.2009.09.072.

[246] J. Más Estellés, A. Vidaurre, J. M. Meseguer Dueñas, and I. Castilla Cortázar, "Physical characterization of polycaprolactone scaffolds," *J Mater Sci: Mater Med*, vol. 19, no. 1, pp. 189–195, Jan. 2008, doi: 10.1007/s10856-006-0101-2.

[247] Y. Ikada and H. Tsuji, "Biodegradable polyesters for medical and ecological applications," *Macromolecular Rapid Communications*, vol. 21, no. 3, pp. 117–132, 2000, doi: 10.1002/(SICI)1521-3927(20000201)21:3<117::AID-MARC117>3.0.CO;2-X.

[248] S. Alix, A. Mahieu, C. Terrie, J. Soulestin, E. Gerault, M. G. J. Feuilloley, R. Gattin, V. Edon, T. Ait-Younes, and N. Leblanc, "Active pseudo-multilayered films from polycaprolactone and starch based matrix for food-packaging applications," *European Polymer Journal*, vol. 49, no. 6, pp. 1234–1242, Jun. 2013, doi: 10.1016/j.eurpolymj.2013.03.016.

[249] G. Gaucher, M.-H. Dufresne, V. P. Sant, N. Kang, D. Maysinger, and J.-C. Leroux, "Block copolymer micelles: preparation, characterization and application in drug delivery," *Journal of Controlled Release*, vol. 109, no. 1, pp. 169–188, Dec. 2005, doi: 10.1016/j.jconrel.2005.09.034.

[250] G. Gaucher, P. Satturwar, M.-C. Jones, A. Furtos, and J.-C. Leroux, "Polymeric micelles for oral drug delivery," *European Journal of Pharmaceutics and Biopharmaceutics*, vol. 76, no. 2, pp. 147–158, Oct. 2010, doi: 10.1016/j.ejpb.2010.06.007.

[251] K. Gorna and S. Gogolewski, "In vitro degradation of novel medical biodegradable aliphatic polyurethanes based on ϵ-caprolactone and Pluronics® with various hydrophilicities," *Polymer Degradation and Stability*, vol. 75, no. 1, pp. 113–122, Jan. 2002, doi: 10.1016/S0141-3910(01)00210-5.

[252] V. Guarino, M. Lewandowska, M. Bil, B. Polak, and L. Ambrosio, "Morphology and degradation properties of PCL/HYAFF11® composite scaffolds with multi-scale degradation rate," *Composites Science and Technology*, vol. 70, no. 13, pp. 1826–1837, Nov. 2010, doi: 10.1016/j.compscitech.2010.06.015.

[253] V. Guarino, P. Taddei, M. D. Foggia, C. Fagnano, G. Ciapetti, and L. Ambrosio, "The Influence of Hydroxyapatite Particles on In Vitro Degradation Behavior of Poly ε-Caprolactone–Based Composite Scaffolds," *Tissue Engineering Part A*, vol. 15, no. 11, pp. 3655–3668, Nov. 2009, doi: 10.1089/ten.tea.2008.0543.

[254] A. Raizada, A. Bandari, and B. Kumar, "Polymers in drug delivery: A review," *Int. J. Pharm. Res. Dev*, vol. 2, no. 8, pp. 9–20, 2010.

[255] V. R. Sinha, K. Bansal, R. Kaushik, R. Kumria, and A. Trehan, "Poly-ϵ-caprolactone microspheres and nanospheres: an overview," *International Journal of Pharmaceutics*, vol. 278, no. 1, pp. 1–23, Jun. 2004, doi: 10.1016/j.ijpharm.2004.01.044.

[256] A. Iwamoto and Y. Tokiwa, "Effect of the phase structure on biodegradability of polypropylene/poly(ε-caprolactone) blends," *Journal of Applied Polymer Science*, vol. 52, no. 9, pp. 1357–1360, 1994, doi: 10.1002/app.1994.070520920.

[257] H. Tsuji and T. Ishizaka, "Porous biodegradable polyesters, 3. Preparation of porous Poly (ϵ-caprolactone) films from blends by selective enzymatic removal of Poly (l-lactide)," *Macromol Biosci*, vol. 1, pp. 59–65, 2001.

[258] S. Eshraghi and S. Das, "Mechanical and Microstructural Properties of Polycaprolactone Scaffolds with 1-D, 2-D, and 3-D Orthogonally Oriented Porous Architectures Produced by Selective Laser Sintering," *Acta Biomater*, vol. 6, no. 7, pp. 2467–2476, Jul. 2010, doi: 10.1016/j.actbio.2010.02.002.

[259] A. Ostafinska, I. Fortelny, M. Nevoralova, J. Hodan, J. Kredatusova, and M. Slouf, "Synergistic effects in mechanical properties of PLA/PCL blends with optimized composition, processing, and morphology," *RSC Adv.*, vol. 5, no. 120, pp. 98971–98982, Nov. 2015, doi: 10.1039/C5RA21178F.

[260] A. Ostafinska, I. Fortelný, J. Hodan, S. Krejčíková, M. Nevoralová, J. Kredatusová, Z. Kruliš, J. Kotek, and M. Šlouf, "Strong synergistic effects in PLA/PCL blends: Impact of PLA matrix viscosity," *Journal of the Mechanical Behavior of Biomedical Materials*, vol. 69, pp. 229–241, May 2017, doi: 10.1016/j.jmbbm.2017.01.015.

[261] I. Fortelny, A. Ujcic, L. Fambri, and M. Slouf, "Phase Structure, Compatibility, and Toughness of PLA/PCL Blends: A Review," *Frontiers in Materials*, vol. 6, 2019, Accessed: Sep. 13, 2022. [Online]. Available: https://www.frontiersin.org/articles/10.3389/fmats.2019.00206

[262] C. Chu, G. Graf, and D. W. Rosen, "Design for Additive Manufacturing of Cellular Structures," *Computer-Aided Design and Applications*, vol. 5, no. 5, pp. 686–696, Jan. 2008, doi: 10.3722/cadaps.2008.686-696.

[263] F. P. W. Melchels, M. A. N. Domingos, T. J. Klein, J. Malda, P. J. Bartolo, and D. W. Hutmacher, "Additive manufacturing of tissues and organs," *Progress in Polymer Science*, vol. 37, no. 8, pp. 1079–1104, Aug. 2012, doi: 10.1016/j.progpolymsci.2011.11.007.

[264] R. Leal, F. M. Barreiros, L. Alves, F. Romeiro, J. C. Vasco, M. Santos, and C. Marto, "Additive manufacturing tooling for the automotive industry," *Int J Adv Manuf Technol*, vol. 92, no. 5, pp. 1671–1676, Sep. 2017, doi: 10.1007/s00170-017-0239-8.

[265] M. Richardson and B. Haylock, "Designer/maker: the rise of additive manufacturing, domestic-scale production and the possible implications for the automotive industry," *Computer-Aided Design & Applications PACE*, vol. 2, pp. 33–48, 2012.

[266] T. Lecklider, "3D printing drives automotive innovation," *EE-Evaluation Engineering*, vol. 56, no. 1, pp. 16–20, Jan. 2017.

[267] S. C. Joshi and A. A. Sheikh, "3D printing in aerospace and its long-term sustainability," *Virtual and Physical Prototyping*, vol. 10, no. 4, pp. 175–185, Oct. 2015, doi: 10.1080/17452759.2015.1111519.

[268] L. J. Kumar and C. G. Krishnadas Nair, "Current Trends of Additive Manufacturing in the Aerospace Industry," in *Advances in 3D Printing & Additive Manufacturing Technologies*, D. I. Wimpenny, P. M. Pandey, and L. J. Kumar, Eds., Singapore: Springer, 2017, pp. 39–54. doi: 10.1007/978-981-10-0812-2_4.

[269] F. Calignano, D. Manfredi, E. P. Ambrosio, S. Biamino, M. Lombardi, E. Atzeni, A. Salmi, P. Minetola, L. Iuliano, and P. Fino "Overview on Additive Manufacturing Technologies," *Proceedings of the IEEE*, vol. 105, no. 4, pp. 593–612, Apr. 2017, doi: 10.1109/JPROC.2016.2625098.

[270] P. Parandoush and D. Lin, "A review on additive manufacturing of polymer-fiber composites," *Composite Structures*, vol. 182, pp. 36–53, Dec. 2017, doi: 10.1016/j.compstruct.2017.08.088.

[271] W. Gao, Y. Zhang, D. Ramanujan, K. Ramani, Y. Chen, C. B. Williams, C. C. L. Wang, Y. C. Shin, S. Zhang, and P. D. Zavattieri, "The status, challenges, and future of additive manufacturing in engineering," *Computer-Aided Design*, vol. 69, pp. 65–89, Dec. 2015, doi: 10.1016/j.cad.2015.04.001.

[272] B. Wittbrodt and J. M. Pearce, "The effects of PLA color on material properties of 3-D printed components," *Additive Manufacturing*, vol. 8, pp. 110–116, Oct. 2015, doi: 10.1016/j.addma.2015.09.006.

[273] B. M. Tymrak, M. Kreiger, and J. M. Pearce, "Mechanical properties of components fabricated with open-source 3-D printers under realistic environmental conditions," *Materials & Design*, vol. 58, pp. 242–246, Jun. 2014, doi: 10.1016/j.matdes.2014.02.038.

[274] A. Lanzotti, M. Grasso, G. Staiano, and M. Martorelli, "The impact of process parameters on mechanical properties of parts fabricated in PLA with an open-source 3-D printer," *Rapid Prototyping Journal*, vol. 21, no. 5, pp. 604–617, Jan. 2015, doi: 10.1108/RPJ-09-2014-0135.

[275] M. F. Afrose, S. H. Masood, P. Iovenitti, M. Nikzad, and I. Sbarski, "Effects of part build orientations on fatigue behaviour of FDM-processed PLA material," *Prog Addit Manuf*, vol. 1, no. 1, pp. 21–28, Jun. 2016, doi: 10.1007/s40964-015-0002-3.

[276] S. Ahn, M. Montero, D. Odell, S. Roundy, and P. K. Wright, "Anisotropic material properties of fused deposition modeling ABS," *Rapid Prototyping Journal*, vol. 8, no. 4, pp. 248–257, Jan. 2002, doi: 10.1108/13552540210441166.

[277] A. Dorigato, V. Moretti, S. Dul, S. H. Unterberger, and A. Pegoretti, "Electrically conductive nanocomposites for fused deposition modelling," *Synthetic Metals*, vol. 226, pp. 7–14, Apr. 2017, doi: 10.1016/j.synthmet.2017.01.009.

[278] F. Zhang, L. Wang, Z. Zheng, Y. Liu, and J. Leng, "Magnetic programming of 4D printed shape memory composite structures," *Composites Part A: Applied Science and Manufacturing*, vol. 125, p. 105571, Oct. 2019, doi: 10.1016/j.compositesa.2019.105571.

[279] S. R. Rajpurohit and H. K. Dave, "Analysis of tensile strength of a fused filament fabricated PLA part using an open-source 3D printer," *Int J Adv Manuf Technol*, vol. 101, no. 5, pp. 1525–1536, Apr. 2019, doi: 10.1007/s00170-018-3047-x.

[280] T. F. Abbas, F. M. Othman, and H. B. Ali, "Influence of layer thickness on impact property of 3D-printed PLA," *Int. Res. J. Eng. Technol.(Irjet)*, vol. 5, pp. 1–4, 2018.

[281] A. K. Aworinde, S. O. Adeosun, F. A. Oyawale, E. T. Akinlabi, and S. A. Akinlabi, "Parametric Effects of Fused Deposition Modelling on the Mechanical Properties of Polylactide Composites: A Review," *J. Phys.: Conf. Ser.*, vol. 1378, no. 2, p. 022060, Dec. 2019, doi: 10.1088/1742-6596/1378/2/022060.

[282] S. Wang, Y. Ma, Z. Deng, S. Zhang, and J. Cai, "Effects of fused deposition modeling process parameters on tensile, dynamic mechanical properties of 3D printed polylactic acid materials," *Polymer Testing*, vol. 86, p. 106483, Jun. 2020, doi: 10.1016/j.polymertesting.2020.106483.

[283] S. Martin, H. Jiří, B. Jiří, Š. Jiří, and B. Luboš, "Mechanical Properties of Products Made of Abs with Respect to Individuality of Fdm Production Processes," 2017, doi: 10.17973/MMSJ.2017_02_2016188.

[284] D. Croccolo, M. De Agostinis, and G. Olmi, "Experimental characterization and analytical modelling of the mechanical behaviour of fused deposition processed parts made of ABS-M30," *Computational Materials Science*, vol. 79, pp. 506–518, Nov. 2013, doi: 10.1016/j.commatsci.2013.06.041.

[285] C. M. S. Vicente, T. S. Martins, M. Leite, A. Ribeiro, and L. Reis, "Influence of fused deposition modeling parameters on the mechanical properties of ABS parts," *Polymers for Advanced Technologies*, vol. 31, no. 3, pp. 501–507, 2020, doi: 10.1002/pat.4787.

[286] M. Dawoud, I. Taha, and S. J. Ebeid, "Mechanical behaviour of ABS: An experimental study using FDM and injection moulding techniques," *Journal of Manufacturing Processes*, vol. 21, pp. 39–45, Jan. 2016, doi: 10.1016/j.jmapro.2015.11.002.

[287] M. S. Priya, K. Naresh, R. Jayaganthan, and R. Velmurugan, "A comparative study between in-house 3D printed and injection molded ABS and PLA polymers for low-frequency applications," *Mater. Res. Express*, vol. 6, no. 8, p. 085345, Jun. 2019, doi: 10.1088/2053-1591/ab2776.

[288] K. Chockalingam, N. Jawahar, and J. Praveen, "Enhancement of Anisotropic Strength of Fused Deposited ABS Parts by Genetic Algorithm," *Materials and Manufacturing Processes*, vol. 31, no. 15, pp. 2001–2010, Nov. 2016, doi: 10.1080/10426914.2015.1127949.

[289] B. D. Josephson, "The discovery of tunnelling supercurrents," *Rev. Mod. Phys.*, vol. 46, no. 2, pp. 251–254, Apr. 1974, doi: 10.1103/RevModPhys.46.251.

[290] J. López-García, V. Sánchez-Alarcos, V. Recarte, J.A. Rodríguez-Velamazán, I. Unzueta, J.A. García, F. Plazaola, P. La Roca, and J. I. Pérez-Landazábal, "Effect of high-energy ball-milling on the magneto-structural properties of a $Ni_{45}Co_5Mn_{35}Sn_{15}$ alloy," *Journal of Alloys and Compounds*, vol. 858, p. 158350, Mar. 2021, doi: 10.1016/j.jallcom.2020.158350.

[291] G. Cavazzini, F. Cugini, F. Puglielli, S. Fabbric, D. Delmonte, G. Trevisi, L. Nasi, L. Righi, S. Ener, L. Pfeuffer, D. Koch, O. Gutfleisch, F. Albertini, and M, Solzi, "Effect of size and disorder on martensitic phase transition and thermal hysteresis in milled Ni-Mn-In-Co micro-particles," *Journal of Alloys and Compounds*, vol. 906, p. 164377, Jun. 2022, doi: 10.1016/j.jallcom.2022.164377.

[292] J. López-García, I. Unzueta, V. Sánchez-Alarcos, V. Recarte, J. I. Pérez-Landazábal, J.A. Rodríguez-Velamazán, J. A. García, and F. Plazaola, "Correlation between defects and magneto-structural properties in Ni-Mn-Sn metamagnetic shape memory alloys," *Intermetallics*, vol. 94, pp. 133–137, Mar. 2018, doi: 10.1016/j.intermet.2017.12.028.

[293] J. I. Pérez-Landazábal, V. Sánchez-Alarcos, V. Recarte, O. A. Lambri, F. G. Bonifacich, D. L.R. Khanna, I. Unzueta, J.A. García, F. Plazaola, J. López-García, Jimenez Ruiz, J.A. Rodríguez-Velamazán, and E. Cesari, "Influence of Structural Defects on the Properties of Metamagnetic Shape Memory Alloys," *Metals*, vol. 10, no. 9, Art. no. 9, Sep. 2020, doi: 10.3390/met10091131.

[294] L. A. Aslanov, G. V. Fetisov, and J. A. K. Howard, *Crystallographic Instrumentation*. International Union of Crystallography, 1998.

[295] J. I. Pérez-Landazábal, V. Sánchez-Alarcos, V. Recarte, O. A. Lambri, F. G. Bonifacich, D. L.R. Khanna, I. Unzueta, J.A. García, F. Plazaola, J. López-García, Jimenez Ruiz, J.A. Rodríguez-Velamazán, and E. Cesari, "Influence of Structural Defects on the Properties of Metamagnetic Shape Memory Alloys," *Metals*, vol. 10, no. 9, Art. no. 9, Sep. 2020, doi: 10.3390/met10091131.

[296] G. T. Li, Z. H. Liu, X. Q. Ma, S. Y. Yu, and Y. Liu, "Grinding-induced martensite stabilization in Mn50Ni33.5Sn8Co8.5 alloy," *Materials Letters*, vol. 107, pp. 239–242, Sep. 2013, doi: 10.1016/j.matlet.2013.06.027.

[297] B. Tian, F. Chen, Y. X. Tong, L. Li, and Y. F. Zheng, "Phase Transformation and Magnetic Property of Ni-Mn-Ga Powders Prepared by Dry Ball Milling," *J. of Materi Eng and Perform*, vol. 21, no. 12, pp. 2530–2534, Dec. 2012, doi: 10.1007/s11665-012-0365-2.

[298] X. H. Tian, J. H. Sui, X. Zhang, X. H. Zheng, and W. Cai, "Grain size effect on martensitic transformation, mechanical and magnetic properties of Ni–Mn–Ga alloy fabricated by spark plasma sintering," *Journal of Alloys and Compounds*, vol. 514, pp. 210–213, Feb. 2012, doi: 10.1016/j.jallcom.2011.11.077.

[299] J. I. Pérez-Landazábal, V. Sánchez-Alarcos, V. Recarte, O. A. Lambri, F. G. Bonifacich, D. L.R. Khanna, I. Unzueta, J.A. García, F. Plazaola, J. López-García, Jimenez Ruiz, J.A. Rodríguez-Velamazán, and E. Cesari, "Influence of Structural Defects on the Properties of Metamagnetic Shape Memory Alloys," *Metals*, vol. 10, no. 9, Art. no. 9, Sep. 2020, doi: 10.3390/met10091131.

[300] M. Piao, K. Otsuka, S. Miyazaki, and H. Horikawa, "Mechanism of the A_s Temperature Increase by Pre-deformation in Thermoelastic Alloys," *Materials Transactions, JIM*, vol. 34, no. 10, pp. 919–929, 1993, doi: 10.2320/matertrans1989.34.919.

[301] S. Kustov, J. Pons, E. Cesari, M. Morin, and J. Van Humbeeck, "Athermal stabilization of Cu–Al–Be β1′ martensite due to plastic deformation and heat treatment," *Materials Science and Engineering: A*, vol. 373, no. 1, pp. 328–338, May 2004, doi: 10.1016/j.msea.2004.02.001.

[302] H. C. Lin, S. K. Wu, T. S. Chou, and H. P. Kao, "The effects of cold rolling on the martensitic transformation of an equiatomic TiNi alloy," *Acta Metallurgica et Materialia*, vol. 39, no. 9, pp. 2069–2080, Sep. 1991, doi: 10.1016/0956-7151(91)90177-3.

[303] Y. Liu and D. Favier, "Stabilisation of martensite due to shear deformation via variant reorientation in polycrystalline NiTi," *Acta Materialia*, vol. 48, no. 13, pp. 3489–3499, Aug. 2000, doi: 10.1016/S1359-6454(00)00129-4.

[304] G. Tan and Y. Liu, "Comparative study of deformation-induced martensite stabilisation via martensite reorientation and stress-induced martensitic transformation in NiTi," *Intermetallics*, vol. 12, no. 4, pp. 373–381, Apr. 2004, doi: 10.1016/j.intermet.2003.11.008.

[305] S. Belyaev, N. Resnina, T. Rakhimov, and V. Andreev, "Martensite stabilisation effect in Ni-rich NiTi shape memory alloy with different structure and martensitic transformations," *Sensors and Actuators A: Physical*, vol. 305, p. 111911, Apr. 2020, doi: 10.1016/j.sna.2020.111911.

[306] C. Picornell, J. Pons, A. Paulsen, J. Frenzel, V. Kaminskii, K. Sapozhnikov, J. Van Humbeeck, and S. Kustov, "Burst-like reverse martensitic transformation during heating, cooling and under isothermal conditions in stabilized Ni-Ti-Nb," *Scripta Materialia*, vol. 180, pp. 23–28, Apr. 2020, doi: 10.1016/j.scriptamat.2020.01.018.

[307] C. Picornell, J. Pons, and E. Cesari, "Stabilisation of martensite by applying compressive stress in Cu-Al-Ni single crystals," *Acta Materialia*, vol. 49, no. 20, pp. 4221–4230, Dec. 2001, doi: 10.1016/S1359-6454(01)00308-1.

[308] S. Kustov, J. Pons, E. Cesari, and J. Van Humbeeck, "Chemical and mechanical stabilization of martensite," *Acta Materialia*, vol. 52, no. 15, pp. 4547–4559, Sep. 2004, doi: 10.1016/j.actamat.2004.06.012.

[309] S. Kustov, J. Pons, E. Cesari, and J. Van Humbeeck, "Pinning-induced stabilization of martensite: Part II. Kinetic stabilization in Cu–Zn–Al alloy due to pinning of moving interfaces," *Acta Materialia*, vol. 52, no. 10, pp. 3083–3096, Jun. 2004, doi: 10.1016/j.actamat.2004.03.010.

[310] V. A. Chernenko, J. Pons, E. Cesari, and I. K. Zasimchuk, "Transformation behaviour and martensite stabilization in the ferromagnetic Co–Ni–Ga Heusler alloy," *Scripta Materialia*, vol. 50, no. 2, pp. 225–229, Jan. 2004, doi: 10.1016/j.scriptamat.2003.09.024.

[311] R. Chulist, P. Czaja, T. Tokarski, and M. Faryna, "Martensite stabilisation in single crystalline Ni-Mn-Ga and Ni-Mn-Sn magnetic shape memory alloys," *Materials Letters*, vol. 230, pp. 266–269, Nov. 2018, doi: 10.1016/j.matlet.2018.07.140.

[312] R. Kainuma, Y. Imano, W. Ito, Y. Sutou, H. Morito, S. Okamoto, O. Kitakami, K. Oikawa, A. Fujita, T. Kanomata, and K. Ishida, "Magnetic-field-induced shape recovery by reverse phase transformation," *Nature*, vol. 439, no. 7079, pp. 957–960, Feb. 2006, doi: 10.1038/nature04493.

[313] V. K. Sharma, M. K. Chattopadhyay, K. H. B. Shaeb, A. Chouhan, and S. B. Roy, "Large magnetoresistance in Ni50Mn34In16 alloy," *Appl. Phys. Lett.*, vol. 89, no. 22, p. 222509, Nov. 2006, doi: 10.1063/1.2399365.

[314] V. Recarte, J. I. Pérez-Landazábal, S. Kustov, and E. Cesari, "Entropy change linked to the magnetic field induced martensitic transformation in a Ni–Mn–In–Co shape memory alloy," *Journal of Applied Physics*, vol. 107, no. 5, p. 053501, Mar. 2010, doi: 10.1063/1.3318491.

[315] K. Otsuka and X. Ren, "Mechanism of martensite aging effects and new aspects," *Materials Science and Engineering: A*, vol. 312, no. 1, pp. 207–218, Aug. 2001, doi: 10.1016/S0921-5093(00)01877-3.

[316] C. Seguí, E. Cesari, J. Font, J. Muntasell, and V. A. Chernenko, "Martensite stabilization in a high temperature Ni-Mn-Ga alloy," *Scripta Materialia*, vol. 53, no. 3, pp. 315–318, Aug. 2005, doi: 10.1016/j.scriptamat.2005.04.009.

[317] K. Tsuchiya, D. Ohtoyo, M. Umemoto, and H. Ohtsuka, "Effect of Isothermal Aging on Martensitic Transformation in Ni-Mn-Ga Alloys".

[318] H. Seiner, "Mobile Interfacial Microstructures in Single Crystals of Cu-Al-Ni Shape Memory Alloy," *Shap. Mem. Superelasticity*, vol. 1, no. 2, pp. 268–274, Jun. 2015, doi: 10.1007/s40830-015-0009-0.

[319] B. Lu and J. Liu, "Elastocaloric effect and superelastic stability in Ni-Mn-In-Co polycrystalline Heusler alloys: hysteresis and strain-rate effects," *Sci Rep*, vol. 7, no. 1, Art. no. 1, May 2017, doi: 10.1038/s41598-017-02300-3.

[320] B. Lu, F. Xiao, A. Yan, and J. Liu, "Elastocaloric effect in a textured polycrystalline Ni-Mn-In-Co metamagnetic shape memory alloy," *Appl. Phys. Lett.*, vol. 105, no. 16, p. 161905, Oct. 2014, doi: 10.1063/1.4899147.

[321] Yu. V. Kaletina, E. D. Greshnova, A. Yu. Kaletin, N. Yu. Frolova, and V. P. Pilyugin, "Structure and Properties of Ni47Mn42In11 Alloy after Severe Plastic Deformation," *Phys. Metals Metallogr.*, vol. 120, no. 2, pp. 171–176, Feb. 2019, doi: 10.1134/S0031918X19020078.

[322] A. A. Mendonça, L. Ghivelder, P. L. Bernardo, Hanlin Gu, R. D. James, L. F. Cohen, and A. M. Gomes, "Experimentally correlating thermal hysteresis and phase compatibility in multi-functional Heusler alloys," *Phys. Rev. Materials*, vol. 4, no. 11, p. 114403, Nov. 2020, doi: 10.1103/PhysRevMaterials.4.114403.

[323] H. Z. Lu, H.W. Ma, W.S. Cai, X. Luo, Z. Wang, C.H. Song, S. Yin, and C. Yang, "Stable tensile recovery strain induced by a Ni_4Ti_3 nanoprecipitate in a $Ni_{50.4}Ti_{49.6}$ shape memory alloy fabricated via selective laser melting," *Acta Materialia*, vol. 219, p. 117261, Oct. 2021, doi: 10.1016/j.actamat.2021.117261.

[324] X. Song, C. Xiong, F. Zhang, Y. Nie, and Y. Li, "Strain induced martensite stabilization in β Ti-Zr-Nb shape memory alloy," *Materials Letters*, vol. 259, p. 126914, Jan. 2020, doi: 10.1016/j.matlet.2019.126914.

[325] L. Mañosa, X. Moya, A. Planes, O. Gutfleisch, J. Lyubina, M. Barrio, Josep-Lluís Tamarit, S. Aksoy; T. Krenke, and M. Acet, "Effects of hydrostatic pressure on the magnetism and martensitic transition of Ni-Mn-In magnetic superelastic alloys," *Appl. Phys. Lett.*, vol. 92, no. 1, p. 012515, Jan. 2008, doi: 10.1063/1.2830999.

[326] P. Czaja, J. Przewoźnik, M. Kowalczyk, A. Wierzbicka-Miernik, J. Morgiel, and W. Maziarz, "Microstructural origins of martensite stabilization in Ni49Co1Mn37.5Sn6.5In6 metamagnetic shape memory alloy," *J Mater Sci*, vol. 54, no. 5, pp. 4340–4353, Mar. 2019, doi: 10.1007/s10853-018-3112-8.

[327] E. Villa, V. A. Chernenko, E. Cesari, and P. Lazpita, "Low-frequency Elastic and Thermomechanical Analysis of Ni-Mn-In(Co) Single Crystals," *Materials Today: Proceedings*, vol. 2, pp. S871–S874, Jan. 2015, doi: 10.1016/j.matpr.2015.07.420.

[328] J. I. Pérez-Landazábal, V. Recarte, V. Sánchez-Alarcos, M. J. Ruiz, and E. Cesari, "Outstanding role of the magnetic entropy in arrested austenite in an ordered $Ni_{45}Mn_{36.7}In_{13.3}Co_5$ metamagnetic shape memory alloy," *Scripta Materialia*, vol. 168, pp. 91–95, Jul. 2019, doi: 10.1016/j.scriptamat.2019.04.035.

[329] J. I. Pérez-Landazábal, V. Recarte, V. Sánchez-Alarcos, J. J. Beato-López, J. A. Rodríguez-Velamazán, J. Sánchez-Marcos, C. Gómez-Polo, and E. Cesari, "Giant direct and inverse magnetocaloric effect linked to the same forward martensitic transformation," *Sci Rep*, vol. 7, no. 1, Art. no. 1, Oct. 2017, doi: 10.1038/s41598-017-13856-5.

[330] V. V. Khovailo, T. Takagi, A. N. Vasilev, H. Miki, M. Matsumoto, and R. Kainuma, "On order-disorder (L21 → B2′) phase transition in $Ni_{2+x}Mn_{1-x}Ga$ Heusler alloys," *Physica Status Solidi (A) Applied Research*, vol. 183, no. 2, pp. R1–R3, Feb. 2001, doi: 10.1002/1521-396X(200102)183:23.0.CO;2-B.

[331] S. Larumbe, I. Unzueta, V. Sánchez-Alarcos, J.I. Pérez-Landazábal, V. Recarte, J.A. García, and F. Plazaola, "Low temperature magnetic properties of a $Ni_{50}Mn_{34}In_{16}$ ball-milled metamagnetic shape memory alloy," *Journal of Non-Crystalline Solids*, vol. 447, pp. 16–20, Sep. 2016, doi: 10.1016/j.jnoncrysol.2016.05.023.

[332] R. Y. Umetsu, A. Fujita, W. Ito, T. Kanomata, and R. Kainuma, "Determination of the magnetic ground state in the martensite phase of Ni-Mn-Z (Z= In, Sn and Sb) off-stoichiometric Heusler alloys by nonlinear AC susceptibility," *J. Phys.: Condens. Matter*, vol. 23, no. 32, p. 326001, Jul. 2011, doi: 10.1088/0953-8984/23/32/326001.

[333] J. A. Mydosh, *Spin Glasses: An Experimental Introduction*. London: CRC Press, 2014. doi: 10.1201/9781482295191.

[334] J. A. Mydosh, "Spin glasses: redux: an updated experimental/materials survey," *Reports on Progress in Physics*, vol. 78, no. 5, p. 052501, 2015.

[335] K. Binder and A. P. Young, "Spin glasses: Experimental facts, theoretical concepts, and open questions," *Rev. Mod. Phys.*, vol. 58, no. 4, pp. 801–976, Oct. 1986, doi: 10.1103/RevModPhys.58.801.

[336] A. K. Khorwal, Nancy, S. Dash, A. Kumar, A.V. Lukoyanov, E.I. Shreder, Y. Bitla, M. Vasundhara, and A. K. Patra, "Evidence for canonical spin glass behaviour in polycrystalline $Mn_{1.5}Fe_{1.5}Al$ Heusler alloy," *Journal of Magnetism and Magnetic Materials*, vol. 546, p. 168752, Mar. 2022, doi: 10.1016/j.jmmm.2021.168752.

[337] M. Bałanda and S. M. Dubiel, "An AC magnetic susceptibility study of a sigma-phase $Fe_{65.9}V_{34.1}$ alloy," *Journal of Alloys and Compounds*, vol. 663, pp. 77–81, Apr. 2016, doi: 10.1016/j.jallcom.2015.11.054.

[338] B. Venkateswarlu, R. Hari Krishnan, J. Arout Chelvane, P. D. Babu, and N. Harish Kumar, "Coexistence of cluster ferromagnetism and cluster spin-glass like behaviour in melt-quenched

$Cu_2Mn_{0.5}Fe_{0.5}Al$ Heusler alloy," *Journal of Alloys and Compounds*, vol. 777, pp. 373–381, Mar. 2019, doi: 10.1016/j.jallcom.2018.10.327.

[339] F. F. Barquín, J. C. G. Sal, P. Gorria, J. S. Garitaonandia, and J. M. Barandiarán, "Dynamic susceptibility of reentrant Fe-rich inhomogeneous amorphous alloys," *Eur. Phys. J. B*, vol. 35, no. 1, pp. 3–12, Sep. 2003, doi: 10.1140/epjb/e2003-00250-0.

[340] S. Mukherjee, R. Ranganathan, P. S. Anilkumar, and P. A. Joy, "Static and dynamic response of cluster glass in $La_{0.5}Sr_{0.5}CoO_3$," *Phys. Rev. B*, vol. 54, no. 13, pp. 9267–9274, Oct. 1996, doi: 10.1103/PhysRevB.54.9267.

[341] O. F. de Lima, J. a. H. Coaquira, R. L. de Almeida, and S. K. Malik, "Magnetic phase separation and cluster-spin-glass behavior in LaMn1−xFexO3+y," *Journal of Applied Physics*, vol. 107, no. 9, p. 09E107, May 2010, doi: 10.1063/1.3364056.

[342] S. Takahashi, A. Chiba, and E. Takahashi, "The influence of plastic deformation on the spin-glass in Fe-37.0 at.% Al compound," *Physics Letters A*, vol. 197, no. 4, pp. 350–352, Jan. 1995, doi: 10.1016/S0375-9601(05)80016-7.

[343] A. L. Alves, E. C. Passamani, V. P. Nascimento, A. Y. Takeuchi, and C. Larica, "Influence of grain refinement and induced crystal defects on the magnetic properties of $Ni_{50}Mn_{36}Sn_{14}$Heusler alloy," *Journal of Physics D: Applied Physics*, vol. 43, no. 34, p. 345001, 2010, doi: 10.1088/0022-3727/43/34/345001.

[344] J. López-García, V. Sánchez-Alarcos, V. Recarte, J.A. Rodríguez-Velamazán, I. Unzueta, J.A. García, F. Plazaola, P. La Roca, and J. I. Pérez-Landazábal "Effect of high-energy ball-milling on the magneto-structural properties of a $Ni_{45}Co_5Mn_{35}Sn_{15}$ alloy," *Journal of Alloys and Compounds*, vol. 858, p. 158350, Mar. 2021, doi: 10.1016/j.jallcom.2020.158350.

[345] E. C. Passamani, V.P. Nascimento, C. Larica, A.Y. Takeuchi, A.L. Alves, J.R. Proveti, M.C. Pereira, and J.D. Fabris, "The influence of chemical disorder enhancement on the martensitic transformation of the $Ni_{50}Mn_{36}Sn_{14}$ Heusler-type alloy," *Journal of Alloys and Compounds*, vol. 509, no. 30, pp. 7826–7832, 2011, doi: https://doi.org/10.1016/j.jallcom.2011.05.018.

[346] B. Tian, F. Chen, Y. Liu, and Y. F. Zheng, "Effect of ball milling and post-annealing on magnetic properties of Ni49.8Mn28.5Ga21.7 alloy powders," *Intermetallics*, vol. 16, no. 11–12, pp. 1279–1284, Nov. 2008, doi: 10.1016/j.intermet.2008.08.002.

[347] V. Sánchez-Alarcos, V. Recarte, J.I. Pérez-Landazábal, S. Larumbe, R. Caballero-Flores, I. Unzueta, J.A. García, F. Plazaola, and J.A. Rodríguez-Velamazán, "Mechanically induced disorder and crystallization process in Ni-Mn-In ball-milled alloys," *Journal of Alloys and Compounds*, vol. 689, pp. 983–991, Dec. 2016, doi: 10.1016/j.jallcom.2016.08.068.

[348] J. I. Pérez-Landazábal, V. Sánchez-Alarcos, V. Recarte, O. A. Lambri, F. G. Bonifacich, D. L.R. Khanna, I. Unzueta, J.A. García, F. Plazaola, J. López-García, M. Jimenez Ruiz, J.A. Rodríguez-Velamazán, and E. Cesari, "Influence of Structural Defects on the Properties of Metamagnetic Shape Memory Alloys," *Metals* , vol. 10, no. 9. 2020. doi: 10.3390/met10091131.

[349] A. M. Tishin, "Magnetic refrigeration in the low-temperature range," *Journal of Applied Physics*, vol. 68, no. 12, pp. 6480–6484, Dec. 1990, doi: 10.1063/1.347186.

[350] O. Gutfleisch, T. Gottschall, M. Fries, D. Benke, I. Radulov, K. P. Skokov, H. Wende, M. Gruner, M. Acet, P. Entel and M. Farle, "Mastering hysteresis in magnetocaloric materials," *Philosophical Transactions of the Royal Society A: Mathematical, Physical and Engineering Sciences*, vol. 374, no. 2074, p. 20150308, Aug. 2016, doi: 10.1098/rsta.2015.0308.

[351] A. Waske, M. E. Gruner, T. Gottschall, and O. Gutfleisch, "Magnetocaloric materials for refrigeration near room temperature," *MRS Bulletin*, vol. 43, no. 4, pp. 269–273, Apr. 2018, doi: 10.1557/mrs.2018.69.

[352] E. Özen Öner, M. E. Pekdemir, E. Ercan, Y. Say, M. Kök, and Y. Aydoğdu, "Novel of (PLA/PCL blend)/Gd2O3 rare earth oxide nanocomposites: Shape memory effect, thermal, magnetic, and mechanical properties," *Polymer Composites*, vol. 43, no. 5, pp. 3096–3103, 2022, doi: 10.1002/pc.26602.

[353] C. Yue, M. Li, Y. Liu, Y. Fang, Y. Song, M. Xu and J. Li, "Three-dimensional printing of cellulose nanofibers reinforced PHB/PCL/Fe3O4 magneto-responsive shape memory polymer composites with excellent mechanical properties," *Additive Manufacturing*, vol. 46, p. 102146, Oct. 2021, doi: 10.1016/j.addma.2021.102146.

[354] Y. S. Nam and T. G. Park, "Biodegradable polymeric microcellular foams by modified thermally induced phase separation method," *Biomaterials*, vol. 20, no. 19, pp. 1783–1790, Oct. 1999, doi: 10.1016/S0142-9612(99)00073-3.

[355] H.-P. Hentze and M. Antonietti, “Porous polymers and resins for biotechnological and biomedical applications,” *Reviews in Molecular Biotechnology*, vol. 90, no. 1, pp. 27–53, Mar. 2002, doi: 10.1016/S1389-0352(01)00046-0.

[356] P. van de Witte, P. J. Dijkstra, J. W. A. van den Berg, and J. Feijen, “Metastable liquid–liquid and solid–liquid phase boundaries in polymer–solvent–nonsolvent systems,” *Journal of Polymer Science Part B: Polymer Physics*, vol. 35, no. 5, pp. 763–770, 1997, doi: 10.1002/(SICI)1099-0488(19970415)35:5<763::AID-POLB4>3.0.CO;2-N.

[357] E. Rezabeigi, P. M. Wood-Adams, and R. A. L. Drew, “Production of porous polylactic acid monoliths via nonsolvent induced phase separation,” *Polymer*, vol. 55, no. 26, pp. 6743–6753, Dec. 2014, doi: 10.1016/j.polymer.2014.10.063.

[358] T. Duan, Y. Lv, H. Xu, J. Jin, and Z. Wang, “Structural Effects of Residual Groups of Graphene Oxide on Poly(ε-Caprolactone)/Graphene Oxide Nanocomposite,” *Crystals*, vol. 8, no. 7, Art. no. 7, Jul. 2018, doi: 10.3390/cryst8070270.

[359] G. Wang, S. Yang, Z. Wei, X. Dong, H. Wang, and M. Qi, “Facile preparation of poly(ε-caprolactone)/Fe3O4@graphene oxide superparamagnetic nanocomposites,” *Polym. Bull.*, vol. 70, no. 8, pp. 2359–2371, Aug. 2013, doi: 10.1007/s00289-013-0957-5.

[360] F. Liu, C. Mao, S. Wu, B. Wang, C. Wu, T. Hu, X. Gong, “Preparation and characterization of poly(ε-caprolactone)/Fe3O4 nanocomposites,” *POLYMER CRYSTALLIZATION*, vol. 4, no. 4, p. e10196, 2021, doi: 10.1002/pcr2.10196.

[361] G. Zhu, Q. Xu, R. Qin, H. Yan, and G. Liang, “Effect of γ-radiation on crystallization of polycaprolactone,” *Radiation Physics and Chemistry*, vol. 74, no. 1, pp. 42–50, Sep. 2005, doi: 10.1016/j.radphyschem.2004.11.006.

[362] S. Qian, H. Zhang, W. Yao, and K. Sheng, “Effects of bamboo cellulose nanowhisker content on the morphology, crystallization, mechanical, and thermal properties of PLA matrix biocomposites,” *Composites Part B: Engineering*, vol. 133, pp. 203–209, Jan. 2018, doi: 10.1016/j.compositesb.2017.09.040.

[363] T. Duan, Y. Lv, H. Xu, J. Jin, and Z. Wang, “Structural Effects of Residual Groups of Graphene Oxide on Poly(ε-Caprolactone)/Graphene Oxide Nanocomposite,” *Crystals*, vol. 8, no. 7, Art. no. 7, Jul. 2018, doi: 10.3390/cryst8070270.

[364] S. Qian, H. Mao, K. Sheng, J. Lu, Y. Luo, and C. Hou, “Effect of low-concentration alkali solution pretreatment on the properties of bamboo particles reinforced poly(lactic acid) composites,” *Journal of Applied Polymer Science*, vol. 130, no. 3, pp. 1667–1674, 2013, doi: 10.1002/app.39328.

[365] P. V. Trevizoli, A. T. Nakashima, G. F. Peixer, and J. R. Barbosa, “Performance assessment of different porous matrix geometries for active magnetic regenerators,” *Applied Energy*, vol. 187, pp. 847–861, Feb. 2017, doi: 10.1016/j.apenergy.2016.11.031.

[366] N. Chujo, F. Kino, K. Kume, T. Aoyama, and M. Fukuda, “Effect of Packing Fraction on Magnetic Properties of the Fe-Si-Al Powder Cores by Coarse Powder and Fine Powder Mixing,” 粉体および粉末冶金, vol. 63, no. 7, pp. 624–629, 2016, doi: 10.2497/jjspm.63.624.

[367] V. Wong, K. Wai Chan, and A. Kwok Hung Kwan, “Applying Theories of Particle Packing and Rheology to Concrete for Sustainable Development,” *Organization, technology & management in construction : an international journal*, vol. 5, no. 2, pp. 844–851, Dec. 2013.

[368] R. K. McGEARY, “Mechanical Packing of Spherical Particles,” *Journal of the American Ceramic Society*, vol. 44, no. 10, pp. 513–522, 1961, doi: 10.1111/j.1151-2916.1961.tb13716.x.

[369] T. Lei, K. Engelbrecht, K. K. Nielsen, and C. T. Veje, “Study of geometries of active magnetic regenerators for room temperature magnetocaloric refrigeration,” *Applied Thermal Engineering*, vol. 111, pp. 1232–1243, Jan. 2017, doi: 10.1016/j.applthermaleng.2015.11.113.

[370] J. Tušek, A. Kitanovski, S. Zupan, I. Prebil, and A. Poredoš, “A comprehensive experimental analysis of gadolinium active magnetic regenerators,” *Applied Thermal Engineering*, vol. 53, no. 1, pp. 57–66, Apr. 2013, doi: 10.1016/j.applthermaleng.2013.01.015.

[371] J. D. Moore, D. Klemm, D. Lindackers, S. Grasemann, R. Träger, J. Eckert, L. Löber, S. Scudino, M. Katter, A. Barcza, K. P. Skokov and O. Gutfleisch, “Selective laser melting of La(Fe,Co,Si)13 geometries for magnetic refrigeration,” *Journal of Applied Physics*, vol. 114, no. 4, Art. no. 4, Jul. 2013, doi: 10.1063/1.4816465.